

Copyright
by
Todd Philip Meyrath
2005

The Dissertation Committee for Todd Philip Meyrath
certifies that this is the approved version of the following dissertation:

**Experiments with Bose-Einstein Condensation in an
Optical Box**

Committee:

Mark G. Raizen, Supervisor

Michael F. Becker

Manfred Fink

Lothar W. Frommhold

Greg O. Sitz

**Experiments with Bose-Einstein Condensation in an
Optical Box**

by

Todd Philip Meyrath, B.S.;B.S.;M.S.;M.S.

DISSERTATION

Presented to the Faculty of the Graduate School of
The University of Texas at Austin
in Partial Fulfillment
of the Requirements
for the Degree of

DOCTOR OF PHILOSOPHY

THE UNIVERSITY OF TEXAS AT AUSTIN

May 2005

To my parents, Frank and Donna Meyrath,
for so many years of love and support,
without which I would have never made it this far.

Acknowledgments

I would like to thank Professor Mark Raizen who has been my advisor during these years. Mark has been an endless source of ideas and directions for interesting experiments. He is an outstanding physicist and genuine individual. Working in Mark's laboratory has been an excellent and unique privilege.

During my years at UT, I have interacted with quite a number of people. In recent years I have worked with Jay Hanssen, Florian Schreck, and Chih-sung Chuu on the projects presented here. I've known Jay since the beginning of graduate school, we had many of our classes together as well as being work partners in the lab for many projects. In addition to being a very talented physicist, Jay is one of the best karaoke singers I have ever seen (not heard). Jay and I enjoyed the pain and thrill of learning to make a BEC from scratch and a multitude of barbecue runs. Florian was our postdoc. He always amazed me with his limitless drive and determination. He is a first class experimentalist — whom I expect will be a big star the physics community. No matter what was happening or how problematic a system could become, he had an idea. Seeing Florian program was like watching an action movie. He is also a pretty mean in-line skater, and I have the wounds to prove it. Chih-sung joined our experiment sometime shortly after our BEC apparatus was started. Chih-sung is an extremely smart if not very audible guy and is

as dedicated to the experiment as he is to his beloved homeland. He has an excellent understanding of physics and experimental work. Our experiment was joined recently by Gabriel Price. Off to a good start, he and Chih-sung will take the experiment to the next stages in the future.

On the sodium experiment, Braulio Gutiérrez has lead a mammoth project, narrowly losing to us the race for the BEC in our lab. Of course, he knows that the deck was stacked with rubidium. I've known Braulio all of my graduate career. He is an outstanding physicist with a detailed understanding of science and also a man of broad interest. The memory of our year as senior lab TAs will linger on forever. Kevin Henderson is a tremendously hardworking scientist and a bright and intuitive experimentalist. Another man of broad interests, he was always an interesting one with whom to converse. His tales are always fascinating to hear. Hrishikesh Kelkar is a very talented individual with a strong grasp of physics and the elbow grease to go with it. He is also a mean bowler. The sodium experiment was recently joined by Tongcang Li, I can't say that I know him well yet, but I am confident he will have an enjoyable time in the lab that has treated me so well.

Artëm Dudarev and Chuanwei Zhang have done amazing theoretical work that has supported our experimental thrust. Artëm is an extremely talented physicist with a vast knowledge of interesting physics. He has also shared an apartment with me for some years and has always been an interesting one with whom to converse. He brought to me an interest in eastern European language and culture. Chuanwei has a most impressive understanding physics

and a keen ability to solve problems.

To everything, there is a beginning. When I arrived, there were already senior students Martin Fischer, Daniel Steck, and Windell Oskay as well as postdoc Valery Milner. When I first walked through the doors I was stunned by the knowledge and experience of these individuals. I was fortunate enough to spend time with each of them. As I worked on projects in the first years, it was most helpful to have their various opinions and ideas which seemed limitless.

I had the unique opportunity to interact with Kirk Madison. A physicist who graduated from our lab before my time, but came back to UT as a postdoc in the high energy laser group. Discussions that Jay and I had with Kirk laid much of the ground work for this experiment. Kirk and I had many interesting conversations especially about the many technical issues of building a BEC apparatus.

Outside of the lab, the department has provided us with the unparalleled support of a world-class machine shop run by Allen Schroeder. He is an amazing machinist and an outstanding coordinator of the machine shop effort. His team never failed to dazzle me with their skill and speed. Allen has a keen ability to get the jobs done right and never failed to rapidly respond to our many emergency situations. Jack Clifford has run the student machine shop all my time at UT. In addition to being an extremely friendly individual, he has a keen skill with the machines and taught me all I know about machining. Lanny Sandefur and Ed Baez have been excellent support

in the cryogenics shop. The Center for Nonlinear Dynamics administrative staff Olga Vera, Rosie Tovar, and Elena Simmons made sure our orders went through and made all the paper work go smoothly. They also provided their friendly smiles and kind words.

Thanks would not be complete without mentioning mentioning my beginning in laboratory work as an undergraduate in Mike Schatz's lab at Georgia Tech. Prof. Schatz introduced me to the exciting world of experimental physics. Summer 1997, which I spent as an undergraduate researcher at Los Alamos, was also an outstanding learning experience. I thank Daniel James for his encouragement to pursue graduate studies in physics. I am grateful to my committee who has taken the time to read this dissertation and who have provided guidance and inspiration over the years.

I appreciate the comments and corrections of Jay Hanssen and Artëm Dudarev. I would also like to acknowledge Jay Hanssen who helped with the writing of several sections describing the experimental systems that he designed and built and the dissertation figures that we have shared.

I also must thank the National Science Foundation for three years of support through the NSF Graduate Research Fellowship.

T.P.M.
Austin, Texas
April 2005

Experiments with Bose-Einstein Condensation in an Optical Box

Publication No. _____

Todd Philip Meyrath, Ph.D.
The University of Texas at Austin, 2005

Supervisor: Mark G. Raizen

This dissertation details the experimental methods used to produce a Bose-Einstein condensate (BEC) in an optical box trap. This novel optical trap type has strong confinement in two directions comparable to that which is possible in an optical lattice, yet produces individually addressable condensates. The optical trap is based on a pair of elongated Hermite-Gaussian TEM_{01} mode beams and tailored by designer box wall beams. Using this method, we have succeeded in producing individual highly confined lower dimensional condensates. The box trap is integrated with single atom detection capability, paving the way for studies of quantum atom statistics.

Table of Contents

Acknowledgments	v
Abstract	ix
List of Tables	xvi
List of Figures	xvii
Chapter 1. Overview	1
1.1 Units and Orders of Magnitude	1
1.2 Bose-Einstein Condensation	2
1.3 Why MOTs, Magnetic Traps, and Optical Traps?	3
1.4 Why a Single High Frequency Optical Trap?	4
1.5 Chapter Overview	5
Chapter 2. Operational Concepts	7
2.1 Light Forces on Atoms	7
2.2 Magneto-Optical Trapping	9
2.2.1 Optical Molasses in 1-D	9
2.2.2 1D-MOT	10
2.3 Magnetic Trapping	13
2.4 Optical Trapping	14
2.5 Absorptive Imaging	15
Chapter 3. Experimental Apparatus	17
3.1 Introduction	17
3.2 Vacuum Chamber	19
3.2.1 Upper Chamber	19
3.2.2 Lower Chamber	22

3.2.2.1	Pumping Region	23
3.2.2.2	Science Chamber Region	25
3.3	The Near Resonance Lasers	29
3.3.1	The Grating Stabilized Lasers	31
3.3.1.1	The MOT Master Laser	34
3.3.1.2	The Repump Laser	36
3.3.2	Injection Locked MOT Lasers	38
3.3.2.1	Upper MOT Horizontal Slave Laser	40
3.3.2.2	Upper MOT Diagonal Slave Laser	42
3.3.2.3	Lower MOT Slave Laser	44
3.4	The Far-Off Resonance Lasers	44
3.5	The Magnetic Trap	46
3.5.1	Quadrupole Ioffe Configuration	47
3.5.2	Experimental Characterization	50
3.5.3	Decompressed Ioffe Configuration	52
3.5.4	Auxiliary Coils	57
3.5.5	Coil Structure and Construction	58
3.5.6	Current Control	65
3.6	Computer Control	69
3.7	Experimental Sequence	70
3.7.1	Upper MOT	70
3.7.2	Lower MOT	72
3.7.3	Optical Pumping and Magnetic Trap Loading	75
3.7.4	Evaporative Cooling	79
3.7.5	The Signature of Condensation	84
3.8	Imaging of Atoms	86
3.8.1	Absorption Imaging	86
3.8.2	Florescence Imaging	90
3.8.3	Atom Counting	90

Chapter 4. Lower Dimensional BEC	98
4.1 Bose-Einstein Statistics	98
4.2 Weakly Interacting Gas	100
4.3 Three-Dimensional Condensates	102
4.4 Two-Dimensional Condensates	104
4.5 One-Dimensional Condensates	106
Chapter 5. Bose-Einstein Condensate in an Optical Box	109
5.1 Introduction	109
5.2 Beam Overview	110
5.3 Other Optical Traps	115
5.3.1 Gravito-optical Trap	115
5.3.2 Compressed Gaussian Sheets Optical Trap	118
5.4 Hermite-Gaussian TEM ₀₁ Trap	120
5.5 Hermite-Gaussian Beam Production	123
5.6 Optical Trap Beam Layout	126
5.7 Beam Multiplexing	130
5.8 Loading Sequence for the Optical Trap	132
5.9 Two-Dimensional BEC in hTEM ₀₁ Trap	136
5.10 Box Wall Beams	138
5.11 Compensation Beam	139
5.12 Bose-Einstein Condensate in a Box	140
5.13 Comments on the Optical Trap	144
Chapter 6. A Quantum Tweezer for Atoms	148
6.1 The Quantum Tweezer Concept	148
6.2 Quantum Tweezer Theory	150
6.3 Experimental Possibilities	156
6.4 Counting Atoms in the Optical Trap	158
6.5 Future Outlook	163
Appendices	164

Appendix A. Magnetic Coils	165
A.1 Some Theory of Electromagnets	165
A.1.1 Exact Field of a Circular Current Loop	165
A.1.2 Approximations for Circular Current Loops	167
A.1.3 Circular Coil Pairs	167
A.1.4 Exact Field of a Square Current Loop	169
A.1.5 Approximations for Square Current Loops	171
A.1.6 Square Coil Pairs	172
A.2 Numerical Calculations of Fields	174
A.3 Power and Cooling	175
A.3.1 Power into a Coil	175
A.3.2 Water Cooling	176
A.3.3 Stability of a Magnetic Trap	177
A.4 Some Standard American Wire Types	178
A.5 Inductance and Switching	179
A.5.1 Inductance and Parasitics	179
A.5.2 Switching	181
A.5.3 Comment on Steel Chambers	183
Appendix B. Magnetic Trap Schematics and Photos	184
Appendix C. Analog Control Electronics	191
C.1 Multipurpose PID Controller	191
C.2 Current Controller for Laser Diodes	198
C.3 Laser Intensity Stabilization	198
C.4 Uni- and Bi-directional Current Output Stages	201
C.5 Main Power Output Stage for QUIC Trap	205
C.6 Shunt Power Circuit for QUIC Trap Coils	207
C.7 Analog Optocouplers	210

Appendix D. Computer Control System Hardware	213
D.1 Digital Bus System	213
D.1.1 Overview	213
D.1.2 Concept	218
D.1.3 Why a Strobe?	218
D.1.4 Flat Ribbon Connection Diagram	219
D.1.5 Computer Output	221
D.2 Digital Output Boards	221
D.2.1 Features	222
D.2.2 The Printed Circuit Board	223
D.2.3 Circuit Theory	223
D.3 Analog Output Boards	226
D.3.1 Features	227
D.3.2 Advantages and Disadvantages	227
D.3.3 Outputs	228
D.3.4 The Printed Circuit Board	229
D.3.5 Circuit Theory	229
D.4 Digital Radio Frequency Synthesizer	236
D.4.1 Digital Side	236
D.4.2 Programming the DDS	237
D.4.3 Clock Options	238
D.4.4 Analog Side	239
D.4.5 Output Options	239
D.4.6 FSK, BPSK, Hold, Shaped Keying Options	240
D.4.7 Jumper Options	241
D.4.8 Comments and Improvement Possibilities	242
D.4.9 Soldering Method	243
Appendix E. Optics Concepts	244
E.1 Beam Propagation	244
E.1.1 The Propagation Equation	244
E.1.2 Gaussian Beams	245

E.1.3 Hermite-Gaussian Beams	246
E.2 Fourier Optics	247
E.3 Optical Modulators	249
E.3.1 Acousto-Optic Modulators	249
E.3.2 Electro-Optic Modulators	251
Appendix F. Rubidium Properties	253
Bibliography	257
Vita	266

List of Tables

3.1	Characteristics of the laser diodes.	31
3.2	Current states of QUIC trap	65
5.1	Beams and parameters for the optical trap.	114
A.1	Wire standards.	178
F.1	^{87}Rb physical properties.	254
F.2	^{87}Rb D ₂ ($5^2\text{S}_{1/2} \rightarrow 5^2\text{P}_{3/2}$) transition optical properties. . . .	254
F.3	^{87}Rb D ₁ ($5^2\text{S}_{1/2} \rightarrow 5^2\text{P}_{1/2}$) transition optical properties. . . .	254

List of Figures

2.1	1-D MOT diagram.	11
3.1	The main optical table.	18
3.2	The shared optical table.	18
3.3	The upper chamber region.	20
3.4	The UHV pumping region.	24
3.5	The lower chamber.	25
3.6	The upper chamber photograph.	27
3.7	The science chamber photograph.	27
3.8	Vacuum chamber photo.	28
3.9	D ₂ line diagram with laser frequencies.	30
3.10	Master laser photo.	32
3.11	The MOT master laser locking setup.	33
3.12	The MOT saturated absorption signal.	35
3.13	MOT master laser distribution scheme.	37
3.14	Repump saturated absorption signal.	38
3.15	Repump laser distribution scheme.	39
3.16	Pictures of the slave lasers.	40
3.17	Beam distribution for the upper MOT horizontal slave laser.	41
3.18	Beam distribution for the upper MOT diagonal beam slave laser.	43
3.19	Beam distribution for the lower MOT beam slave laser.	45
3.20	Functional diagram of the QUIC trap.	47
3.21	Calculated field for the QUIC trap.	49
3.22	Vector field plot for the compressed QUIC trap.	51
3.23	Experimental characterization of magnetic trap.	53
3.24	Calculated field for the decompressed QUIC trap.	55
3.25	QUIC trap coil schematic.	60
3.26	Operational QUIC trap photo.	63

3.27	Functional schematic for QUIC current.	67
3.28	Current ramp pictorial plots.	68
3.29	A fluorescence image of the upper MOT.	71
3.30	The optical setup for the lower MOT.	73
3.31	An absorption image of the lower MOT.	74
3.32	An absorption image of the lower MOT after polarization gradient cooling.	75
3.33	Diagram of the optical pumping scheme.	76
3.34	Absorption images of atoms within different configurations of the magnetic trap.	79
3.35	Functional schematic of RF evaporative cooling.	80
3.36	Phase space density during the sequence.	82
3.37	Images of the atomic cloud at various points during the evaporation sequence.	83
3.38	The bimodal distribution of a condensate.	85
3.39	Absorption image of a nearly pure BEC.	86
3.40	Atom counting pictorial.	91
3.41	Single atom detection “super lens”.	92
3.42	Photon count rates taken during the operation of a weak MOT.	94
3.43	A histogram of the counts shown in Figure 3.42.	95
3.44	A plot of the reliability of the single atom detection system.	96
5.1	Optical Box Pictorial.	109
5.2	Optical trap beam orientation.	112
5.3	Designer blue beams.	113
5.4	Potential of a gravito-optical trap.	117
5.5	Potential of a compressed Gaussian sheet trap	119
5.6	Potential of a TEM ₀₁ trap.	122
5.7	TEM ₀₁ beam production method.	123
5.8	Photo of phase plate.	124
5.9	Profile of vTEM ₀₁ mode beam.	125
5.10	Optics layout for production of the optical trap beams.	127
5.11	Layout of the horizontal optical trap beams.	129

5.12	Layout of the vertical optical trap beams.	130
5.13	Multiple frequency AOM.	131
5.14	Loading sequence of the optical box.	135
5.15	BEC Expansion from hTEM ₀₁ trap.	136
5.16	Box wall beam profile.	138
5.17	Compensation beam profile.	139
5.18	BEC in a box.	141
5.19	Compensation and small BECs.	142
6.1	Pictorial of tweezer operation.	151
6.2	Energy diagrams for the tweezer system.	153
6.3	Extraction probability for a harmonic and box trap.	156
6.4	Box wall beam as a tweezer lattice.	157
6.5	Pictorial of cleaning.	159
6.6	Fluorescence signal for 10 ³ atoms from the optical trap.	161
6.7	Fluorescence signal for a single atom from the optical trap.	162
A.1	Coordinates for a circular current loop.	166
A.2	Helmholtz and Anti-Helmholtz coil pairs.	168
A.3	Coordinates for a square current loop.	170
A.4	Inductor coil geometry.	180
A.5	Coil equivalent circuit.	180
A.6	Method for measuring practical coil resonance.	181
A.7	Coil switch off circuits.	182
B.1	Wire winding schematic for QUIC trap primary coils.	185
B.2	Assembled schematic of QUIC trap.	186
B.3	Assembled QUIC trap photo	187
B.4	Assembly photos of a quadrupole coil.	188
B.5	Assembly photos of the Ioffe coil.	189
B.6	QUIC trap electrical connectors photo.	190
C.1	Multipurpose PID controller schematic.	197
C.2	Functional schematic of laser intensity stabilization.	200

C.3	Photo of multipurpose PID PCB as for laser intensity stabilization.	201
C.4	Bidirectional output stage schematic.	204
C.5	Main QUIC trap current controller output stage schematic. . .	206
C.6	Shunt power circuit for QUIC trap primary coils.	209
C.7	Analog optocoupler schematic.	212
D.1	General layout of the control system.	214
D.2	Digital Bus Output Concept.	217
D.3	Pin configuration for 50-pin connector.	219
D.4	Strobe Generator Schematic.	220
D.5	Photo of PCB for Digital Outputs.	222
D.6	Digital Output Board Schematic.	225
D.7	Photo of PCB for Analog Outputs.	226
D.8	DAC Board Schematic, digital side.	233
D.9	DAC Board Schematic, analog side.	234
D.10	Photo of Radio Frequency Synthesizer PCB.	235
D.11	9th Order 135 MHz Low Pass Elliptic Filter. This filter gives a very fast drop off after 135 MHz, below 60 dB stopband begins just above 150 MHz. Resonances occur for the LC modes at 155.1 MHz, 156.5 MHz, 193.0 MHz, and 306.0 MHz. The starred capacitors to the ground include estimated stray capacitance due to board layout of 2.1 pF, 1 pF, 1 pF, 1 pF, and 3.5 pF left to right, respectively. These values were estimated from pad area at the nodes. Errors in these capacitances principally affect ripple in both the pass band and stop band. Note that the capacitor values given on the circuit diagram at the end are those of the 1206 chip capacitors which are to be attached to the PCB and are all of standard available values. The chip capacitors and inductors also have some small error, generally order 5% or less which can have an effect on the filter transfer characteristics. The inductors used (see parts list) all have a tiny stray capacitance (order 0.3 pF) which adds to that of its parallel capacitor. The theoretical transfer function is plotted in Figure D.12.	240
D.12	Filter Transfer Function. Theoretical — SPICE plot.	241
E.1	Acousto-Optic Modulator.	250

E.2	Electro-Optic Modulator.	252
F.1	Rubidium 87 D_2 line hyperfine structure.	255
F.2	Rubidium 87 D_1 line hyperfine structure.	256

Chapter 1

Overview

The experiment that is discussed in this dissertation uses neutral rubidium 87 atoms. This is one isotope from the family of alkali metals. The experiments take place inside an ultra-high vacuum chamber. Interactions between the atoms and the outside world is through light in the form of laser beams and magnetic fields produced by controlled electromagnets. In this chapter, the basic ideas and motivation of the experiment are discussed.

1.1 Units and Orders of Magnitude

When referring to ultra-cold atoms, typically the atoms are confined by some sort of trap. In many cases, the trap is harmonic and characterized by ω which corresponds to the classical trap oscillation frequency. For magnetic traps, this is typically of order several hundred Hz and for optical traps as much as several hundred kHz. Traps also have a trap depth. When we speak of trap depth, we mean energy depth. That is, atoms with energy below the trap depth are trapable. The SI unit for energy is Joules, but this is not always convenient for atom traps. Often this quantity is cast in units of temperature by dividing by Boltzmann's constant $k_B = 1.38 \times 10^{-23}$ J/K. The trap depths

of a magnetic trap are typically of the order tens of mK, whereas for an optical trap up to hundreds of μK .

Another unit often used, especially in the context of motion in optical lattices, is photon recoils. This is the amount of mechanical energy transferred to an atom during an absorption event. The recoil energy is given by

$$E_{\text{rec}} = \frac{\hbar^2 k^2}{2m}, \quad (1.1)$$

where k is the wavevector of the light (resonant light for rubidium is at $\lambda \cong 780\text{ nm}$), and m is the mass. The quantity may also be written in terms of temperature. For rubidium 87, this is approximately 360 nK which corresponds to a velocity of about 5.9 mm/s.

Ultra-cold alkali atoms in magnetic or optical traps are typically treated as dilute gases. Peak number density in such systems is on the order of 10^{13} to 10^{15} cm^{-3} — a far cry from solid state densities of order 10^{22} to 10^{23} cm^{-3} . With these densities and with low velocities corresponds to a situation where atom-atom interactions are predominantly two-body and independent of scattering angles.

1.2 Bose-Einstein Condensation

The concept of Bose-Einstein condensation (BEC) can be understood by recalling that particles have a wave nature. The characteristic wavelength is the thermal de Broglie wavelength given by

$$\lambda_{\text{dB}} = \frac{h}{mv} \propto \frac{1}{\sqrt{T}}, \quad (1.2)$$

where h is Planck's constant, m is atomic mass, v is thermal velocity, and T is temperature. This length is of order $10^{-5} \mu\text{m}$ for room temperature atoms and of order $10 \mu\text{m}$ for atoms at around 10 nK. A cloud of atoms enters a BEC state when the inter-atom distance is comparable to the thermal de Broglie wavelength. This typically occurs at temperatures of order 100 nK with densities of order 10^{14}cm^{-3} . This situation can be described in terms of phase space density ρ , the number of atoms in a 3D box with side equal to the thermal de Broglie wavelength. A cloud enters the BEC regime when ρ is near unity.

The extremely low temperatures required can be obtained with initial trapping and cooling in a MOT followed by evaporative cooling in a magnetic or optical trap. One of the most impressive aspects of BEC production in a dilute gas is that the atoms are brought to this final temperature without the use of cryogenic equipment, only the vacuum is necessary.

1.3 Why MOTs, Magnetic Traps, and Optical Traps?

The magneto-optical trap (MOT) is the workhorse of cold atom physics and is used for the loading of atoms in our experiment. The MOT captures atoms from a room temperature thermal distribution and cools them to order $10 \mu\text{K}$. MOTs have the capacity to load on the order of 10^9 atoms. In route towards a BEC, where phase space density of around unity is needed, the MOT takes initial $\rho \cong 10^{-12}$ room temperature atoms to $\rho \cong 10^{-6}$. Although providing a major step in the cooling and trapping of atoms, the MOT has

a limitation. This is that it uses near resonant light which results in recoil heating of the atoms. That is, the MOT can not cool atoms to an arbitrary level. Because of this, magnetic and/or optical dipole traps are required.

The magnetic trap relies on the magnetic moment of atoms and is created using an inhomogeneous magnetic field. A strength of the magnetic trap is that it is used without near resonant light and is therefore not limited in cooling like the MOT. These traps are suitable for evaporative cooling. In route towards a BEC, evaporation can take initial $\rho \cong 10^{-6}$ MOT atoms to $\rho \cong 1$ to produce a BEC. There is a downside to the magnetic trap also. This is that the conventional magnetic trap is limited in trapping strength. Trap oscillation frequencies of order several hundred Hz for rubidium are not sufficient for many experiments. Because of the flexibility of optical beam profiles, it is possible to make high frequency traps either at the focus of a beam or set of beams or in an optical lattice. Optical traps differ from MOTs in that they are far-off resonance and result in conservative potentials. These powerful tools have the advantage of being able to make traps with strengths up to several hundred kHz, see Section 1.4.

1.4 Why a Single High Frequency Optical Trap?

In recent years there has been much interest in development of strongly confining traps for ultra-cold atoms. Such traps are particularly attractive for the production of lower dimensional BEC. Although condensates were initially produced in magnetic traps [1, 2], optical traps are an attractive alternative

due to their flexibility and may be used to generate traps of strength greatly beyond those of conventional magnetic traps. A widely used optical trap of this sort is an optical lattice [3]. Optical lattice experiments have been performed in a wide variety of contexts and may be made of very high strength for the study of some quantum mechanical phenomenon [4–7]. Lattice traps, despite this capacity, have a limitation. Typically an optical lattice has a spacing of half the laser wavelength — order a few hundred nanometers. Condensates loaded into these traps which are initially of a size greater than $10\ \mu\text{m}$ are typically split into thousands of distinct condensates. This limits the addressability of the individual condensates which is desirable for direct atom statistics study of some states such as the Mott-insulator transition [4] and the Tonks-Girardeau gas regime [5–7] and required for others such as the proposed quantum tweezer for atoms [8]. We present a novel optical trap that has the desired characteristics of addressability and high strength.

1.5 Chapter Overview

Chapter 2 reviews some of the operational concepts needed to understand our experimental methods. This includes light forces on atoms, Doppler cooling, magneto-optical trapping (MOT), magnetic and optical trapping, and absorptive imaging. Chapter 3 gives a detailed description of the experimental apparatus and the sequence to produce a BEC in the magnetic trap. This apparatus description includes the vacuum chamber, near and far-off resonance lasers, the magnetic trap, and computer control system. In Chapter 4, a re-

view and summary of the important equations describing lower dimensional BECs are given. This is all in the context of BECs produced in our optical traps. In Chapter 5, we present an optical trap that is used to create lower dimensional condensates. Production of one and two dimensional condensates in this single site high frequency optical trap is a primary result of this thesis. Chapter 6 discusses the theory and possible implementation of a quantum tweezer for atoms. This idea proposed a few years ago [8] has the potential for experimental investigation in our system. The optical trap discussed in Chapter 5 represents a potential reservoir for single atom extraction with the described method.

Lengthy appendices are given at the end which provide many technical details which may be useful to the reader. These appendices include a summary of fields produced by some common electromagnet configurations used in our lab, some magnetic trap schematics and photos from during their construction, current control electronics for various applications, our home built output hardware for the computer control system, a review of some useful optics concepts including Hermite-Gaussian beams, a subject critical for our optical trap, and a summary of the relevant properties of rubidium 87.

Chapter 2

Operational Concepts

2.1 Light Forces on Atoms

Rather than jumping into a derivation of light forces on atoms, which is a topic covered well in many works (see for example [9–11]), some basic ideas will be given.

There are two sorts of mechanical forces of light on atoms that are of interest here. These are the scattering force and the optical dipole force. The scattering force is the work-horse of Doppler cooling, it is based on near resonant absorption followed by spontaneous emission. This is used in our magneto-optical traps, as well as in absorption imaging. The second is used in our far-off resonance optical dipole traps. These are conservative forces.

Consider the absorption process of a photon by a two-level atom in the ground state. After the event, the internal state of the atom has changed to the excited state and the momentum of the photon is absorbed as a recoil which modifies the atom's velocity. The internally excited atom may then undergo spontaneous emission which also produces a recoil of the atom. Since spontaneous emission is equally likely in all directions, the recoil of a large number of spontaneous emission events averages to zero. The average force an

atom feels due to a large number of absorption/emission events is

$$\mathbf{F}_{\text{sp}} = R\hbar\mathbf{k}, \quad (2.1)$$

where \mathbf{k} is the wavevector of the light and R is the rate of scattering. This rate is given by

$$R = \frac{\Gamma}{2} \frac{I/I_s}{1 + I/I_s + (2\delta/\Gamma)^2}, \quad (2.2)$$

where Γ is the rate of decay of the excited state, I is the laser intensity, $I_s = \pi\hbar c/3\lambda^3\tau \cong 1.67 \text{ mW/cm}^2$ is the saturation intensity for rubidium 87, and $\delta = \omega - \omega_0$ is the laser detuning from atomic resonance ω_0 . The laser frequency is ω .

The derivation of Equation 2.2 uses a semiclassical approach where the atom is treated as a two-level quantum system and the light is considered a classical wave. The rotating-wave approximation is also used where $|\omega - \omega_0| \ll \omega + \omega_0$ which is the case for near resonance light. The significance of Equation 2.2 will be discussed in Section 2.2.

Far-off resonance, equations may be obtained from a classical damped driven oscillator model with Γ damping rate. This yields the same results as those for the semiclassical far-off resonance where saturation effects are neglected. The results for the optical dipole potential U and scattering rate R are [9]

$$U(\mathbf{r}) = -\frac{\hbar\Gamma^2}{8I_s} \left(\frac{1}{\omega_0 - \omega} + \frac{1}{\omega_0 + \omega} \right) I(\mathbf{r}), \quad (2.3)$$

and

$$R(\mathbf{r}) = \frac{\Gamma^3}{8I_s} \left(\frac{\omega}{\omega_0} \right)^3 \left(\frac{1}{\omega_0 - \omega} + \frac{1}{\omega_0 + \omega} \right)^2 I(\mathbf{r}). \quad (2.4)$$

The significance of these equations will be discussed in Section 2.4.

Note that Equations 2.2 and 2.4 are the same in the limit of low intensity compared to I_s ($I/I_s \ll 1$), and far detuning compared to linewidth ($(2\delta/\Gamma)^2 \gg 1$). This also requires the rotating wave approximation to neglect the second term in parenthesis in Equation 2.4. Generally, we will use Equation 2.2 for descriptions of MOTs and Equation 2.4 for optical traps because of the beam characteristics of each.

2.2 Magneto-Optical Trapping

This section discusses a one-dimensional model of Doppler cooling and magneto-optical trapping.

2.2.1 Optical Molasses in 1-D

Suppose there are a pair of counterpropagating laser beams of intensity I and frequency ω . The laser detuning is defined as

$$\delta = \omega - \omega_0, \tag{2.5}$$

for which the laser is said to be *red-detuned* or *blue-detuned* for negative or positive values, respectively. More generally, since the atoms are moving, we consider an effective detuning of

$$\delta_{\pm} = \delta \mp kv, \tag{2.6}$$

where the second term on the right is due to the Doppler effect. The total scattering force on an atom in this light field is the sum of the forces from each

laser: $\mathbf{F} = \mathbf{F}_+ + \mathbf{F}_-$. This can be written out as

$$F(v) = \frac{1}{2} \hbar k \Gamma \frac{I}{I_s} \left[\frac{1}{1 + I/I_s + (2\delta_+/\Gamma)^2} - \frac{1}{1 + I/I_s + (2\delta_-/\Gamma)^2} \right]. \quad (2.7)$$

Suppose the lasers are red-detuned. In this case, we see that when an atom is moving towards the source of one of the laser beams it is closer to resonance with that beam and farther from resonance with the other beam. The atom, therefore, scatters more photons traveling in the direction opposite to atomic motion and is slowed down. We can consider this more explicitly in the small velocity limit $v \ll \delta/k$. Equation 2.7 can be expanded to first order in v :

$$F(v) = \frac{4\hbar k(I/I_s)(2\delta/\Gamma)}{[1 + I/I_s + (2\delta/\Gamma)^2]^2} kv. \quad (2.8)$$

Since the laser is red-detuned, Equation 2.8 describes a damping force:

$$F(v) = -\beta v. \quad (2.9)$$

With this in mind, we see that atomic motion in this laser field obeys the differential equation for particle motion in a viscous fluid. Hence, the name *optical molasses* is used.

2.2.2 1D-MOT

Now, consider the situation of a two-level atom with $M_e = -1, 0, +1$ excited state Zeeman levels in a linear magnetic field given by:

$$B = G_m z, \quad (2.10)$$

where G_m is the magnetic field gradient, typically written in units gauss/centimeter. Suppose that we have a pair of counterpropagating circularly polarized laser beams of opposite helicity detuned by δ as in Figure 2.1. The σ_+ light

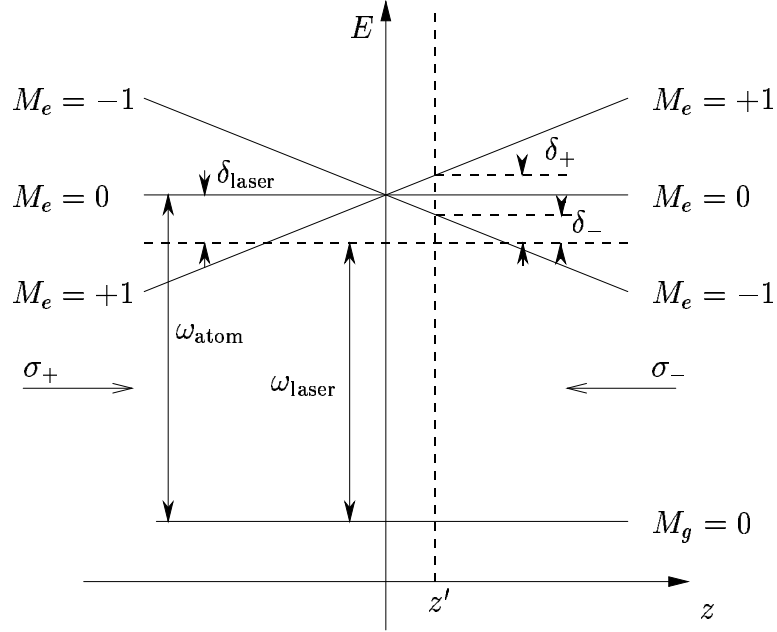


Figure 2.1: Counter propagating σ_+ and σ_- laser beams detuned from atomic resonance by δ are shown. The atomic levels are shifted due to the Zeeman effect in a linear magnetic field. The effective detuning for a stationary atom at position z' is $\delta_{\pm} = \delta \pm g_e \mu_B G_m z' / \hbar$ as in Equations 2.10 and 2.11.

couples to the $M_g = 0 \rightarrow M_e = +1$ transition and the σ_- light to the $M_g = 0 \rightarrow M_e = -1$. The effective detuning, as in Equation 2.2, is

$$\delta_{\pm} = \delta \mp kv \pm (g_e M_e - g_g M_g) \mu_B B / \hbar, \quad (2.11)$$

in general, where M_g and M_e are Zeeman sub-levels of the ground and excited states, and g_g and g_e are corresponding Landé g -factors, $\mu_B \cong h \cdot 1.4 \text{ MHz/G}$

is the Bohr magneton, \hbar is Planck's constant. The second term on the right of Equation 2.11 is due to the Doppler effect and the third to the Zeeman effect. In the case of this simple example, of course, the M_g term on the right does not appear since $M_g = 0$.

The force that an atom feels in this situation is also described by Equation 2.7 but now with δ_{\pm} as defined in Equation 2.11 rather than Equation 2.6. This adds position dependence to F (in addition to velocity dependence):

$$F(z, v) = \frac{1}{2} \hbar k \Gamma \frac{I}{I_s} \left[\frac{1}{1 + I/I_s + (2\delta_+/\Gamma)^2} - \frac{1}{1 + I/I_s + (2\delta_-/\Gamma)^2} \right]. \quad (2.12)$$

In the small velocity and weak field limit, *i.e.* where $v \ll \delta/k$ and $B \ll \hbar\delta/\mu_B$, Equation 2.12 can be expanded:

$$F(z, v) = \frac{4\hbar k(I/I_s)(2\delta/\Gamma)}{[1 + I/I_s + (2\delta/\Gamma)^2]^2} (kv + (g_e\mu_B G_m/\hbar)z). \quad (2.13)$$

The equation of motion is therefore:

$$\ddot{z} + \gamma_{\text{trap}}\dot{z} + \omega_{\text{trap}}^2 z = 0, \quad (2.14)$$

where

$$\gamma_{\text{trap}} = \frac{4\hbar k^2(I/I_s)(2(-\delta)/\Gamma)}{m [1 + I/I_s + (2\delta/\Gamma)^2]^2}, \quad (2.15)$$

$$\omega_{\text{trap}}^2 = \frac{4\hbar k(g_e\mu_B G_m/\hbar)(I/I_s)(2(-\delta)/\Gamma)}{m [1 + I/I_s + (2\delta/\Gamma)^2]^2},$$

and m is the atomic mass. In a MOT, the laser detuning δ is red, so Equation 2.14 is that of a damped harmonic oscillator. This motion can be characterized by

$$\alpha \equiv \frac{\gamma_{\text{trap}}^2}{4\omega_{\text{trap}}^2} = \frac{\hbar k^3(I/I_s)(2(-\delta)/\Gamma)}{(g_e\mu_B G_m/\hbar)m [1 + I/I_s + (2\delta/\Gamma)^2]^2}. \quad (2.16)$$

In a typical experimental situation, with $G_m \approx 10 \text{ G/cm}$ and $\delta \approx 20 \text{ MHz}$, α is of order 100 which clearly makes the motion strongly over damped. Any displacement therefore decays exponentially towards the center.

2.3 Magnetic Trapping

Magnetic trapping is a result of the Zeeman effect. Classically, for an atom with magnetic moment $\boldsymbol{\mu}$ in magnetic field $\mathbf{B}(\mathbf{r})$, the potential energy is given by $U(\mathbf{r}) = -\boldsymbol{\mu} \cdot \mathbf{B}(\mathbf{r})$. The classical magnetic dipole, has some projection along \mathbf{B} which is quantum mechanically given by m_F , that is, $\mu = \hat{\mathbf{B}} \cdot \boldsymbol{\mu} = \mu_B g_F m_F$. Here, $\mu_B \cong h \cdot 1.4 \text{ MHz/G}$ is the Bohr magneton, g_F is the Landé g -factor, m_F is the magnetic quantum number along the axis of the local B-Field, and B is the magnitude [12]. The moment precesses around the local magnetic field at the Larmor frequency $\omega_L = \mu B / \hbar$. Viewing each atom as a magnetic dipole moment, if the external magnetic field direction changes slowly as an atom moves through space, that is $d\theta/dt \ll \omega_L$, where θ is the angle of the magnetic field with respect to some axis, the moment will adiabatically follow the field direction. The condition may also be written

$$\frac{\mathbf{v} \cdot \nabla B}{\omega_L B} \ll 1. \quad (2.17)$$

Typically, with ∇B of at most order 250 G/cm , B at least 1 G , the above ratio can be below 0.01 for atomic velocities of order several hundred recoil velocities. The adiabaticity condition, therefore, applies to atoms in a magnetic trap loaded from a MOT such as in the experiment system described here. For the

^{87}Rb ground state $5^2\text{S}_{1/2}$, the Landé factors are $g_{F=1} = -1/2$ and $g_{F=2} = 1/2$ (see Figure F.1 in Appendix F). This means that the $|F, m_F\rangle$ states $|2, 1\rangle$, $|2, 2\rangle$, $|1, -1\rangle$ are low field seeking states and may be trapped. In the case of a magnetic trap with too weak a field, as discussed above, atoms of sufficient temperature will see a trapping field that varies too quickly and may move to a different m_F state (likely an untrapped state). Such transitions are called Majorana flips and result in trap loss. This is especially problematic for a trap with a field zero which results in Majorana flips for arbitrarily cold atoms.

The depth of a magnetic trap is given by

$$U_d = \mu\Delta B, \quad (2.18)$$

where ΔB is the the difference between the field maximum (at the vacuum container walls) and the field minimum where the atom cloud is centered. Typically, with a difference of ΔB order 10 G this gives a trap depth of order $k_B \cdot 1 \text{ mK}$, where k_B is the Boltzmann constant.

Section 3.5 discusses the details of our magnetic trap. The field geometries of $\mathbf{B}(\mathbf{r})$ and the trap oscillation frequencies are given there.

2.4 Optical Trapping

In general, the rotating wave approximation is valid where the second term in parenthesis of Equations 2.3 and 2.4 may be neglected resulting in

$$U(\mathbf{r}) = \frac{\hbar\Gamma^2}{8I_s} \frac{1}{\delta} I(\mathbf{r}), \quad (2.19)$$

and

$$R(\mathbf{r}) = \frac{\Gamma^3}{8I_s} \left(\frac{\omega}{\omega_0} \right)^3 \frac{1}{\delta^2} I(\mathbf{r}). \quad (2.20)$$

An important thing to note here is that the dipole potential scales as I/δ and the scattering rate as I/δ^2 . This means that the scattering rate may be made small by using a large detuning. Even so, a high enough intensity will allow for a strong dipole potential. This is how optical dipole traps are made. These are conservative traps, where scattering events do not occur on the time scale of the experiment.

Far-off resonance lasers can make attractive or repulsive potentials depending on detuning. For light detuned red of resonance (of the D doublet for alkali atoms such as rubidium), the potential is attractive. For blue detunings, the potential is repulsive. This is because a change in sign of δ changes the sign of U .

2.5 Absorptive Imaging

An important method of imaging atom clouds is with absorption imaging. The basic idea is that an atom cloud has some optical density to a near resonant beam. We image this. Section 3.8.1 discusses absorptive imaging in context of our experimental setup. The idea is explained here.

Considering a near resonant beam traveling through a dilute cloud of

atoms, the scattered power per unit volume is

$$\begin{aligned}\frac{dI}{dz} &= -\hbar\omega Rn, \\ &= -\sigma nI,\end{aligned}\tag{2.21}$$

where $n = n(x, y, z)$ is the atom number density, R is given by Equation 2.2, and scattering cross section is

$$\sigma = \frac{3\lambda^2}{2\pi} \frac{1}{1 + I/I_s + (2\delta/\Gamma)^2}.\tag{2.22}$$

This gives an exponential decay solution of the form

$$I(x, y) = I_0(x, y) \exp \left[-\sigma \int n(x, y, z) dz \right].\tag{2.23}$$

This intensity distribution is imaged onto a CCD camera. This raw form quantity contains two-dimensional spatial information about the density of the atom cloud. Section 3.8.1 discusses extraction of information from $I(x, y)$ and experimental implementation. Most of the atom cloud images described in this thesis were made with this method.

Chapter 3

Experimental Apparatus

This chapter introduces many of the major devices and techniques of the experimental system. These include the vacuum system, the laser systems, the magnetic trap, the computer control system, and the imaging techniques. The experimental sequence up to BEC production in the magnetic trap is also discussed in this chapter.

3.1 Introduction

The vacuum chamber and most lasers and optics are on a $12' \times 5'$ optical table shown in Figure 3.1. The table holds thousands of optical elements, dozens of optical modulators, dozens of mechanical shutters, all five of the near resonance lasers (Section 3.3), the infrared far-off resonance laser (Section 3.4). The experiment shares a secondary table with the Sodium BEC experiment [13]. This table is shown in Figure 3.2. It is an $8' \times 4'$ optical table and is the site of the Verdi laser — our other far-off resonance laser (Section 3.4). A waveplate on a computer controlled translation stage in conjunction with a polarizing beam splitter cube sends the beam to either one of the experiments.

The following sections describe the major parts of the experimental

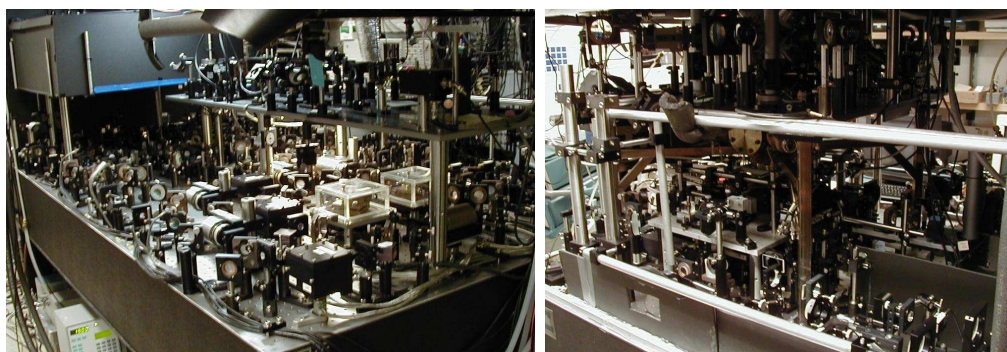


Figure 3.1: The main optical table. The table is divided into two sections. The image on the left shows the section of table devoted to the lasers. The image on the right shows the section for the vacuum chamber.

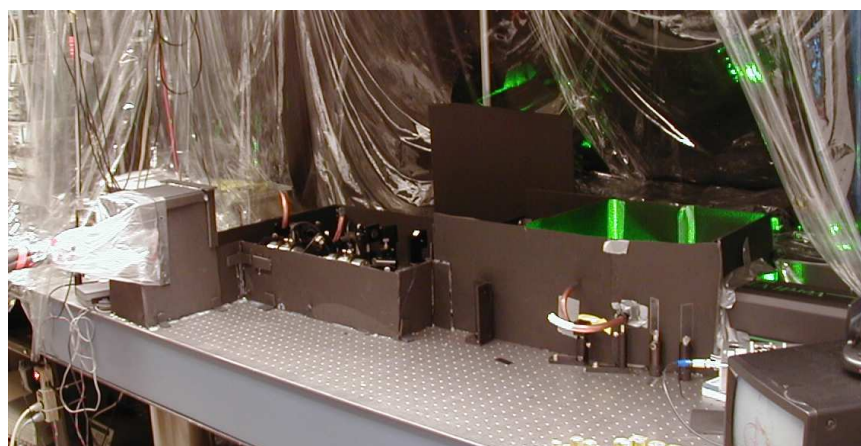


Figure 3.2: The shared optical table. It holds the Verdi laser as well as some of the beam control optics for that laser. A box constructed from black foam board surrounds most of the optics to protect the beam from air currents and shield against scattered light.

apparatus in more detail. There are also significant technical appendices which provide greater detail on some of the specifics of various designs.

3.2 Vacuum Chamber

Our vacuum chamber was designed to be used as a double MOT system [14]. The upper chamber is used as a vapor cell MOT where the atoms are captured from a background of rubidium vapor. This is a high pressure region (of order 10^{-7} torr); a differential pumping tube provides a connection to the lower chamber and maintains more than three orders of magnitude of pressure difference with the lower chamber. The lower chamber is an ultra-high vacuum region (UHV); it contains the vacuum pumps and the science chamber [15]. These items are all discussed in this section. Figures 3.6 and 3.7 show photographs of the upper chamber and the science chamber in the experimental setup. Figure 3.8 shows a photograph of the vacuum chamber before other experiment components were added.

3.2.1 Upper Chamber

The upper chamber consists of a glass cell and is separated from the lower chamber by a differential pumping tube. The upper chamber is shown schematically in Figure 3.3. The glass cell is $4'' \times 1.25'' \times 1.25''$ and made of Pyrex. It is attached by a graded glass-to-metal seal to a $2.75''$ steel flange. The seal is from Larson Electronic Glass Inc. and Technical Glass Inc. performed the assembly. We operate a vapor cell Magneto-optical trap (MOT) in this

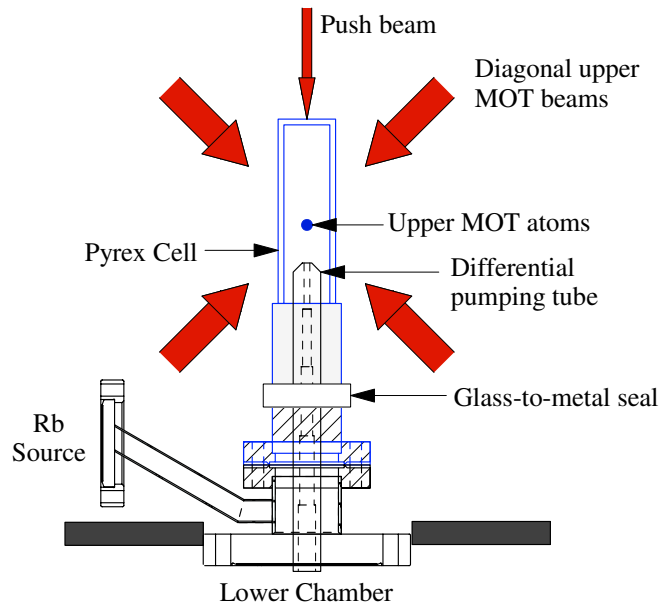


Figure 3.3: The upper chamber consists of a glass cell and is separated from the lower chamber by a differential pumping tube. The orientation of the diagonal upper MOT beams is shown. The horizontal beam pair is omitted from the figure, they counterpropagate perpendicular to the plane of the paper. The push beam hits the atoms from above and is focused to pass through the differential pumping tube. The vertical absorption imaging beam also follows a similar path (see Section 3.8.1).

chamber. The MOT consists of 3 pairs of counter propagating beams: 2 diagonal pairs and one horizontal pair. This forms a standard six-beam MOT. As in Ref. [14], we use an additional beam, the push beam, to produce an atom funnel situation. Here, the atoms are captured from the background vapor and then stream through the differential pumping tube into the lower chamber where they are recaptured and used for experiments. More details are explained in Section 3.7.

The upper chamber operates near the room temperature vapor pressure of rubidium, around 10^{-7} torr. This high pressure is required to allow for a significant number of atoms in the capture velocity range of the MOT (order 10 m/s). So, in fact, the MOT captures only the low velocity tail of a room temperature velocity distribution. The extra atoms which are not captured only serve as a collisional loss mechanism to the traps. It is for this reason that a differential pumping tube is employed which separates the science chamber from this high pressure loading chamber. The tube consists of a 6" 304 stainless steel rod which has been drilled to have a 1/8" hole at the top and the hole widens out with an angle of about 2° . This is intended to increase the solid angle for the pushed atoms yet keep the vacuum conductance low. The conductance of this tube is order 0.05 liters/s which leads to greater than three orders of magnitude of pressure difference. Despite being an efficient block for the thermal atoms in the upper chamber, the MOT atoms may be pushed into the lower chamber with high efficiency. It is these atoms which are loaded into the lower MOT and used to make condensates.

It is worth noting that this upper chamber involving the pyrex glass cell is the newest version of the upper chamber which in the past had problematic versions. Previous generations used a steel upper chamber which had Kovar sealed zero-length windows. These windows are standard and available from many vacuum companies. The problem was that the seals decayed over time — they formed small cracks. In some cases, this was temporarily fixed by the use of Vacseal (a vacuum compatible brush-on sealant) and/or by forming an auxiliary vacuum chamber outside the window for differential pumping. In our experiences, these quick fixes provided a life support for the chamber for some period of time from weeks to months, but ultimately had to be replaced with the design we have here. It is likely that the problems that occurred in our previous upper chambers were due to a reaction with the rubidium metal present. A primary concern here is the relatively high rubidium vapor pressure in the upper chamber (of order 10^{-7} torr). It is likely that the rubidium ate away at the seals of the zero-length viewports. The seal of the glass cell upper chamber described in this section is of a different sort and has a larger sealing area. A glass cell with this sort of seal in a similar setting has produced years of reliable service [16].

3.2.2 Lower Chamber

The lower chamber consists of two regions. One is the pumping region. This is the location of the ion pump and the Titanium sublimation (Ti:sub) pump. These pumps maintain the lower chamber at a pressure below

10^{-10} torr. The science chamber is a high quality glass cell that is attached to the bottom of the lower chamber pump region. This is the location of the lower MOT, magnetic trap, and optical trap procedures.

3.2.2.1 Pumping Region

The pumping region is shown schematically in Figure 3.4. The center component of this chamber region is a modified six-way steel cross with 4.5" flanges supplemented by 1.5" tubes with 2.75" flanges. This piece was originally used in the cesium experiments by our predecessors [17–19]. The pumps run continuously. The ion pump from Varian has a pumping speed of 75 liters/s. The Ti:sublimation pump has a pumping speed which depends on the surface area of the steel tube which contains it and also on the cleanliness of the Titanium getter material deposited there. In normal operation, this pump has a speed of around 300 liters/s. This pump is flashed on as needed. There is also a Bayard-Alpert ion gauge, which was used for diagnostics in some of the initial stages of the chamber after the evacuation/bakeout procedure. In principle, this gauge can read pressures in the 10^{-10} torr range, but in practice, the operation of the gauge partially spoils the vacuum. The most sensitive pressure measurement we have, and the only relevant vacuum measurement is the atom lifetime in the magnetic trap. When the vacuum chamber is healthy, this is typically greater than one minute.

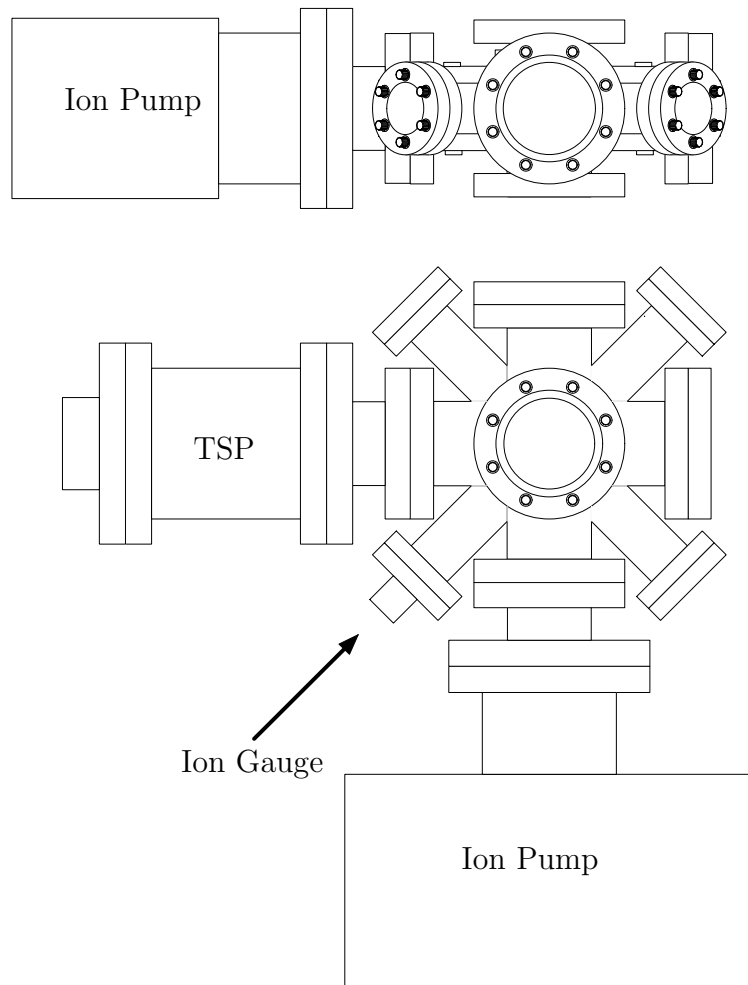


Figure 3.4: The UHV pumping region. Attached to the main vacuum chamber are two pumps and an ion gauge. Directly below this region is the science chamber (not shown here, see Figure 3.5). The upper drawing is a side view and the lower drawing is a top view.

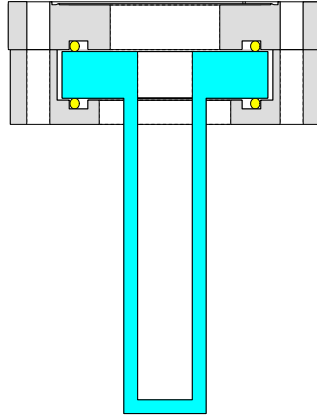


Figure 3.5: The lower chamber. The glass cell is where the experiments take place. The metal adaptor and the gold colored helicoflex seals connect the glass cell to the lower chamber pumping region.

3.2.2.2 Science Chamber Region

The science chamber consists of a high quality glass cell which is attached directly below the pumping region of the lower chamber. The experimental apparatus really centers around this location. The cell is shown schematically in Figure 3.5. The cell itself has outer dimensions $30 \times 30 \times 115$ mm with 5 mm thick walls. The material is Spectrosil, a synthetic fused silica. The cell is attached to a 75 mm diameter, 17 mm thick circular flange of the same material. The center of the flange has a 20 mm diameter hole drilled to make contact with the pumping region. It was manufactured by Helma Cells Inc. which uses impressive fabrication techniques. They polish the sides and optically contact the cell together. It is then fired near the material melting point to fuse the edges. This is all done without any cementing material so

the windows are left very clean of auxiliary material. The upper glass flange is attached to the steel chamber by the use of a Helicoflex seal. These seals (Garlock-Helicoflex part H-307330 REV NC) consist of a helical spring with a metal lining. The top and bottom of the seals have a delta shaped ridge. When compressed to some specified distance, the ridge bites into the materials on each side to form a good seal and the spring acts as a restoring force against compression. The ridge effectively bonds with the glass of the flange on one side and the steel receptacle piece on the other. In this setup, we used two of these circular seals, one makes the actual seal (top in Figure 3.5), and a lower one which acts as a cushion against the counter steel part which pushes up on the glass flange. Altogether this procedure makes an effective UHV seal, which has only shown problems in the case of a baking procedure which may involve too quick thermal changes.

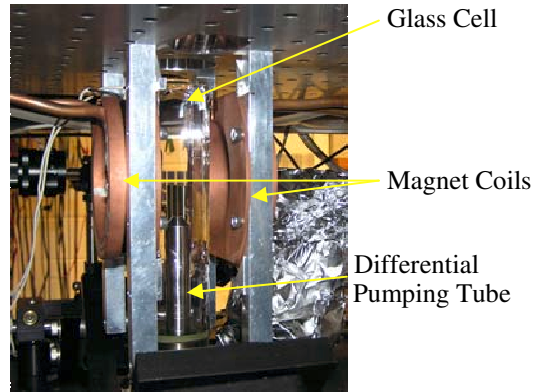


Figure 3.6: The upper chamber consists of a glass cell. The photograph also shows the top of the differential pumping tube inside the chamber. The vapor cell MOT is formed here from the background vapor, the quadrupole coil pair of the upper MOT is visible.

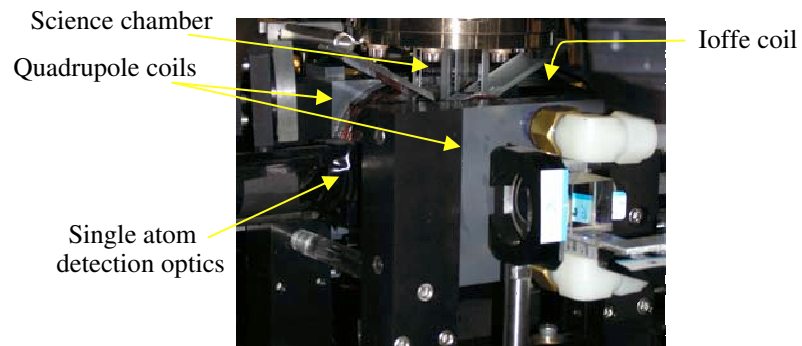


Figure 3.7: The science chamber consists of a glass cell. The QUIC trap coils are visible in the photo as well as the initial optics for the single atom detection system.

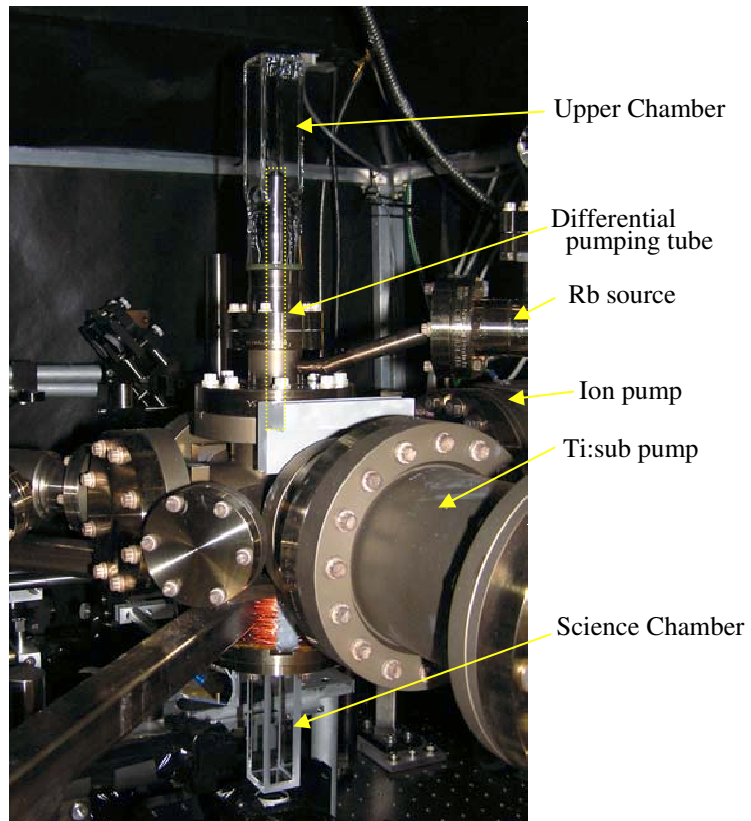


Figure 3.8: The vacuum chamber. This photo shows the vacuum chamber on the optical table before all of the obstacles are installed.

3.3 The Near Resonance Lasers

The near resonance lasers are used for the operation of the MOTs, absorption imaging, and optical pumping. The various wavelengths relative to the level structure are shown in Figure 3.9. The figure also shows the far-off resonance lasers (Section 3.4).

The near resonance lasers are all around the D_2 line of rubidium 87 at about 780 nm. The laser system consists of several distinct parts. One is the Littrow configuration master diode lasers which are locked onto the MOT and repump transitions by saturation absorption spectroscopy methods. The other part is the set of three injection locked (slave) diode lasers which supply the actual MOT light. These lasers and their generated beam paths are discussed in this section. The properties of the diodes used for these lasers are summarized in Table 3.1. All of the diodes produce a 3:1 spatially elliptical beam which is corrected in each case by an anamorphic prism pair. All lasers are followed by some number of acousto-optic modulators (AOM) which are used for frequency tuning and intensity control. Because the AOM intensity control is very fast, they act as fast, but imperfect beam shutters. When operating the magnetic trap or optical trap, the chamber must be dark of the near resonant light since this can cause major heating and trap loss. Even with RF switches on the drive of the AOMs, there is some light leakage into the diffracted orders of the AOMs which results in the need of additional home-built mechanical shutters [20] to block the residual light.

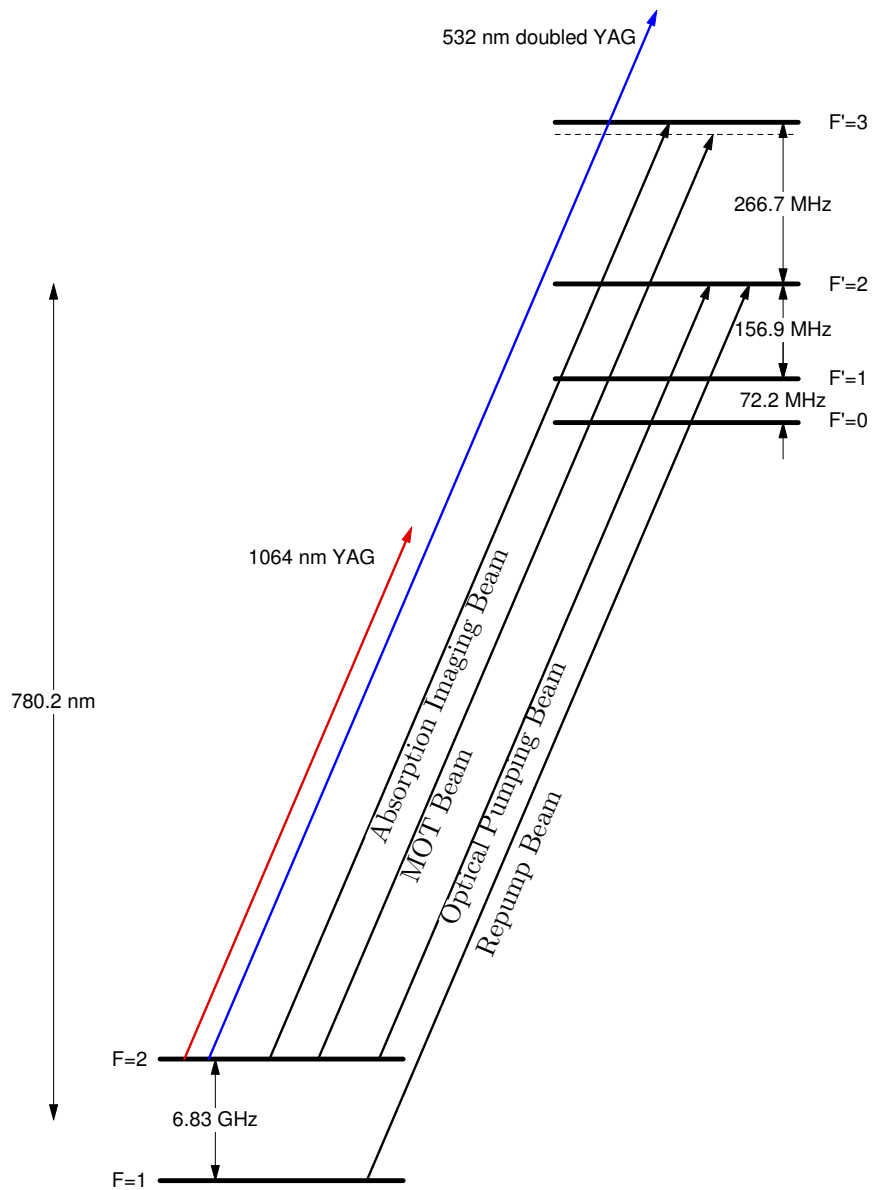


Figure 3.9: D₂ line diagram shown with the multitude of laser frequencies used in the experiment. The near resonance laser are discussed in Section 3.3 and the far-off resonance lasers in Section 3.4. Diagram not to scale.

Laser Diodes		
property	MLD780-100S5P	GH0781JA2C
distributor	Intelite, Inc.	Digi-Key
nominal wavelength	780 nm	784 nm
maximum output power	100mW	120mW
threshold current	30mA	30mA
operating current	120mA	140mA
maximum operating current	140mA	167mA
maximum reverse voltage	2V	2V
manufacturer		Sharp

Table 3.1: Characteristics of the lasers diodes used in the experiment. The Intelite diodes are used in the grating stabilized MOT master and repump. The Digikey diodes are used in the injection locked slave lasers. Note that the 784nm nominal wavelength is brought near 780 nm by controlling the diode temperature.

3.3.1 The Grating Stabilized Lasers

The construction of the MOT master and the repump lasers are similar. The design is a modified version of the lasers used in the previous cesium experiment [17–19] for the rubidium wavelength (grating angle changed). One of the lasers is shown in Figure 3.10. Both the MOT master and the repump laser are grating stabilized lasers. The Plexiglass cover is used to provide some amount of thermal isolation from the environment and the brass blocks that compose the device are temperature stabilized actively with a thermoelectric cooler and a PID circuit. In this structure, the diode itself is the MLD780-100S5P in Table 3.1 and is contained inside a Thorlabs collimation tube (model LT230P-B). The idea is to use the specular reflection from the grating as the output beam whereas the diffracted beam feeds back into the diode to form an

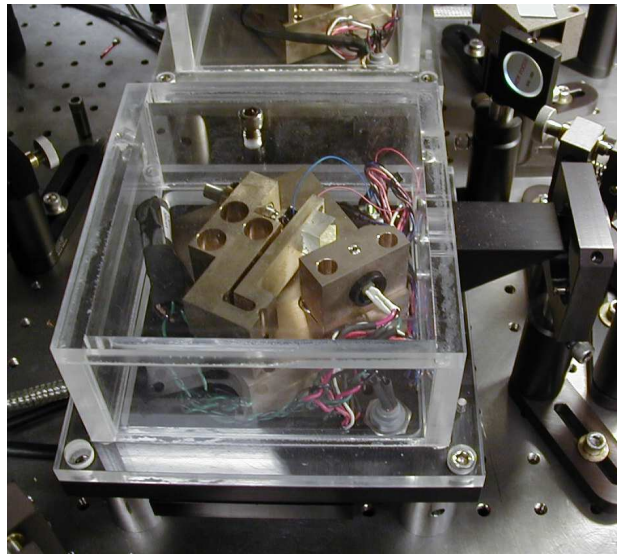


Figure 3.10: The master lasers. Both the MOT master and the repump laser are grating stabilized lasers. The Plexiglass cover is used to provide thermal isolation from the environment.

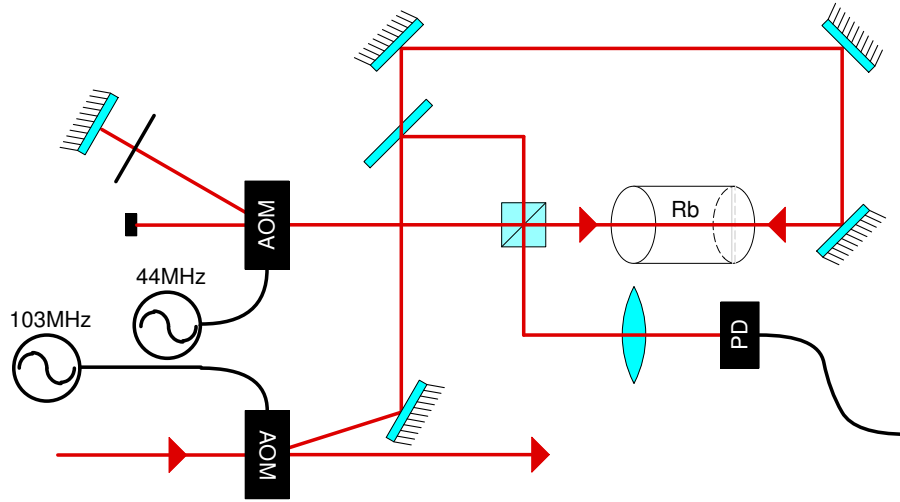


Figure 3.11: The MOT master laser locking setup. A small portion of the MOT master beam is sent through the depicted saturation absorption spectroscopy setup.

external cavity. This allows the output wavelength to be tuned with grating angle. The Littrow angle, α , is given by [21]

$$m\lambda = 2d \sin \alpha, \quad (3.1)$$

where $m = 1$ is the diffraction order we use, $\lambda = 780 \text{ nm}$, $d = 0.833 \mu\text{m}$ is the line spacing of the grating (1200 lines/mm). This gives $\alpha \cong 27.9^\circ$. The grating is mounted so it may be grossly positioned by mechanical screws manually, and may be fine adjusted by the voltage on a piezo-electric transducer stage.

3.3.1.1 The MOT Master Laser

The MOT master is frequency locked using the setup shown in Figure 3.11, a version of the standard saturation absorption spectroscopy setup [22, 23]. Some amount of light is picked off by the 103 MHz AOM (also shown in Figure 3.13). This 1 mW first order beam is frequency upshifted by 103 MHz. The beam is split so that part double passes a frequency modulated AOM with 44 MHz center frequency with modulation frequency of 50 kHz over the range between 40 MHz and 48 MHz. Due to the curved mirror retroreflection, the output beam may be modulated without walking the beam position. The modulated beam counterpropagates with the unmodulated beam in a rubidium absorption cell and then is detected by a photodiode. In the cell, the two beams interact with a velocity class of atoms corresponding to a frequency shift of 44 MHz.

The resultant signal of the spectroscopy setup is shown in Figure 3.12. The signal shows the Doppler free structure of the line with transitions between the $F = 2$ ground state to the excited states $F' = 1, 2, 3$ and the cross-over transitions. This $F = 2 \rightarrow F'$ group has a spectral width of about 425 MHz. The laser is locked to the $F = 2 \rightarrow F' = 2/3$ crossover transition because it is the strongest line in the dispersive signal. This line is 133 MHz red of the $F = 2 \rightarrow F' = 3$ cycling transition required for the MOT light. Because the initial pick-off AOM shifts the beam up by 103 MHz and the light is then shifted up an additional 44 MHz by the double passed AOM, the MOT master laser is then locked 280 MHz red of the $F = 2 \rightarrow F' = 3$ cycling transition.

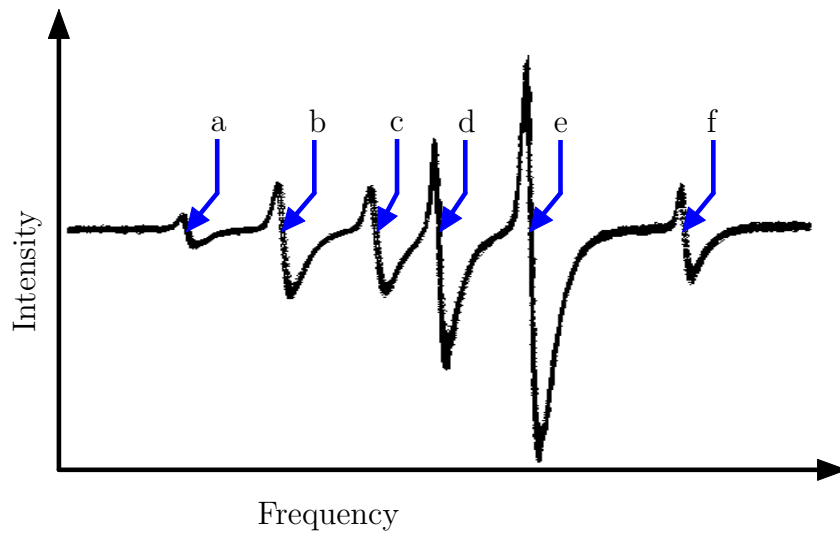


Figure 3.12: The MOT saturated absorption spectroscopy dispersive signal. The different dispersive lineshapes refer to the following transitions: a) $F = 2 \rightarrow F' = 1$, b) $F = 2 \rightarrow F' = 1/2$, c) $F = 2 \rightarrow F' = 2$, d) $F = 2 \rightarrow F' = 1/3$, e) $F = 2 \rightarrow F' = 2/3$, f) $F = 2 \rightarrow F' = 3$.

The MOT master light is distributed to the slave lasers as shown in Figure 3.13. The power that does not go to the saturation locking setup receives additional frequency shifting by an 80 MHz double pass AOM with 40 MHz bandwidth. The resultant seed light for the injection locked slave lasers is then between 80 MHz and 160 MHz red of the $F = 2 \rightarrow F' = 3$ cycling transition. Because each slave laser is followed by its own 80 MHz single pass AOM (see Section 3.3.2), the output light will be between resonance and 80 MHz red of the cycling transition. This allows for various beams to be generated including the absorption beams (on resonance), the MOT beams ($3\Gamma = 18$ MHz from resonance), and polarization gradient cooling light (at up to 60 MHz red of resonance). The specifics of these and other beams are discussed with the slave laser setups, see Section 3.3.2.

3.3.1.2 The Repump Laser

For the repump laser, we are interested in the $F = 1 \rightarrow F'$ transitions which have a spectral width of about 230 MHz. The Doppler free profile is shown in Figure 3.14. Specifically, the desired repump transition is $F = 1 \rightarrow F' = 2$. For the atoms which end up in the $F = 1$ ground state, this laser ‘repumps’ them back into the cycling state. The problem is that without the repump light, atoms are eventually pumped into this dark state and the MOTs do not work well.

Because it is the strongest line, the repump is locked using the $F = 1 \rightarrow F' = 1/2$ crossover transition. This results in laser output 78.5 MHz

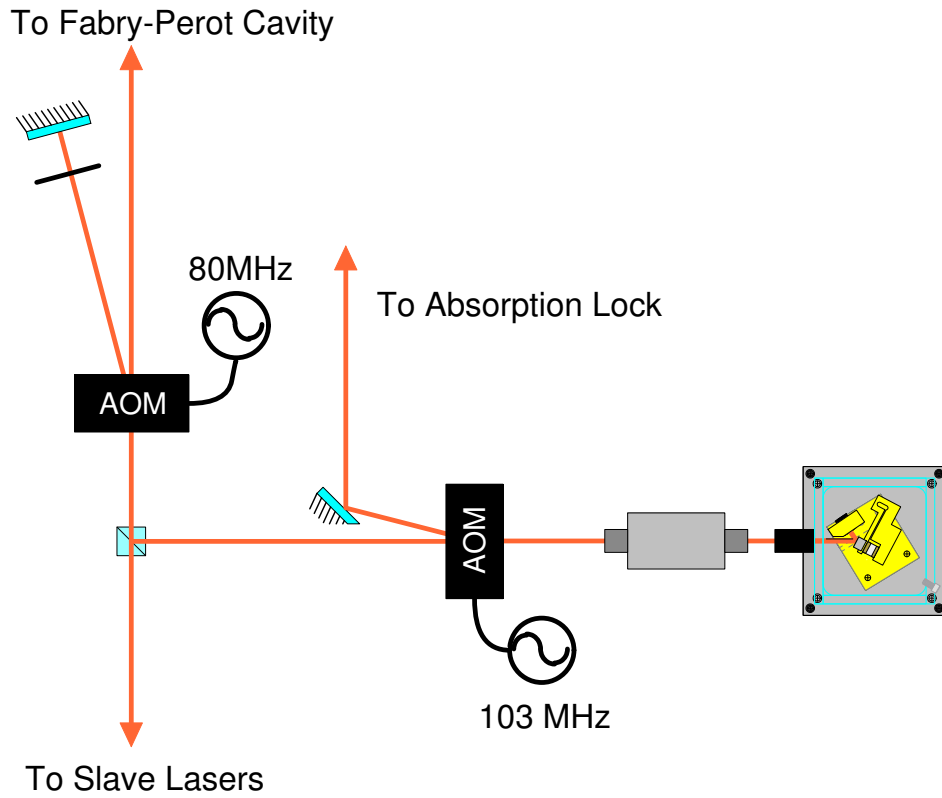


Figure 3.13: MOT master laser distribution scheme. The diode laser assembly appears on the right followed by an optical isolator. The light from the MOT master laser goes through different frequency shifting devices in order to correctly set the frequency of the light before it is used to injection lock the slave lasers.

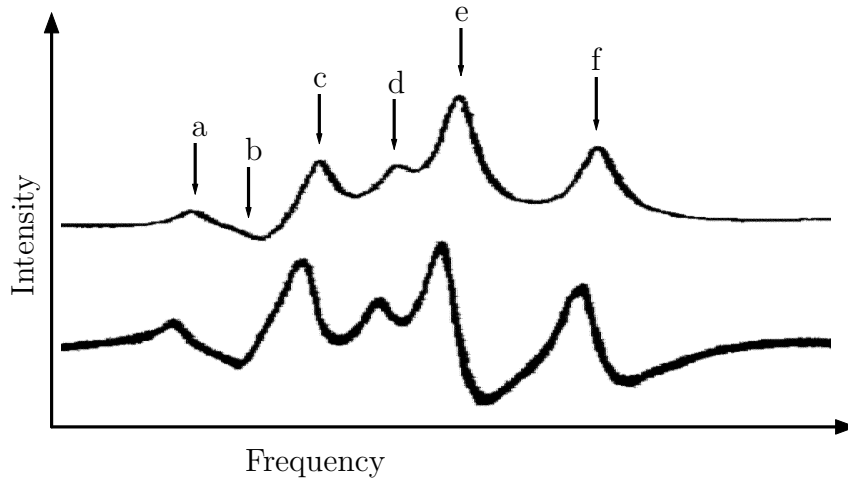


Figure 3.14: Repump saturated absorption profile. The different dispersive lineshapes refer to the following transitions: a) $F = 1 \rightarrow F' = 0$, b) $F = 1 \rightarrow F' = 0/1$, c) $F = 1 \rightarrow F' = 1$, d) $F = 1 \rightarrow F' = 0/2$, e) $F = 1 \rightarrow F' = 1/2$, f) $F = 1 \rightarrow F' = 2$.

red of the repump line ($F = 1 \rightarrow F' = 2$). The light is distributed to the upper and lower MOTs as in Figure 3.15. The 80 MHz AOM shifts the light to 1.5 MHz blue of the resonance which has little operational effect. This light is directly sent to the MOTs for repumping. Typically, we send 5 mW to the upper MOT and 4 mW to the lower MOT.

3.3.2 Injection Locked MOT Lasers

In order to provide sufficient MOT light for the upper and lower MOTs, we use injection locked lasers. Alone, these lasers are free running lasers near 780 nm. We use the GH0781JA2C diodes in Table 3.1. Although the diodes are ‘nominally’ specified to free run at 784 nm, the free running wavelength may be adjusted with temperature. We chose these diodes because of their high power,

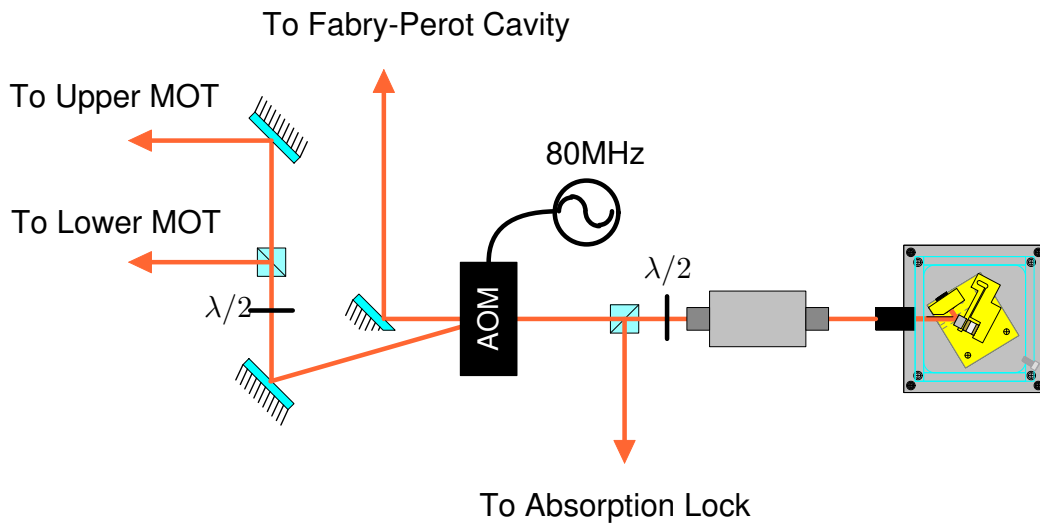


Figure 3.15: The distribution network for the repump grating stabilized laser. The diode laser assembly appears on the right followed by an optical isolator.

availability, and low cost. The diodes are held in a Thorlabs collimation tube (LT230P-B) which is housed in a temperature controlled bronzed aluminum block. This block sits atop a thermal electric cooler (TEC) which is controlled by a PID circuit. An anodized aluminum housing acts as a heat sink for the TEC and hold an output brewster window. A slave laser is shown in Figure 3.16.

The slaves are locked using the light from the MOT master laser. The method of injection locking involves sending a small amount of light into the diode which is matched well spatially to the diode output [22, 24]. The injection light is sent into the reject port of the optical isolator which is placed after each slave laser. We typically use around 2 mW of injection power. There are

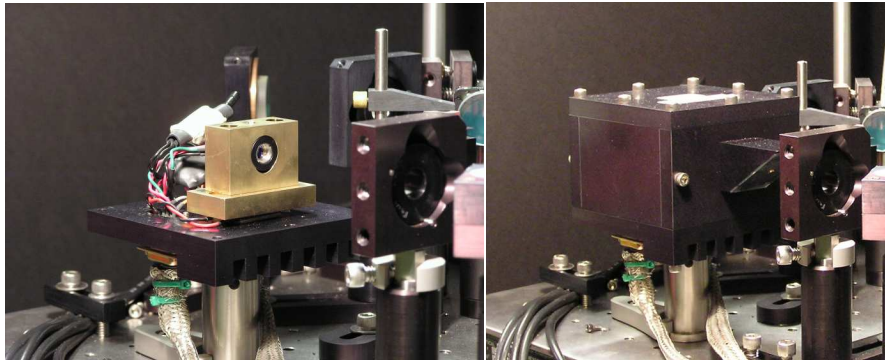


Figure 3.16: Pictures of the slave lasers. The image on the right shows the slave laser housing complete with the outer covering. The image on the left shows the housing minus the cover allowing one to see the laser diode holder as well as the electrical connections.

three injection locked slave lasers. Their layouts are discussed in the following sections. Each slave uses a 3:1 anamorphic prism pair for beam shaping and a ConOptics optical isolator (model 712B).

3.3.2.1 Upper MOT Horizontal Slave Laser

The upper MOT horizontal laser also supplies the light for the vertical imaging beam and the push beam as shown in Figure 3.17.

The first order of the 80 MHz AOM provides the upper MOT light. This AOM also serves as a beam intensity control and fast shutter. There is also a mechanical shutter which blocks the MOT light when the atoms are to be in the dark. Even with an RF switch, the AOM has some level of leakage light into the first order.

The zeroth order beam from this AOM is then used for the vertical

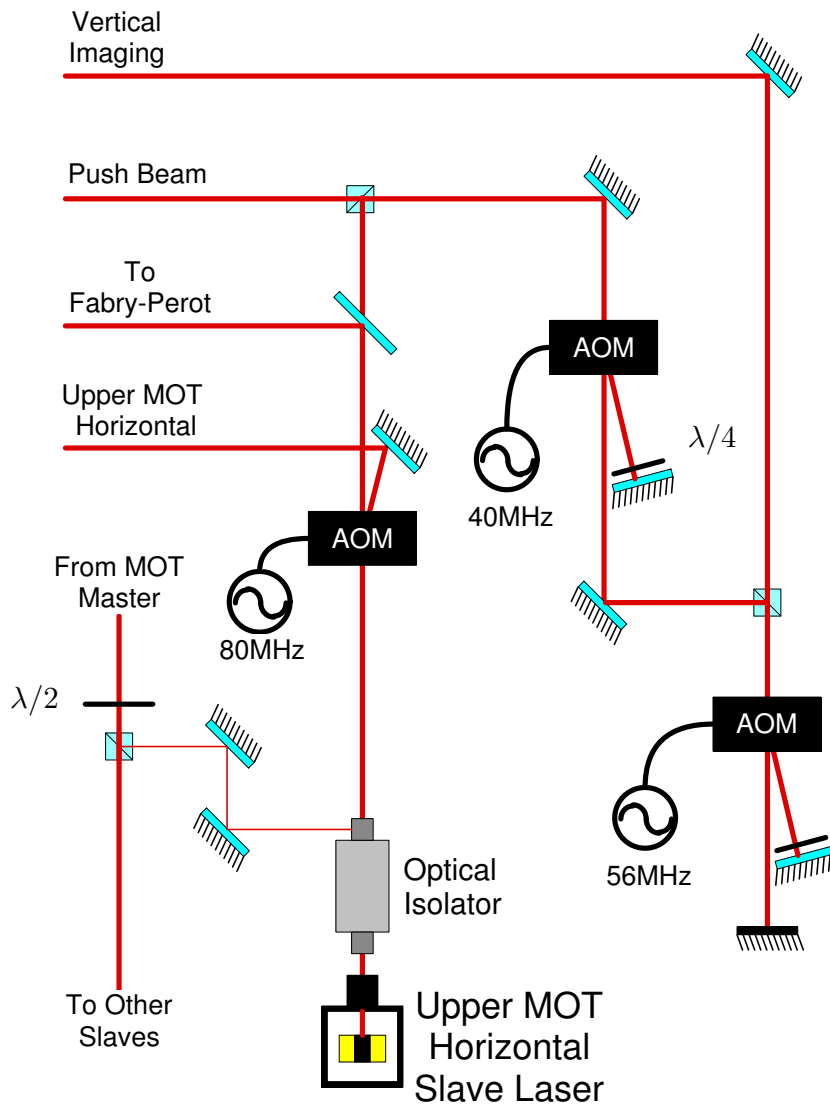


Figure 3.17: Beam distribution for the upper MOT horizontal slave laser.

imaging and the push beam. The push beam is put near the MOT resonance by the 40 MHz double passed AOM and sent into the top port of the upper chamber. The zeroth order of this AOM double passes a 56 MHz AOM which puts the vertical absorption imaging beam on resonance with appropriate setting of the MOT master laser. This beam also enters the chamber through the top port of the upper chamber.

3.3.2.2 Upper MOT Diagonal Slave Laser

The upper MOT diagonal laser also supplies the light for the horizontal imaging beam and the optical pumping beam as shown in Figure 3.18.

The first order of the 80 MHz AOM provides the upper MOT light. This AOM also serves as a beam intensity control and fast shutter. In addition, there is a mechanical shutter which blocks the MOT light when the atoms are to be in the dark as with the horizontal laser.

The zeroth order beam from this AOM is then used for the other two beams. The imaging beam is put on the MOT resonance by the 56 MHz double passed AOM and sent horizontally through the science chamber to make images. The zeroth order of this AOM double passes through a 80 MHz AOM using the minus first order. This lowers the frequency by 160 MHz which puts the beam in the range so that with appropriate master laser setting during the sequence, the light will be on the $F = 2 \rightarrow F' = 2$ transition for optical pumping. Both horizontal imaging beam and optical pumping beam follow similar paths and have 15 mm waists at the location of the atoms.

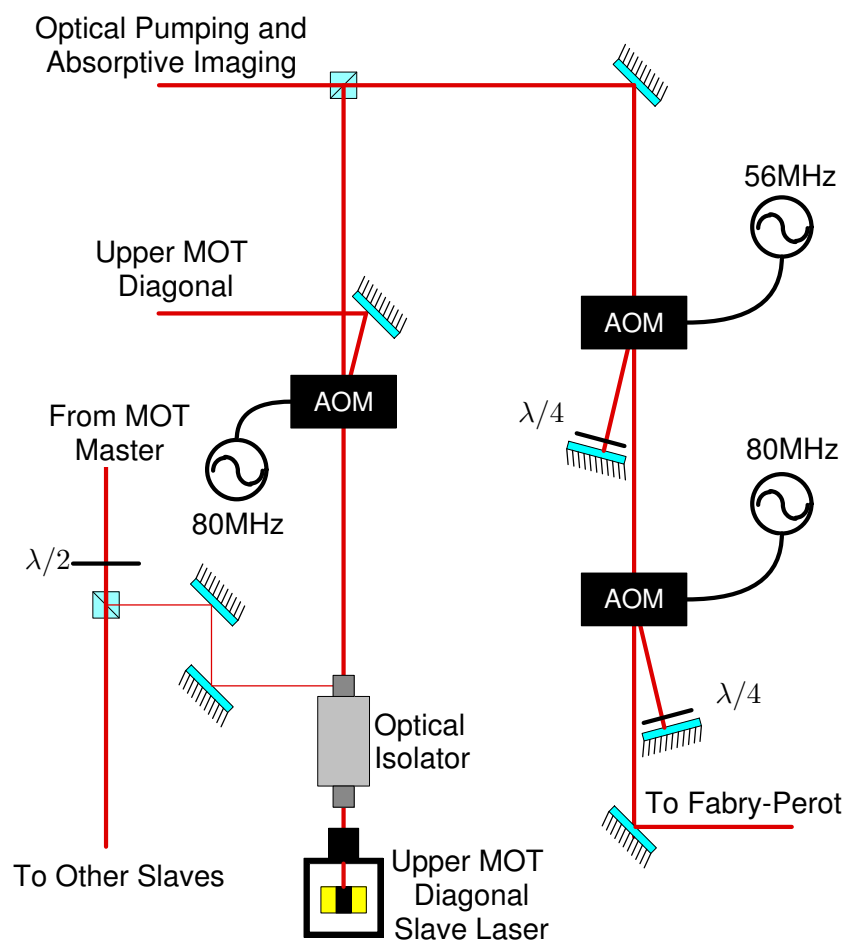


Figure 3.18: Beam distribution for the upper MOT diagonal beam slave laser.

3.3.2.3 Lower MOT Slave Laser

The lower MOT slave laser supplies light for the lower MOT in two configurations. One is the standard lower MOT which is used to capture atoms sent from the upper MOT. These are the atoms which are eventually used in making the condensate. The other is the single atom detection (SAD) MOT (or SAM for Single Atom MOT). This is used in the few atom detection system (see Section 3.8.3). The basic difference between the configurations is the beam size at the atoms. Only one of the two is used at once. As shown in Figure 3.19, each use an 80 MHz AOM for frequency shifting as in the other MOT beams described in previous sections.

3.4 The Far-Off Resonance Lasers

The far-off resonance lasers are commercial and therefore slightly more ‘turn-key’ to operate. These are the lasers used for optical trapping. As discussed in Section 2.1, far-off resonance lasers may be used to create dipole potentials, *i.e.* conservative traps. Because of their large detuning from the atomic lines they cause very little spontaneous scattering — which can be a source of heating and trap loss. Unlike the 780 nm lasers, these lasers may not be used to cool, only to trap.

As explained in Section 2.4, far-off resonance lasers can make attractive or repulsive potentials depending on detuning. For light detuned red of resonance (the D doublet), the potential is attractive. For blue detunings, the potential is repulsive.

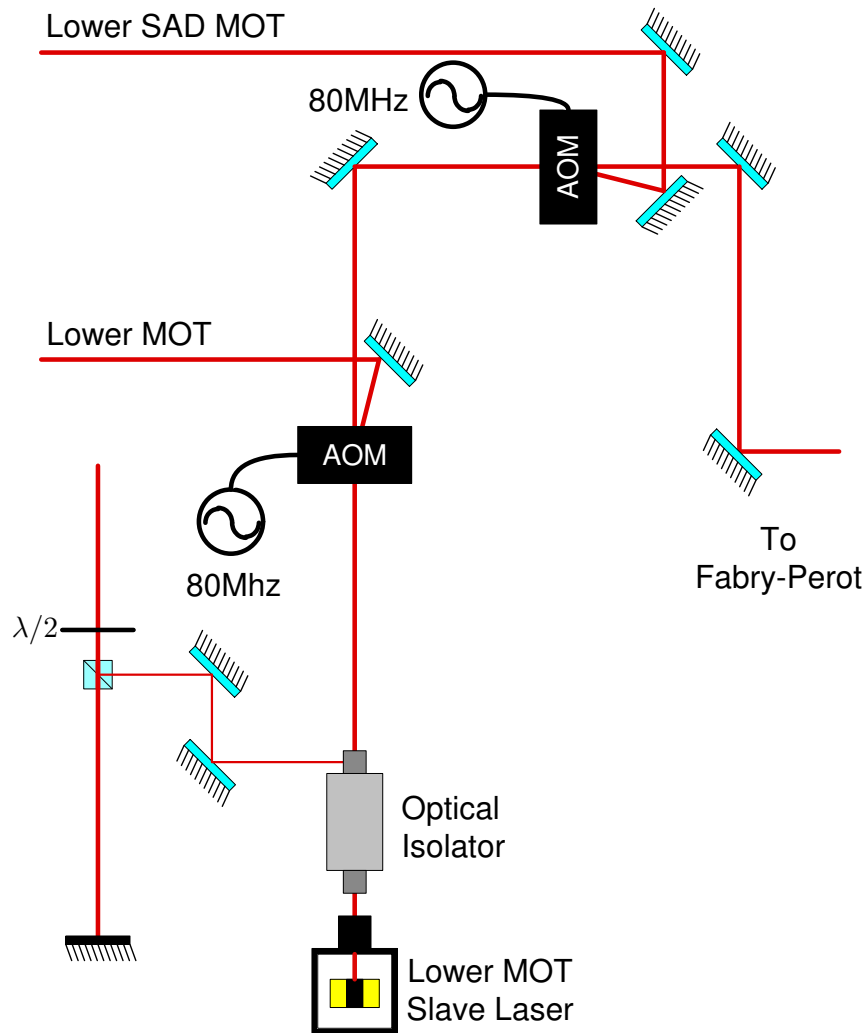


Figure 3.19: Beam distribution for the lower MOT beam slave laser.

For these reasons, we have two high power, commercial, far-off resonance lasers. The first is the Verdi laser (Coherent Inc.). It is a diode pumped frequency doubled Nd:Vanadate solid state laser which produces 10 W of 532 nm light continuously. It has high stability and low noise. This laser is used for a number of the optical trapping beams, most notably the TEM₀₁ beams. This light is blue of resonance and produces a repulsive potential.

The second is the TLD-10-1064 (IPG Photonics) Ytterbium fiber laser. The output is 10W at 1064 nm continuously. It is randomly polarized and has a rather wide line width.

For the far-off resonance lasers, the line width of the light has little importance since the detuning is so large. The intensity stability, however is very important. Most of the beam paths are surrounded by tubes and foam boxes to prevent air currents which will cause index fluctuations in the air.

3.5 The Magnetic Trap

A common method to create a BEC is to use a magnetic trap in conjunction with evaporative cooling. This requires a magnetic trap that avoids the problem of Majorana flip loss as in a quadrupole trap (see Section 2.3), but it was preferred to remove some of the complexities of other magnetic traps (*i.e.* the standard Ioffe-Pritchard trap and variants). The Quadrupole Ioffe Configuration (QUIC) trap, first designed by the group of Theodor W. Hänsch in Germany, fills that role [25]. Our version produces similar fields but involves a design where the cooling water directly contacts the magnet wire

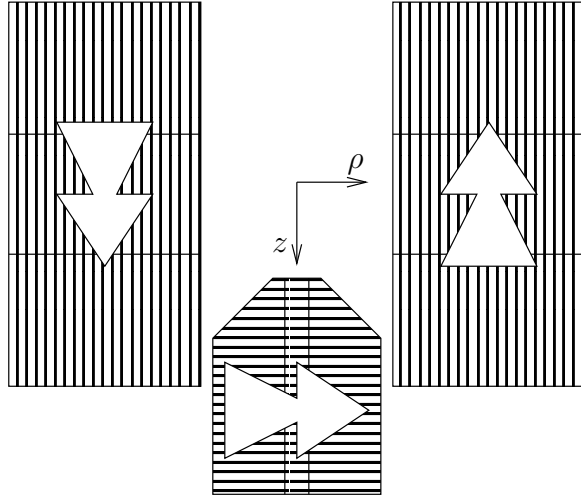


Figure 3.20: Functional diagram of the QUIC trap. The trap consists of a quadrupole coil pair and a Ioffe coil. Alone, the pair makes a quadrupole magnetic field, which is suitable at lower currents for running a MOT. The large arrows show the direction of the current in the coils.

for exceptional thermal stability.

3.5.1 Quadrupole Ioffe Configuration

The QUIC trap consists of three coils: a quadrupole coil pair and a Ioffe coil as shown in Figure 3.20. Alone, the pair makes a quadrupole magnetic field, which is suitable at lower currents for running a MOT. This is a principle advantage to this magnetic trap, in that others require more difficult mode matching to transfer atoms from a MOT into the trap.

The basic idea of operation is that the quadrupole coil pair run at a low current to provide the fields for a MOT. At some point, the atoms are

optically pumped (see Section 3.7.3) into a trapable state of the magnetic trap and the coil currents are then ramped up to make a quadrupole magnetic trap. The MOT atoms are in the same location as the magnetic trap, so mode matching of the traps is not needed. Before evaporatively cooling, the Ioffe coil current is ramped up to equal that of the quadrupole coils. At this point, with identical current in all coils, the fields have maximum stability. Also, the magnetic trap is now compressed and is suitable for evaporative cooling. The disadvantage of this design is that the field minimum has moved toward the Ioffe coil. This places a limit on optical access to the BEC. Figure 3.21 shows the field magnitude along the z -axis while transferring from a purely quadrupole to the quadrupole-Ioffe trap.

The QUIC trap fields are similar to those of a standard Ioffe-Pritchard configuration near the trap minimum [26]. A vector field plot is shown in Figure 3.22. The potential, $U(\mathbf{r}) = \mu|B(\mathbf{r})|$, near the minimum is given by

$$U(\mathbf{r}) = \mu B_0 + \frac{m}{2}(\omega_z^2 z^2 + \omega_\rho^2 \rho^2), \quad (3.2)$$

where \mathbf{r} is specified by axial, z , and radial, ρ , components relative to the field minimum, and m is the atomic mass. This is a harmonic potential with trap frequencies given by $\omega = \sqrt{\mu B''/m}$, where B'' is the field curvature in the given direction. In the case of the radial direction, the curvature is

$$B''_\rho = \frac{B_\rho'^2}{B_0} - \frac{B_z''}{2}. \quad (3.3)$$

This is approximately $B''_\rho \cong B_\rho'^2/B_0$ in the full trap configuration (*i.e.* B'_ρ is

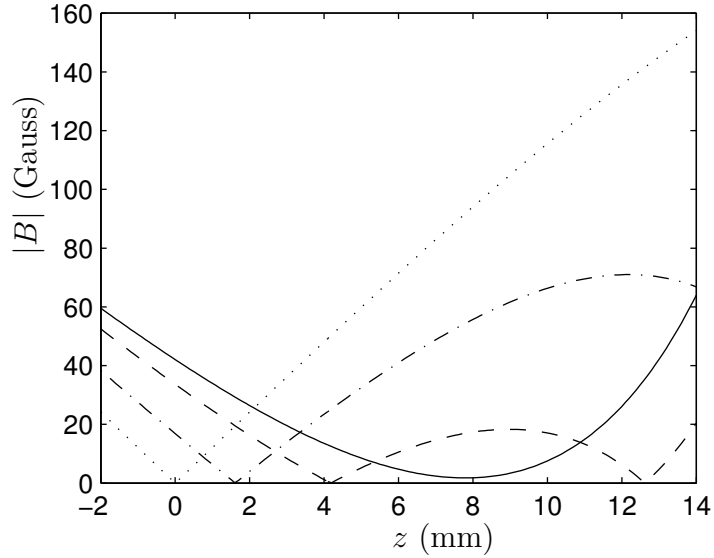


Figure 3.21: Calculated field for our QUIC trap. Field magnitude along the z -axis is shown for different situations. In all cases, the current in the quadrupole coils is $I_Q = 25$ A. The dotted curve is for Ioffe current $I_I = 0$ A, which corresponds to the case of a purely quadrupole field. The dot-dashed and dashed curves correspond to $I_I = 10$ A and $I_I = 20$ A, respectively. The solid curve is when $I_I = I_Q = 25$ A. This curve corresponds to a situation with trap frequencies of $\omega_z = 2\pi \cdot 18$ Hz and $\omega_\rho = 2\pi \cdot 225$ Hz with $B_0 = 1.8$ G. The Ioffe coil location is to the right.

large and B_0 small). The trap frequencies are therefore given by

$$\omega_z = \sqrt{\mu B_z''/m}, \quad (3.4)$$

and

$$\omega_\rho = \sqrt{\mu B_\rho'^2/mB_0}, \quad (3.5)$$

where B_ρ' is the radial field gradient, B_z'' is the axial field curvature, and B_0 is the field minimum. Since the quadrupole trap has gradients $B_x' = B_y'/2$, where B_x' is the gradient along the quadrupole coil axis, the radial gradient is the geometric mean: $B_\rho' = \sqrt{B_x'B_y'} = B_x'/\sqrt{2}$. For the $|F = 2, m_F = +2\rangle$ ground state of ^{87}Rb , the factor $\sqrt{\mu/m} = 2\pi \cdot 1.2765 \text{ Hz}$ and the trap frequencies are

$$\omega_z = 2\pi \cdot (1.2765 \text{ Hz}/\sqrt{\text{G}/\text{cm}^2})\sqrt{B_z''}, \quad (3.6)$$

and

$$\omega_\rho = 2\pi \cdot (1.2765 \text{ Hz}/\sqrt{\text{G}/\text{cm}^2}) B_\rho'/\sqrt{B_0}. \quad (3.7)$$

At $I_I = I_Q = 25 \text{ A}$, theoretical values are $B_\rho' = 235 \text{ G}/\text{cm}$, $B_z'' = 195 \text{ G}/\text{cm}^2$ and $B_0 = 1.8 \text{ G}$. This corresponds to trap frequencies of about $\omega_z = 2\pi \cdot 18 \text{ Hz}$ and $\omega_\rho = 2\pi \cdot 225 \text{ Hz}$. Small adjustments in B_0 are made by an auxiliary Ioffe coil, thus setting the operating value of ω_{ax} .

3.5.2 Experimental Characterization

The magnetic trap is characterized by its trap frequencies and the magnetic field strength at the trap minimum. The trap frequencies are determined by ‘kicking’ the cloud of atoms within the trap and observing the oscillations.

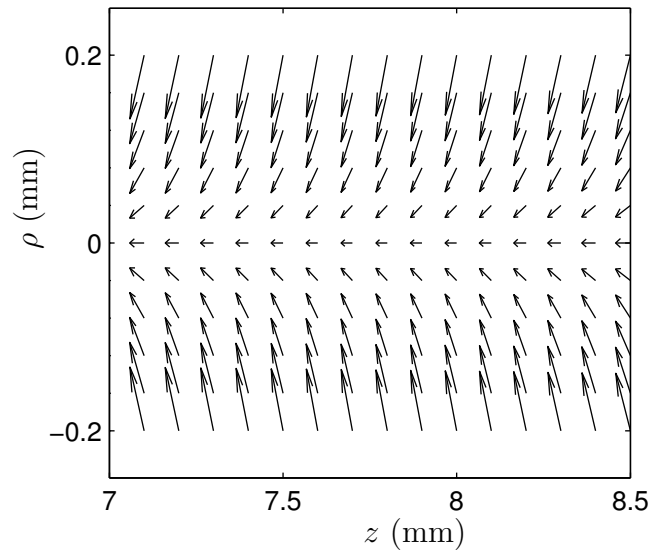


Figure 3.22: Vector field plot for the compressed QUIC trap. The lower axis is z , the distance from the pure quadrupole zero. The Ioffe coil is located to the right.

The cloud is ‘kicked’ by offsetting the trap center slightly with a bias field, then letting the cloud evolve in the trap before taking an image. Figure 3.23 shows the results of such a measurement. In this case, the trap frequencies are 120 Hz in the strong direction and 19 Hz in the weak direction. Since the trap frequencies are dependent on the trap minimum, it is also important to know this value. The field minimum can be found through RF evaporation by continuing the evaporation sweep until there are no atoms left. The frequency at which this happens corresponds to the energy offset at the bottom of the trap, which can be converted into the magnetic field value at that point. In the case of the trap frequency measurements, the field minimum was 3.9 G. During typical operation, the field minimum is roughly 1.4 G. This yields trap frequencies of $\omega_{\text{rad}} = 2\pi \cdot 200\text{Hz}$ and $\omega_{ax} = 2\pi \cdot 19\text{Hz}$.

3.5.3 Decompressed Ioffe Configuration

There are two ways that one might use the term ‘decompressed Ioffe’ trap. One would be the situation of the full QUIC trap — where the currents are equal in all coils and the field is shown in the dark line in Figure 3.21. Because the magnetic field is proportional to the current, a decompressed version would just have lower current. This version would maintain the same trap shape but just have a different strength, that is, the trap center is still 7.5 mm from the center of the glass cell and elongated. The term, as we use it refers to decompressing the trap ‘into the center’ of the glass cell. In this case, the final trap configuration is a symmetric trap of about 20 Hz in the center of

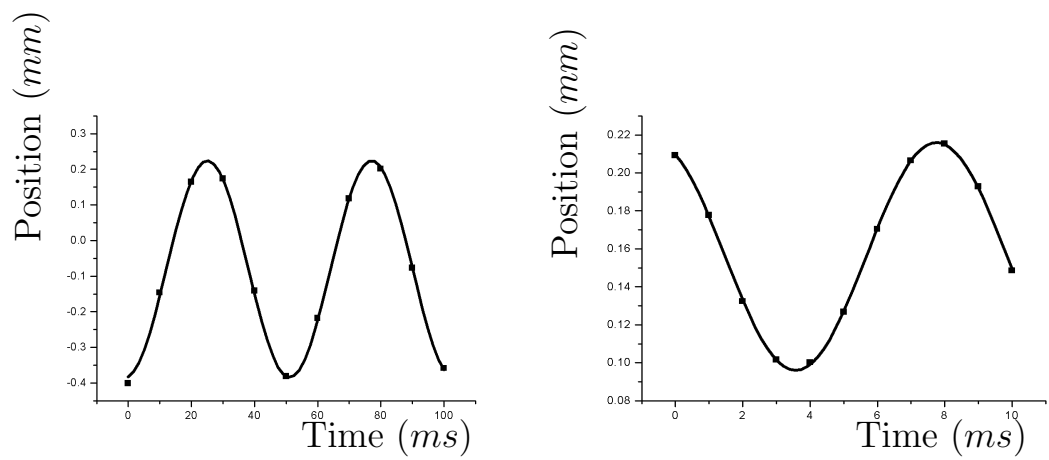


Figure 3.23: Plots showing the motion of the atomic cloud in the magnetic trap. From this measurement, it is possible to calculate the trap frequencies. The plot on the left shows oscillations along the weak axial direction corresponding to a trap frequency of 19 Hz. The plot on the right shows oscillations along the strong radial direction corresponding a trap frequency of 120 Hz.

the glass cell ($z = 0$ in Figure 3.21). This is a desirable configuration because there is much better optical access at that location.

Decompressing the Ioffe trap is accomplished by lowering the current in the quadrupole coils and keeping the current high in the Ioffe coil. The full compressed trap is when the field minimum is small and the gradients are high. In that configuration, the trap is suitable for evaporative cooling. In the decompressed case, the gradients, especially in the radial direction, are decreased. Using a numerical simulation, a plot of the fields for this case is shown in Figure 3.24. In the figure, for $I_I = 25$ A and $I_Q = 7.5$ A, the field has approximate values of $B'_\rho = 71$ G/cm, $B''_z = 42$ G/cm² and $B_0 = 42$ G. This corresponds to trap frequencies of about $\omega_z = 2\pi \cdot 8.25$ Hz and $\omega_z = 2\pi \cdot 12.7$ Hz. In this case, the simulation shows the trap center moving past the center position demonstrating the capability. In the experiment, the same behavior is observed. The Ioffe coil is held at 28 A while the quadrupole coils are reduced to a current of roughly 8.5 A to bring the trap back to the center along the Ioffe coil axis and the resulting trap frequencies are roughly 20 Hz symmetrically. The trap frequencies are not very important in this configuration, the effect that we were looking for is the location change back to the glass cell center.

Theoretically, with appropriate current ratio between the quadrupole pair and Ioffe coil, the atoms should end up exactly in the center. However, since the construction of the coils is imperfect, the auxiliary coils are needed to return the trap to the center in the two other axes. A vertically oriented levitation coil is necessary to counteract gravity. Since the trap is very weak

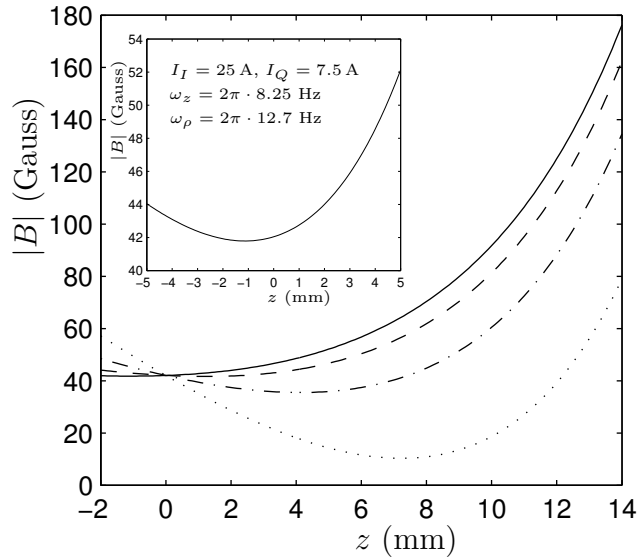


Figure 3.24: Calculated field for the decompressed QUIC trap. Field magnitude along the z -axis is shown for different situations. In all cases, the current in the Ioffe coil is $I_I = 25$ A. The dotted curve is for quadrupole current $I_Q = 25$ A, which corresponds to the compressed trap. The dot-dashed and dashed curves correspond to $I_Q = 15$ A and $I_Q = 10$ A, respectively. The solid curve is when $I_Q = 7.5$ A. This curve corresponds to a situation with approximate trap frequencies of $\omega_z = 2\pi \cdot 8.25$ Hz and $\omega_\rho = 2\pi \cdot 12.7$ Hz, with $B_0 = 42$ G. This roughly symmetric trapping minimum is near the center of the chamber. The plot inset shows a closer view of the trap minimum in the final case; clearly it has moved slightly beyond the chamber center.

in this configuration, gravity is strong enough to pull the trap center down. A water cooled coil located just above the science chamber (visible in Figure 3.8) provides a magnetic gradient field for this purpose. With a current of about 8A, the coil can provide enough force on the atoms to counter gravity and return the trap to its original position in the vertical direction. The optical pumping bias coils are used to shift the magnetic trap back to the center along the quadrupole axis.

During the switch on of the QUIC trap's primary coils, it is not important to worry about kinks in the current because the atoms are hot. After evaporation, the atoms are very cold, and when decompressing the trap back to the quadrupole center it is necessary to carefully choose a current profile which will not excite the atoms. More specifically, a continuous acceleration is needed. If the acceleration is chosen to be of the form $a(t) = -A\omega^2 \sin \omega t$, with $A > 0$, this can be integrated to find the velocity $v(t) = \omega A \cos \omega t + C$ and the position $x(t) = A \sin \omega t + Ct + x_0$, where $\omega t_{\text{end}} = 2\pi$. Using the boundary values $a(0) = a(t_{\text{end}}) = 0$ and $v(0) = v(t_{\text{end}}) = 0$, yields the constants $A = (x_0 - x_{\text{end}})/2\pi$ and $C = (x_{\text{end}} - x_0)/t_{\text{end}}$, where $x_{\text{end}} = x(t_{\text{end}})$. So, the trap center position is moved in time according to

$$x(t) = \frac{x_0 - x_{\text{end}}}{2\pi} \sin \frac{2\pi t}{t_{\text{end}}} + \frac{x_{\text{end}} - x_0}{t_{\text{end}}} t + x_0. \quad (3.8)$$

In order to actually move the atoms, the current in the quadrupole pair has to be adjusted. The position moves from the QUIC trap center at 28 A to the region of the quadrupole center at around 8.5 A. Because the current

dependence is rather complicated, it was simplest to determine the positions experimentally, by varying the current settings and imaging the cloud. The current for the desired position was determined numerically from the above equation.

3.5.4 Auxiliary Coils

In addition to the primary coils of the QUIC trap, various auxiliary coils were added. These coils visible in the photo in Figure 3.26. For each of these, the coils are self-supported with the turns attached together with epoxy. They were slipped over the PVC forms of the primary coils and are held in place by a few dabs of epoxy to the PVC. These coils are uncooled.

The first is the auxiliary Ioffe coil. This coil consists of about 40 turns of 20 gauge wire and has a resistance of about $0.28\ \Omega$. The purpose of this coil is to slightly alter the minimum field B_0 . One can think about this coil as a small adjustment to the current in the actual Ioffe coil. Since the coil is uncooled, there is a limit to the current that is reasonable to put through it. The change in field minimum is approximately $\Delta B_0 \simeq (1\ \text{G/A}) \cdot I_{\text{IAux}}$. In practice, this coil can change B_0 by several Gauss.

The optical pumping pair, which is mounted on the outside of the PVC holders of the main quadrupole coils, consist of 30 turns each of 16 gauge wire, and each coil has a resistance of about $0.64\ \Omega$. The pair is in Helmholtz configuration and produces a uniform field near the trap center along the axis of the quadrupole pair. The value of this field is about $B_{\text{HH}} = (2.6\ \text{G/A}) \cdot I_{\text{HH}}$.

The third auxiliary coil is the z -compensation coil. It is not attached to the QUIC trap. This coil is used for adjusting the magnetic trap center in the vertical direction. It is attached to the vacuum chamber supports directly above the science chamber. The coil consists of about 150 turns of 20 gauge wire wound on a brass tube with copper water lines attached for some cooling. Since it is not nearly as well cooled at the QUIC trap, this coil is generally only run at high currents for a short time. The coil serves two functions. One is to compensate the Earth's magnetic field in the vertical direction during the MOT and molasses phase of the experiment. The second is to compensate for gravitational sag in the decompressed Ioffe trap (see Section 3.5.3). At the location of the atoms, the coil provides roughly 1 G/A. The coil is typically run at around 8 A during the decompressed phase.

3.5.5 Coil Structure and Construction

In Appendix B, some construction schematics are given in Figures B.1 and B.2 as well as photographs at various stages of construction in Figures B.3 to B.5. There is also a photograph of the electrical feedthrough connectors in Figure B.6.

The approximate dimensions of the wire coils are as follows. The quadrupole coils have a 34 mm inner diameter, a 68.5 mm outer diameter, and a 32 mm thickness. The Ioffe coil has a partially conical end, with a 7.5 mm inner diameter, a 26 mm outer diameter, a 37 mm inner thickness, and a 33 mm outer thickness. The quadrupole coils are separated by 75 mm (be-

tween the centers of the coils) and the Ioffe coil is displaced 38 mm from the quadrupole center to its center. These dimensions should not be taken too seriously, because they approximate the shape of the actual round wires and their locations. Figure 3.25 shows the coils and location of the magnetic wire. Each coil is wound around a PVC rod and encased in a water-tight PVC holder for cooling (see below). A schematic for the locations of the wire turns and the spaces is given in the schematic in Figure B.1 in Appendix B. The Ioffe coil has 4 layers of windings with 20 gauge magnet wire. There is a set of 1/16" nylon rods from Small Parts, Inc. oriented perpendicular to the direction of winding between each layer. The coil was wound such that there is a spacer layer, 42 turns, a spacer layer, 41 turns, a spacer layer, 39 turns, another spacer layer, and finally 37 turns for a total of 159 turns. The quadrupole coils use 14 gauge magnet wire and have a set of 3 layers of turns then a nylon spacer followed by another set of 3 layers and spacer followed by a set of 4 layers. The number of turns per layer are: spacer, 18, 17, 18, spacer, 18, 17, 18, spacer, 18, 17, 18, 17. This is a total of 176 turns for each quadrupole coil.

To wind the coils, a pair of Teflon winding blocks was made to hold the inner PVC rod in a lathe which was slowly turned by hand. Teflon was used since epoxy does not stick to it strongly. Around the inner rod and after each subsequent layer of turns for the Ioffe coil, or after 3 layers of turns for the quadrupole coils, a set of spacers was put in place with 5 minute epoxy. These rods were placed around the the circumference of the coil approximately 1/2" to 3/4" apart and oriented perpendicular to the windings. After each coil

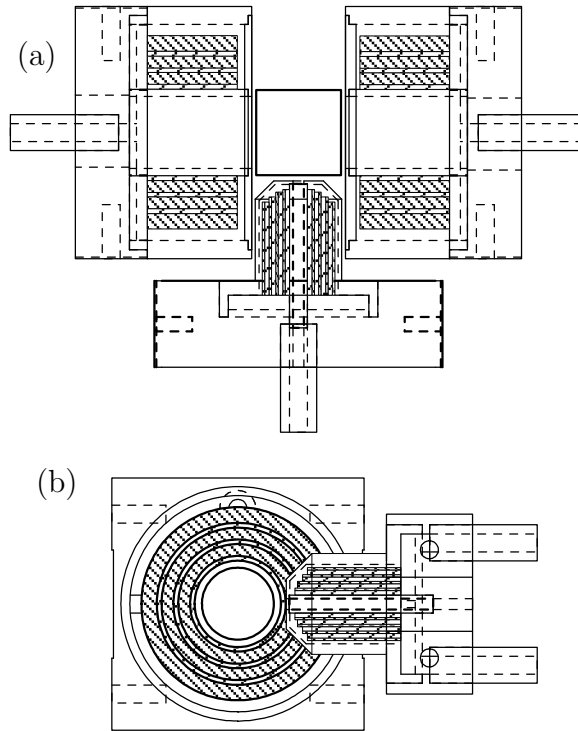


Figure 3.25: The three primary coils of the QUIC trap: (a) top view, (b) side view. Magnet wire is encased in PVC holders. The darker regions represent the copper wires and the lighter regions between the wires represent the nylon spacers. The spacers are oriented perpendicular to the coil turns. That is, in (a) all spacers are parallel with the plane of the paper and in (b) spacers come out of the paper for the quadrupole coils and parallel to the paper for the Ioffe. The PVC rods exiting the rear of each coil form base is a water tube connector.

was completed, it could easily be removed from the Teflon blocks. Each coil was then glued with a much stronger 24 hour epoxy called Cold Weld from Permatex. This gluing was in various places, mostly on the outside, along the rim to make sure the coil can not unwind in anyway, at the ends of the spacers to make sure there is a solid connection between them and the wire, and also from the wire and spacers to the inner PVC rod. This epoxy was intended to provide additional support for the coil against any strain and reinforce the 5 minute epoxy which may weaken in water. Great care was taken to not scratch the wire in this process. Figure 3.25 shows schematics of the PVC coil holders with appropriately sized magnet wire inside, see Appendix B for details. The darker regions represent the copper wires and the lighter regions between the wires represent the nylon spacers. The spacers are oriented perpendicular to the coil turns. The inner PVC rods were then inserted into the PVC holders. Each holder has a base piece and an inner rod. Both holders have a single hat piece. In the case of the Ioffe coil, that piece fits over the the entire coil and attaches to the base piece. For the Quadrupole coils, the hat slips down the inner rod and over the coil attaching to the baseplate at two places. The position of the coil on the inner rod was set by the Teflon winding blocks so the coils are correctly positioned when they slip into place. The PVC holders were cemented together using standard PVC cement. In addition, an external PVC weld was made along all the seams of the seal. The wire ends from each coil exit the housing and pass down each of the plastic water tubes attached to the coils. The wire then travels about 1.5 feet down the tube where it reaches

a modified 0.5" brass Swagelock union tee. The tee has a small hole that was drilled into it opposite the perpendicular port. In addition, a copper tab was silver soldered onto the side of the tee. The wire was soft soldered into the hole with the use of a propane torch. The extra slack of magnet wire was left inside the water tube beyond the brass connector in case of a future break due to electro-chemical etching at the connection. In this scenario, the tee could be removed and re-soldered using some of the slack wire. The inside of the tee was also covered with Cold Weld. On the outside of the brass tee, the electrical connection is made to 10 gauge wire by bolting the lug on the wire to a hole in the copper tab on the side of the tee. The copper tabs were first cleaned with sandpaper to remove oxides from the soldering process. The coils are cooled with water. Each PVC holder has two water connectors which are attached to 1/2" plastic tubes with nylon Swagelock connectors. The water enters each holder in the lower tube and exits the top allowing air bubbles to escape. The water then either passes through the gaps in the coil formed by the nylon spacers or goes around the outside of the windings. The water is primarily prevented from going straight from the inlet to the outlet and not passing the coil by a barrier that is machined into the PVC baseplate. The process water comes from the recirculating refrigeration chiller Merlin M-33 from Neslabs which is buffered by a massive water tank. This chiller has a cooling capacity of 1250 W. The quadruple coils each have a resistance of 0.29Ω and the Ioffe coil has 0.40Ω . At a maximum reasonable current of 30 A, this gives powers of about 260 W in each quadruple coil and 360 W in the

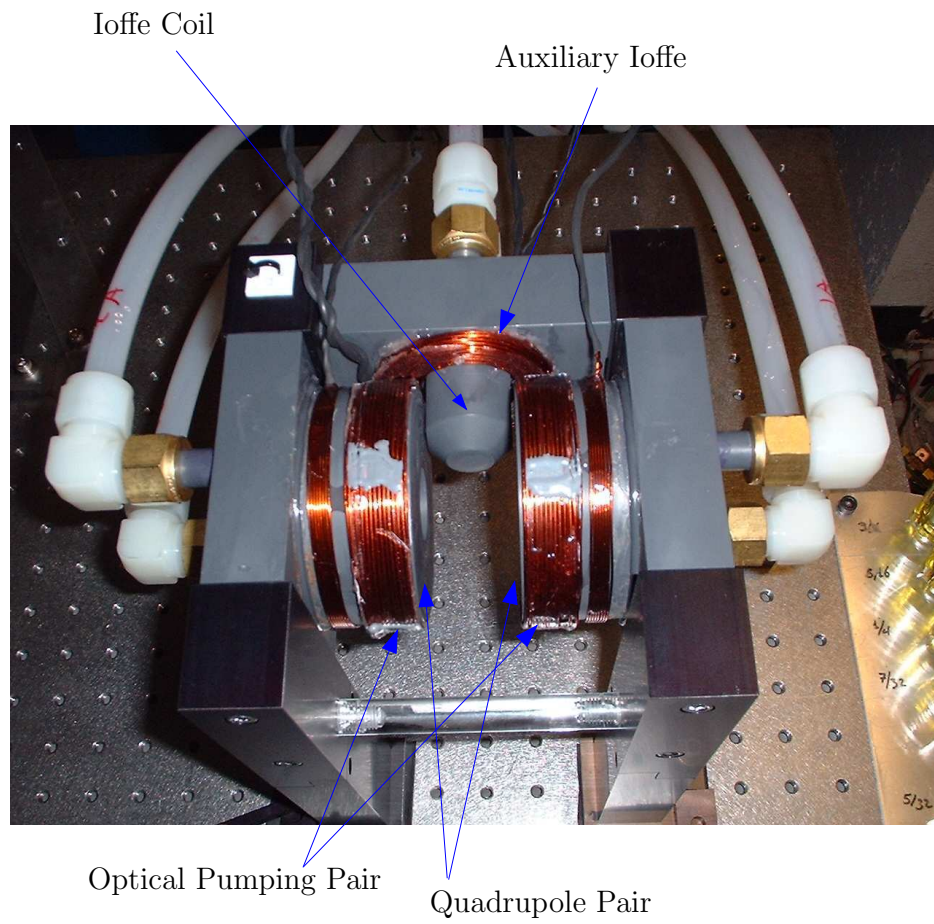


Figure 3.26: A photograph showing the coils of the QUIC trap.

Ioffe coil. The chiller's positive displacement pump puts out about 12 l/min at a maximum pressure of 60 psi. Half of this goes to the magnetic trap and half recirculates with the water tank. When individually operated at 6 l/min, the quadruple coils individually drop about 25 psi, the Ioffe coil 15 psi, and electronics FET heatsink about 50 psi. So when run in parallel the Ioffe coil receives about 2.4 l/min, each quadruple coil about 1.44 l/min, and the FETs about 0.72 l/min and the output pressure is only 6 psi. With these flows and the outstanding thermal contact, the coils only change temperature by about 2°C.

The decision to use PVC for the coil housings was based on leaking problems that were associated with a former design. Originally, the housings had been made out of Plexiglass and sealed with the chemical Dichloroethane. Dichloroethane melts the Plexiglass allowing two adjacent surfaces to fuse together. The Plexiglass containers had leaking problems which were difficult to fix. This likely occurred due to small gaps that the Dichloroethane did not seal because of the fact that small gaps are not filled by the substance since it only fuses contacting faces and adds no material. Also, Plexiglass tends to absorb water and swell [27]. This could further weaken the seal made by the Dichloroethane and lead to leaks. This problem was temporarily remedied by using the epoxy Cold Weld. The epoxy was put on the surface of the joints and at noticeable leaks. This brought temporary relief, but eventually it gave way to a leak that was not able to be patched. With the use of PVC cement and PVC welding, the current coils were constructed and sealed — and they

state	Quadrupole Current (A)	Ioffe Current (A)
Lower MOT	1.4 A	0 A
Initial quadrupole trap	15 A	0 A
Compressed quadrupole trap	28 A	0 A
Full QUIC trap [†]	28 A	28 A
Decompressed Ioffe trap	8 A	28 A

Table 3.2: Current states of the QUIC trap. In between states generally involve smooth ramps, see Figure 3.28. [†]In the full QUIC trap, suitable for evaporation, the currents in the quadrupole and Ioffe coils are identically equal.

have not leaked a drop.

3.5.6 Current Control

The QUIC trap draws from a single power supply: 0 – 60 V, 0 – 30 A linear single phase supply, TCR series model 605-30-1-D from Lambda EMI. The QUIC trap has several modes of operation with currents outlined in Table 3.2. In order to control the trap coils in all of these configurations and provide smooth ramps where appropriate, it was necessary to construct a power circuit which can direct the current as desired. A functional schematic of this circuit is given in Figure 3.27. To understand this circuit, one must only keep in mind the current relation

$$I_{\text{main}} = I_{\text{quad}} + I_{\text{QShunt}} = I_{\text{Ioffe}} + I_{\text{IShunt}}. \quad (3.9)$$

By setting the main current to some value, the current in both the quadrupole pair or the Ioffe coil may be set independently of each other to any value between zero and I_{main} . This is accomplished by the computer control of the

shunt current sources shown in the figure. The actual circuits are more complicated than this functional diagram. Full schematics are given in Appendix C. The schematic for the main current source is discussed in Section C.5 and for the power circuit involving the shunt regulators in C.6.

Figure 3.28 shows pictorial plots of the various ramps of current during the experiments. Figure 3.28(a) shows a sequence that may be used to prepare a condensate in the QUIC trap. The sudden shut off at the end of the plot will drop the atoms which may be imaged at that time. When it is intended to continue the sequence in the optical traps, the current is not suddenly switched off there, but rather continues as in Figure 3.28(b). This is the current sequence for the decompression of the trap into the glass cell center for future transfer to the optical trap.

One important motivation for this circuit is that the coils may be truly run in series. This is because it is possible to shut the shunt current sources off entirely. In this case, the QUIC trap is in a mode that is most stable and suitable for evaporative cooling. If the coils have approximately the same current, but not really, the fields will be much less stable.

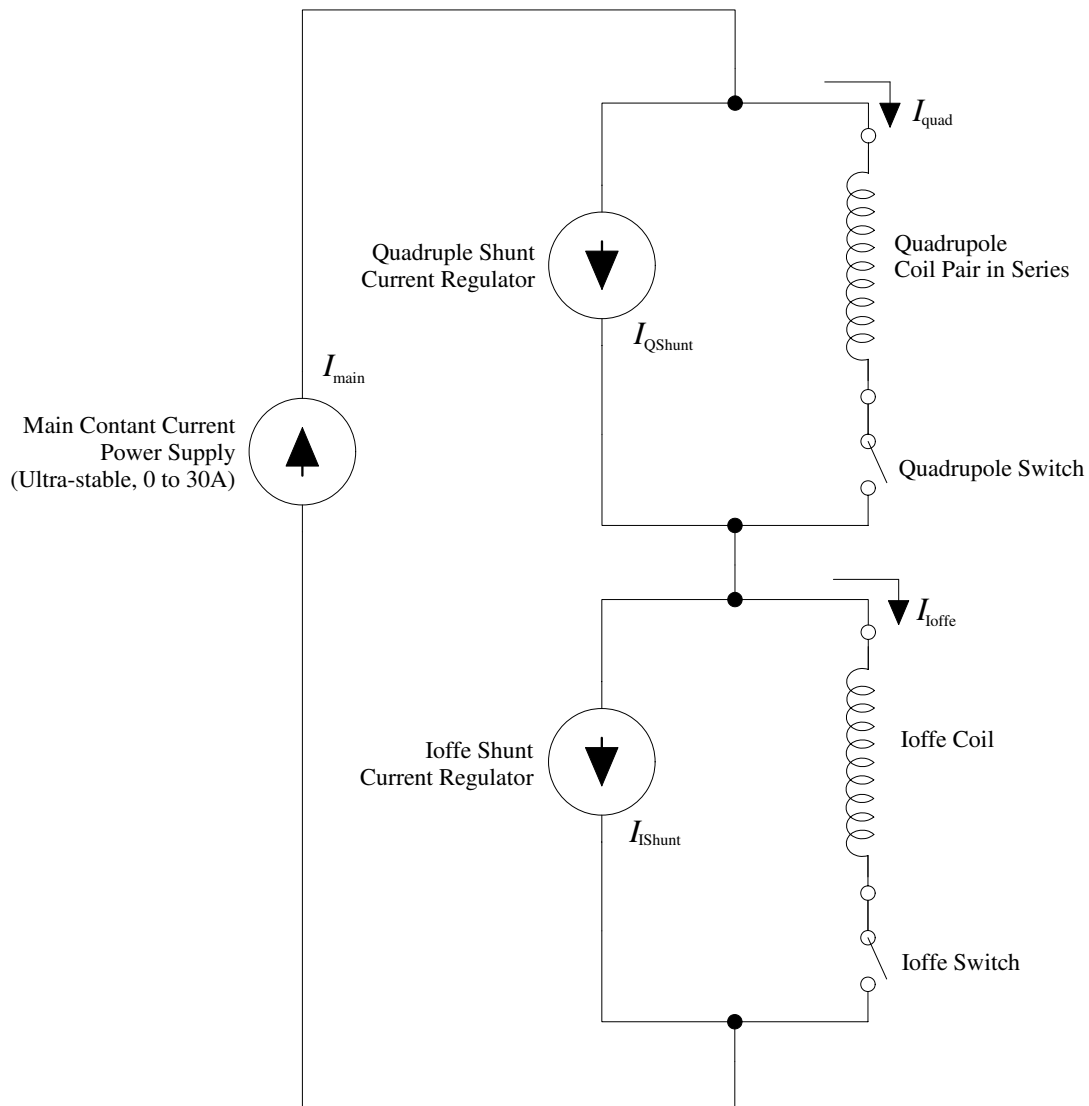


Figure 3.27: Functional schematic of the power circuit for the QUIC trap coils. Full schematics are given in Appendix C. The schematic for the main current source is discussed in Section C.5 and for the power circuit involving the shunt regulators in C.6.

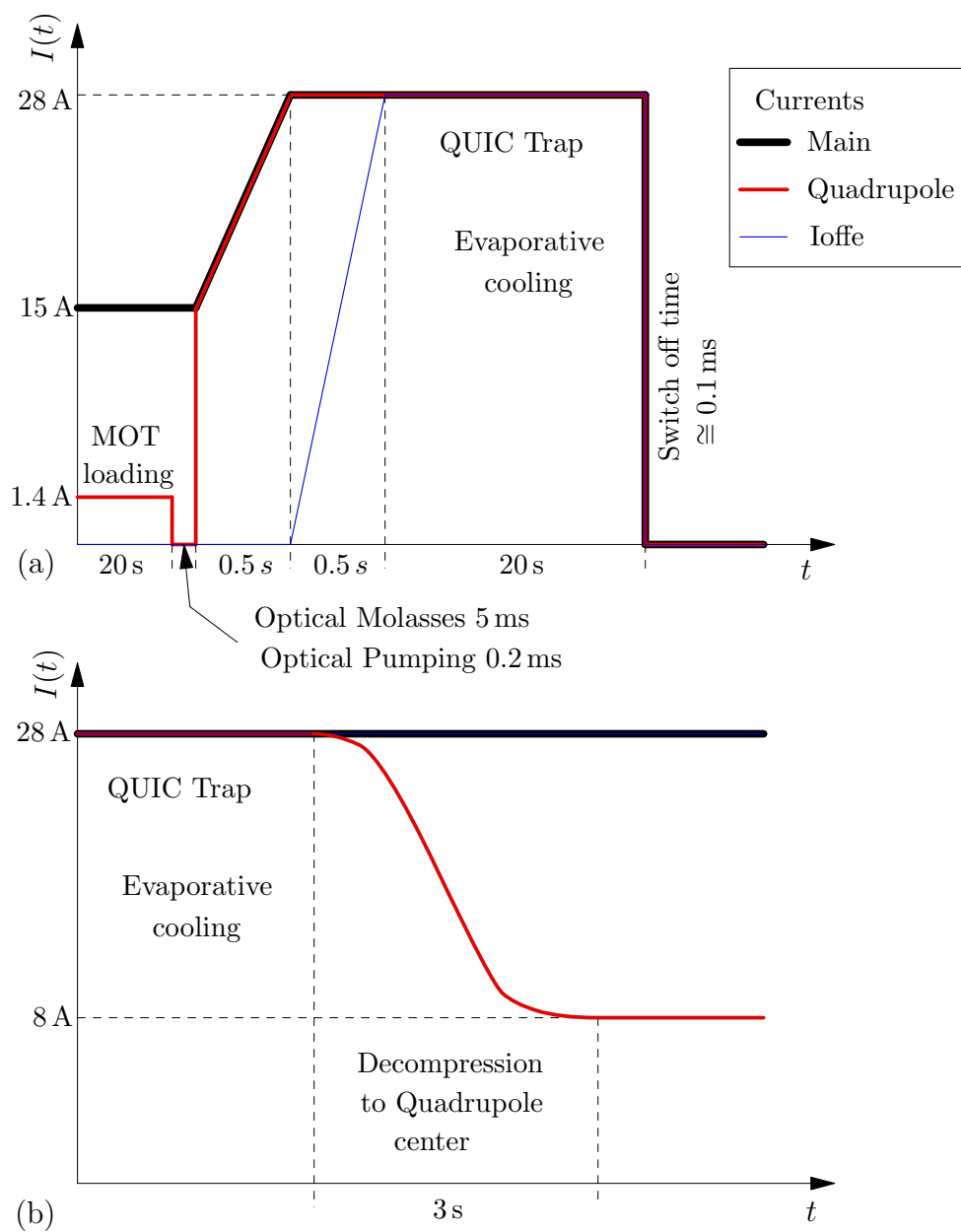


Figure 3.28: Pictorial plots showing the currents of the coils as a function of time. The “Main” is the current through the main regulator. (a) shows the currents for the initial sequence down to production of BEC in the magnetic trap, the switch off is done at that point if that is the end sequence. (b) shows the currents following the configuration of (a) for the decompression of the magnetic trap to the glass cell center.

3.6 Computer Control

The computer control centers around one desktop PC (running Windows 2000) which contains output boards from National Instruments. On the hardware side, the digital NI board is used as a digital output bus to operate a sophisticated and expandable home-build hardware output system described in Appendix D as well as on our website, see [28]. Our experiment presently uses 64 analog outputs and 80 digital outputs.

The software *control* was written in Visual C++ by our postdoc Florian Schreck, also available at [28]. The program is designed as to be easy to update for new routines in the experimental sequence and includes a friendly graphical user interface. It controls the experimental sequence through output waveforms to the NI cards.

The data acquisition is performed on a second PC using the software *vision* also by Florian Schreck [28]. This software talks to two separate computers which control the horizontal and vertical imaging CCD camera through TCP/IP. *Vision* has a sophisticated graphical user interface and provides a convenient platform for on site data analysis.

A third PC, communicating with *vision* through the network, operates the Apogee camera for the vertical imaging system. For the horizontal imaging system, the Princeton Instruments camera is operated by a Macintosh because of its antiquated NuBus technology.

The hardware bus concept that we designed for this experiment is based

to some degree on that which was used in Florian's Ph.D. group at the ENS in Paris [29]. The software is also an expansion of that used there as well.

3.7 Experimental Sequence

This section describes the primary experimental sequence which can produce a BEC in the magnetic trap alone, or supply the initial atom cloud to be loaded into the optical trap as discussed in Chapter 5.

3.7.1 Upper MOT

The upper chamber was described in Section 3.2.1. Figure 3.3 shows the beam layout relative to the upper glass cell. This is a vapor cell MOT. The low energy tail of the thermal background of rubidium atoms is captured in this MOT. Approximately 10^9 atoms are loaded in 0.5 seconds. We use a pair of low-cost CCD cameras to view the fluorescence from the MOT. These cameras are essentially black and white TV cameras which operate continuously to monitor operation (Ramsey Electronics model CCD338). A fluorescence image of the upper MOT is shown in Figure 3.29.

The six beam MOT consists of a horizontal beam and a pair of diagonal beams each which is retroreflected. The beams are all initially linearly polarized and an appropriately aligned quarter-wave plate before the entry to the chamber gives the input beam circular polarization. An additional quarter-wave plate is placed before the retroreflection mirror which results in the counterpropagating beam having the opposite helicity. The horizontal

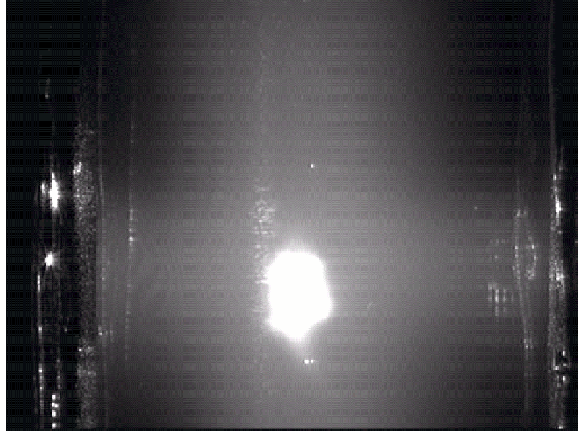


Figure 3.29: A fluorescence image of the upper MOT.

beam uses about half the power from one of the slave lasers and has a $1/e^2$ waist size of about 8 mm with 15 mW. The diagonal beams come from another slave laser, each with the same waist size as the horizontal and 40 mW between them. A repump beam of the same waist size and 5 mW of power couples into the input horizontal MOT beam using a 2" polarizing beam splitter cube.

The required quadrupole field for the MOT to operate is produced by a circular anti-Helmholtz coils pair. The pair consists of 91 windings each of 20 gauge magnet wire. Typically operating at about 2.5 A, the coils produce a field gradient at the MOT location of about 15 G/cm, which is normal for operating a large MOT of this sort. The coils have a diameter 8 cm and are spaced 6 cm apart, nearly in the ideal Helmholtz configuration. They are held by water cooled copper circular mounting blocks. The current is driven by our home built current controllers (see Appendix C). Typically the coils are

run with independent currents. This allows the MOT location to be adjusted slightly if needed and does not result in drift because the current controllers have high stability.

The MOT shown in Figure 3.29 is not typical for loading. A push beam is added to the system from the upper port of the chamber as in Figure 3.3. This setup creates an ‘atom funnel’ where the atoms from the upper MOT are streaming down into the lower chamber through the differential pumping tube [14]. The push beam comes from the upper MOT horizontal slave laser as in Figure 3.17. Although the double-pass AOM may be used to adjust the push beam detuning, typically it is set to be the same as the upper MOT. The beam has about 5 mW of power and is focused to about $100\ \mu\text{m}$ at a location about 5 cm above the upper MOT and diverges to 1 cm at the location of the lower MOT without clipping on the differential pumping tube. This method allows for the loading of the lower MOT.

3.7.2 Lower MOT

The lower MOT is located in the science chamber. It is loaded from the upper MOT. One of the slave lasers produces the light for this MOT as was shown in Figure 3.19. With about 45 mW and a waist of 0.75 mm after spatial filtering, the beam is split into six roughly equal intensity beams. This MOT, in contrast to the upper MOT, operates with the six beams independently controlled. The beam layout is shown in Figure 3.30. The beams are expanded to a waist of about 1 cm. The repump beam has similar size and

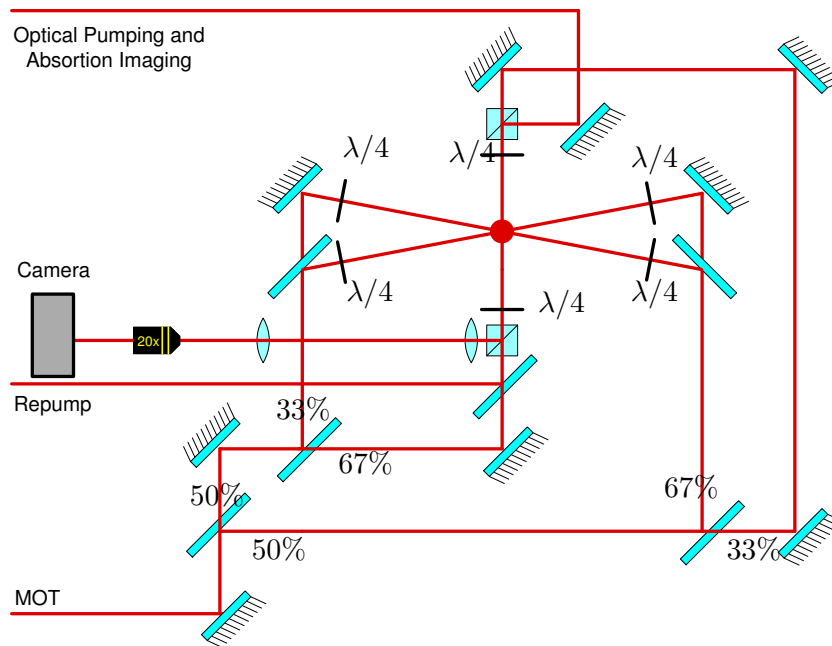


Figure 3.30: The optical setup for the lower MOT.

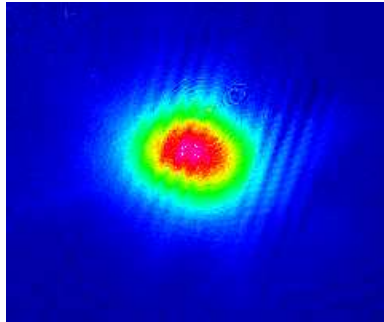


Figure 3.31: An absorption image of the lower MOT. The MOT contains $\approx 1.5 \times 10^9$ atoms. The image was taken with a probe beam detuning of 5 MHz to avoid saturating the image.

5 mW of power. The required quadrupole field for the operation of the MOT is generated by the QUIC trap quadrupole coils running at about 1.4 A. This current results in a gradient of about 15 G/cm.

As mentioned the atoms are loaded from the upper MOT. The initial loading rate is about 1.5×10^8 atoms/second. After a few seconds, this rate drops because of saturation effects. The lower MOT is loaded for about 20 s to reach a final number of about 1.5×10^9 atoms. Figure 3.31 shows an absorption image of such a lower MOT. The cloud has a $1/e^2$ diameter of about 2 mm and a temperature between $100 \mu\text{K}$ and $150 \mu\text{K}$.

After the lower MOT has loaded, the cloud undergoes polarization gradient cooling [30, 31]. The intensity of the lower MOT beams is reduced to 50% of the loading intensity. At the same time the beams are detuned to 50 MHz red of the $F = 2 \rightarrow F' = 3$ atomic transition and the magnetic field is shut off. The atoms remain in the light for 5 ms after which they have been

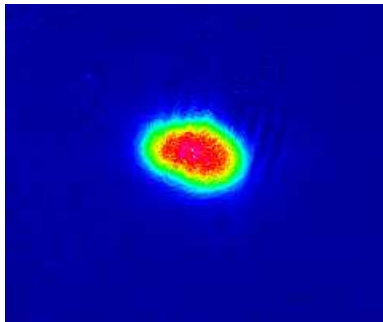


Figure 3.32: An absorption image of the lower MOT after polarization gradient cooling. The MOT contains $\approx 1.3 \times 10^9$ atoms. The image was taken with a probe beam detuning of 7 MHz in order to avoid saturating the image.

cooled down to a typical temperature of $25 \mu\text{K}$ with only a slight loss in atom number. An absorption image of a cloud after this stage is shown in Figure 3.32.

3.7.3 Optical Pumping and Magnetic Trap Loading

As mentioned in Section 2.3, there are several trapping states for rubidium atoms and the others are non-trapping states. We operate with all atoms in the $|F = 2, m_F = +2\rangle$ state. At the end of the lower MOT part of the sequence, the atoms are in various ground states and must be optically pumped into this desired state before transferring into the magnetic trap. The optical pumping scheme is illustrated in Figure 3.33. A small uniform magnetic field defines a quantization axis. The field also produces small energy shifts between the m_F states but these do not have a strong effect on the absorption rate. The optical pumping beam is resonant with the $F = 2 \rightarrow F' = 2$ transition and it is σ_+ polarized with respect to the guiding magnetic field. It is impor-

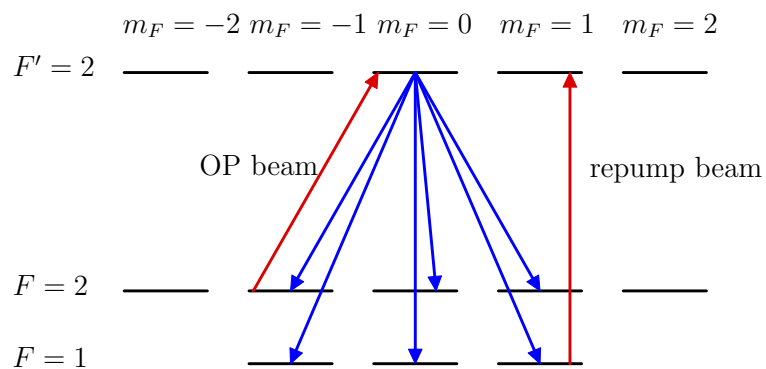


Figure 3.33: Diagram of the optical pumping scheme. Two beams are applied to the sample of atoms shown in red in the figure. The optical pumping beam (OP beam) is resonant on the $F = 2 \rightarrow F' = 2$ transition. Once in that state, the atom spontaneously decays to either the $F = 2$ or $F = 1$ ground state, shown in blue in the figure. A repump beam is needed as well to ensure that atoms that decay to the $F = 1$ are thrown back into the optical pumping cycle.

tant that the magnetic field not be too strong because the energy shifts would result in the laser not being at resonance with all the magnetic sublevels. The magnetic field is produced by the Helmholtz pair discussed in Section 3.5.4. They operate in series and are typically used to produce a uniform magnetic field at the location of the atoms with magnitude of about a one Gauss.

In order to understand Figure 3.33, note that the σ_+ laser drives transitions from $|2, i\rangle$ state to the $|2, i + 1\rangle$ state. Recall that since the state $|2, +2\rangle$ is a stretched state, there is no state to which it can be excited. This state is referred to as a dark state since the atoms no longer see the resonant light. Once in a dark state, atoms will remain in that state. If an atom does become excited, it will decay to one of the ground states available by selection rules with a probability determined by the Clebsch-Gordan coefficients. Since it is possible for the atoms to decay down to the $F = 1$ ground state, the repump laser is also turned on to keep atoms in the optical pumping cycle. After several cycles of excitation and decay, the atoms accumulate in the dark stretched state that is desired for the magnetic trap.

The optical pumping beam is derived from the upper MOT diagonal slave laser as in Figure 3.18. The light is tuned to be on resonance with the $F = 2 \rightarrow F' = 2$ transition; it has a Gaussian profile with a 15 mm waist and is clipped by a 19 mm diameter iris. The beam follows a very similar path as the horizontal absorption beam (see Section 3.8.1). The beam combines with one of the lower MOT horizontal beams in a polarizing beam splitter cube as in Figure 3.30.

The optical pumping time is typically about $200\ \mu\text{s}$ and results in a heating of approximately $5\ \mu\text{K}$. The heating is acceptable since the result is a great increase in atom number in the magnetic trap. The location in time of the optical pumping relative to the operation of the QUIC trap primary coils is shown in Figure 3.28. It occurs between the lower MOT and the magnetic trap stage.

After optical pumping, all the light is turned off and the QUIC trap quadrupole coils are switched on in a few milliseconds to 15 A. They produce a quadrupole magnetic trap with a gradient of approximately 140 G/cm. The switch-on time is fast enough so that the atoms do not fall very far and slow enough that the atoms mostly arrange themselves to remain in the $|2, 2\rangle$ trapping state as discussed in Section 2.3. The quadrupole trap is then compressed as the current is increased to 28 A in a half second after which the Ioffe coil is ramped on in another half second. With the three primary coils of the QUIC trap running in series at 28 A, the trap is a Ioffe-Prichard type with a harmonic potential in the center and no magnetic field zero, which is suitable for evaporative cooling. Figure 3.34 shows absorption images of atoms in various states of the magnetic trap. Figure 3.34(a) and (b) are at the same location in the science chamber as the lower MOT, but the cloud shown in Figure 3.34(c) has a center offset from that location by about 7.5 mm towards the Ioffe coil.

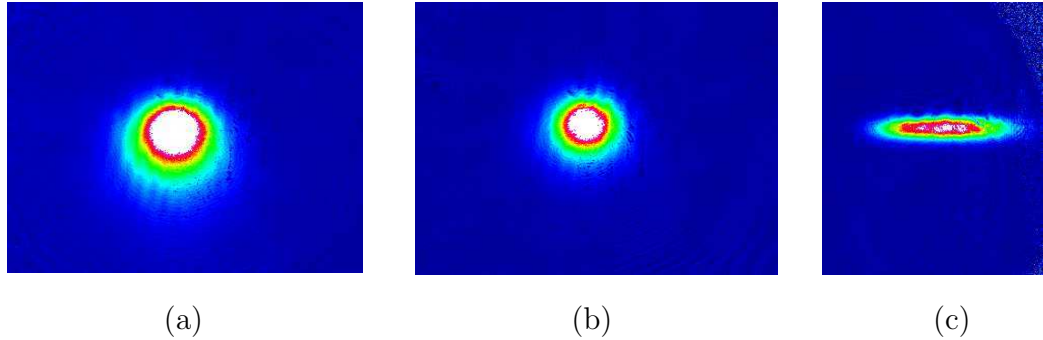


Figure 3.34: Absorption images of atoms within different configurations of the magnetic trap. Image (a) shows the magnetic trap with 15 A in the two quadrupole coils. Image (b) shows the magnetic trap in the compressed trap configuration, and finally, image (c) shows the magnetic trap in the QUIC trap configuration.

3.7.4 Evaporative Cooling

There are a number of mathematical models that describe evaporative cooling [32, 33], but the principle can be explained with a short example. Consider a system of N particles at temperature T_i . The energy distribution for such an ensemble of particles is given by a Maxwell distribution [34]. Now, imagine that the particles with energy greater than some value E_{cut} are removed from the group. The total energy of the group is lower, but the energy distribution of the particles is no longer thermal. To reach equilibrium again, the cloud rethermalizes through elastic collisions. The end product is an ensemble of particles with a lower final temperature, $T_f < T_i$. This is repeated many times with the value of E_{cut} adjusted to remove the same section of the distribution. This process may reduce the temperature to an arbitrarily low

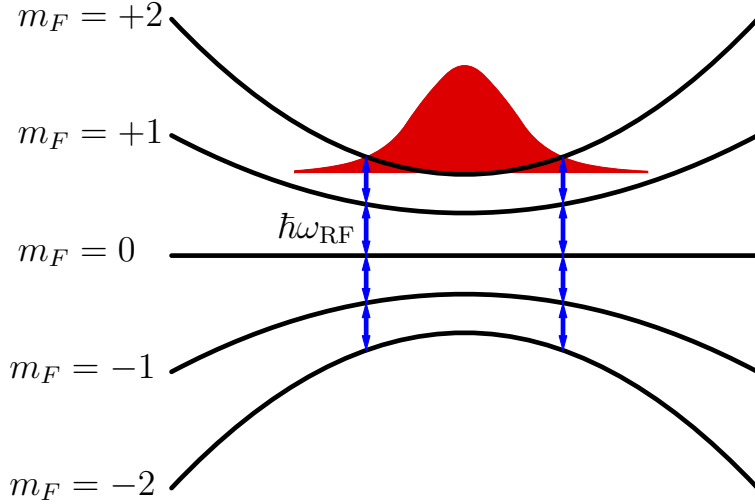


Figure 3.35: A Functional schematic of RF evaporative cooling. Each magnetic sublevel feels a different potential due to the magnetic field. Only the states $|F = 2, m_F = +2\rangle$ and $|F = 2, m_F = +1\rangle$ feel a trapping potential. Radio frequency photons create a position dependent resonance condition that forces higher energy atoms to flip their spins to untrapped states, thereby ejecting them from the trapping region.

value with the price paid in lost atom number. In practice, the value of E_{cut} changes continuously as the atoms undergo rethermalization.

Experimentally, evaporative cooling is done in the magnetic trap with the application of appropriate radio frequency (RF) fields. Figure 3.35 shows a functional schematic of the RF evaporative cooling process. As mentioned earlier, the atoms are loaded into a magnetic trap in a specific magnetic sublevel of the ground state, $|F = 2, m_F = +2\rangle$. The energy of the atom within the trap is the sum of the kinetic energy and the potential energy ($U = m_F g_F \mu_B |\mathbf{B}|$). As an atom moves around the trap, it exchanges kinetic energy for potential

energy, with the more energetic atoms able to explore farther away from the trap center. These more energetic atoms are ejected from the trap through radio frequency (RF) spin flip transitions. The RF creates a position dependent resonance condition forming an effective energy cut in the sample. At some position $\boldsymbol{\rho}_{\text{cut}}$, the energy difference between the different magnetic sublevels ($\Delta U(\boldsymbol{\rho}_{\text{cut}}) = g_F \mu_B |\mathbf{B}(\boldsymbol{\rho}_{\text{cut}})|$) is equal to the energy of the RF photon ($E = \hbar\omega_{\text{RF}}$) and atoms that reach that position will make a transition to a high field seeking magnetic sublevel and are ejected from the trap. After some time longer than the inverse of the trap frequency, all the atoms with energy greater than the cutoff energy are removed from the trap. This is a single step evaporation process.

Forced evaporation refers to the process by which evaporation is artificially made to continue. In a single step process, the hot atoms are ejected and the cloud cools down. The number of atoms with an energy greater than the energy cut decreases, assuming that the collision rate stays constant. Therefore, the efficiency of cooling slows down and the process eventually comes to a halt. In order to force continuation of the evaporation process, the energy of the cut has to be continually reduced.

Efficient evaporative cooling relies on a constant elastic collision rate throughout the evaporative process. The elastic collision rate,

$$\Gamma_{\text{el}} = \bar{n}\sigma_{\text{el}}v, \tag{3.10}$$

depends on the mean density, \bar{n} , the scattering cross section, σ_{el} , and the

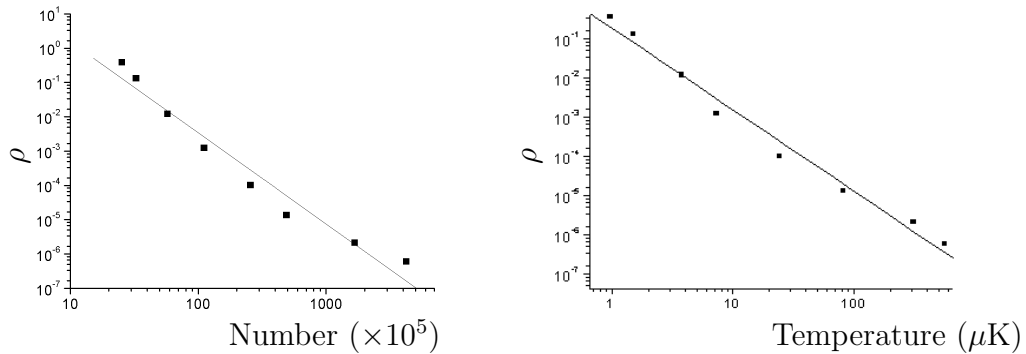


Figure 3.36: Plots of the change in phase space density, ρ , as a function of the change in atom number and the change in temperature of the cloud during evaporation.

relative velocity of the atoms, v . Since $\bar{n} \propto N/T^{3/2}$ and $v \propto T^{1/2}$, it is clear that $\Gamma_{\text{el}} \propto N/T$. Therefore, for evaporation to continue and not slow down, the temperature must decrease proportionally to the atom number.

The real quantity of interest here is the phase space density, ρ , which has a dependence given by $\rho = n\lambda_{\text{deBroglie}}^3 \propto N/T^3 \propto \Gamma_{\text{el}}/T^2$. By appropriately tailoring the decrease in the energy cut, it is possible to keep the elastic collision rate constant and increase the phase space density as the temperature drops. This is referred to as runaway evaporation. Figure 3.36 shows the change in phase space density as a function of atom number as well as a function of temperature. In the experiment, the phase space increases as the inverse of temperature squared indicating that we are in the runaway evaporation regime. Figure 3.37 shows images of atoms within the magnetic trap at various points during the evaporation process. The final result of this entire procedure is a

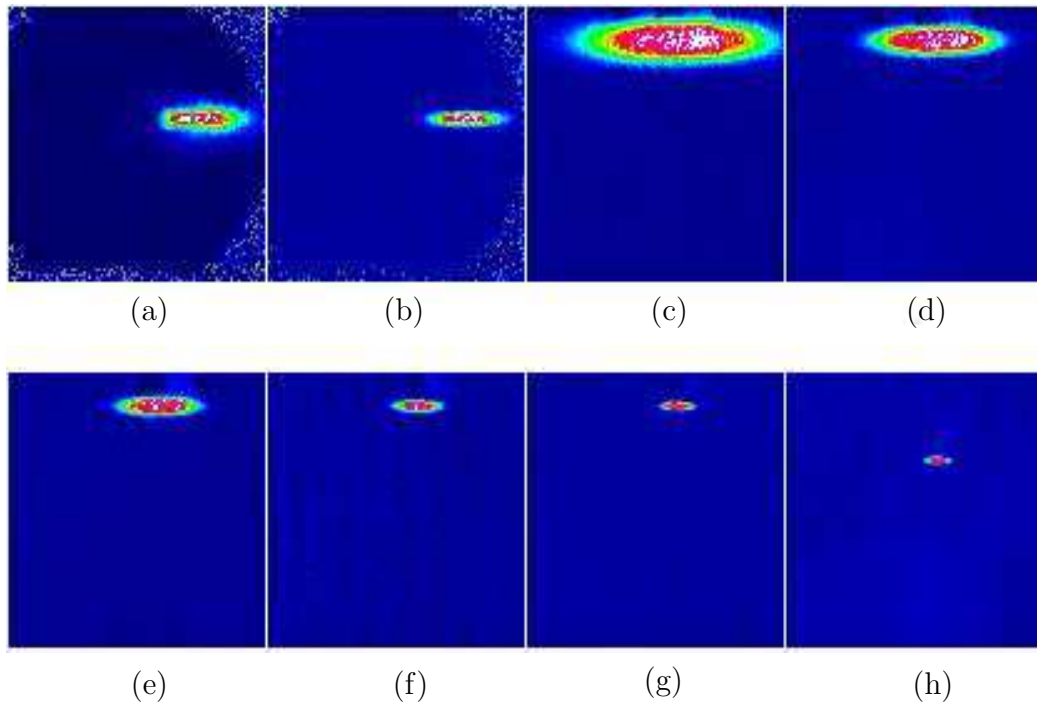


Figure 3.37: Images of the atomic cloud at various points during the evaporation sequence. Images (a) and (b) were taken with the wide angle imaging configuration while the rest of the images were taken with the close-in imaging configuration. The images were taken at the following points in the RF sweep of the evaporation sequence: (a)initial loading, (b)15 MHz, (c)5 MHz, (d)3 MHz, (e)2.1 MHz, (f)1.75 MHz, (g)1.65 MHz, (h)1.55 MHz.

^{87}Rb condensate with approximately 10^6 atoms.

Within the experiment, a Stanford Research Systems function generator model SRS DS-345 is used to generate the radio frequency signal at a power level of 3 dBm. This signal is then amplified with a MiniCircuits RF amplifier model ZHL-3A with a minimum gain of 24 dB and a maximum output of 29.5 dBm. The signal is sent to a small coil located just below the glass cell. The coil radiates the RF signal, thereby supplying the RF knife for forced evaporation. The impedance matching of the coil to the RF source was improved by an in series $50\ \Omega$ resistor.

The frequency of the RF signal is ramped down exponentially. The ramp down starts at a value of 20 MHz and is ramped down to ≈ 1.4 MHz in a period of twenty seconds with a time constant of five seconds. The trap minimum can be found by evaporating until no atoms remain. Under normal operating parameters this corresponds to a magnetic field offset at the trap center of 1.4 G.

3.7.5 The Signature of Condensation

Generally, when detecting a condensate or thermal cloud of atoms we use absorption imaging (see Section 3.8.1). Because of the condensate's small size in the magnetic trap, we drop the cloud by suddenly switching off the magnetic trap. Typically we image after about 18 ms, which is limited by the field of view of the absorption imaging optics. During this time the cloud expands. A thermal cloud in a harmonic trap has a Gaussian density distribution and

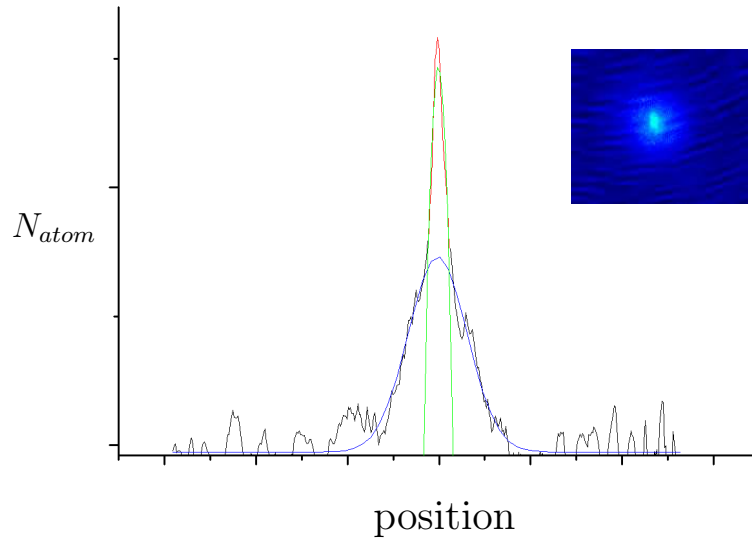


Figure 3.38: The bimodal distribution of a condensate. The inset absorption image shows a cloud of atoms with both a condensate and a thermal part. The plot is a profile of the density along one direction. The black and red lines are the raw data. The red line is the condensate and the black line is the thermal cloud. The green line is a parabolic fit to the condensate data, and the blue line is a Gaussian fit to the thermal data.

spreads equally in all directions. The final position distribution of the cloud at the imaging time reflects the momentum distribution in the trap as discussed in Section 3.8.1. In contrast to the thermal cloud, the condensate has an asymmetric momentum distribution. This causes a greater expansion rate in the strongly trapped direction (see Section 4.3). This results in a change of aspect ratios. This is a clear signature that the threshold for a BEC phase transition has occurred in the trap. Figure 3.38 shows an absorption image and profile of a cloud that contains both a condensed and a non-condensed (thermal) portion. The data curves are fit to an inverted parabola for the

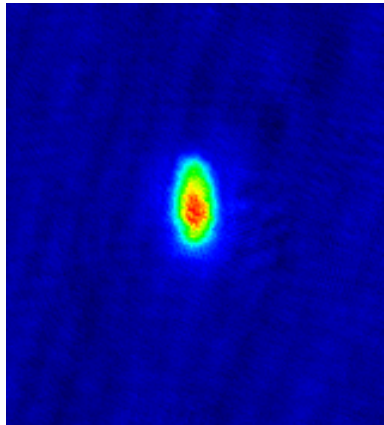


Figure 3.39: A Bose-Einstein condensate of ^{87}Rb . This image of a condensate with 8×10^5 atoms was taken 18 ms after being released from the magnetic trap. The asymmetry results from the asymmetry in the magnetic trap and is a clear sign of condensation. The cloud is a nearly pure BEC with little thermal cloud visible.

condensate (see Section 4.3) and a gaussian for the thermal cloud. Figure 3.39 shows an absorption image of a nearly pure BEC. The difference in experimental sequence producing Figures 3.38 and 3.39 is only in the final steps of evaporation. In the latter, evaporation has continued to a slightly lower energy in the magnetic trap and the result is a nearly pure condensate.

3.8 Imaging of Atoms

3.8.1 Absorption Imaging

Section 2.5 discussed absorption in terms of scattering rate. Typically, we use a zero detuning and an intensity much less than saturation intensity,

I_s . This gives

$$I(x, y) = I_0(x, y) \exp \left[-\sigma \int n(x, y, z) dz \right], \quad (3.11)$$

where $\sigma = 3\lambda^2/2\pi$ is the resonant cross section. This intensity is imaged on a CCD camera. Afterwards, with no atoms present, a second reference image of $I_0(x, y)$ is also taken. From this, the computer can extract necessary information. The optical density is given by

$$D_{\text{opt}}(x, y) = -\ln \left(\frac{I(x, y)}{I_0(x, y)} \right) = \sigma \int n(x, y, z) dz, \quad (3.12)$$

which is directly proportional to the integrated column density of the cloud. The number of atoms is given by

$$N = \int \int n(x, y) dx dy = \frac{1}{\sigma} \int \int D_{\text{opt}}(x, y) dx dy. \quad (3.13)$$

The relative elastic collision rate may also be determined from absorption images. The elastic collision rate is given by Equation 3.10 as $\Gamma_{\text{el}} = \bar{n}\sigma_{\text{el}}v$. The following proportionalities exist

$$v \propto \sqrt{T}, \quad \text{and} \quad \bar{n} \propto \frac{N}{V} \propto \frac{N}{T^{3/2}}, \quad (3.14)$$

where the final expression is due to the fact that the volume of a classical gas may be characterized by a Gaussian standard deviation $\sigma_x \propto \sqrt{T}$. The elastic collision rate is therefore proportional to N/T . This means that the optical density in the center of the cloud is proportional to the elastic collision rate as in

$$D_{\text{opt}}(0, 0) \propto \int n(0, 0, z) dz \propto \frac{N}{T} \propto \Gamma_{\text{el}}. \quad (3.15)$$

A sequential analysis of optical density during the evaporation process, therefore, can show that runaway evaporation occurs — that is, the elastic collision rate remains constant or increases.

Another important quantity to determine is the temperature. For a thermal cloud released from a trap, temperature may be determined by time-of-flight expansion. During this time, the momentum distribution is converted in to a position distribution. The final density distribution imaged is a convolution of the initial spatial distribution with the momentum distribution. The density distribution in time is characterized by its $1/\sqrt{e}$ size

$$\sigma_x^2(t) = \sigma_x^2(0) + \frac{\sigma_p^2}{m^2}t^2, \quad (3.16)$$

where σ_x and σ_p characterize the Gaussian position and momentum distributions. The momentum distribution may be written

$$\phi(p) = \frac{1}{\sqrt{2\pi}\sigma_p} \exp\left(-\frac{p^2}{2\sigma_p^2}\right). \quad (3.17)$$

From this, if we note that $(1/2)k_B T = \langle E_k \rangle_p$ is the average kinetic energy and $E_k = p^2/2m$, we have the temperature

$$T = \frac{\sigma_p^2}{mk_B}, \quad (3.18)$$

where σ_p^2 is given by Equation 3.16 and determined from an image taken at time t .

Equation 3.12 gives the optical density. This two-dimensional quantity is line integrated in the third dimension. In order to obtain complete spatial

information about the atom clouds, we employ a pair of orthogonally oriented absorption imaging systems which we call the horizontal and the vertical systems.

The horizontal probe beam comes from the upper MOT diagonal slave laser as discussed in Section 3.3.2.2 and shown in Figure 3.18. The beam is on resonance, with a diameter of about 30 mm at a power of about 5 mW. The beam is cut by an iris of about 19 mm in diameter. The beam enters the chamber as in Figure 3.30. It combines with one of the horizontal MOT beams with a 1" polarizing beam splitter cube (PBS) and is then separated by a second PBS after the chamber after which it is transported by a pair of $f = 120$ mm lenses. The beam is imaged onto a CCD camera by an interchangeable lens system. The CCD camera is a Princeton Instruments model TE/CCD-5122TK/1UV. The chip has a 512×512 array of $20 \mu\text{m}$ pixels. The interchangeable lenses consist of a 38.1 mm focal length lens and a $4\times$ microscope objective leading to magnifications of $0.67\times$ and $3.33\times$ respectively. The imaging system was calibrated against a known reference.

The vertical probe beam comes from the upper MOT horizontal slave laser as discussed in Section 3.3.2.1 and shown in Figure 3.17. The beam is on resonance with a power of about 3.5 mW. The beam combines with the push beam in a 1.2" PBS and enters the vacuum system through the top port of the upper chamber as shown in Figure 3.3. It is focused through the differential pumping tube and expands to approximately 15 mm at the location of the atoms in the lower chamber. It is collected by the same optics

used for the vertical optical trap beams in Figure 5.2 and then transported to a CCD camera. The CCD camera is the Apogee Alta series U47+ with 1024×1024 pixels. This camera *theoretically* has a frame-shift option which should allow for fast acquisition of the probe beam with and without atoms for very clear images. The option, however, has not been implemented at this writing because Apogee has not delivered the drivers. The beam is imaged onto the CCD with a 38.1 mm focal length lens giving a magnification of $4.33\times$.

3.8.2 Florescence Imaging

The vertical imaging system has the possibility of making fluorescence images. The atom number may be estimated from [17]

$$N_{\text{atoms}} = \frac{8\pi [1 + 4(\delta/\Gamma)^2 + (6I_0/I_s)]}{\Gamma(6I_0/I_s)t_{\text{exp}}\eta_{\text{count}}d\Omega} N_{\text{counts}}, \quad (3.19)$$

where δ is the detuning from the atomic transition, Γ is the natural linewidth of that transition, I_0 is the intensity of one of the MOT beams, I_s is the saturation intensity, t_{exp} is the exposure time, η is the quantum efficiency of the camera, N_{counts} is the integrated number of counts on the CCD, and $d\Omega$ is the solid collection angle of the camera.

3.8.3 Atom Counting

Because some of the goals of this experimental setup involve extraction of single atoms and very small condensates, it was necessary to construct an atom counting system. Our system is similar to that of the group of Meschede in Bonn [35]. The system is based on a very weak MOT, a large collection

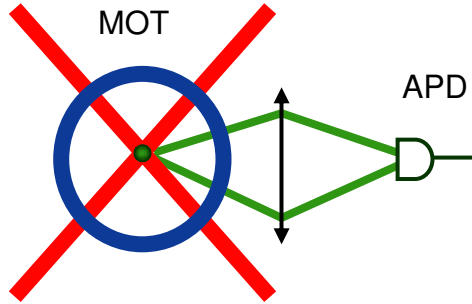


Figure 3.40: Atom counting pictorial. A lens collects the MOT florescence which is measured by the avalanche photodiode (APD).

angle lens system, and an avalanche photodiode (APD). We conventionally call the weak MOT a single atom detection MOT (SAD MOT or SAM).

The setup concept is shown pictorially in Figure 3.40. The weak MOT involves several factors that separate it from the regular lower MOT used for large number collection. Those are: very strong gradients (265 G/cm vs. 15 G/cm), small waist size (0.5 mm vs. 1 cm), near resonance detuning (3.5 MHz vs. 18 MHz red). These factors result in a MOT with a very small capture volume and a load rate from background vapor of order 1 atom per 10 seconds. The power in the SAM beams is generally about 0.1 mW which actually gives a larger intensity than the regular MOT beams, but this is unimportant because both operate well above the saturation intensity. A dedicated SAD MOT beam was created out of the zeroth order of the lower MOT beam as shown in Figure 3.19. This beam is transported to the lower MOT region where it is combined with the regular lower MOT beams. This was

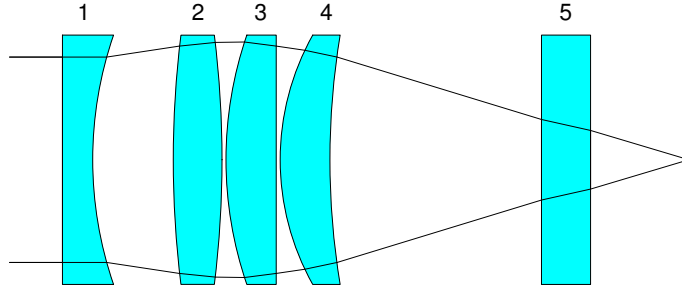


Figure 3.41: Single atom detection “super lens”. The lens system consists of four lenses: 1) 40.0 mm focal length plano-concave lens, 2) 50.0 mm focal length bi-convex lens, 3) 40.0 mm focal length plano-convex lens, 4) meniscus lens with 26 mm and 78 mm radii of curvature, and 5) 5 mm thick slab of fused silica.

accomplished by mixing the SAD MOT beams with the regular MOT beams on a 90%-10% beam splitter. A mechanical flipper with a 1 mm aperture was placed in the repump beam path. When the SAD MOT is activated, the aperture is flipped into place reducing the repump beam to 1 mm in diameter. The reduction in size of all of these beams makes the MOT weak, but it also has the benefit of reducing the amount of scattered light that reaches the APD. The required quadrupole field for the SAM operates from the QUIC trap quadrupole coils run at 28 A resulting in a gradient of roughly 265 G/cm.

The collection lens used in this scheme is actually a carefully chosen collection of lenses. The design is identical to that used by Alt [36]. Four lenses, in addition to one wall of the glass cell that comprises the vacuum chamber, are appropriately spaced to create a “super lens” assembly (see Figure 3.41) with a solid collection angle of roughly 2% of 4π . The lens system was designed

to reduce spherical aberrations up to 7th order and astigmatism to 3rd order. Designed for imaging, this system is more than adequate since we are only interested in light collection. Regardless, the lens system works well for the purposes of this experiment.

The lens system was first aligned to image a small (but not SAD) MOT onto a small CCD camera, then replace it with the APD. The fluorescence is collected by the lens assembly and transported. An achromat doublet focuses the light through a $100\ \mu\text{m}$ pinhole to reduce the off axis light collected. A final lens focuses the collected light onto the APD sensor. After this rough alignment, the signal is optimized on the SAM fluorescence count.

The APD is manufactured by Perkin Elmer, model SPCM-AQR-14. The APD has an active area of $175\ \mu\text{m} \times 175\ \mu\text{m}$ and an overall photon detection efficiency of $\approx 66\%$ at $780\ \text{nm}$. The dark count for the APD is 50 counts per second with a maximum of 100 counts per second. The APD is capable of a mean count rate of 5 million counts per second before saturation effects start to become appreciable. The module can withstand count rates up to 15 million counts per second before damage occurs. This limit is never approached during the course of the experiment.

The APD is an extremely sensitive device that can be easily destroyed by an excessive amount of light, therefore, a series of protection devices are in place. Immediately in front of the APD is an interference filter with a $10\ \text{nm}$ bandwidth centered at $780\ \text{nm}$. This filter reduces the fluorescence signal by $\approx 50\%$ but reduces scattered light outside the bandwidth by roughly

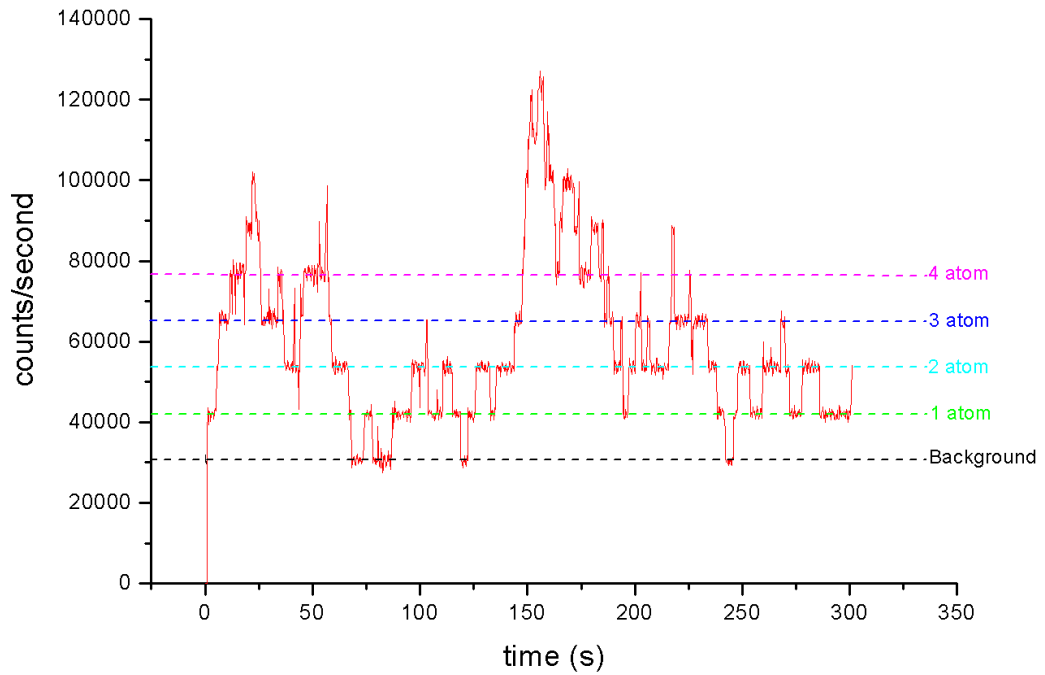


Figure 3.42: Photon count rates taken during the operation of a weak MOT. This data was taken with a MOT detuning of 3.75 MHz, MOT intensity of 20% maximum, repump intensity of 20% maximum, and a magnetic field gradient of 265 G/cm. The average background scattered light signal is 30,700 counts per second. Each atom provides an additional signal of 11,400 counts per second. The quantized levels corresponding to different numbers of atoms within the MOT are highlighted with colored lines.

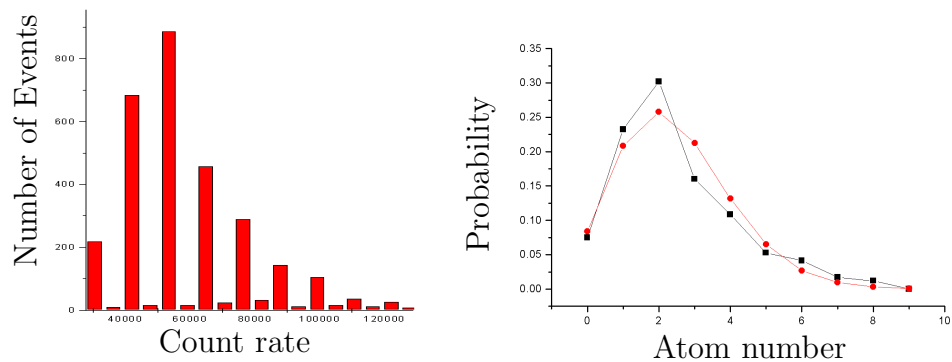


Figure 3.43: A histogram of the counts shown in Figure 3.42. The data was sorted into a histogram with bin sizes that are half the single atom signal rate centered at the background signal rate. The plot on the right shows the fit of the histogram peaks to a poissonian distribution as would be expected for a random process such as the loading of a MOT. The poissonian fit had an average atom number of 2.475.

four orders of magnitude. Additionally, a UniBlitz shutter is in front of the APD. It only opens during the measurement of few atoms. This reduces the possibility of stray light hitting the APD. An electronic security box was also built for additional protection. The security circuit is based on a photodiode used to detect excess light in the area of the APD and cancels commands to open the APD shutter or turn on the gate voltage.

Because the SAM generally operates with a few atoms loading in some seconds, it is easy to confirm that it is possible to observe and distinguish few atom numbers. A fluorescence plot is given in Figure 3.42. The data was taken with a MOT detuning of 3.75 MHz, MOT intensity of 20% maximum, repump intensity of 20% maximum, and a magnetic field gradient of 265 G/cm. The

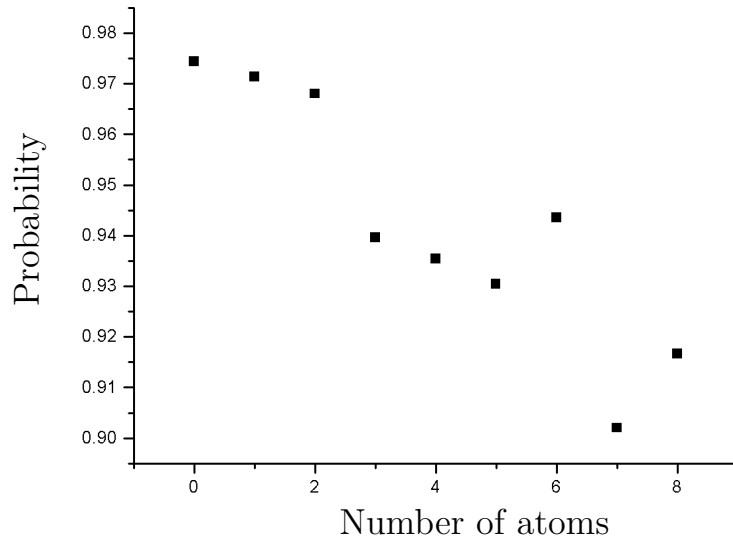


Figure 3.44: A plot of the reliability of the single atom detection system. The probability displayed is that of finding the same number of atoms on the next measurement cycle as a function of the measured atom number.

average background scattered light signal is 30,700 counts per second. Each atom provides an additional signal of 11,400 counts per second. In the plot, the quantized steps of singles, doubles, etc... are easily distinguished. The background rate was also measured by recording the fluorescence with the magnetic fields off. Figure 3.43 shows a histogram plot of the Figure 3.42 data. The data was sorted into bins 5,700 counts per second wide in size, starting at the background counting rate. The histogram clearly shows distinct peaks every 11,400 counts per second that arise from an integer number of atoms in the trap. A comparison of the peaks to the valleys estimates the error rate of the number detection of the system. For the zero, one, and two atom cases,

the correct number of atoms is determined at least 95% of the time or better. The Poissonian fit in Figure 3.43 for this run gives an average number of about 2.5 atoms. The probability distribution is Poissonian because loading of the MOT in this case is random. Figure 3.44 shows the reliability of atom number measurements and the dependence on atom number. The probability is over 97% for zero to two atoms.

The discussion thus far was a diagnostic approach to detecting single atoms that were randomly loaded from the background. Section 6.4 discusses methods to transfer atoms from the optical traps into the SAD for atom counting. This is for post detection of atom number at the end of an experimental run.

Chapter 4

Lower Dimensional BEC

This chapter starts with a review of Bose-Einstein condensate concepts in three dimensions, a topic covered in detail in several texts [37, 38]. We then continue with the relevant equations for lower dimensional BECs, which are very important for the experimental system.

4.1 Bose-Einstein Statistics

The topics of classical and quantum statistics are covered well in many texts [34, 39]. Here we give a brief on the relevance to Bose-Einstein condensation. In this section, we refer to an ideal gas of non-interacting bosons.

Indistinguishable particles with zero or integer spin are called bosons. Bosons do not obey the Pauli exclusion principle and there is, therefore, no limit to the number of bosons that can occupy a single particle state. For a system of bosons with chemical potential μ and quantum states of energy E , the state occupation is given by the Bose-Einstein distribution

$$f(E) = \frac{1}{e^{(E-\mu)/k_B T} - 1}, \quad (4.1)$$

where T is the temperature of the system and k_B is Boltzmann's constant.

An important concept is that of *phase-space density*. Denoted by ρ , phase-space density is the number of particles contained within a volume of size λ_{dB}^3 , where $\lambda_{\text{dB}} = \sqrt{2\pi\hbar^2/mk_{\text{B}}T}$ is the thermal de Broglie wavelength. This is written as

$$\rho = n \left(\frac{2\pi\hbar^2}{mk_{\text{B}}T} \right)^{3/2}, \quad (4.2)$$

for number density n . Bose-Einstein condensation occurs when the phase space density of the system becomes comparable to unity. This is a situation where the average distance between the particles is similar to the thermal de Broglie wavelength. It is clear that this is the case for low temperatures and high densities.

For some trap geometry, a density of states may be derived and from this a critical temperature calculated. For a uniform bose gas in a box with volume V , the critical temperature is given by

$$T_{\text{c}} = \frac{2\pi\hbar^2}{mk_{\text{B}}} \left(\frac{n}{\zeta(3/2)} \right)^{2/3} \quad (4.3)$$

where $n = N/V$ is the number density and $\zeta(3/2) \cong 2.612$ is the Riemann zeta function at $3/2$. For a gas in a harmonic trap with geometric mean trap frequency $\bar{\omega}$, the critical temperature is given by

$$T_{\text{c}} = \frac{\hbar\bar{\omega}N^{1/3}}{k_{\text{B}}[\zeta(3)]^{1/3}}, \quad (4.4)$$

where N is the atom number and $\zeta(3) \cong 1.202$.

For a uniform gas, this gives a critical phase space density of

$$\rho\lambda_{\text{dB}}^3 \geq \zeta(3/2) \approx 2.612 \dots, \quad (4.5)$$

to be in the condensation region. The condensate fraction at some T below T_c is given by

$$N_o = N \left[1 - \left(\frac{T}{T_c} \right)^3 \right]. \quad (4.6)$$

In the QUIC trap with $\bar{\omega} \cong 2\pi \cdot 90$ Hz and about 2 million atoms, $T_c \cong 450$ nK.

4.2 Weakly Interacting Gas

In the previous section, we reviewed the basics of Bose-Einstein statistics for non-interacting particles. Because our experiments all involve dilute gases, this section puts the concept in context. These concepts are discussed in detail in [37, 38].

Consider a gas of number density $n = N/V$. If r_0 is the range of interatomic forces, the gas is considered dilute if

$$r_0 \ll n^{-1/3}. \quad (4.7)$$

The distance between the particles, therefore, is long enough to use the asymptotic approximation for the wavefunction that describes the relative motion of a pair of particles and interactions with three or more particles may be neglected. Considering particles with momentum p , the low energy limit is where $pr_0 \ll \hbar$. In this case, the scattering amplitude of two-body interactions is independent of the energy and of the scattering angle. The single parameter a , the s-wave *scattering length*, describes the interactions. The condition for diluteness may then be written as $|a| \ll n^{1/3}$.

The quantum mechanics of elastic scattering is a topic covered well in many textbooks, see for example [40] for an outstanding discussion. For r relative distance between two particles, in the asymptotic region where $r \gg r_0$, the Schrödinger equation has a solution of the form

$$\psi(\mathbf{r}) = e^{ikz} + f(\theta) \frac{e^{ikz}}{r}, \quad (4.8)$$

which is the sum of the initial z propagating wave and the outgoing spherical scattered wave with scattering amplitude $f(\theta)$. It can be shown that as $E \rightarrow 0$, $f(\theta) \rightarrow -a$ the s-wave scattering length. This is to say that low energy collisions are with no angular dependence. For identical particles, the scattering cross-section is

$$d\sigma = |f(\theta) \pm f(\pi - \theta)|^2 d\Omega, \quad (4.9)$$

for solid angle $d\Omega$, carried out on the half-sphere $0 \leq \theta \leq \pi/2$. The plus corresponds to bosons and the minus to fermions. In the low energy limit, this results in

$$\sigma = 8\pi a^2, \quad (4.10)$$

for bosons and zero for fermions. For rubidium 87, the s-wave scattering length is approximately $a \cong 5.29 \text{ nm} \cong 100a_0$, where a_0 is the Bohr radius.

The preceding discussion referred to two-body elastic processes. In the dilute gas approximation, interactions between three or more particles simultaneously was neglected. In practice this is actually what limits the peak density possible in our atom clouds. Typically three body effects become

important for densities of the order 10^{14} atoms/cm². This results in a rate of trap loss given by

$$\frac{dN}{N} = -k_3 \langle n^2 \rangle dt, \quad (4.11)$$

where $k_3 = 1.81 \times 10^{-29}$ cm⁶/s for rubidium 87 [41] and $\langle n^i \rangle = 1/N \int n^{i+1} dV$ is the weighted average density. This equation gives an exponential loss rate with time constant

$$\tau_3 = \frac{1}{k_3 \langle n^2 \rangle}, \quad (4.12)$$

which will typically have a value of several seconds for our three-dimensional condensates in the QUIC trap.

4.3 Three-Dimensional Condensates

Considering the s-wave interactions discussed in the previous section, it is possible to derive a nonlinear Schrödinger equation known as the Gross-Pitaevskii (GP) equation [37, 38]

$$\left(-\frac{\hbar^2}{2m} \nabla^2 + V(\mathbf{r}) + g_{3D} |\psi(\mathbf{r})|^2 \right) \psi(\mathbf{r}) = \mu_{3D} \psi(\mathbf{r}), \quad (4.13)$$

where

$$g_{3D} = \frac{4\pi \hbar^2 a_s}{m}, \quad (4.14)$$

is the *coupling factor* which describes the interactions between atoms and μ_{3D} is the chemical potential. These parameters are written with the ‘3D’ subscript because, as discussed in the following sections the expressions depend on dimensionality of the system. The wavefunction satisfies the normalization

condition for atom number

$$N = \int |\psi(\mathbf{r})|^2 d\mathbf{r}, \quad (4.15)$$

where $n(\mathbf{r}) = |\psi(\mathbf{r})|^2$ is the density.

A simplified viewpoint of the GP equation can be obtained in the Thomas-Fermi (TF) approximation. This is an approximation where the kinetic energy is assumed to be small compared to the potential and the interaction terms. This is a valid approximation for condensates of sufficient number and/or interaction strength [37, 38]. This leads to an equation of the form

$$(V(\mathbf{r}) + g_{3D}|\psi(\mathbf{r})|^2) \psi(\mathbf{r}) = \mu_{3D}\psi(\mathbf{r}) \quad (4.16)$$

which immediately gives a number density of

$$n(\mathbf{r}) = |\psi(\mathbf{r})|^2 = \frac{\mu_{3D} - V(\mathbf{r})}{g_{3D}}. \quad (4.17)$$

Assuming a harmonic potential in three directions, the extent of the cloud may be given by three semi-axes written as

$$R_i^2 = \frac{2\mu_{3D}}{m\omega_i^2}, \quad (4.18)$$

where $\omega_i/2\pi$ are the trap frequencies. Integrating on the scaled sphere then gives the atom number in terms of μ_{3D} which results in

$$\begin{aligned} \mu_{3D} &= \frac{15^{2/5}}{2} \left(\frac{Na_s}{\bar{a}} \right)^{2/5} \hbar\bar{\omega} \\ &= \frac{15^{2/5}}{2} (N^2 a_s^2 \hbar^4 m \bar{\omega}^6)^{1/5}, \end{aligned} \quad (4.19)$$

where $\bar{\omega}/2\pi = (\omega_x\omega_y\omega_z)^{1/3}/2\pi$ is the geometric mean of the trapping frequencies and $\bar{a} = \sqrt{\hbar/m\bar{\omega}}$ is the geometric mean of the harmonic oscillator lengths. For a similar configuration, but assuming a three-dimensional box-like potential where x and y axis are harmonic as with Equation 4.18, and the z direction is flat with length L_z , a similar analysis results in

$$\mu_{3D} = \left[4N \frac{a_s}{L_z} (\hbar\omega_x)(\hbar\omega_y) \right]^{1/2}. \quad (4.20)$$

This equation is easier to handle if the potential is box-like in one direction.

4.4 Two-Dimensional Condensates

Assume a condensate is confined in a trap with one direction much stronger than the other two, say $\omega_x \gg \omega_y, \omega_z$. This may be considered a two-dimensional condensate under the condition

$$\hbar\omega_x \geq \mu_{3D}. \quad (4.21)$$

Under this condition, the wavefunction in the x direction may be approximated by a single particle wavefunction for the harmonic oscillator. In the other two directions, it is possible to use the Thomas-Fermi approximation. When this condition is far from met, the condensate is really a squished three-dimensional condensate with a Thomas-Fermi profile in all directions.

It can be shown that the maximum number of atoms for this configuration is given by [42]

$$N_{2D} = \sqrt{\frac{32\hbar}{225ma_s^2}} \sqrt{\frac{\omega_x^3}{\omega_\perp^4}}, \quad (4.22)$$

where $\omega_{\perp}/2\pi = \sqrt{\omega_y\omega_z}/2\pi$ is the geometric mean of the trapping frequencies in the two weakly confining directions. The GP equation may be rewritten assuming the solution

$$\psi(x, y, z) = \phi(y, z) \left(\frac{m\omega_x}{\pi\hbar} \right)^{1/4} e^{-\frac{m\omega_x}{2\hbar}x^2}, \quad (4.23)$$

where $\phi(y, z)$ is the two-dimensional condensate wavefunction. Integrating out the strong direction x , this results in the two-dimensional GP equation

$$\left(-\frac{\hbar^2}{2m} \nabla_{y,z}^2 + V(y, z) + g_{2D} |\phi(y, z)|^2 \right) \phi(y, z) = \mu_{2D} \phi(y, z), \quad (4.24)$$

where

$$\begin{aligned} g_{2D} &= \left(\frac{m\omega_x}{2\pi\hbar} \right)^{1/2} g_{3D} \\ &= \left(\frac{8\pi\omega_x\hbar^3 a_s^2}{m} \right)^{1/2} \end{aligned} \quad (4.25)$$

is the two-dimensional coupling factor and μ_{2D} is the two-dimensional chemical potential. Using the TF approximation in the two weak directions, the chemical potential may be written as

$$\begin{aligned} \mu_{2D} &= (8\pi)^{1/4} \left(\frac{3}{8} \right)^{1/2} \left(\frac{Na_s}{a_x} \right)^{1/2} \hbar\bar{\omega}_{\perp} \\ &= \left(\frac{9}{8} \pi N^2 a_s^2 m \hbar^3 \omega_x \omega_y^2 \omega_z^2 \right)^{1/4}, \end{aligned} \quad (4.26)$$

where $a_x = \sqrt{\hbar/m\omega_x}$ is the harmonic oscillator length in the tight confining direction.

For purposes of estimating three-body loss rates as in Equation 4.12, in a two-dimensional condensate, the average squared density is

$$\langle n^2 \rangle = \frac{9N}{32\sqrt{3}\pi} \frac{1}{a_s} \frac{1}{a_x} \frac{1}{\bar{a}_{\perp}^4}, \quad (4.27)$$

where $\bar{a}_\perp = \sqrt{\hbar/m\bar{\omega}}$ is the geometric mean of the harmonic oscillator lengths in the two weak directions.

4.5 One-Dimensional Condensates

Assume a condensate is confined in a trap with two direction much stronger than the other, say $\omega_x, \omega_y \gg \omega_z$. This may be considered a one-dimensional condensate, under the condition

$$\hbar\omega_x, \hbar\omega_y \geq \mu_{3D}. \quad (4.28)$$

Under this condition, the wavefunction in the x and y directions may be approximated by the single particle wavefunctions for the harmonic oscillator. In the other direction, it is possible to use the Thomas-Fermi approximation. When this condition is far from met, the condensate is really a squished three dimensional condensate with a Thomas-Fermi profile in all directions.

It can be shown that the maximum number of atoms for this configuration is given by [42]

$$N_{1D} = \sqrt{\frac{32\hbar}{225ma_s^2}} \sqrt{\frac{\omega_\perp}{\omega_z^2}}. \quad (4.29)$$

$\omega_\perp/2\pi = \sqrt{\omega_x\omega_y}/2\pi$ is the geometric mean of the tight confining trap frequencies and $\omega_z/2\pi$ is the weak trap frequency. In the case of a flat trap of length L_z , the maximum number is actually independent of the transverse trapping frequencies and is given by

$$N_{1D} = \frac{L_z}{4a_s}. \quad (4.30)$$

The two-dimensional GP equation may be rewritten assuming a solution to Equation 4.24 of

$$\phi(y, z) = \varphi(z) \left(\frac{m\omega_y}{\pi\hbar} \right)^{1/4} e^{-\frac{m\omega_y}{2\hbar}y^2}, \quad (4.31)$$

where $\varphi(z)$ is the one-dimensional many-body wavefunction. Integrating out the y direction, the result is a one-dimensional GP equation

$$\left(-\frac{\hbar^2}{2m} \frac{\partial^2}{\partial z^2} + V(z) + g_{1D}|\varphi(z)|^2 \right) \varphi(z) = \mu_{1D}\varphi(z), \quad (4.32)$$

where

$$\begin{aligned} g_{1D} &= g_{2D} \left(\frac{m\omega_y}{2\pi\hbar} \right)^{1/2} = g_{3D} \frac{m\omega_{\perp}}{2\pi\hbar} \\ &= 2\hbar a_s \omega_{\perp} \end{aligned} \quad (4.33)$$

is the one-dimensional coupling constant and μ_{1D} is the one-dimensional chemical potential. Using the TF approximation in the weak direction, the chemical potential may be written as

$$\begin{aligned} \mu_{1D} &= \left(\frac{9}{32} m \omega_z^2 g_{1D}^2 N^2 \right)^{1/3} \\ &= \left(\frac{9}{8} N^2 m a_s^2 \hbar^2 \omega_z^2 \omega_{\perp}^2 \right)^{1/3} \end{aligned} \quad (4.34)$$

Rather than assuming a harmonic potential in the z direction, if it is assumed that the trap is flat with a length L_z in the weak direction, the chemical potential is given by

$$\begin{aligned} \mu_{1D} &= g_{1D} \frac{N}{L_z} \\ &= 2\hbar a_s \omega_{\perp} N / L_z. \end{aligned} \quad (4.35)$$

For purposes of estimating three-body loss rates as in Equation 4.12, in a one-dimensional condensate, the average squared density is

$$\langle n^2 \rangle = \frac{3}{35\pi^2} \sqrt[3]{\frac{3}{2}} \frac{1}{a_{\perp}^4} \left(\frac{a_{\perp}^2}{a_s a_z^4} \right)^{2/3} N^{4/3}, \quad (4.36)$$

where a_{\perp} is the geometric mean of the harmonic oscillator lengths in the tight confining directions and a_z is the harmonic oscillator length in the weak direction.

Chapter 5

Bose-Einstein Condensate in an Optical Box

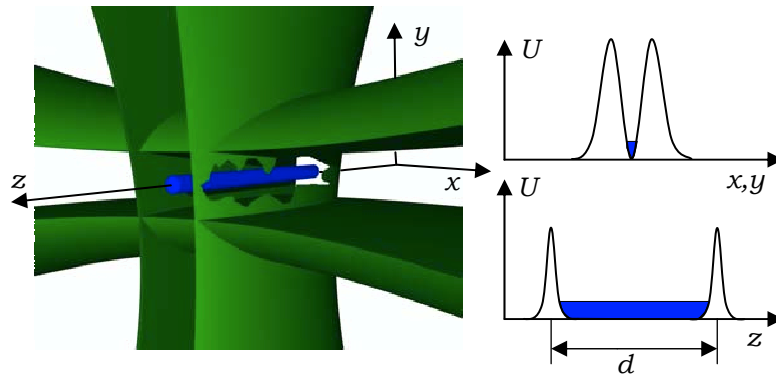


Figure 5.1: The crossed TEM_{01} beams ($x\text{TEM}_{01}$) are shown pictorially on the left. The potential shapes of the trap are given in arbitrary units on the right. The potential, U , in the x and y directions have the shape of their respective TEM_{01} beams. The end-cap beams produce a trap along the z axis, the Gaussian walls are separated by $d = 80 \mu\text{m}$. The end-caps are not shown on the left; gravity is down in the pictorial. The atoms are shown in blue.

5.1 Introduction

The goal here is to produce a one-dimensional condensate in a highly confined trap. Our approach is to use a crossed pair of elongated Hermite-Gaussian TEM_{01} mode beams: horizontal (hTEM_{01}) and vertical (vTEM_{01})

supplemented by Gaussian beam end-caps¹. The geometry is illustrated pictorially in Figure 5.1. With this setup we obtain trap frequencies in two dimensions which are comparable to those typically reported for optical lattices, however there is only a single condensate in one-dimension (1D). The axial motion is confined by optical end-caps, producing the textbook geometry of a “particle in a box.” The resulting atomic number in this box is generally under 3500 and is controlled by evaporation timing and spacing of the end-caps. The results discussed in this chapter are the subject of our publications [43, 44].

Work using Laguerre-Gaussian (LG) optical traps (so-called donut modes) has produced individual 1D condensates [45], but not with radial confinement sufficient for experiments of the Mott-insulator [4] or quantum tweezer [8] sort. This geometry also is limited in trap uniformity because small waist sizes result in a short Rayleigh range which is along the axial trapping direction. Our trap geometry intrinsically overcomes this limitation due to beam orientation.

The far-off resonance lasers discussed in Section 3.4 provide the light for the optical traps. A detailed discussion of optical dipole traps is provided in reference [9] and was reviewed in Sections 2.1 and 2.4.

5.2 Beam Overview

The concepts of beam propagation and the Hermite-Gaussian beam modes are reviewed in Appendix E. Equation E.15 gives the general form of

¹End-cap beams will generally be referred to as ‘Box Wall Beams’, and sometimes as ‘Tweezer Beams’.

the Hermite-Gaussian family of solutions to the propagation equation. Because our setup involves several beams of different orientations, in this chapter we adopt a notation where the coordinates axes q and p are orthogonal to the axis of propagation s and refer to either x , y , or z depending on the beam orientation: $q = y$, $p = z$, and $s = x$ for horizontally and $q = x$, $p = z$, and $s = y$ for vertically propagating beams as in Figure 5.2. The waist sizes in the respective directions will be referred to as W_q and W_p where their dependence on propagation distance s is given by

$$W_{q,p}^2(s) = W_{q,p}^2(0) + \left(\frac{\lambda s}{\pi W_{q,p}(0)} \right)^2, \quad (5.1)$$

from Equation E.8.

The various trap configurations use red and blue beams. The TEM₀₁ traps discussed here as well as the end-cap and compensation beams use laser wavelength $\lambda = 532$ nm and the infrared vertical trap uses $\lambda = 1064$ nm. These are *blue* and *red* relative to the strong transitions of rubidium near 780 nm. Blue traps result in a repulsive potential whereas red traps result in an attractive potential.

The science chamber schematic in Figure 5.2 shows the beam interaction and imaging region of the setup. The setup includes horizontal and vertical input ports for visible light. The horizontal port is used for the hTEM₀₁ and the compensation beam (see Section 5.11), and the vertical port for the vTEM₀₁ and the box wall beam (see Section 5.10). There is also an input port for a vertical infrared beam which is used for radial confinement.

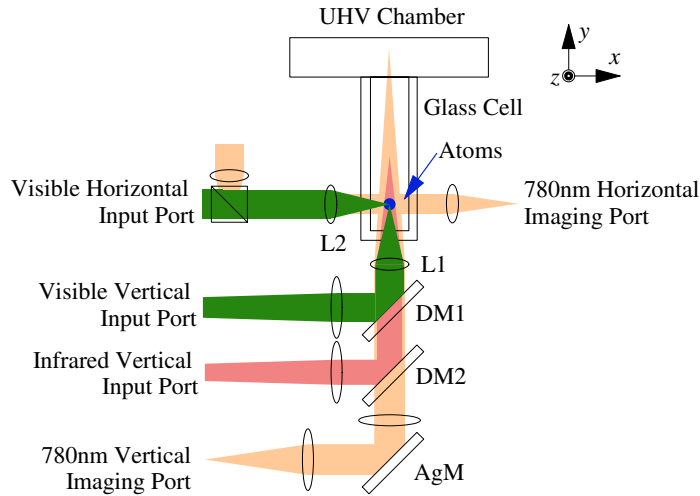


Figure 5.2: Optical trap beam input ports and imaging ports in the science chamber are shown in this schematic. The setup has the capacity to accept vertical and horizontal visible beams as well as a vertical infrared beam. There are 780 nm absorption imaging beams for both vertical and horizontal diagnostics. L1 and L2 are the final lenses in the vertical and horizontal beam paths, DM1 and DM2 are dichroic mirrors, AgM is a silver mirror. Gravity in the figure is in the $-y$ direction.

The lenses L1 and L2 provide the final focusing of the optical trap beams. The trap involves several configurations which allow for loading of atoms into the TEM_{01} nodes which are discussed in Section 5.8. The horizontal and vertical imaging systems are discussed in Section 3.8.1. The beam parameters for various configurations are summarized in Table 5.1 and the beam profiles are shown in Figure 5.3.

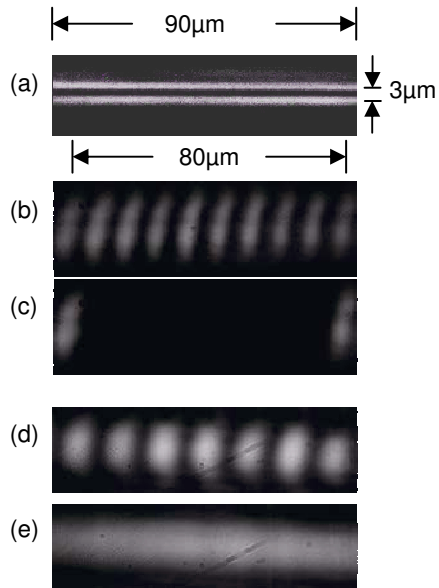


Figure 5.3: Designer blue beams. Above are CCD pictures of various beams as imaged on the atom cloud. (a) $v\text{TEM}_{01}$ beam. (b) End-cap beam in a general setting showing 10 spots. (c) End-cap beam as to end cap the $x\text{TEM}_{01}$ trap. (d) Compensation beam driven with 7 frequencies. (e) Compensation beam with 80 frequencies.

Beam ^a	W_q^b (μm)	W_p^c (μm)	P^d (W)	$\omega_q/2\pi^e$ (kHz)	U_0/k_B^f (μK)
hTEM ₀₁ (Blue)	2.4	125			
gavito-optical			0.165	0.85	15
weak trap			0.165	8.3	15
trap, evap.			0.1	6.5	9.3
full trap			1.0	21	93
vTEM ₀₁ (Blue)	1.8	125			
weak trap			0.74	27	92
full trap			3.7	61	460
End-cap (Blue)	6.1	2.5	0.011		28
Compensation (Blue)	9.8	7.2	0.001		0.54
Vert. Circular ^g (Red)	50	50	0.021	0.056	0.8
Vert. Elliptical ^g (Red)	10	125	0.085	0.8	6.6

^aThe blue beams are at 532 nm, and the red beams are at 1064 nm, which produce repulsive and attractive potentials, respectively. These beams are *blue* and *red* relative to the strong transitions of rubidium near 780 nm.

^bMeasured radial beam waist.

^cMeasured beam waist in axial direction.

^dMeasured beam power.

^eCalculated trap frequency in the radial direction. Measured values for full hTEM₀₁ and vTEM₀₁ are 24 ± 4 kHz and 66 ± 7 kHz.

^fCalculated peak potential height/depth divided by the Boltzmann constant.

^g‘Circular’ and ‘Elliptical’ refer to the shape of the intensity profile of the beam, not the polarization. All beams here are linearly polarized.

Table 5.1: Beams and parameters for the optical trap.

5.3 Other Optical Traps

One can imagine other configurations which may be used to produce a single high frequency trap. Two of these are discussed here. They are the gravito-optical trap or alternatively the compressed Gaussian sheet trap.

5.3.1 Gravito-optical Trap

Unlike the compressed Gaussian sheet trap (see Section 5.3.2), the gravito-optical trap is actually used in our sequence. See the step shown in Figure 5.14(c) except that the optical part is a TEM₀₁ beam rather than a Gaussian.

The configuration consists of a Gaussian (or TEM₀₁) beam in conjunction with gravity. The potential is plotted in Figure 5.4 and in the q direction is of the form

$$U(q) = U_1 \exp\left(-\frac{2q^2}{W_q^2}\right) + mgq, \quad (5.2)$$

or (for the TEM₀₁)

$$U(q) = U_2 x^2 \exp\left(-\frac{2q^2}{W_q^2}\right) + mgq, \quad (5.3)$$

where U_1 and U_2 are given by the coefficient of Equation 2.3 for these intensity distributions. Either equation is actually rather difficult to solve for trap frequency in analytical form. Numerically it was solved for the gravito-hTEM₀₁ trap as given in Table 5.1. The beam parameters $W_q = 2.4 \mu\text{m}$, $W_p = 125 \mu\text{m}$, $P = 0.165 \text{ W}$ give a trap frequency of $\omega_q/2\pi = 850 \text{ Hz}$ with a well depth of $U_0/k_B = 15 \mu\text{K}$. This corresponds to the situation where the

atoms are pressed against the top of the $h\text{TEM}_{01}$ beam, not inside. Although high powers can increase the well depth substantially, the frequency dependence on beam power is rather weak. In practice, with our beam capabilities, the trap frequency is limited to under a few kiloHertz. This was not strong enough for the experiments we had in mind.

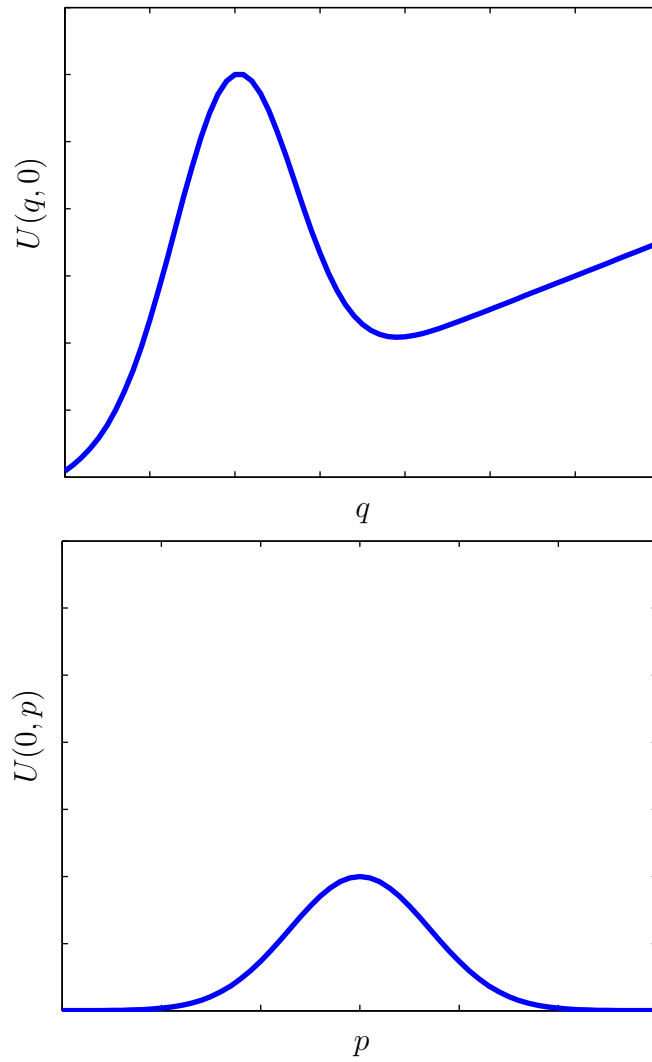


Figure 5.4: Potential of a gravito-optical trap shown in arbitrary units. Gravity is to the left on the top plot and out of the page in the bottom plot. This is the potential in the q direction in the step shown in Figure 5.14(c) except that the optical part is a TEM_{01} beam rather than a Gaussian. In that case the p anti-trapping potential is compensated by the vertical IR beam.

5.3.2 Compressed Gaussian Sheets Optical Trap

The next geometry one might consider is to add an additional gaussian sheet above the the atoms and squeeze them together. This compressed Gaussian sheet trap is described by

$$U(q, p) = U_3 \left[\exp \left(-\frac{2(q - d/2)^2}{W_q^2} \right) + \exp \left(-\frac{2(q + d/2)^2}{W_q^2} \right) \right] \exp \left(-\frac{2p^2}{W_p^2} \right), \quad (5.4)$$

where the Gaussian pair is separated by a distance d , U_3 is given by the coefficient of Equation 2.3 for this intensity distribution. The potentials are plotted in Figure 5.5. The trap frequency in the q direction is maximum when the separation is $d = \sqrt{3}W_q$ and is given by

$$\frac{\omega_q}{2\pi} = \frac{1}{\pi e^{3/4}} \sqrt{\frac{4U_3}{mW_q^2}}. \quad (5.5)$$

The fact that there is an optimum separation of the sheets means that there is a limit to how much they can compress the atoms. If the sheets are brought closer together, the potential in the center just rises and reduces the trapping strength. This geometry, however, can produced rather high trap frequencies, but they are reduced by a factor of $e^{-3/4} \cong 0.47$ versus the TEM₀₁ trap. An additional difficulty is the strong anti-trap produced in the p direction. This is because the line along $q = 0$ is not dark. This problem requires a relatively strong IR trap to compensate. These issues are discussed in more detail in Section 5.13.

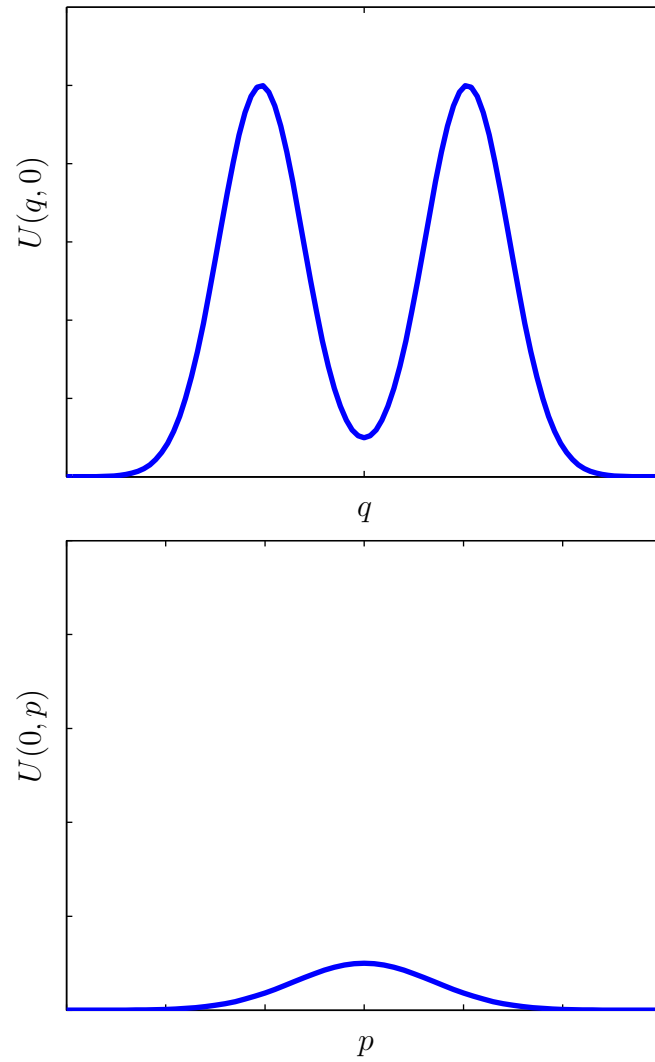


Figure 5.5: Potential of a compressed Gaussian sheet trap shown in arbitrary units.

5.4 Hermite-Gaussian TEM₀₁ Trap

As mentioned, our approach for creating a high frequency trap for a BEC is based on Hermite-Gaussian TEM₀₁ mode beams. This beam profile has the advantage of having a dark line in the center of the profile. For light detuned blue of an atomic transition this provides a strongly confining trap. The intensity of a Hermite-Gaussian TEM₀₁ beam from Equation E.16 is given by:

$$I(q, p) = \frac{P}{\pi W_q W_p} \frac{8q^2}{W_q^2} \exp\left(-\frac{2q^2}{W_q^2} - \frac{2p^2}{W_p^2}\right), \quad (5.6)$$

in terms of the beam power P and waist sizes W_q and W_p . From Equation 2.3, the optical dipole potential for a two-level atom with transition frequency $\omega_0/2\pi$ produced by light of frequency $\omega/2\pi$ with intensity profile $I(q, p)$ is

$$U(q, p) = U_0 \frac{2eq^2}{W_q^2} \exp\left(-\frac{2q^2}{W_q^2} - \frac{2p^2}{W_p^2}\right), \quad (5.7)$$

where the peak trap depth is given by

$$U_0 = -\frac{\hbar\Gamma^2}{8I_s} \left(\frac{1}{\omega_0 - \omega} + \frac{1}{\omega_0 + \omega} \right) \frac{4P}{\pi e W_q W_p}, \quad (5.8)$$

where Γ is the natural line width of the transition, $I_s = \pi\hbar c\Gamma/3\lambda^3$ is the saturation intensity, and $e = \exp(1)$. The potential is shown in Figure 5.6. By expanding Eq. (5.7) about $q = 0$, the trap oscillation frequency in the q direction inside the TEM₀₁ trap can be shown to be

$$\frac{\omega_q}{2\pi} = \sqrt{\frac{eU_0}{\pi^2 m W_q^2}}, \quad (5.9)$$

where m is the mass of the atom. From Equation 5.9, it is clear that the trap frequency increases with larger power and smaller waist size in the q

direction. It also increases with decreasing W_p , but this leads to an increased anti-trapping potential along the axis as discussed in Section 5.13.

An optical trap based on TEM₀₁ beams has several advantages over the previously mentioned traps. Firstly, of course, the trap frequencies in the q direction are much higher. Secondly, because the profile is dark along the line $q = 0$ there is no anti-trap due to the light profile at this location. There is an much weaker anti-trap due to ground state level shifts, see Section 5.13.

For calculations of the trapping characteristics, we use values for the D₂ line of rubidium 87: $I_s \cong 1.67 \text{ mW/cm}^2$, $\Gamma \cong 2\pi \cdot 6.065 \text{ MHz}$, and $\omega_0 \cong 2\pi \cdot 384.23 \text{ THz}$ (see Appendix F). In Equation 5.8, it is important not to use the common rotating wave approximation (which is to assume $|\omega_0 - \omega| \ll \omega_0 + \omega$ and neglect the second term in parenthesis) because the detuning is too far for this to be valid. This is a larger effect than explicitly including the D₁ line which is typically done for nearer detunings.

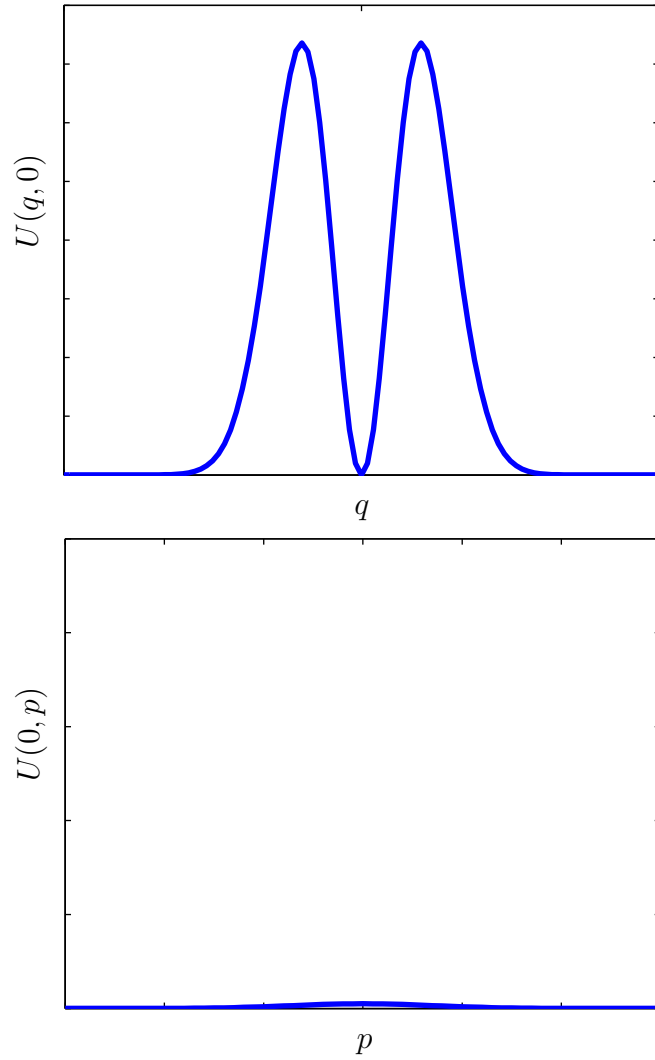


Figure 5.6: Potential of a TEM₀₁ trap. Because the profile is dark along the line defined by $q = 0$, the weak anti-trap shown in the lower plot is not due to the same effect as in the double Gaussian trap as in Figure 5.5. This is due to spatially dependant ground state level and is a much smaller effect, see Section 5.13.

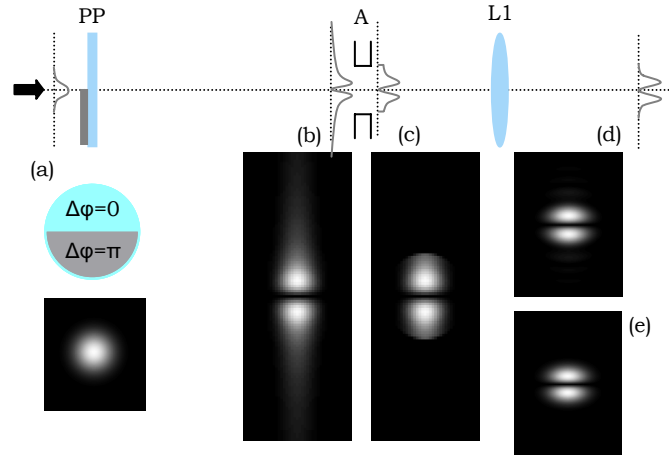


Figure 5.7: Optics pictorial showing production of a TEM₀₁ from an input Gaussian. (a) An input Gaussian passes the phase plate (PP) giving a relative π phase shift between the halves of the beam. (b) The aperture (A) is in the far field of the output beam from PP. This produces the Fourier transform at A. (c) Higher spatial modes are truncated by A. (d) Lens L1 produces the Fourier transform of the output of A resulting in a near TEM₀₁ mode profile. (e) A true TEM₀₁ beam, the profile in (d) only deviates in small fringes outside the main lobes. The images are numerically calculated beam profiles shown as $\sqrt{I(q, p)}$.

5.5 Hermite-Gaussian Beam Production

Although it is possible to have a laser directly output a non-Gaussian beam, we use a simple holographic method to produce the TEM₀₁ mode beams which are used for the optical trap. The concept is illustrated in Figure 5.7. The input Gaussian beam passes a coated phase plate which produces a relative π phase difference between two halves of the beam. This eliminates the Gaussian component of the beam and leaves it as some superposition of the higher modes. Because higher spatial frequencies correspond to larger angles,

they are filtered by the aperture which truncates the large wings of the beam. This output is then imaged to produce a nearly TEM_{01} profile. In Figure 5.7(e) a true TEM_{01} profile is shown along side the output of the optical system (d) which is very similar save a few small fringes.

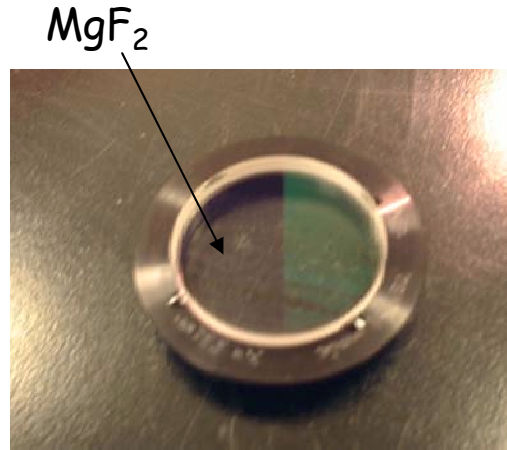


Figure 5.8: Phase Plate for TEM_{01} mode beam. The phase plate consists of a standard BK7 AR coated window which has an additional coating on one side with a sharp line boundary. The coating produces a π phase difference between the window halves and converts an incoming Gaussian beam into a TEM_{01} beam.

The phase plate consists of a standard BK7 double-sided anti-reflection coated window which has an additional coating on one side. The coating is a 6900\AA thick MgF_2 layer that extends along half of the face with a sharp straight line boundary. The windows we have used were masked and coated in a vapor deposition machine. A photo of one such window is shown in Figure 5.8. The plate takes an input Gaussian mode beam which is aligned as to intersect the plate with half of the beam on the MgF_2 coating and half

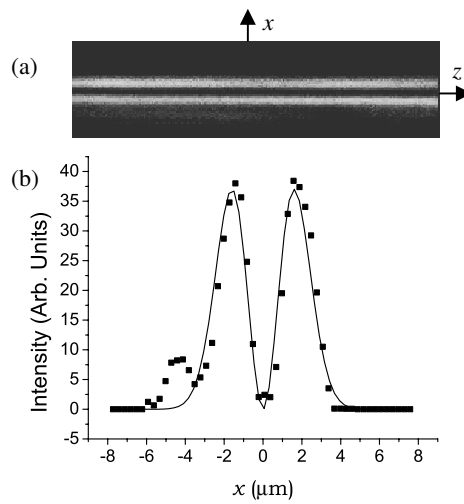


Figure 5.9: Profile of $v\text{TEM}_{01}$ mode beam. (a) A CCD picture of the $v\text{TEM}_{01}$ trapping beam imaged as seen by the atoms. The image extends only $100\ \mu\text{m}$ in the z direction. (b) The profile along the narrow axis, the boxes are points integrated along the z axis for the center $10\ \mu\text{m}$ and the solid line is a fit to an ideal TEM_{01} mode profile in Equation 5.6, giving a waist size of $W_x = 1.8\ \mu\text{m}$.

off. This is the first element of the optical system shown in Figure 5.7. The beam is then elongated with a cylindrical lens in the direction along the dark line to make an elliptical TEM_{01} beam which is focused onto the atoms. A CCD image of the focus is shown in Figure 5.9 along with a profile in the narrow direction. The TEM_{01} beam shown has a waist radius of $125\ \mu\text{m}$ in the axial direction which is much longer than the BEC region to provide a relatively uniform trap. The figure shows a fit to the ideal intensity profile of a TEM_{01} given in Equation 5.6 which results in $W_x = 1.8\ \mu\text{m}$. It is noted that the measured profile fits that of an actual TEM_{01} beam very well which justifies our use of the simple formula given by Equation 5.6 for calculations relating to the properties of the trap itself.

5.6 Optical Trap Beam Layout

The optical setups for producing the various beams for the blue detuned optical traps are shown in Figures 5.10, 5.11, and 5.12.

Figure 5.10 gives the layout beginning with the Verdi laser. Not shown directly after the output is a high energy polarizing beam splitter (PBS) and a half-wave plate on a motorized translation stage which sends the light either to the rubidium or the sodium experiment. The first telescope is to make a small spot for shuttering purposes. There are two mechanical shutters in series, the first is a homebuilt shutter [20] and the second a commercial 1" UniBlitz shutter. The first has a silver mirror rather than a metal blade which reflects the light into the metal beam dump when closed. The UniBlitz shutter

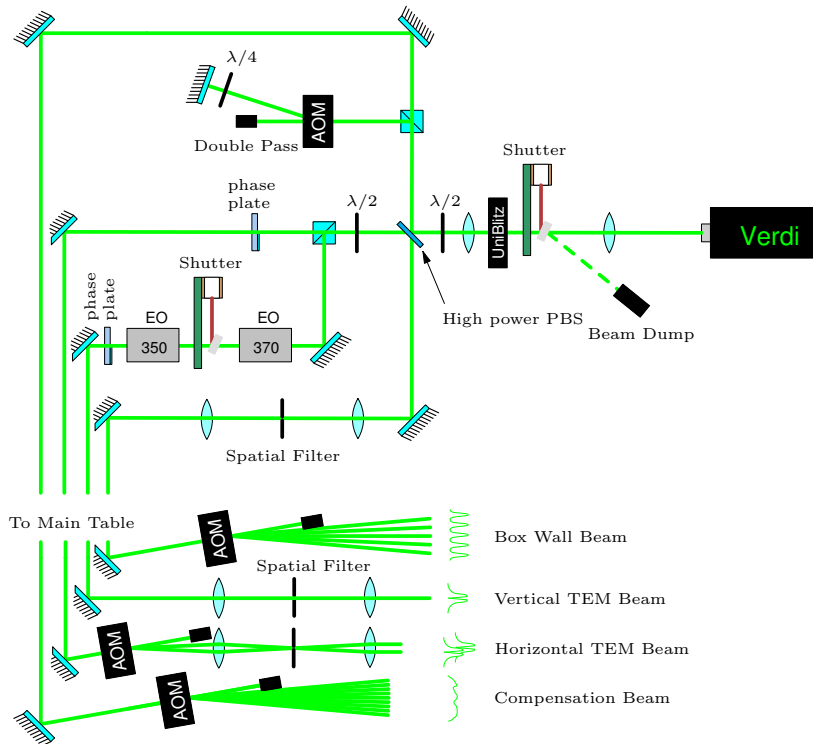


Figure 5.10: Optics layout for production of the optical trap beams. Most the initial optics are located on the Verdi table (Figure 3.2) and come to the main table (Figure 3.1) through tubes.

is much faster but can not take the power for long. Together they can shutter the full beam quickly.

After the shutters, the beam passes a half-wave plate and a high power PBS which selects the power for the box wall and compensation beams. The box wall light is double passed in an AOM which gives the beam around 5 orders of magnitude of dynamic intensity range. It is then sent to the main table and passes a multiple frequency AOM (see Section 5.7) driven with up

to 11 frequencies. This produces the desired box wall spots, see Section 5.10. The remainder of the light that is not double passed is also sent to the main table where another multiple frequency AOM driven with up to 80 frequencies produces a compensation beam profile, see Section 5.11.

The light passing the high power PBS goes into the $h\text{TEM}_{01}$ and $v\text{TEM}_{01}$ beams. The phase plates for each are located on the Verdi table to have the final imaging lenses in their far field. The intensity of the $v\text{TEM}_{01}$ beam is controlled by a pair of electro-optic (EO) modulators from ConOptics Inc. in series. The two EOs in series provide about 50 dB dynamic range without the power loss of a double pass AOM. The EOs are each driven by a Trek high voltage amplifier which is operated by a pair of computer controlled analog outputs. The other arm goes for the $h\text{TEM}_{01}$ beam. The beam passes another multiple frequency AOM driven with two frequencies. These go to make the lower and upper $h\text{TEM}_{01}$ beams which are used in the horizontal loading (see Section 5.8).

The horizontal beams enter the science chamber as shown in Figure 5.11. The final lens of the horizontal system is a 50 mm achromat. It is located inside the housing of one of the quadrupole coils. For the horizontal TEM_{01} beam, we obtained an optimal focus of $2.4\ \mu\text{m}$. Because this lens intersects the input of one of the lower MOT beams, a similar lens is set up in the MOT beam path to compensate. The horizontal absorption imaging beam also follows a similar path to the MOT beam. Before hitting the dichroic mirror, the $h\text{TEM}_{01}$ and the compensation beams are overlapped in a PBS

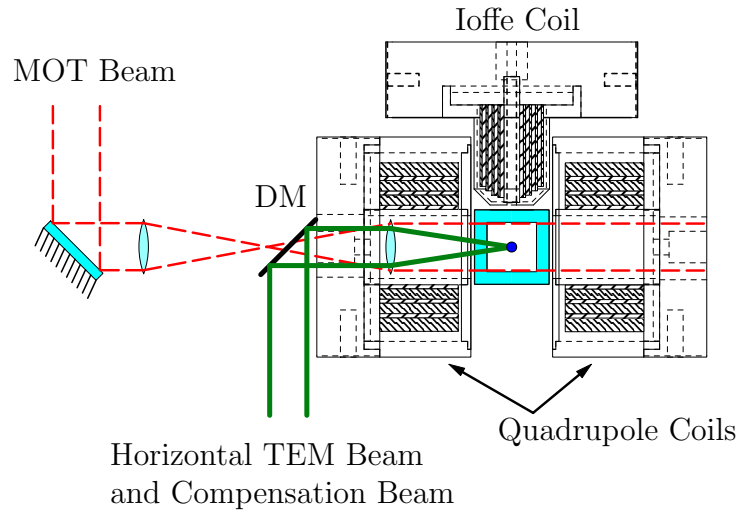


Figure 5.11: Layout of the horizontal optical trap beams. These beams intersect the lower MOT horizontal beams at the dichroic mirror (DM). The final lens of the horizontal optical trap is located inside the quadrupole coil housing. A similar lens compensates the MOT beam.

cube.

The vertical beams enter in the optics tower shown in Figure 5.12. As shown in Figure 5.2, the optics tower has a visible port, an IR port, and a 780 nm port. The first is used for the $v\text{TEM}_{01}$ and the box wall beams, the second for the vertical IR beams, and the final as the vertical absorption imaging output. The 50 mm gradient lens has $f/\# = 2.2$ and is the focusing lens of the vertical trapping beams and the objective of the vertical imaging system. The beams are aligned to be parallel transported inside the tower. The $v\text{TEM}_{01}$ beam obtains a waist size of $1.8 \mu\text{m}$.

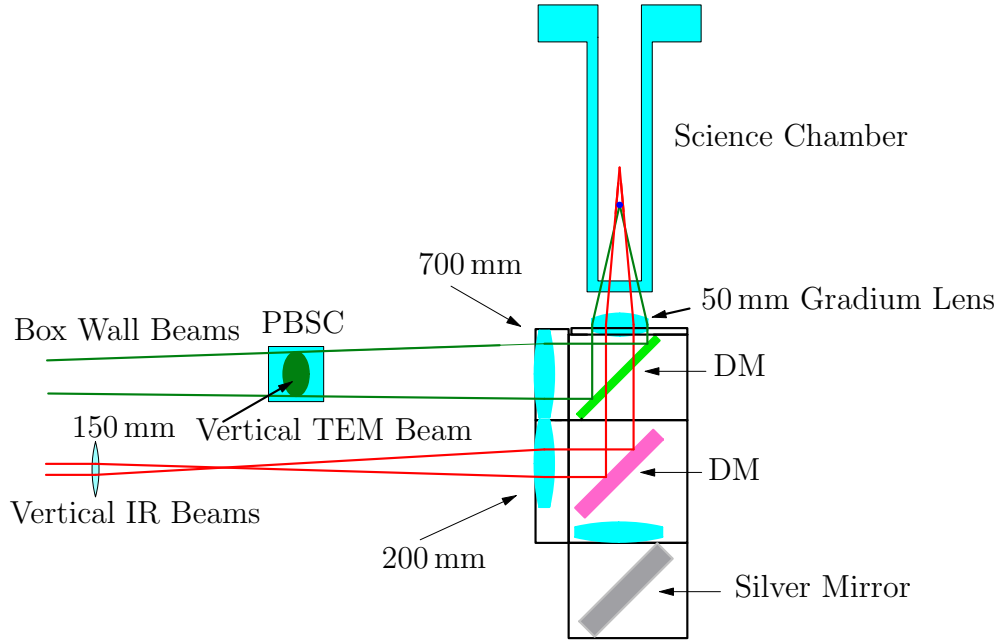


Figure 5.12: Layout of the vertical optical trap beams. The optics tower is located directly below the science chamber and is designed to have multiple entry and exit ports as shown (see also Figure 5.2). DM refers to dichroic mirrors.

5.7 Beam Multiplexing

The function of an acousto-optic modulator is summarized in Appendix Section E.3.1. Several of our optical trap AOMs are driven with N frequencies of the form

$$P_{\text{ac}} = \sum_{i=1}^N P_i \sin^2 2\pi\nu_i t, \quad (5.10)$$

where P_i and ν_i are the power and frequency of the i^{th} component. The signal is generated either by an arbitrary function generator or by several distinct RF sources and combined with an RF power combiner. Equation E.24 give the

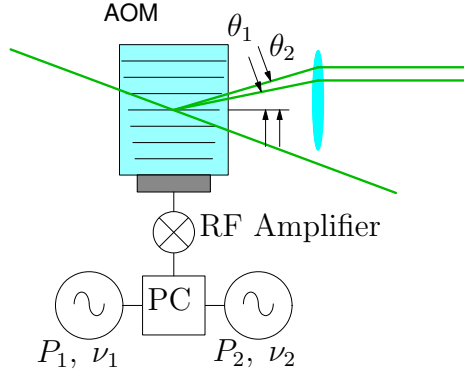


Figure 5.13: Acousto-optic modulator (AOM) setup driven with multiple frequencies. For the $h\text{TEM}_{01}$ beam, we use an AOM with center frequency of 110 MHz and RF bandwidth of 50 MHz. It is driven with different RF sources with independent frequency (ν_i) and power (P_i) control added together with an RF power combiner (PC). This results an individually controlled spot on the imaging plane for each input frequency.

angle for the first order spot for a single drive frequency. A driving function of the form of Equation 5.10 produces N distinct first order diffraction angles

$$\theta_i = \frac{\lambda\nu_i}{2v}. \quad (5.11)$$

When imaged, as in Figure 5.13, this leads to N spots which produce some of our designer optical traps. Because of the bandwidth of an AOM transducer circuit, which is typically $\Delta f = 50$ MHz, there is a decrease in power coupled into the crystal for frequencies away from the center frequency. This results in a tapering of the intensity of the output spots. This, however, is easy to compensate by increasing the power into the outlying frequencies and producing a flat intensity profile across the spots. Independent control of the frequencies and intensities of the driving RF modes provides a powerful technique in

optical trapping experiments. This method is used both for our loading of horizontal TEM_{01} trap and for our tweezer and compensation beams.

5.8 Loading Sequence for the Optical Trap

The optical trap beams are oriented with the science chamber (see Section 3.2.2.2) as in Figure 5.2. The experimental sequence for production of a condensate in the magnetic trap discussed in Section 3.7 has the option to continue with the optical trap. The location of the optical trap is at the center of the science chamber; this is where the atoms are placed in the decompressed Ioffe trap (Section 3.5.3) before the beginning of the optical trapping sequences. Placing the atoms back in the center of the glass cell allows for good optical access for the optical trap beams and for imaging of the atoms. It is not possible to directly capture the atoms into the TEM_{01} beams because the node spacing is only a few micrometers, but the size of the initial cloud is of order $200 \mu\text{m}$.

The preparation of atoms in a 1D box trap consists of several steps shown pictorially in Figure 5.14 and outlined here: (1) transfer the atoms into a combined optical-magnetic trap, (2) produce a pancake shaped BEC by evaporation while ramping off the magnetic trap, (3) transfer the BEC into the hTEM_{01} trap, (4) squeeze the BEC in another direction with the elliptical red vertical trap, (5) load the elongated cloud into the vTEM_{01} trap and add end-caps, (6) remove the red beams and add the compensation beam, (7) ramp up the xTEM_{01} trap to full power.

The initial configuration in step (1) consists of the addition of a horizontal blue sheet of light below the atoms in the 20 Hz magnetic trap along with the vertical circular red trap ('hTEM₀₁ , gavitto-optical' and 'Vert. Circular' in Table 5.1). The blue sheet is actually a TEM₀₁ mode beam which is located below the magnetically trapped atoms. The atoms are initially above the beam rather than in the node because the cloud is too large to be captured directly from the magnetic trap. The center of the magnetic trap is shifted downwards such that the atoms are pressed against the sheet and the elastic collision rate is high enough for evaporation. The magnetic trap is ramped off while the circular red beam intensity is slightly lowered to allow for radial evaporation resulting in a BEC of up to 3×10^5 atoms. Gravity presses the cloud into a pancake shape as shown in Figure 5.14(c). In order to transfer the atoms into the hTEM₀₁ beam, an upper hTEM₀₁ beam is ramped on in addition to and $4 \mu\text{m}$ above the lower sheet hTEM₀₁ in 200 ms. This additional beam is a multiplex of the same beam ('hTEM₀₁ , weak trap' in Table 5.1). It surrounds the pancake shaped BEC in the vertical direction and the lower sheet is then removed. This location in the sequence is shown in Figure 5.14(e). At this point, to continue to the one-dimensional BEC in the box it is necessary to compress the pancake shaped cloud in another direction in order to fit into the vTEM₀₁ beam. Alternatively, the hTEM₀₁ beam may be ramped up to full power to analyze the two-dimensional BEC. The latter is discussed in Section 5.9.

Compressing the pancake shaped cloud in another direction is accom-

plished by ramping up the elliptical and ramping down the circular vertical infrared traps. This transfers the atoms into an elongated geometry and occurs in two 100 ms stages. With the cloud elongated, the $v\text{TEM}_{01}$ beam is ramped up in 100 ms to the weak value given in the table and the end-cap beams are added, spaced $80\ \mu\text{m}$ apart along the z axis. The red trap is ramped off and the compensation beam ramped on. This beam is used to improve the smoothness of the axial potential giving it a box-like shape, see Section 5.11. The atoms are now in the weak $x\text{TEM}_{01}$ box. That is, the atoms sit in a potential such that on axis there are Gaussian walls spaced $80\ \mu\text{m}$ with radial harmonic confinement of order 15 kHz geometric mean trap frequency. In order to reach the desired final number in the range of order 10^4 to 10^2 , the cloud is further evaporated through the $h\text{TEM}_{01}$ trap for up to 50 ms (' $h\text{TEM}_{01}$, trap, evap.' in Table 5.1). Finally, the $v\text{TEM}_{01}$ and $h\text{TEM}_{01}$ beams are ramped to the full value ('full trap' in Table 5.1) producing a mean radial trap frequency of order 40 kHz. The final beam pictorial is shown in Figure 5.14(i) and in Figure 5.1. The BEC in this box is discussed in Section 5.12.

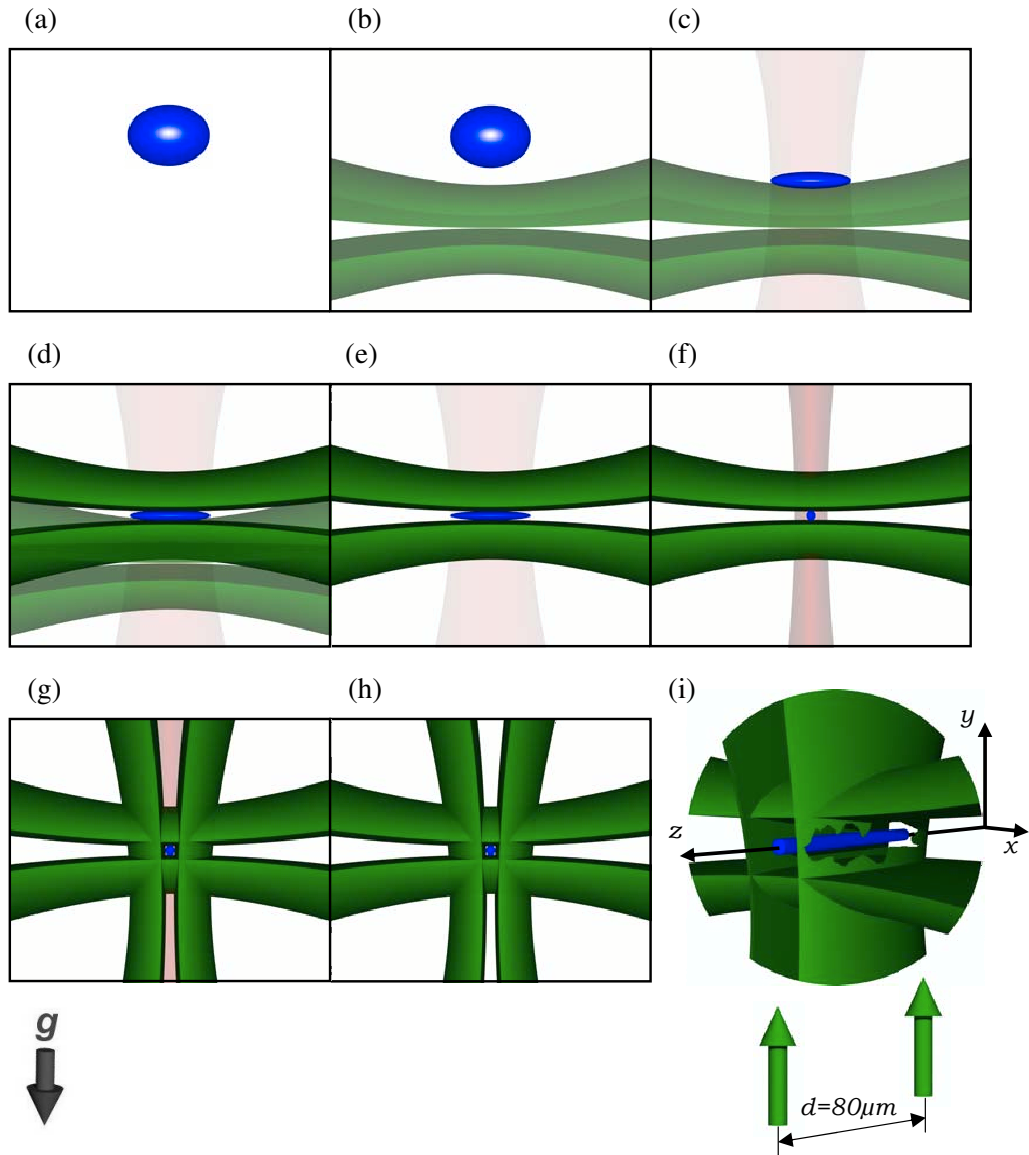


Figure 5.14: Loading sequence of the optical box. (a) Atoms in decompressed Ioffe magnetic trap. (b) Combined optical and magnetic trap. (c) Combined gravito-optical trap, vertical trap frequency $\omega_y \cong 850$ Hz. (d) Transfer into hTEM₀₁ beam. (e) Remove lower hTEM₀₁. (f) Ramp off vertical circular infrared beam while ramping on elliptical infrared beam. (g) Ramp on vTEM₀₁ to capture atoms. (h) Add box wall beams (not shown) and remove vertical infrared trap. Increase to full intensity. (i) Final optical box geometry. Blue represents the atoms, green the TEM₀₁ beams and end-caps, light red the IR beams. Gravity is down in the pictorial.

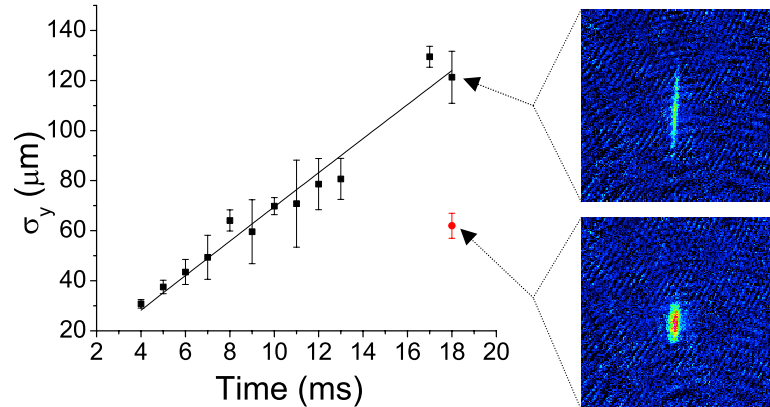


Figure 5.15: BEC Expansion from $h\text{TEM}_{01}$ trap. The black squares give data points for σ_y as a function of time for condensates released at time zero. The data is consistent with the 21 kHz expected trap frequency for this TEM_{01} trap. The images to the right are absorption images of one of the shots of the indicated data point. The upper picture is of a condensate released from the inside the TEM_{01} trap, and the lower was released from above the sheet (the gravito-optical trap) as in Figure 5.14(c). This is the red circle data point on the plot. The lower picture is a 3-D condensate and does not obey Equation 5.12.

5.9 Two-Dimensional BEC in $h\text{TEM}_{01}$ Trap

As discussed in Section 5.8, after loading the atoms into the $h\text{TEM}_{01}$ as shown in Figure 5.14(e) and ramping the beam to full intensity, there is a two-dimensional BEC. This step is enroute to the one-dimensional BEC in a box, but is interesting in its own right. This section gives a brief discussion of this condensate.

In order to observe the trapping strength, the atoms are released suddenly and allowed to fall. During this time, the cloud shows a change of

aspect ratio which indicates that the cloud had crossed the BEC transition in the trap [46]. The atom clouds are observed destructively with absorption imaging. The BEC is two-dimensional; this means that the wavefunction in the strongly confined direction is Gaussian — that of the harmonic oscillator ground state (see Section 4.4). The cloud image may be fit and vertical size characterized by σ_y . The rate of vertical expansion in this case depends on the trap frequency in that direction as in

$$\sigma_y(t) = \sqrt{\frac{2\hbar}{m\omega_y}}(1 + t^2\omega_y^2)^{1/2}. \quad (5.12)$$

Condensates in a high frequency trap exhibit a much larger rate of expansion in this direction. Figure 5.15 shows expansion of atoms from a hTEM₀₁ trap. The beam used in this case had parameters: $W_y = 2.4 \mu\text{m}$, $W_z = 125 \mu\text{m}$, and $P = 1.0 \text{ W}$ with wavelength $\lambda = 532 \text{ nm}$, from which Equations 5.8 and 5.9 give a trap depth of $U_0/k_B = 93 \mu\text{K}$ and a trap frequency of $\omega_y/2\pi = 21 \text{ kHz}$ as in Table 5.1. The spontaneous scattering rate may be estimated from Equation 2.4 at the harmonic oscillator length $a_q = 75 \text{ nm}$, which results in $R(a_q, 0) \cong 6 \times 10^{-3} \text{ s}^{-1}$ per atom, meaning that there are few events over the time of the experiment compared to the BEC population. The line fit in Figure 5.15 indicates a trap frequency of $24 \pm 4 \text{ kHz}$, consistent with calculations.

Figure 5.15 shows absorption images of one of the shots of the indicated data point. The upper picture is of a condensate released from the inside the TEM₀₁ trap, and the lower was released from above the sheet (the gravito-optical trap) as in Figure 5.14(c). This is the red circle data point on the plot.

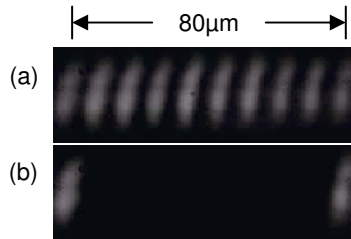


Figure 5.16: Above are CCD pictures of the box wall beam as imaged on the atom cloud. (a) Box wall beam in a general setting showing 10 spots. (b) The same beam used as optical end-caps for the $x\text{TEM}_{01}$ trap.

The lower picture is a squished 3-D condensate and does not obey Equation 5.12.

5.10 Box Wall Beams

The box wall beam is a flexible designer blue beam which may be used as the end-caps of the optical box or for various other applications forming controllable optical quantum dots or lattices, see Chapter 6. As mentioned in Section 5.6, the beam is supplied by a multiple frequency AOM.

Figure 5.16(a) shows a CCD image of the box wall beam in a general setting. Here the AOM is driven with $N = 10$ independent frequencies chosen to give an equally spaced nine site lattice. This image demonstrates the capacity of this beam where a pair of spots may be used to form an optical quantum dot inside the cloud. In the case of the optical box, only a pair of spots ($N = 2$) are used, spaced by $80 \mu\text{m}$ as the end caps shown in Figure 5.16(b). Because the RF frequencies for this beam are generated by separate

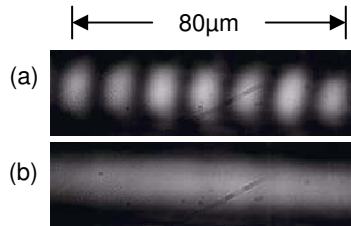


Figure 5.17: Above are CCD pictures of the compensation beam as imaged on the atom cloud. (a) Compensation beam driven with 7 frequencies. (b) Compensation beam with 80 frequencies.

RF sources each with an individual RF intensity control, the number of spots, their intensities and positions may be controlled independently on the $10 \mu\text{s}$ time scale. This method allows for precise control of the positions and intensities of the spots relative to each other and provides a powerful tool for condensate manipulation.

5.11 Compensation Beam

Although the $x\text{TEM}_{01}$ trap is of good quality, it does suffer from the problem of irregular axial potential variations of order $1 \mu\text{K} \cdot k_B$. This is most likely due to scattering from the holographic plate used to produce the TEM_{01} beams and other imperfect optics. This irregularity is observed to break the cloud into small sections, a phenomenon that was also observed in atom chip experiments [47]. In either case, this is due to potential variations on the order of the BEC chemical potential. Another designer blue beam, the compensation beam, is used to fill in valleys in the axial potential. This

beam is also generated by a multiple frequency AOM, but rather than driving it with separate RF sources, a single arbitrary function generator is used to produce a stable frequency comb which results in an array of spots. Figure 5.17(a) shows the compensation beam driven with $N = 7$ different frequencies. Because the number of spots and their intensities are arbitrary, it is possible in principle to create a beam with any intensity profile. Figure 5.17(b) shows the compensation beam with $N = 80$ driving frequencies. The size of the structures which may be added to the profile is limited by the spot size of the beam (as in Table 5.1). The closeness of spacing between the frequencies is limited by the possibility of parametric heating of the atoms in the optical trap. This is due to beating of the neighboring spots at their difference frequencies. Here, we operate at a minimum difference frequency of 500 kHz, which is of order $10\times$ the trap frequencies.

5.12 Bose-Einstein Condensate in a Box

Loading of the atoms into a one-dimensional optical box is described in Section 5.8. An absorption image of a BEC produced in this way is shown in Figure 5.18. The BEC profile reflects the box-like shape in the axial direction. As discussed in Section 4.5, the atom number in one-dimensional condensate in this geometry is limited to $N_{1D} = L_z/4a_s \cong 3500$. The cloud in Figure 5.18, with 3×10^3 atoms, is therefore a one-dimensional BEC.

It is of particular interest to enter a regime where experiments such as performing the quantum tweezer for atoms (see Chapter 6), direct study of

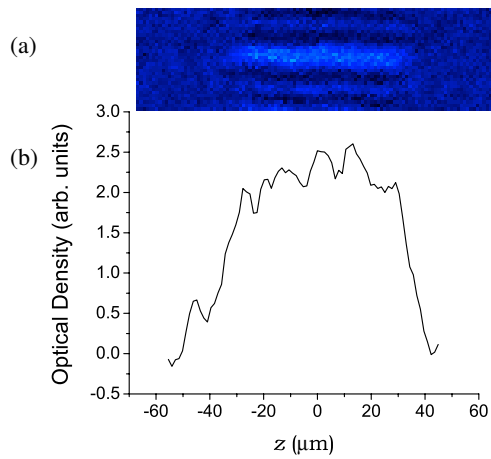


Figure 5.18: (a) An absorption image of a BEC of 3×10^3 atoms in a box with gaussian walls spaced by $80 \mu\text{m}$ along the z axis. (b) The profile of the BEC along the z axis integrated vertically. The image is *in situ*, where the absorption beam is turned on in addition to the optical trap. Resolution is limited by expansion during the $30 \mu\text{s}$ exposure and the upper and lower stripes are imaging artifacts.

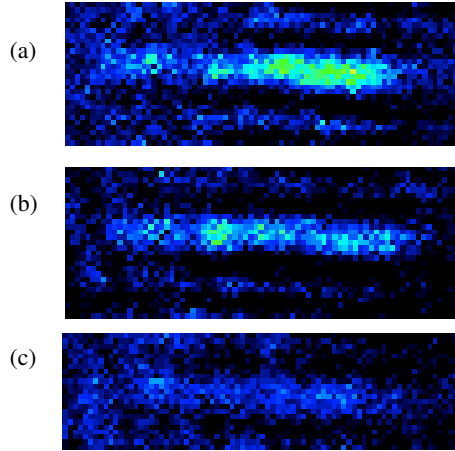


Figure 5.19: Absorption images of BECs in $80\ \mu\text{m}$ boxes. (a) $N \approx 2 \times 10^3$ without compensation beam. The cloud shows a region of higher density to the right. (b) The same as (a) but with the addition of an appropriate compensation beam. (c) $N \approx 5 \times 10^2$ with compensation beam averaged over 10 separate exposures. The color scale is different from that in Fig 5.18.

the Mott-insulator state [4], or Tonks-Girardeau regime [5–7] are possible. To do this, in addition to the very high trap frequencies required, it is necessary to have a very uniform trap and low atom numbers. Although not easily observed in Figure 5.18 because of the high atom number, there are spatial fluctuations in the axial potential. For correction of this, the compensation beam is used. This beam is discussed in Section 5.11. Figure 5.19 shows the effects of compensation. An uncompensated condensate shows a larger density on the right in image (a). This variation can be reduced with the compensation beam, as shown in Figure 5.19(b). The result is a cloud of greater uniformity but still with some irregularities on a finer scale. This

level of compensation allows our optical trap to produce condensates of much smaller number as shown in Figure 5.19(c), where with a better optimized compensation profile, additional evaporation has reduced the atom number to 5×10^2 . The cloud is relatively uniform which is not possible without compensation. The small atom numbers are cross-checked with the single atom counting system [48] which allows for independent verification of atom number. Our atom counting setup has been integrated as to allow for atoms to be transferred from the optical trap into a small magneto-optical trap (MOT) so they may be accurately counted by fluorescence. This setup is discussed in Section 3.8.3 and 6.4.

A BEC of the sort in Figure 5.19(c) is a possible initial condition for further extraction experiments such as the quantum tweezer for atoms as proposed in Reference [8] where the optical quantum dot may be produced with the additional beams in Figure 5.3(b), see Chapter 6. This BEC is an ideal reservoir for single atom extraction because the mean field splitting in the dot is of similar order to the chemical potential of the condensate. Uniformity of the potential is currently limited by the spot size of the compensation beam and the quality of the absorption images used for the optimization. With improvements here, it should be possible to obtain a cloud in the appropriate conditions to directly study small scale Mott-insulator physics at the single well level and the Tonks-Girardeau (TG) regime.

The cloud may be characterized by the interaction parameter $\gamma = mg_{1D}L/\hbar^2N$, where m is the atomic mass [5, 49]. The case of $\gamma \ll 1$ rep-

resents the mean-field (MF) regime whereas $\gamma \gg 1$ is a TG gas. As calculated for our results, we have $\gamma \approx 0.08$ for Figure 5.18 which is clearly MF, however for Figure 5.19(c) $\gamma \approx 0.5$ and for the smallest observed condensate in our system thus far ($N \approx 2.5 \times 10^2$), $\gamma \approx 1$ anticipating a borderline MF-TG regime. With a further flattened axial potential, it should be possible to reduce the number density and push the cloud into the TG area where it may be possible to directly study this state. This trapping geometry has the potential for further interrogation of these systems.

5.13 Comments on the Optical Trap

A TEM₀₁ trap alone produces a two-dimensional condensate. The wavefunction of the condensate may be written assuming a Gaussian profile in the strongly confined direction and a Thomas-Fermi shape in the radial directions [49]. In the strongly confined direction, the atoms occupy the single particle ground state energy level with value $\hbar\omega_q/2$, where $2\pi\hbar$ is Planck's constant. The trap frequency, calculated from Equation 5.9, is that for the center of the trap. Spatially, the trap frequency has a radial dependence $\omega_q = \omega_q(p, s)$ which implies a spatial ground state energy shift. This dependence is due to the Gaussian beam profile along the p axis and the $W_{q,p}^2$ dependence on propagation distance s , see Equation 5.1. The result is a weak potential of the form $m\omega_p^2 p^2/2$ and $m\omega_s^2 s^2/2$ in these directions. The radial trap frequencies may be written as

$$\frac{\omega_p}{2\pi} = \frac{i}{\sqrt{2\pi}} \frac{1}{W_p W_q^{1/2}} \left(\frac{e\hbar^2 U_0}{m^3} \right)^{1/4}, \quad (5.13)$$

and

$$\frac{\omega_s}{2\pi} = \sqrt{\frac{3}{2}} \frac{i}{2\pi^2} \frac{\lambda}{W_q^{5/2}} \left(\frac{e\hbar^2 U_0}{m^3} \right)^{1/4}, \quad (5.14)$$

where the approximation $(W_q/W_p)^4 \ll 1$ was used in deriving Equation 5.14, the peak trap depth U_0 is given in Equation 5.8. These imaginary oscillation frequencies each represent an anti-trapping potential. For the $\omega_q/2\pi = 21$ kHz hTEM₀₁ trap discussed above, these anti-trapping frequencies are $\omega_p/2\pi = 12i$ Hz and $\omega_s/2\pi = 40i$ Hz. The vertical infrared beam which provides a weak radial confinement of 60 Hz over compensates this effect and radially traps the atoms. In the case mentioned using a xTEM₀₁ configuration for a one-dimensional trap, $\omega_s/2\pi$ plays no role because of the geometry. In this case, only the tiny $\omega_p/2\pi$ is an issue.

Here in lies a major advantage of the TEM₀₁ trap over other blue traps, for example, a blue Gaussian sheet pair each with power $P/2$. When the sheets are separated in q by $\sqrt{3}W_q$, they have an optimum trap frequency given by

$$\frac{\omega'_q}{2\pi} = \frac{1}{e^{3/4}} \sqrt{\frac{eU_0}{\pi^2 m W_q^2}}, \quad (5.15)$$

similar to Equation 5.9 but reduced by a factor of $e^{-3/4} \approx 0.47$. Note that U_0 given by Equation 5.8 is the peak trap depth for the TEM₀₁ trap and should be considered to be a parameter here; it is not the depth of the double Gaussian trap. In addition to having a lower trapping frequency in the strong direction, these traps have much larger anti-trapping frequencies. In contrast to the TEM₀₁ trap which has a zero intensity profile along the p axis at $q = 0$, this trap has a Gaussian axial intensity profile which produces an anti-trap

in addition to the weak ground state shift anti-trap described above. These effects result in trap frequencies

$$\frac{\omega'_{p(1)}}{2\pi} = \frac{i}{\sqrt{2}e^{3/4}} \sqrt{\frac{eU_0}{\pi^2 m W_p^2}} \quad \text{and} \quad \frac{\omega'_{p(2)}}{2\pi} = \frac{i}{\sqrt{2}\pi e^{3/8}} \frac{1}{W_p W_q^{1/2}} \left(\frac{e\hbar^2 U_0}{m^3} \right)^{1/4}, \quad (5.16)$$

where $\omega'_{p(1)}/2\pi$ is due to the axial intensity profile and $\omega'_{p(2)}/2\pi$ the ground state shift. These add in quadrature to give the overall $\omega'_p/2\pi$. The first does not exist for the TEM₀₁ trap and is the larger effect. The second corresponds with Equation 5.13. Using the same parameters as the hTEM₀₁ trap above, this double Gaussian trap has trap frequencies $\omega'_q/2\pi = 9.8$ kHz and $\omega'_p/2\pi = 135i$ Hz. That is, this trap has less than half the trap frequency in the q direction and more than an order of magnitude larger anti-trapping frequency in the p direction.

It is worth noting that a blue trap with a dark trapping region as presented here has several advantages over a red trap [50]. A red trap produces an attractive potential where the atoms are high field seeking. This results in a larger spontaneous scattering rate. Because red traps use longer wavelength light, they are also more limited in focus size — this is critical for obtaining very high trap frequencies. An additional limitation is the depth of the traps produced. If one imagines using a single red sheet used to produce a condensate as described in our hTEM₀₁ trap, it is clear that the red trap will have an attractive potential in the radial directions. Because the trap is so deep evaporative cooling is difficult.

Recent work with a TEM_{01} beam combined with a magnetic trap has produced quasi-2D condensates [51]. In their experiment, the authors operate in a regime where the focus in both q and p directions is much larger than in the case presented here. Because of the longer depth of focus and larger W_p used in their experiment, the optical trap has a more uniform potential. This is a preferred regime in which to operate for the study of vortex dynamics in two-dimensions, for example, as the authors point out. The central trap frequencies, however, obtained are considerably smaller: by a factor of 10 for the hTEM_{01} trap and a factor of 30 for vTEM_{01} trap than in the case presented here. For the possibility of entering regimes of quantum gases as mentioned earlier [4–8], such trapping strengths are required.

Chapter 6

A Quantum Tweezer for Atoms

In this chapter, we describe the concept of a quantum tweezer for atoms and the possibility of implementing this method using our BEC in a box discussed in Chapter 5. First, a review of the tweezer concept is given, followed by a discussion of the experimental possibilities in our system and methods of single atom detection from the optical trap.

6.1 The Quantum Tweezer Concept

Controlling the state of a quantum system can allow for direct exploration of fundamental quantum mechanics in addition to having applications to exotic systems such as entangled states, Schrödinger cat states [52], and quantum computers [53]. Primarily active theoretical topics in recent years, experimental realizations of such systems represent a ‘pie-in-the-sky’ of modern experimental physics.

A single neutral atom in the ground state of a microtrap provides a potential starting point for explorations of the sort just mentioned. A method for retrieving such an atom on demand has been put forth [8]. The method involves a BEC used as a reservoir of atoms from which a quantum dot extracts

a single ground state atom. The system relies on the interaction of the atoms inside the quantum dot. This creates tunneling opportunities between the atoms in the dot and the reservoir. By appropriately controlling the properties of the quantum dot in the reservoir, theory has shown that it is possible to obtain a situation where all, save a single atom, will tunnel out of the dot. The method has a robustness in the sense that calculations have shown a wide range of parameters over which this is possible as well as some immunity to anticipated atom number fluctuations in the reservoir.

The aforementioned method for obtaining a single neutral atom is not the only one available. Other ideas have been developed and pursued by various research groups. Several groups are pursuing single atoms through weak magneto-optical traps (MOTs) [54–56]. These MOTs are operated such that the average number of atoms in the trap is on the order of one — not dissimilar from our SAD MOT. When a single atom is detected in the trap, it is then loaded into an optical dipole trap [57, 58]. Differing from the quantum tweezer concept, these schemes are not a deterministic source of atoms. In addition, the atom is not in a well-defined vibrational state of the dipole trap and requires additional cooling to place it into the ground state once it is captured.

Another possible method relies on the Mott-insulator transition in a BEC [4]. The Mott-insulator transition can occur when a condensate is placed in an optical lattice. As the well depth of the lattice increases, a phase transition from a superfluid state to a number state in the lattice sites occurs [59].

This method may produce number states within each lattice site, but has a drawback in addressability. Typically, optical lattices have a site spacing of half a wavelength. Of order several hundred nanometers for visible light, this close spacing makes individual site addressability difficult at best.

6.2 Quantum Tweezer Theory

This section provides a review of the basic ideas of the theory of the extraction system. This theory is described in great detail elsewhere [60, 61].

The system is modeled by the one-dimensional Gross-Pitaevskii (GP) equation given in Equation 4.32 and repeated here

$$\left(-\frac{\hbar^2}{2m}\frac{\partial^2}{\partial z^2} + V(z) + g_{1D}|\varphi(z)|^2\right)\varphi(z) = \mu_{1D}\varphi(z). \quad (4.32)$$

In the GP equation, $V(z)$ represents the external potential in the axial direction. The wavefunction is assumed Gaussian in the other (very strongly confined) directions. The theory was worked out for the case where $V(z)$ is either harmonic or box-like as in the optical potential described in Chapter 5.

The extraction concept is illustrated pictorially in Figure 6.1 for both a harmonic and a box potential. Within the condensate, a quantum dot is slowly turned on at the center of the trap. The tweezer is initially only a small perturbation on the trap potential. The quantum dot is formed by two repulsive Gaussian barriers producing a trapping region. The quantum dot potential takes the form

$$V_{\text{dot}}(z) = V_0 \left[\exp\left(-\frac{2(z-d)^2}{W_z^2}\right) + \exp\left(-\frac{2(z+d)^2}{W_z^2}\right) \right], \quad (6.1)$$

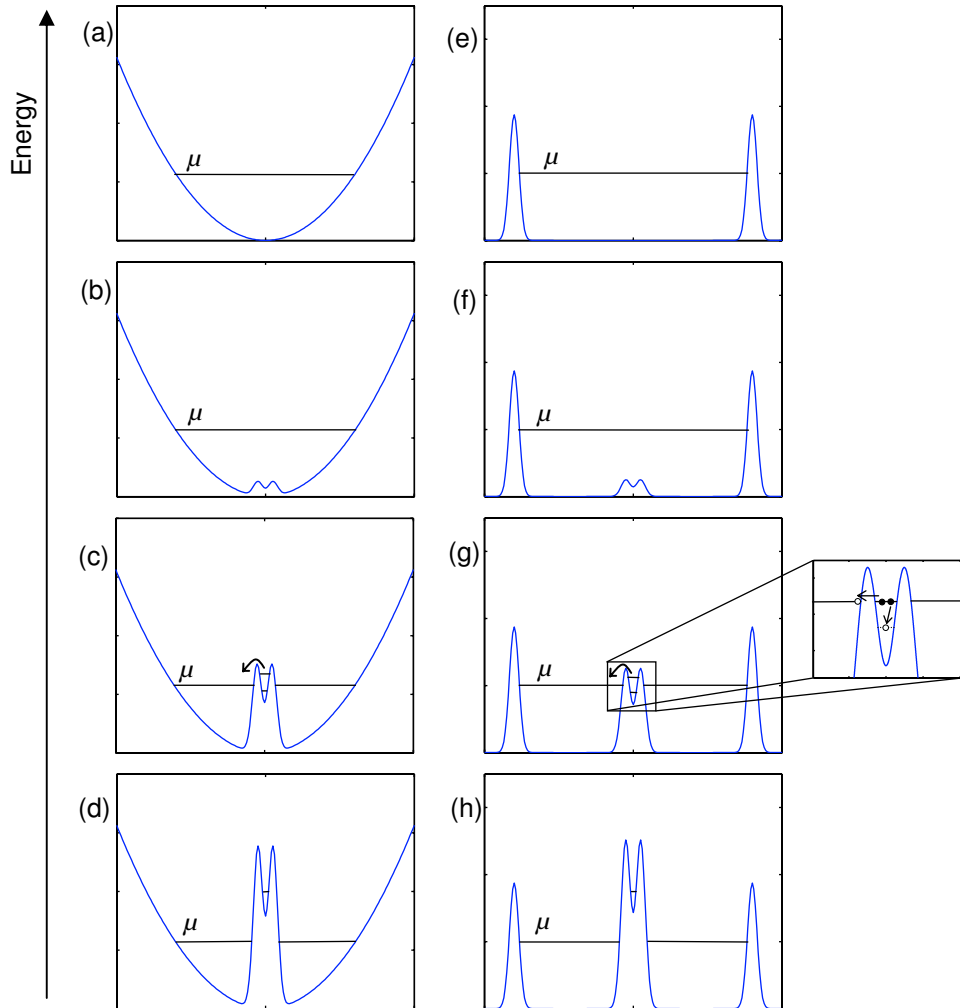


Figure 6.1: The plots show a pictorial view of the operation of the tweezer in a harmonic trap and a box trap. Plots (c) and (g) show the position as the final additional atom leaves the quantum dot. The inset of (g) indicates this. When one of the pair of atoms tunnels into the BEC at the degeneracy location, the single atom remaining in the dot then has a lower energy removing the degeneracy condition.

characterized by a waist W_z and a separation distance $2d$. The trapping frequency of this geometry is given by

$$\omega_z = \sqrt{\frac{8V_0}{mW_z^2} \left(4\frac{d^2}{W_z^2} - 1\right) \exp\left(-\frac{2d^2}{w_x^2}\right)}. \quad (6.2)$$

Note that the external potential is now the sum of the primary trapping potential and the quantum dot potential. The dot is turned on by increasing V_0 and pushing the tweezer up in energy through the condensate. The various multi-atom ground state energy levels become degenerate with the chemical potential of the condensate as the tweezer is ramped up.

Figure 6.1 shows the ramp up of the quantum dot inside the BEC with chemical potential μ . When the energy level of the atoms within the dot and the chemical potential are equal, an atom in the dot can tunnel into the condensate if the levels remain near degenerate for the appropriate amount of time. At this point the number of atoms within the dot decreases and the energy of the atoms within the dot lowers because of reduced interaction energy. This removes the degeneracy condition. As the tweezer potential continues to increase, the energy of the atoms is again degenerate with the chemical potential and an atom can again tunnel out of the dot. This loss of atoms amounts to an adiabatic following of the energy levels depicted in Figure 6.2. When adiabatically following the levels, the multi-atom level inside the dot remains near resonance for sufficient time for the tunneling process to occur. The key to single atom extraction is to tailor the turn on rate such that the process is adiabatic for all but the last level crossing which is the smallest.

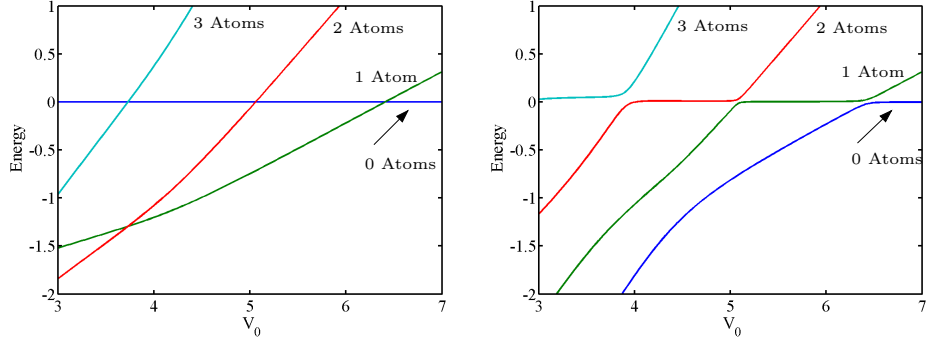


Figure 6.2: Energy diagrams for the multi-atom ground states within the tweezer as a function of the potential height of the tweezer. The diagram on the left corresponds to the case where the coupling between the tweezer and the condensate is neglected. On the right, the coupling is included, causing energy gaps where there were previously crossings. The energies are plotted in units of 5.65 nK. Plots courtesy of Artëm Dudarev [61].

In the case of the final crossing, the energy gap is jumped and the final atom remains. Physically this means that at the end, the quantum dot potential is rising too fast for the last tunneling process to occur. This means that only the single atom ground state has a high probability of being in the dot after extraction.

The energy of the different states depends on the energy level of the trap, the number of atoms in the state, and the coupling of the state to the condensate. It can be shown [8, 60, 61] that for N atoms in the ground state of the quantum dot, the energy is given by

$$E_N = NE_1 + \frac{N(N-1)}{2}\nu, \quad (6.3)$$

where E_1 is the energy of an atom in the trap relative to the chemical potential

and $\nu = g_{1D}J_{0,4}$ represents the repulsion atoms feel within the quantum dot where $J_{l,m}$ is the generalized overlap integral of an atom in the quantum dot with an atom in the condensate given by

$$J_{l,m} = \int (\phi_{\text{BEC}})^l (\phi_{\text{Dot}})^m dz. \quad (6.4)$$

The energy difference between the quantum dot and the chemical potential, E_1 , may be written as

$$E_1 = \epsilon_{\text{Dot}} + V_{\text{offset}} + \frac{g_{1D}}{2} N J_{2,2} - \mu, \quad (6.5)$$

where ϵ_{Dot} is the ground state energy level of the quantum dot, V_{offset} is the potential offset created by the dot, and μ is the chemical potential of the condensate.

The energy levels plotted in Figure 6.2 were calculated using realistic parameters for an tweezer experiment preformed in our optical box trap described in Chapter 5. In the case of the quantum dot itself, the characteristic trap frequency used was 200 Hz for the simulation and a one-dimensional chemical potential of $20 \text{ nK} \cdot k_B$.

To quantify the tunneling rates, analysis of the system including the coupling between the atoms in the quantum dot and the condensate is necessary. The off diagonal terms in the Hamiltonian give rise to this coupling. Figure 6.2 shows the effect of this coupling on the energy levels. An energy gap (avoided crossings) appears at the level intersections. These avoided crossings dictate the parameters under which an atom can tunnel from the tweezer into the condensate.

The possibility of jumping from one energy level to another occurs via Landau-Zener tunneling [62]. The probability of making the transition is given by

$$P = \exp\left(-\frac{(2\pi)^2}{h} \epsilon_{12}^2 / \left| \frac{d}{dt}(\epsilon_1 - \epsilon_2) \right| \right), \quad (6.6)$$

where ϵ_{12} is the energy gap between the two levels and $\frac{d}{dt}(\epsilon_1 - \epsilon_2)$ is the difference in the slope of the energy levels. In the case of the tweezer, this can be approximated by the slope of the lower energy level away from the gap. From this the probability for an atom to tunnel from the tweezer into the condensate can be calculated. In the initial cases depicted in Figure 6.1(b) and (f), the quantum dot is deep inside the condensate with a very weak barrier against the condensate. Therefore, the large coupling give rise to large energy gaps. As the quantum dot potential is increased, the barrier between the dot and condensate grows, reducing the probability of tunneling. This corresponds to the case of smaller energy gaps.

Figure 6.3 shows the probability of extracting various atom numbers depending on the rate of increase of the quantum dot potential ($\alpha = dV_0/dt$ in units of 4.2 nK/ms). The upper family of curves show the probability for extracting a single atom, the lower families for 2 or 3 atoms. Each family of curves is for various atom numbers given on the inset. This is to anticipate immunity to expected number fluctuations in the prepared BEC. Both cases of the harmonic and box potential show more than an order of magnitude of extraction rate where there is greater than 90% extraction probability. The plot also illustrates the grouping of the family, indicating a large degree of

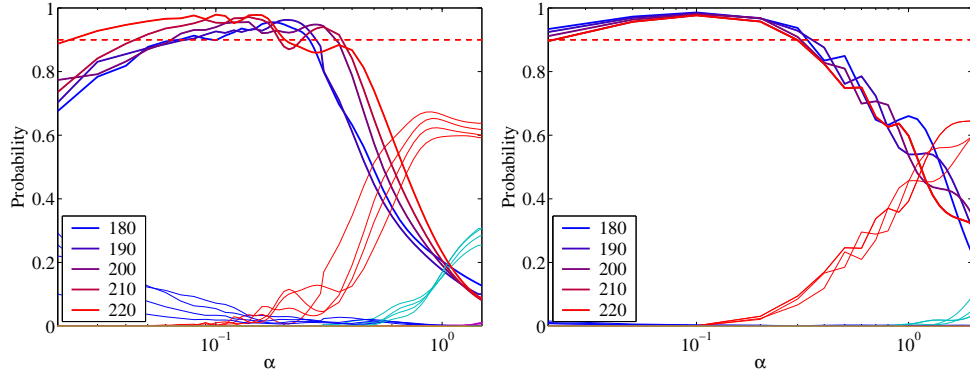


Figure 6.3: Theoretical extraction probability from a harmonic trap is shown on the left and from a box trap on the right. The upper family of curves show the probability for extracting a single atom, the lower families for 2 or 3 atoms. Each family of curves is for various atom numbers given on the inset. The horizontal axis is given in units of 4.2 nK/ms. Plots courtesy of Artëm Dudarev [61].

immunity to number fluctuations especially in the case of the box trap.

6.3 Experimental Possibilities

Performing the extraction described theoretically in the previous section is quite possible with the optical trap system described in Chapter 5. Using the single one-dimensional condensate and the box wall beams from Figure 5.16 to form the quantum dot, the setup fulfills the theoretically required conditions for operation. The box wall beams shown as a tweezer lattice is in Figure 6.4. For the tweezer extraction experiment, only two such spots are needed inside the BEC, but this image illustrates the possibility of doing a lattice-type experiment such as a direct study of a Mott-insulator state [4].

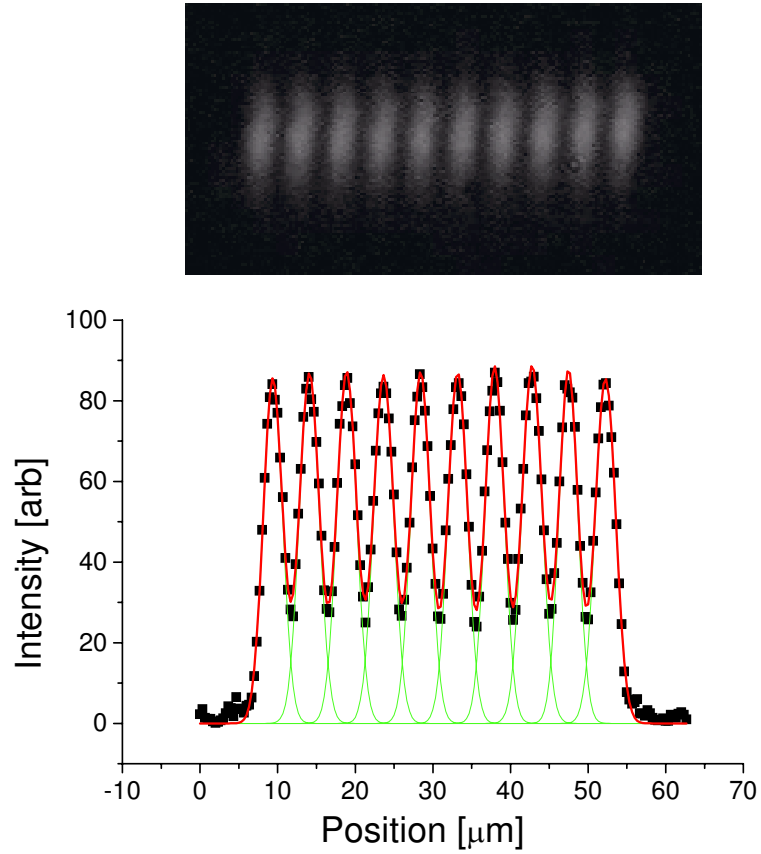


Figure 6.4: Box wall beam as a tweezer lattice. This is the same beam as shown in Figure 5.16, but with closer spacing between the sites. For the tweezer extraction experiment, only two such spots are needed inside the quantum dot, but this image illustrates the possibility of doing a lattice-type experiment such as a direct study of a Mott-insulator state [4].

The BEC shown in Figure 5.19(c) is in the appropriate conditions for performing an extraction experiment. Small number condensates such as that are required so that the energy splitting inside the quantum dot is comparable to the chemical potential of the condensate reservoir. If a very large condensate is used, the ground state splittings in the dot are smaller than the fluctuations of the chemical potential itself. This causes the process to become less robust.

The method of detection was discussed in Section 3.8.3. In the context of a quantum tweezer experiment, where atoms from the optical trap need to be counted, the detection system is put into perspective in the following section.

6.4 Counting Atoms in the Optical Trap

The section title is a bit of a misnomer, we do not actually count the atoms *in* the optical trap, but rather *from* the optical trap. This is done by transferring the final contents of the optical trap into the SAD MOT described in Section 3.8.3.

The concept is relatively simple. The beams and magnetic fields of the SAD MOT are turned on at the same time that the optical trap beams are turned off. Because the capture region of the SAD MOT is roughly a sphere with a diameter of 1 mm and the BEC in the optical box is only $80\ \mu\text{m}$ in the longest direction, overlapping these regions is not difficult. The atoms may, therefore, be transferred very efficiently into the SAD MOT. The fluorescence signal is recorded by the APD as discussed in Section 3.8.3. We are chiefly

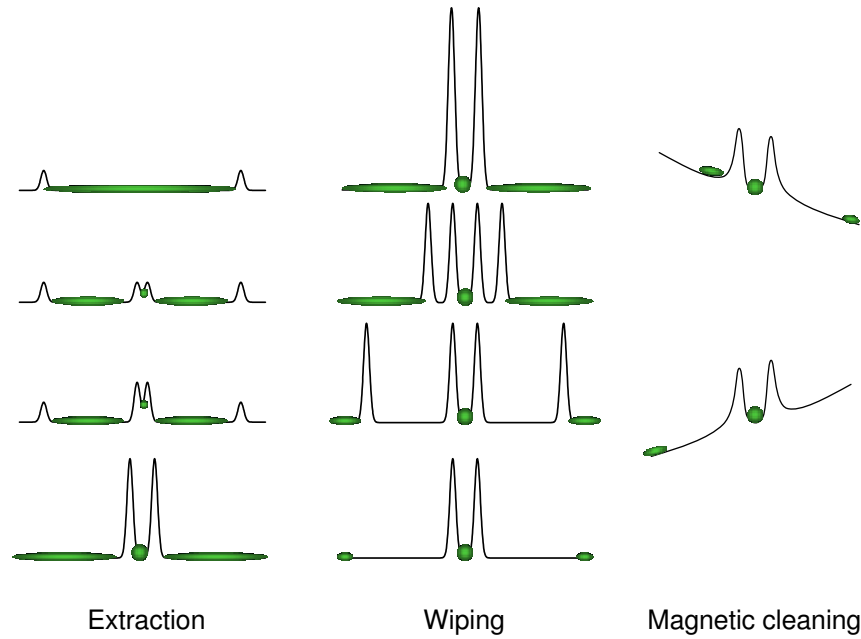


Figure 6.5: Pictorial of cleaning. Following an extraction experiment or any other desired number counting test, a pair of box wall beams are increased in intensity to protect the atoms to be counted. The center column shows a wiping process where moving box wall beams push the atoms away. The right column shows a magnetic cleaning where a gradient of order 5 G/cm allows the extraneous atoms to slide off in either direction.

interested in the initial count because after some period there is random loading and loss from the SAD MOT. The period of time of a reliable signal is typically in the hundreds of milliseconds.

All this said, only numbers of atoms are detected, not the distribution. If it is desired to look at the atom numbers in a single optical quantum dot or in some small optical box, it is required that all other atoms be removed from the region before transferring into the SAD MOT. Such atoms would

cause false results. Removal of the excess atoms is accomplished by a few ‘cleaning’ methods shown pictorially in Figure 6.5. These are denoted as ‘wiping’ and ‘magnetic cleaning’. After an extraction experiment, the detection is destructive of the state of the optical quantum dot and we are not interested in preserving the state, only the number. The tweezer beams may be raised very high to protect the atoms contained within. Afterwards, both wiping and magnetic cleaning are performed.

Because of the flexibility of the designer box wall beams as discussed in Sections 5.10 and 6.3, a pair of Gaussian beams may be used as wipers. These beams are ramped on to overlap slightly the tweezer beam barriers and then moved axially outwards in each respective direction. This process pushed the atoms out of the trap. The second method is to add a weak gradient of order 5 G/cm in both directions. This tilts the potential and the atoms slide out of the trap.

A wonderful thing about this method is that it is easy to check. A criteria for successful cleaning is the ability to remove one of the two large tweezer beam barriers and verify that no atoms are remaining. Additionally, the necessary height of these protection barriers may be determined by lowering the barriers until there is loss during the cleaning process.

Some typical fluorescence time series are shown in Figures 6.6 and 6.7. Figure 6.6 shows a the signal of a case where around 10^3 atoms are transferred from the optical box into the SAD MOT. The signal is initially flat and then decays as atoms are lost from the MOT. The interesting part of the plot,

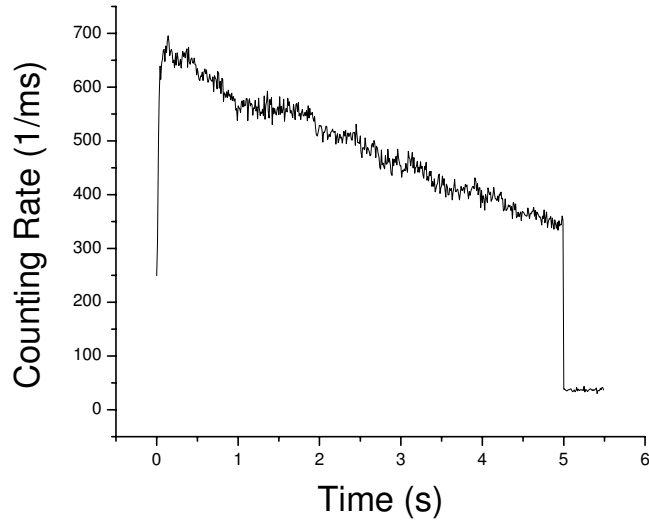


Figure 6.6: Fluorescence signal for 10^3 atoms transferred from the optical trap into the SAD MOT at time zero.

however, is the beginning. The signal level is proportional to the atom number in the final stage of the optical trap for small atom numbers. Using this method of detection is an important cross-check against absorption imaging. Both methods are used for small condensates.

Figure 6.7 shows the Fluorescence signal for a single atom transferred from the optical trap into the SAD MOT. It is important to emphasize that the single atom in this case is the random final product of an nearly-to-zero evaporation in the optical trap. It was not extracted as in the quantum tweezer but rather serves as a proof-of-principle shot indicating that it is very feasible to detect the single atom final result of such an extraction with high probability. The signal shows that a single atom is transferred and held for 2 s. The

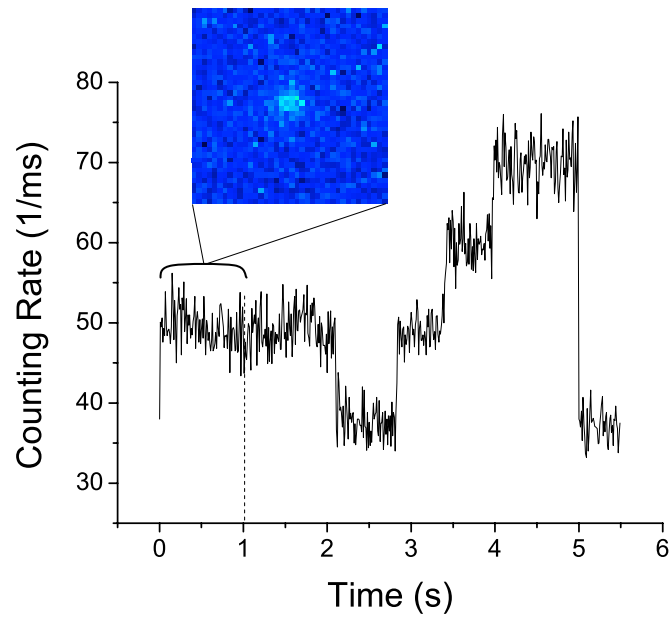


Figure 6.7: Fluorescence signal for an atom transferred from the optical trap into the SAD MOT at time zero. The signal shows a single initial atom is transferred and held for 2 s. The level changes afterwards are due to random loss and background loading. The inset is a fluorescence image of the single atom for a 1 s exposure from the beginning of this run.

level changes afterwards are due to random loss and background loading. The inset is a fluorescence image of the single atom for a 1 s exposure from the beginning of this run.

6.5 Future Outlook

Study of the extraction process experimentally is quite involved. This requires careful collection of statistics of the occupancy of the quantum dot after extraction runs at various rates. Initial attempts at this goal have given Poissonian statistics indicating various technical problems. This is the stage of the experiment at this writing.

The work in the previous chapters describes the major progress that has been made towards actual implementation of a quantum tweezer for atoms — especially the production of a BEC in the appropriate conditions for such an experiment to be possible. In the near future, a detailed characterization of the parameter space of the tweezer will be done and sub-Poissonian statistics are expected as indicated by the theory.

Appendices

Much of the information in these appendices was written during the construction phase of the experiment and is very technical in nature. They are included here to provide greater details of various aspects of the experiment which may be useful to the reader. Perhaps silly to write this, but as a disclaimer note: these designs are what worked for us, and there is no guarantee expressed or implied, if the reader chooses to use any of the information in this dissertation it is at his/her own risk.

Appendix A

Magnetic Coils

Our experimental setup includes a plethora of electromagnets. These include: the QUIC trap primary coils: quadrupole pair, Ioffe coil; the QUIC trap auxilliary coils: (Ioffe) bias adjust coil, optical pumping pair; the upper MOT: quadrupole pair; and the Earth compensation: X and Y pair, Z coil. This section gives the basic equations and concepts for designing electromagnets for cold atom experiments.

A.1 Some Theory of Electromagnets

In this section, some of the equations for circular and square electromagnets are summarized. Here, I is written for the current in Amp-turns. That is, $I = NI_0$ where N is the number of turns in the electromagnet and I_0 is the actual current in Amps. Generally, the permeability, μ , here is the permeability of free space $\mu_0 = 4\pi \times 10^{-7} \text{ Tm/A}$.

A.1.1 Exact Field of a Circular Current Loop

The field for a circular current loop of current I with radius R displaced from the origin by a distance D as shown in Figure A.1 has magnetic field

components given by [63]:

$$\begin{aligned}
 B_z &= \frac{\mu I}{2\pi} \frac{1}{\sqrt{(R+\rho)^2 + (z-D)^2}} \left[K(k^2) + \frac{R^2 - \rho^2 - (z-D)^2}{(R-\rho)^2 + (z-D)^2} E(k^2) \right], \\
 B_\rho &= \frac{\mu I}{2\pi} \frac{1}{\rho} \frac{z-D}{\sqrt{(R+\rho)^2 + (z-D)^2}} \left[-K(k^2) + \frac{R^2 + \rho^2 - (z-D)^2}{(R-\rho)^2 + (z-D)^2} E(k^2) \right],
 \end{aligned}
 \tag{A.1}$$

where

$$k^2 = \frac{4R\rho}{(R+\rho)^2 + (z-D)^2},
 \tag{A.2}$$

and $K(k^2)$ and $E(k^2)$ are the complete elliptic integrals for the first and second kind respectively [64].

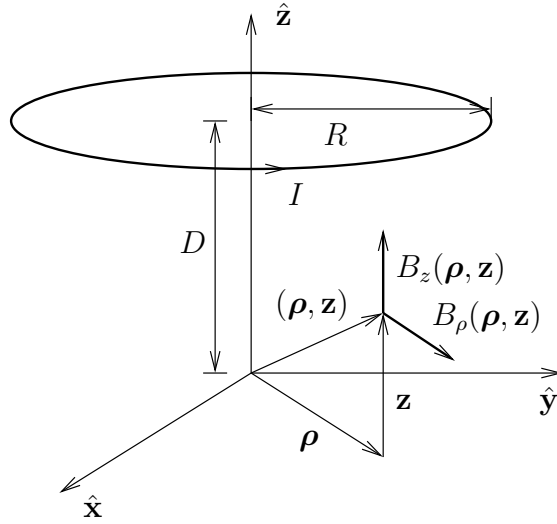


Figure A.1: Cylindrical coordinates for the magnetic field of a single circular current loop centered at axial position $z = D$.

A.1.2 Approximations for Circular Current Loops

Figure A.1 shows a current loop displaced from the origin, here and in the next sections, we look for approximate field equations near the origin. This corresponds to the case where the coils are somewhere outside a vacuum chamber and all the action is near the origin.

Near the origin ($\rho = 0, z = 0$), we can write a power series expansion for the field components to second order:

$$\begin{aligned}
 B_z &= \mu I \frac{1}{2} \frac{R^2}{(D^2 + R^2)^{3/2}} + \overbrace{\mu I \frac{3}{2} \frac{DR^2}{(D^2 + R^2)^{5/2}}}^{\text{axial field gradient}} z \\
 &\quad + \underbrace{\mu I \frac{3}{4} \frac{R^2(4D^2 - R^2)}{(D^2 + R^2)^{7/2}}}_{\text{axial curvature}} (z^2 - \rho^2/2) + \dots, \\
 B_\rho &= - \underbrace{\mu I \frac{3}{4} \frac{DR^2}{(D^2 + R^2)^{5/2}}}_{\text{radial field gradient}} \rho - \mu I \frac{3}{4} \frac{R^2(4D^2 - R^2)}{(D^2 + R^2)^{7/2}} z\rho + \dots.
 \end{aligned} \tag{A.3}$$

These equations may be used for estimations of fields produced by a single coil. For example, earth field biasing without a Helmholtz pair, one may estimate the single coil field and the deviations from constant field over the region of interest.

A.1.3 Circular Coil Pairs

For actual Helmholtz and anti-Helmholtz pairs we have equations for fields near the origin as follows. The distance between the coils is $d = 2D$.

In Figure A.2(a), a Helmholtz coil configuration is shown, the equations

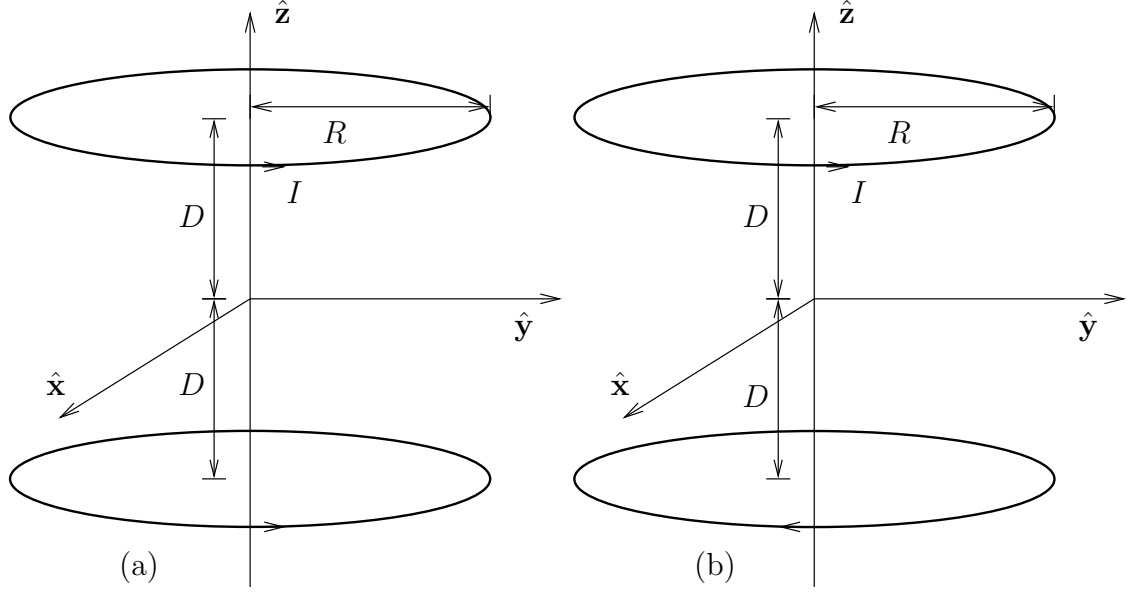


Figure A.2: (a) coil pair in Helmholtz configuration. For most ideal constant field, the configuration needs $R = 2D$, *i.e.* the distance between the coils is the same as coil radius. (b) anti-Helmholtz configuration.

for the field near the origin to third order are:

$$\begin{aligned}
 B_z &= \mu I \frac{R^2}{(D^2 + R^2)^{3/2}} + \mu I \frac{3 R^2 (4D^2 - R^2)}{2 (D^2 + R^2)^{7/2}} (z^2 - \rho^2/2) + \dots, \\
 B_\rho &= -\mu I \frac{3 R^2 (4D^2 - R^2)}{2 (D^2 + R^2)^{7/2}} z\rho + \dots
 \end{aligned}
 \tag{A.4}$$

There are no third order terms in for these fields, the next terms are fourth order. In the ideal case with $R = 2D$, the second order terms vanish giving

$$\begin{aligned}
 B_z &= \mu I \frac{8}{5\sqrt{5}R} + \dots, \\
 B_\rho &= 0 + \dots
 \end{aligned}
 \tag{A.5}$$

to third order. Naturally, one could simply use the zeroth order term in Equation (A.4) as a field estimation in case of an imperfect Helmholtz pair

which may frequently be the case, such as in earth field nulling coils. For the anti-Helmholtz case shown in Figure A.2(b), the equations for the field to third order are:

$$\begin{aligned} B_z &= \mu I 3 \frac{DR^2}{(D^2 + R^2)^{5/2}} z + \mu I \frac{15 R^2 (4D^2 - 3R^2)}{24 (D^2 + R^2)^{9/2}} (4z^3 - 6\rho^2 z) + \dots, \\ B_\rho &= -\mu I \frac{3}{2} \frac{DR^2}{(D^2 + R^2)^{5/2}} \rho + \mu I \frac{15 R^2 (4D^2 - 3R^2)}{16 (D^2 + R^2)^{9/2}} (\rho^3 - 4\rho z^2) + \dots. \end{aligned} \quad (\text{A.6})$$

Most notably, the gradient (first order term) in the axial and radial directions differ only by a factor of 2. It is also noted that the third order terms in both directions vanish for $R = \sqrt{4/3}D$, however this is generally not as important as in the Helmholtz case. A more important figure is that the gradient is maximized for $2D = R$, which gives a gradient

$$\frac{dB_z}{dz} = \mu I \frac{48}{25\sqrt{5}R^2} = 2 \frac{dB_\rho}{d\rho}. \quad (\text{A.7})$$

This is to say it is sensible in both cases of Helmholtz or anti-Helmholtz configuration to space the coils by the coil radius, *spacing* = $2D = R = \textit{radius}$. For most purposes the first order term may be used to estimate the gradient of practical coils in this configuration:

$$B_z \cong \mu I 3 \frac{DR^2}{(D^2 + R^2)^{5/2}} z, \quad (\text{A.8})$$

$$B_\rho \cong -\mu I \frac{3}{2} \frac{DR^2}{(D^2 + R^2)^{5/2}} \rho. \quad (\text{A.9})$$

A.1.4 Exact Field of a Square Current Loop

For the case of a square coil of side length L centered at position $z = D$, as shown in Figure A.3, we can obtain similar equations as for the circular coil.

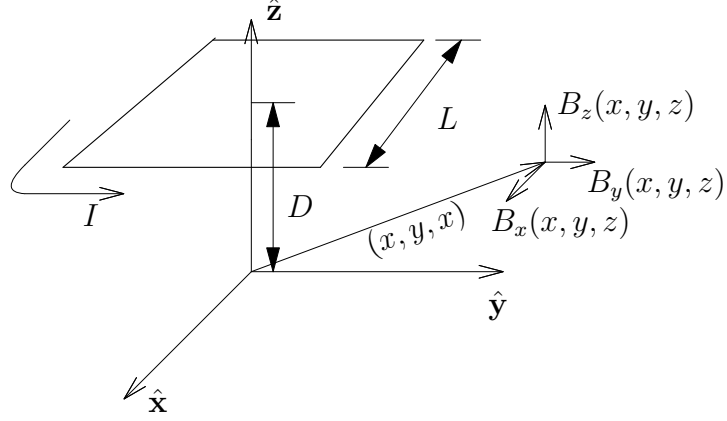


Figure A.3: Rectangular coordinates for the magnetic field of a single square current loop centered at axial position $z = D$.

The exact field for a square current loop can be obtained from the Biot-Savart law, integrating around the square loop. The result is given by:

$$\begin{aligned}
 B_x = \mu I \frac{\sqrt{2}}{2\pi} (z - D) & \left[\left(\frac{L + 2y}{f(-x, y, z - D)g(-x, 0, z - D)} \right. \right. \\
 & - \frac{L + 2y}{f(x, y, z - D)g(x, 0, z - D)} \\
 & + \frac{L - 2y}{f(-x, -y, z - D)g(-x, 0, z - D)} \\
 & \left. \left. - \frac{L - 2y}{f(x, -y, z - D)g(x, 0, z - D)} \right) \right], \tag{A.10}
 \end{aligned}$$

$$\begin{aligned}
 B_y = \mu I \frac{1\sqrt{2}}{2\pi} (z - D) & \left[\left(\frac{L + 2x}{f(x, -y, z - D)g(0, -y, z - D)} \right. \right. \\
 & - \frac{L + 2x}{f(x, y, z - D)g(0, y, z - D)} \\
 & + \frac{L - 2x}{f(-x, -y, z - D)g(0, -y, z - D)} \\
 & \left. \left. - \frac{L - 2x}{f(-x, y, z - D)g(0, y, z - D)} \right) \right], \tag{A.11}
 \end{aligned}$$

$$\begin{aligned}
B_z = \mu I \frac{\sqrt{2}}{4\pi} & \left[\frac{L+2x}{g(x,0,z-D)} \left(\frac{L+2y}{f(x,y,z-D)} + \frac{L-2y}{f(x,-y,z-D)} \right) \right. \\
& + \frac{L-2x}{g(-x,0,z-D)} \left(\frac{L+2y}{f(-x,y,z-D)} + \frac{L-2y}{f(-x,-y,z-D)} \right) \\
& + \frac{L+2y}{g(0,y,z-D)} \left(\frac{L+2x}{f(x,y,z-D)} + \frac{L-2x}{f(-x,y,z-D)} \right) \\
& \left. + \frac{L-2y}{g(0,-y,z-D)} \left(\frac{L+2x}{f(x,-y,z-D)} + \frac{L-2x}{f(-x,-y,z-D)} \right) \right] \quad (\text{A.12})
\end{aligned}$$

where

$$f(x, y, z) = \sqrt{L^2 + 2L(x+y) + 2(x^2 + y^2 + z^2)} \quad (\text{A.13})$$

and

$$g(x, y, z) = L^2 + 4L(x+y) + 4(x^2 + y^2 + z^2). \quad (\text{A.14})$$

A.1.5 Approximations for Square Current Loops

Simplified expressions that give the gradient and curvatures may be obtained by expanding in a power series near the origin as in the figure.

Near the origin ($x = 0, y = 0, z = 0$), we can write the field to second

order as:

$$\begin{aligned}
B_x &= -\mu I \frac{2\sqrt{2}}{\pi} \frac{D(12D^2L^2 + 5L^4)}{(2D^2 + L^2)^{3/2}(4D^2 + L^2)^2} x \\
&\quad - \mu I \frac{2\sqrt{2}}{\pi} \frac{L^2(384D^6 + 288D^4L^2 + 44D^2L^4 - 5L^6)}{(2D^2 + L^2)^{5/2}(4D^2 + L^2)^3} xz + \dots , \\
B_y &= -\mu I \frac{2\sqrt{2}}{\pi} \frac{D(12D^2L^2 + 5L^4)}{(2D^2 + L^2)^{3/2}(4D^2 + L^2)^2} y \\
&\quad - \mu I \frac{2\sqrt{2}}{\pi} \frac{L^2(384D^6 + 288D^4L^2 + 44D^2L^4 - 5L^6)}{(2D^2 + L^2)^{5/2}(4D^2 + L^2)^3} yz + \dots , \\
B_z &= \mu I \frac{2}{\pi} \frac{L^2}{(D^2 + L^2/2)^{1/2}(4D^2 + L^2)} \\
&\quad - \mu I \frac{4\sqrt{2}}{\pi} \frac{D(12D^2L^2 + 5L^4)}{(2D^2 + L^2)^{3/2}(4D^2 + L^2)^2} z \\
&\quad + \mu I \frac{2\sqrt{2}}{\pi} \frac{L^2(384D^6 + 288D^4L^2 + 44D^2L^4 - 5L^6)}{(2D^2 + L^2)^{5/2}(4D^2 + L^2)^3} (z^2 - (x^2 + y^2)/2) + \dots .
\end{aligned} \tag{A.15}$$

These equations can estimate the fields produced by a single square coil.

A.1.6 Square Coil Pairs

Equations for coil pairs may also be obtained similar to those of the circular coils, and following similar geometry as in Figure A.2, equations for

the Helmholtz pair may be given as:

$$\begin{aligned}
B_x &= -\mu I \frac{4\sqrt{2} L^2 (384D^6 + 288D^4L^2 + 44D^2L^4 - 5L^6)}{\pi (2D^2 + L^2)^{5/2} (4D^2 + L^2)^3} xz + \dots , \\
B_y &= -\mu I \frac{4\sqrt{2} L^2 (384D^6 + 288D^4L^2 + 44D^2L^4 - 5L^6)}{\pi (2D^2 + L^2)^{5/2} (4D^2 + L^2)^3} yz + \dots , \\
B_z &= \mu I \frac{4 L^2}{\pi (D^2 + L^2/2)^{1/2} (4D^2 + L^2)} \\
&\quad + \mu I \frac{4\sqrt{2} L^2 (384D^6 + 288D^4L^2 + 44D^2L^4 - 5L^6)}{\pi (2D^2 + L^2)^{5/2} (4D^2 + L^2)^3} (z^2 - (x^2 + y^2)/2) + \dots .
\end{aligned} \tag{A.16}$$

The second order terms vanish in the case of $D = \alpha L$ where

$$\alpha = \frac{1}{2\sqrt{6}} \sqrt{\frac{72^{2/3}}{(36 + \sqrt{610})^{1/3}} + (72 + 2\sqrt{610})^{1/3} - 6} \cong 0.272253. \tag{A.17}$$

So the coils provide maximum uniformity when *spacing* = $2D \cong 0.544506L$.

In this case the field is given by

$$\begin{aligned}
B_x &= 0 + \dots , \\
B_y &= 0 + \dots , \\
B_z &= \mu I \frac{1.29611}{L} + \dots .
\end{aligned} \tag{A.18}$$

Anti-Helmholtz equations may also be obtained as:

$$\begin{aligned}
B_x &= -\mu I \frac{4\sqrt{2}}{\pi} \frac{D(12D^2L^2 + 5L^4)}{(2D^2 + L^2)^{3/2} (4D^2 + L^2)^2} x + \dots , \\
B_y &= -\mu I \frac{4\sqrt{2}}{\pi} \frac{D(12D^2L^2 + 5L^4)}{(2D^2 + L^2)^{3/2} (4D^2 + L^2)^2} y + \dots , \\
B_z &= \mu I \frac{8\sqrt{2}}{\pi} \frac{D(12D^2L^2 + 5L^4)}{(2D^2 + L^2)^{3/2} (4D^2 + L^2)^2} z + \dots .
\end{aligned} \tag{A.19}$$

These give the field up to second order. The second order terms are all zero, but there are a variety of third order terms which I do not display here. The

condition for maximum gradient is the same as for uniformity in the Helmholtz case. Having $spacing = 2D \cong 0.544506L$ gives the maximum gradient of

$$\frac{dB_z}{dz} = \mu I \frac{2.79200}{L^2} = 2 \frac{dB_x}{dx} = 2 \frac{dB_y}{dy}. \quad (\text{A.20})$$

A.2 Numerical Calculations of Fields

It is relatively easy to do a brute-force calculation of the magnetic fields of a more realistic configuration using something like MATLAB. The basic problem with the equations given in the previous section is that they are for infinitesimally thin wires. When one is interested in the fields far from the coil, such a thickness is not relevant, such as when designing typical MOT coils or earth bias coils. However, in the case of a magnetic trap, where the coils may be very close to the region of interest and careful field compensation is required, the size and shape of the coils can make a huge difference. In this situation, it is more critical to calculate the fields carefully for coil sizes as realistic as possible. To do this, we wrote a MATLAB program that viewed the coil as composed of N infinitesimal coils each with identical current. The field at the point of interest was then calculated as the sum of the contributions from each loop. The QUIC trap field plots in Figures 3.21 and 3.24 were calculated in this fashion.

A.3 Power and Cooling

When designing magnetic coils, one important consideration is how to keep them cool. In some instances, when the input power is low (under a few watts) no cooling maybe needed, tens of watts may be air cooled or water cooled. It really depends on the coil holder structure (metal or plastic) and airflow available. There are other concerns with air-cooling coils in optics experiments, i.e. dust and air index variations. Larger power loads (more than 50 W) are generally water cooled. One comment on heating, is that what I am really discussing here is for rms joule heating. Coils that are pulsed infrequently for short periods may not need to be cooled.

A.3.1 Power into a Coil

The field of a coil or set at some point in space is

$$B = CI_0N, \tag{A.21}$$

where C is a constant determined by geometry, I_0 is the current delivered to the coil, and N is the number of turns. Consider this the coil shown in Figure A.4. Suppose the coil consists of a length l of magnet wire of some gauge with cross sectional area A_0 and the coil has bulk cross sectional area $A = \pi a^2 = NA_0$. The length is approximately $l \cong 2\pi\bar{R}N$, where \bar{R} is the average coil radius (the radius to the center of the bulk for relatively thin coils). For copper wire with resistivity, ρ , the net resistance of the coil is $R = \rho l/A_0 \propto N/A_0$. Therefore the power delivered to the coil is $P = I_0^2 R \propto 1/NA_0 = 1/A$. Which is to say,

for a given desired magnetic field, the power required to be delivered to the coil depends only on the cross sectional area of the coil bulk. So, in order to reduce the amount of joule heating in the coil and produce the same magnetic field, it is necessary to make the coil as thick as possible. This, of course, neglects the changes in field due to geometry changes of thinner or thicker coils. For a coil with given cross section, changing size of wire switches the power needed, $P = IV$, between current and voltage. More useful than this philosophy is the approximate power:

$$P = \frac{2\pi \bar{R} \rho (NI_0)^2}{NA_0}, \quad (\text{A.22})$$

the resistivity of copper at room temperature is $\rho \cong 1.70 \times 10^{-8} \Omega \cdot \text{m}$, $I = NI_0$, of course, is the the number of amp-turns, and $A = NA_0$ is the total coil cross sectional area. If tossing in the area, A , which is to contain the wires, one must, of course, consider the packing fraction, that is, the area of copper is $A \rightarrow \alpha \pi a^2$, where α is the packing fraction, and a is the coil cross sectional radius.

A.3.2 Water Cooling

Water has heat capacity $C = 4186 \text{ J/kg } ^\circ\text{C}$ and a mass density $\rho = 1.0 \text{ kg/l}$. The change in temperature of water flowing with rate f (in l/s) sinking power P is

$$\Delta T = \frac{P}{\rho C f}. \quad (\text{A.23})$$

This equation gives the change in temperature from the incoming to the outgoing water which of course depends on the power. The load itself (coil) and

the water may have a temperature difference between them. The better the thermal contact between the water and the load the smaller this difference. In the case of our QUIC trap, with flow rate of about 6l/min = 0.1l/s and total power of nearly 900 W the change in temperature is only about 2°C. Since the water to wire contact is so outstanding the wire heats only these few degrees. This temperature change is not a source of instability since it heats the same each cycle. Another comment, in general, is that more surface area of wire contact with water improves heat transfer. This lends something to the philosophy of using smaller diameter and more of it to obtain the same coil cross section.

A.3.3 Stability of a Magnetic Trap

The stability of magnetic fields is extremely important in a magnetic trap that is used to produce a BEC. The stability depends on three things: current fluctuations, mechanical movements, external field fluctuations. The latter, we don't discuss here, see your local μ -metal distributor. We have not used μ -metal shielding for our magnetic trap. Current fluctuations are due to changes in current supplied to the coil over time. This can be very well controlled, see Appendix C on the magnetic trap electronics. An important source of fluctuations in magnetic field are due to thermal effects in the coils. This is due to a small amount of thermal expansion of the coil itself on the tens of microns scale for degree changes in temperature which may amount to shifts in field minimum, B_0 , of order 1 mG or more. This is important for

a BEC but irrelevant for a MOT or other less sensitive application. For our magnetic trap, to get best stability we found it necessary to make sure that the incoming cooling water was stable to under 0.1°C . This has given us very solid BECs.

A.4 Some Standard American Wire Types

Power requirements were discussed in the previous section in general, but ultimately, one must choose a specific wire type for the coils. The table gives typical wire sizes and specifications for standard American wire types. The diameter given is for the bare wire. Insulation, required for any magnet wire, may add between 0.05 and 0.2 mm to the diameter. The given values

Gauge	Diameter ($2\sqrt{A_0/\pi}$) mm (in)	Coated [†] Diam. mm (in)	Possible ^{††} Current A	Line Resistance (ρ/A_0) Ω/km
8	3.251 (0.128)	3.353 (0.132)	50	2.060
10	2.591 (0.102)	2.642 (0.104)	30	3.278
12	2.057 (0.081)	2.108 (0.083)	25	5.210
14	1.626 (0.064)	1.702 (0.067)	20	8.284
16	1.295 (0.051)	1.346 (0.053)	10	13.18
18	1.016 (0.040)	1.067 (0.042)	5	20.95
20	0.813 (0.032)	0.864 (0.034)	3.2	33.30
22	0.635 (0.025)	0.686 (0.027)	2.0	52.95
24	0.508 (0.020)	0.559 (0.022)	1.25	84.22
26	0.406 (0.016)	0.432 (0.017)	0.8	133.9

Table A.1: Some Standard American Copper Wire Types [65]. [†] approximate, depends on the coating type, number of layers, etc. ^{††} depends on cooling, these numbers are for relatively uncooled wires, i.e. they get quite warm.

for resistivity are for copper at 20°C and the currents are a guideline. In

general, the allowed current really depends on cooling efficiency. In a situation with very high current in a very small wire, extremely good water cooling is needed. For example, in our QUIC trap, the Ioffe coil uses 22 gauge wire and is routinely operated at about 30 A with around 400 W to this tiny coil. During early testing of the design, it had been operated at up to 50 A (about 1 kW), but this is no problem for the wire since contact with the flowing water is so good.

A.5 Inductance and Switching

A.5.1 Inductance and Parasitics

All coils have inductance, this is the principle limit for switch off time. For a coil of radius \bar{R} , thickness $2a$, and number of turns N , shown in Figure A.4 the inductance may be approximated by [66]

$$L \cong N^2 \bar{R} \mu \left[\ln \left(\frac{8\bar{R}}{a} \right) - 2 \right]. \quad (\text{A.24})$$

This equation assumes $\bar{R} \gg a$, which is frequently not the case, but is adequate to estimate for most practical purposes. Figure A.5 shows the an equivalent circuit for a practical inductor. The resistance is obviously due to the line resistance of the wire used. The capacitance is between the closely spaced turns and depends highly on the wire thickness used, spacing, etc. We have found that the capacitance is typically of order 100 pF down to 1 pF for coils that we have used. These may typically give resonance frequencies in the range of 500 kHz to 10 MHz depending on the coil inductance. For our

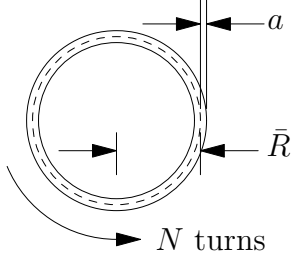


Figure A.4: Inductor coil geometry for Equation (A.24).

QUIC trap, the quadrupole coils have $R = 0.29 \Omega$ (measured), $L \cong 1 \text{ mH}$ (estimated), a resonance frequency $f = 720 \text{ kHz}$ (measured), and a capacitance $C = 1/4\pi^2 L f^2 \cong 50 \text{ pF}$. The Ioffe coil has $R = 0.40 \Omega$ (measured), $L \cong 0.1 \text{ mH}$ (estimated), a resonance frequency $f = 5.4 \text{ MHz}$ (measured), and

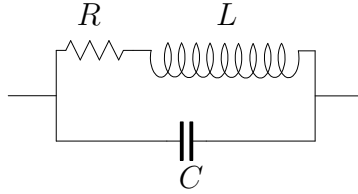


Figure A.5: Inductor coil equivalent circuit.

a capacitance $C = 1/4\pi^2 L f^2 \cong 10 \text{ pF}$. In general, the important numbers are R and L for power estimations and switch off time. The resonance frequency of the coils is its principle natural frequency and is only really important if, when using a magnetic trap, it is found to resonate with evaporative cooling RF or produce its own RF. This may depend on the circuit using to drive the coils, but interesting to keep in mind for system debugging. The resonance

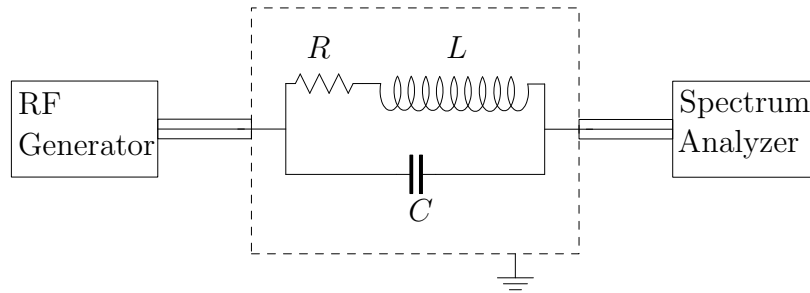


Figure A.6: How to measure resonance frequency of a practical coil [67]

frequency may be measured as follows [67]. Pass an RF signal through the coil as shown in Figure A.6 to a spectrum analyzer. The signal detected will drop in height at the resonance (to virtually nothing). More practically, the coil will exhibit many resonances, most much weaker.

A.5.2 Switching

The switching time is mostly limited by the inductance of the coil. A standard switching scheme used for virtually all of our coils is shown in Figure A.7. The basic idea is that when the current is suddenly disconnected the voltage across the inductor is clamped at a constant value until all the current is gone. Sudden disconnections are typically done by a Power MOSFET or IGBT, in either case having a zener clamp. In any case, we have a clamping voltage V_{so} (switch off voltage) and an inductance L , this gives the equation $V_{so} = -LdI/dt$ so the current in time is

$$I(t) = I_0(1 - t/\tau), \quad (\text{A.25})$$

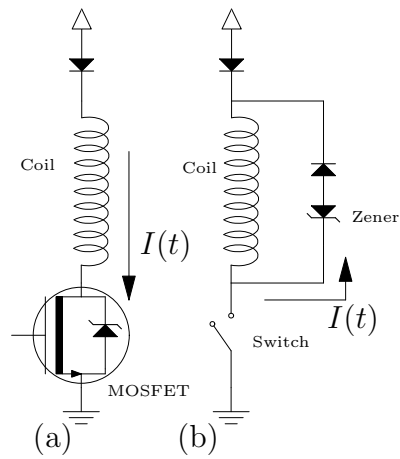


Figure A.7: Switching concept circuits. In (a), V_{so} is the reverse breakdown voltage of the MOSFET, typically 100 V to 500 V. Most modern power MOSFETs are internally connected with the zener as shown. IGBTs frequently are not, whereas one connects an external zener diode which may typically more than 1 kV depending on the IGBT. The concept circuit in (b) is basically equivalent to that in (a) with V_{so} as the zener diode voltage.

where the switch off time is

$$\tau = LI_0/V_{\text{so}}. \quad (\text{A.26})$$

So it is true that, as inductance goes up switch off time goes up. But it is not as bad as it appears, although $L \propto N^2$, $I_0 \propto 1/N$, so in fact $\tau \propto N$ not N^2 . That is, for a coil with a large number of turns, although it takes longer to switch, there is less current to switch, for a given field.

For our QUIC trap, with an inductance of about 2.1 mH and switch off voltage of 500 V, switching time for a typical current of 28 A is about 120 μs .

A.5.3 Comment on Steel Chambers

Most steel chambers have μ very close to the free space μ_0 , so the chamber itself does not cause a major change in the coil inductance. However, the presence of complete rings with finite resistance will result in eddy currents in the metal when the field is switched off. This causes the eddy currents to support the magnetic field after the coil currents have dropped which means that the fields turn off more slowly. In the case of our QUIC trap, we use a glass chamber between the coils, which gives, very well, the above switching time. In general, this can be a problem if coils are outside a steel chamber. If mounting hardware is made of metal, it can be slotted to reduce this effect. In some cases, plastic hardware can do the job, as in our QUIC trap.

Appendix B

Magnetic Trap Schematics and Photos

This appendix gives some schematics of the magnetic trap windings and of the assembled positions relative to the science chamber glass cell. More complete machine drawings are available at the web site [68]. Figure B.1 gives the winding diagram. The spacers consist of 1/16" nylon rods which are oriented perpendicular to the turns. This spacing allows water to flow between the turns for very good thermal contact. Figure B.2 shows the QUIC trap relative to the science chamber glass cell.

Some photographs in various stages of the assembly are given here because they are informative on the design concepts. Figure B.3 show photos of the QUIC trap assembled with and without the auxiliary coils. Figure B.4 show a series of photos of the construction of a quadrupole coil and Figure B.5 for the Ioffe coil. The electrical feed-through connectors are shown in Figure B.6.

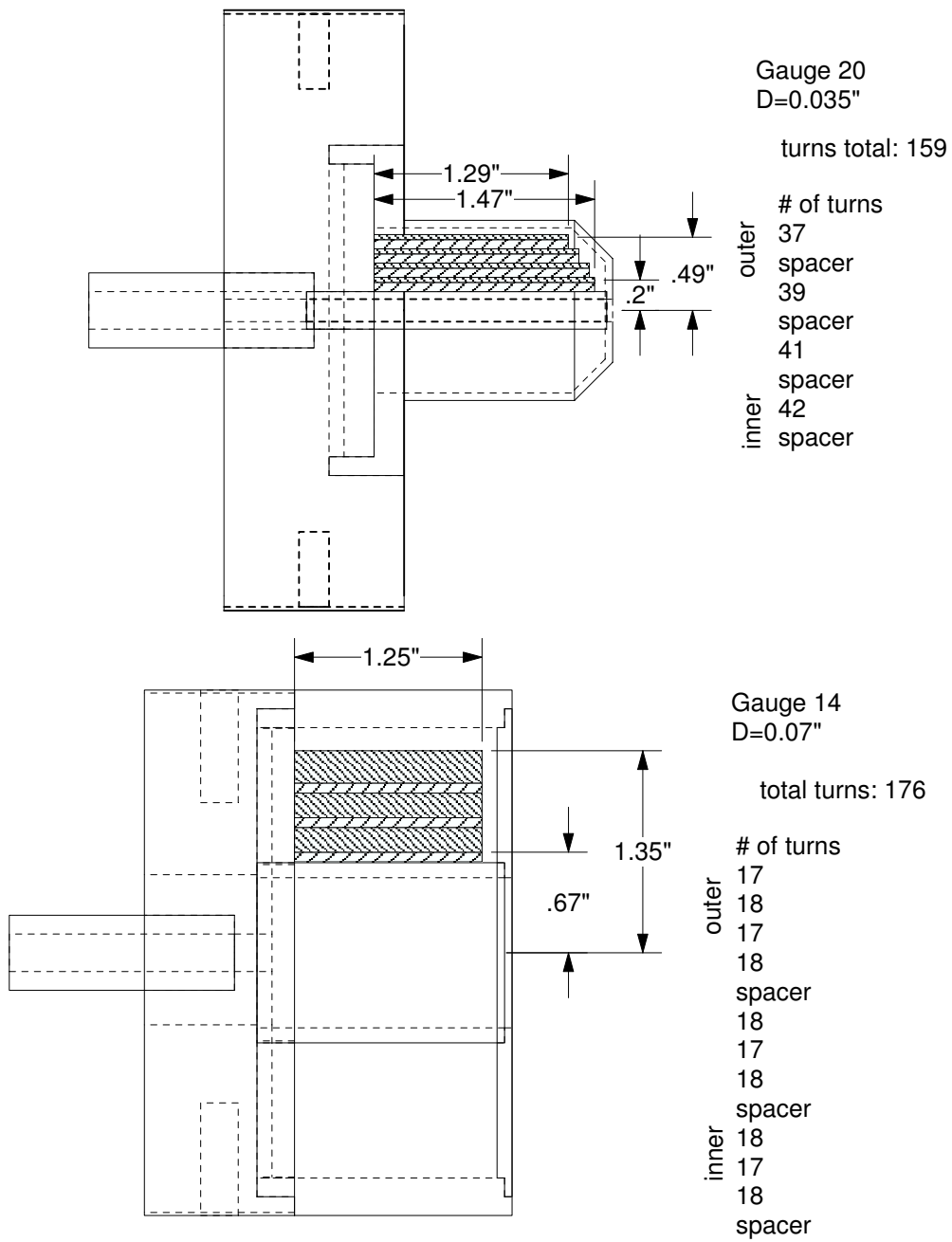


Figure B.1: Wire winding schematic for QUIC trap primary coils.

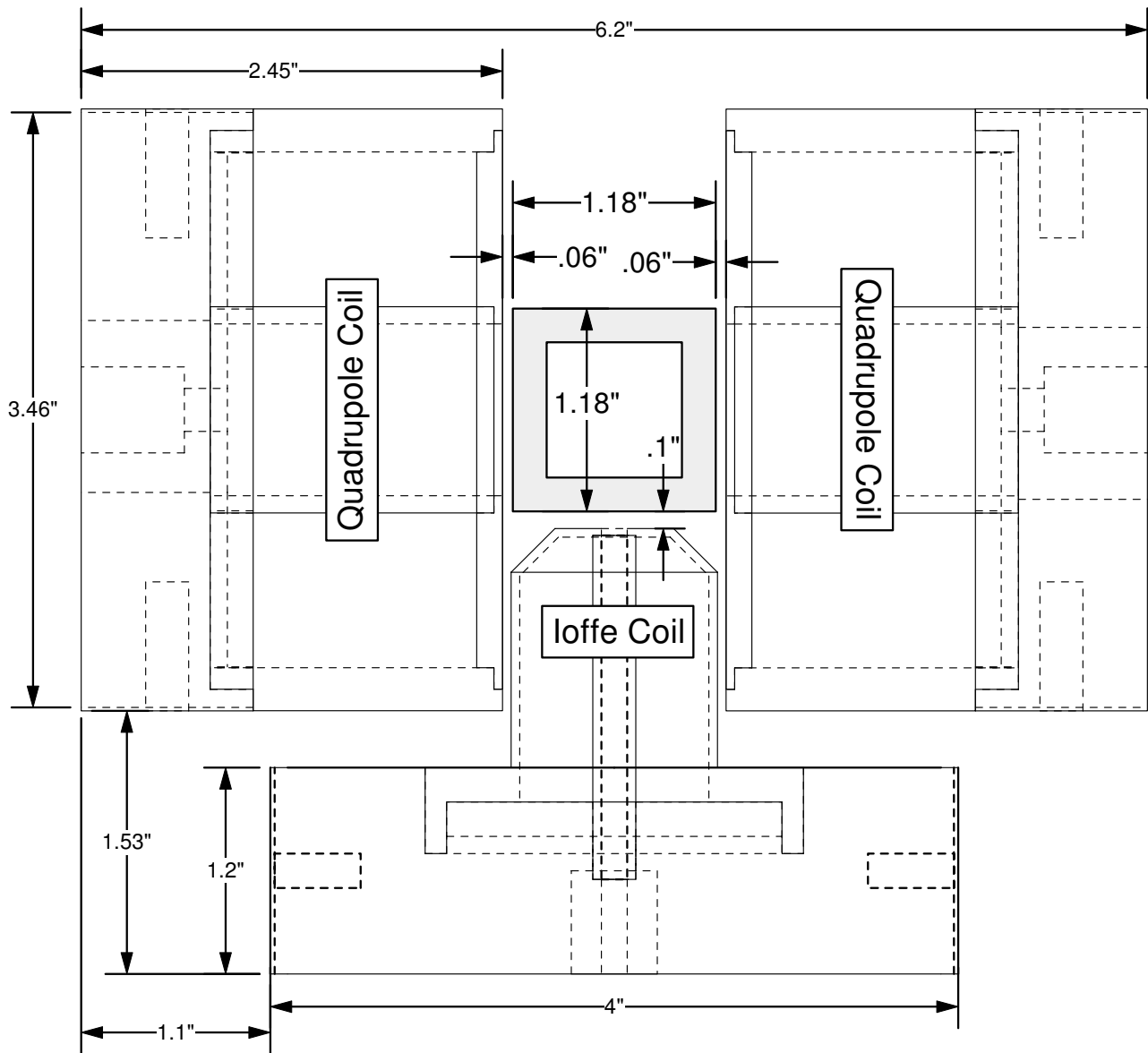


Figure B.2: Assembled schematic of the QUIC trap relative to the science chamber glass cell.

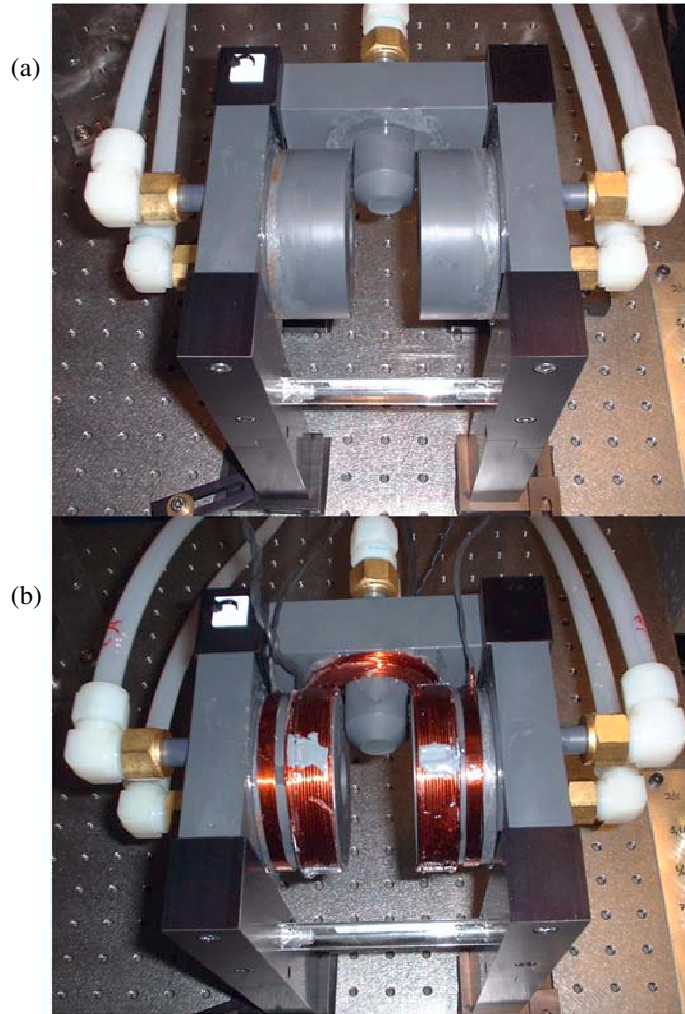


Figure B.3: Photos of the QUIC trap assembled. (a) Before installation of the auxiliary coils. (b) Complete trap before installation in the setup. The auxiliary coils are the ioffe bias adjustment coil, and the optical pumping pair. These coils are attached with epoxy to the outside of the PCV holders. The coils are uncooled.

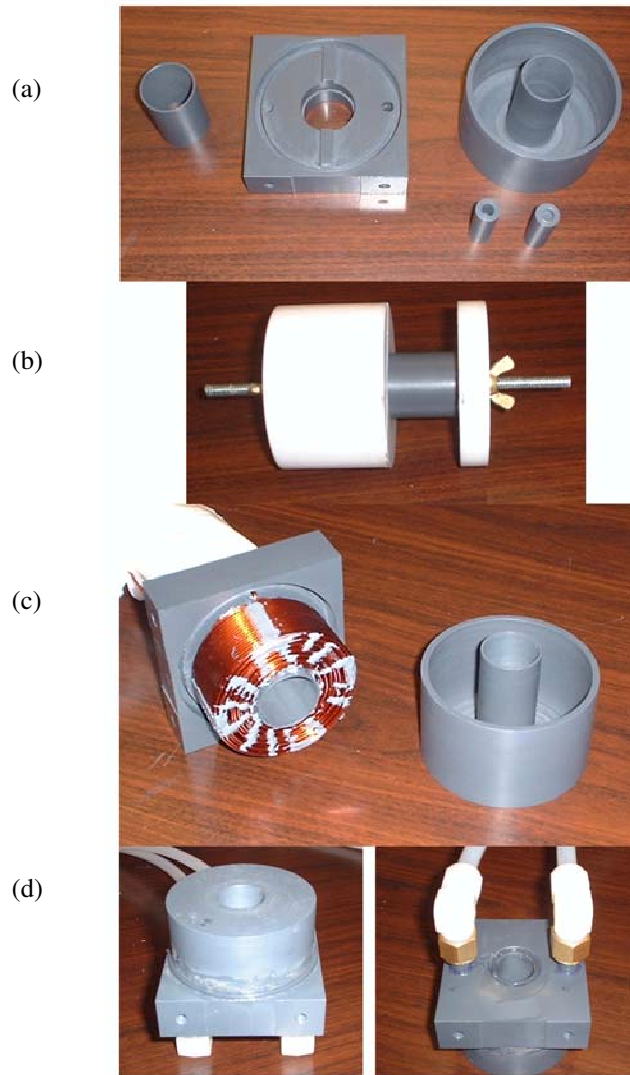


Figure B.4: Assembly photos of a quadrupole coil. (a) The set of PVC parts. (b) The inner rod mounted in Teflon blocks for winding. The blocks are spaces so that the coil of wire is at the appropriate location. (c) After winding, the inner rod is cemented to the base piece. The cover needs to be added. (d) The completed coil bonded together with PVC cement and then welded with a PVC hot air welder. The magnet wires exit the coils in the water tubes.

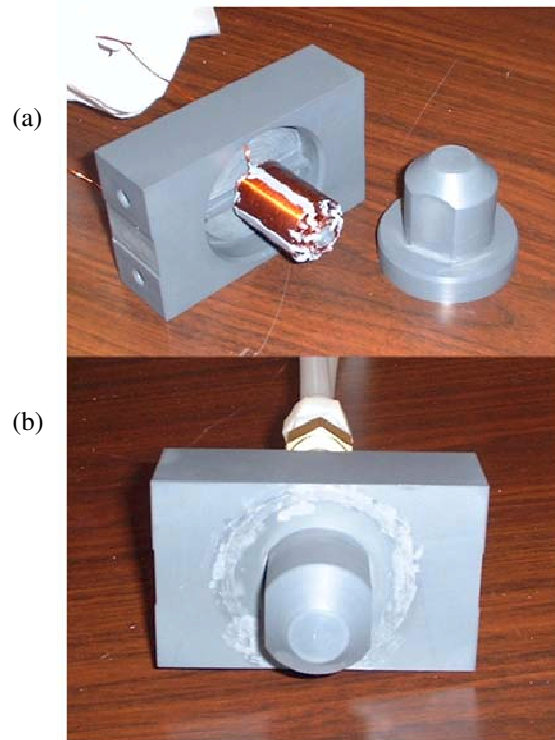


Figure B.5: Assembly photos of the Ioffe coil. (a) After winding, the inner rod is cemented to the base piece. The cover needs to be added. (b) The completed coil bonded together with PVC cement and then welded with a PVC hot air welder. The magnet wires exit the coils in the water tubes.

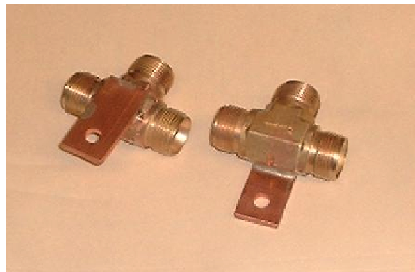


Figure B.6: QUIC trap electrical connectors photo. These connectors are used to connect the wire that is inside the water tube to the outside world. They consist of a standard brass Swagelok connector which has a hole drilled for soft soldering. The pieces are initially silver soldered with a copper tab to be used as a lug terminal. The internal connection is covered with epoxy to protect from etching by the water.

Appendix C

Analog Control Electronics

C.1 Multipurpose PID Controller

This analog circuit is intended to be used as a multipurpose PID controller. The schematic shown in Figure C.1 and PCB (most recent version at [69]) given here may be setup to be used as a laser diode current controller for up to 1/2 Amp directly (see Section C.2), logarithmic laser intensity controller (see Section C.3), temperature controller (we didn't do this), controller for high current device (see Sections C.4 to C.6), laser frequency lock servo [70], etc... These configurations depend on which options are used, and in some cases, what external devices to which it is interfaced. The layout was intended to be flexible so that it can accommodate many different possibilities. I hate redesigning the same circuit for various applications. Most likely I have forgotten many possibilities, but using the simple voltage sense and voltage control output, the circuit should be useful for many applications assuming appropriate external components are used.

There are several options for setpoint input, sense return, and output drive. The PID may be operated using a single opamp, or a multiple opamp setup. These are standard configurations, the former has the advantage of

fewer components but has coupled PID characteristics. The latter has independent PID characteristics so they may be optimized independently. The setpoint circuit includes options for an analog input, a potentiometer or trim-pot offset adjust, a gain or inversion option. The sense possibilities include a voltage/current sense, high current sense, direct output current sense, or a logarithmic photodiode sense. The output stage may be set up to drive up to 1/2 Amp of current either as a control single or directly driven current controller. The circuit requires a dual $\pm 15\text{ V}$ to $\pm 18\text{ V}$ supply.

As mentioned, the circuit may be set to use single or multiple opamp PID, use the single *or* the multiple opamp PID hook-up as in the table:

Single OpAmp PID hook-up	
Use	C1 to C3, R1 to R4, U1, U2
Omit	C4 to C6, R5 to R9, R11, R12, U3 to U5
Short ^a	R10, R13
Proportional Gain	$(R1 + R2)/R3$
Integration time	$R3 \times C2$
Differentiation time	$(R1 + R2) \times C3$
Notes: R4 limits differential gain, C1 gives high frequency roll-off.	
Multiple OpAmp PID hook-up	
Use	R1 to R3, R5 to R9, (R10 to R13 = 1 k Ω) C2, C4 to C6, U1 to U5
Omit	C1, C3, R4
Short ^a	C2
Proportional Gain	$(R1 + R2)/R3$
Integration time	$(R5 + R6) \times C2$
Differentiation time	$(R7 + R8) \times C3$
Notes: R9 limits differential gain, C6 gives high frequency roll-off.	
^a use a 0 Ω resistor, 1206 package.	

The summer used for the multiple opamp PID is an inverting summer,

in some cases, it is desired to re-invert the signal. Use as in the table:

Output inverter option used	
Use	R14, R15 = 1 k Ω , U6
Output inverter option not used	
Omit	U6
Short ^a	R14, R15
^a use a 0 Ω resistor, 1206 package.	

The circuit is naturally bi-polar, however, some cases require a un-polar output. Use the simple diode rectifier as in the table:

Output rectifier option used	
For positive output only, use	R17 = 10 k Ω , D1
For negative output only, use	R17 = 10 k Ω , D1 (reverse diode direction drawn on schematic and layout) omit R61 in either case.
Output rectifier option not used	
Omit	R17
Short ^a	R61
^a use a 0 Ω resistor, 1206 package.	

By convention, we will not list decoupling capacitors to be omitted when the associated IC is listed. The associations are given on the table:

Supply decoupling caps associated with ICs		
IC	Capacitors	Value
U1	C10,C11	0.1 μ F
U2	C12,C13	0.1 μ F
U3	C14,C15	0.1 μ F
U4	C16,C17	0.1 μ F
U5	C18,C19	0.1 μ F
U6	C20,C21	0.1 μ F
U7	C8	0.1 μ F
U8	C22,C23	0.1 μ F
U9	C24,C25	0.1 μ F
U10/U11	C26,C27	0.1 μ F
U10/U11	C28,C29	10 μ F

There are a number of setups for the setpoint, most are summarized in the table here, but the user can have some imagination and come up with others:

Setpoint Options	
Option	Instructions
Analog input only	Use: J1, D2, R22 Short: R18, R57 Omit: R19 to R21, R23 to R35, R58, R59 D3, D4, C9, C34, C35, U9
Potentiometer input (zero adjust) only	Use: R28 or R35 (trimpot <i>or</i> potentiometer), R26, R27, R29, R30, C9, C34, C35, D3, D4 Short: R21, R57, (R31 and R34) <i>or</i> ^a (R32 and R33) Omit: J1, D2, R18 to R20, R22 to R25, U9
Analog input with zero adjust	Use: J1, D2, R22, R28 or R35 (trimpot <i>or</i> potentiometer), R26, R27, R29, R30, C9, C34, C35, D3, D4, U9 Short: (R18 and R20) <i>or</i> ^b (R19 and R21) and (R31 and R34) <i>or</i> ^a (R32 and R33)
add in gain adjust	when using U9, use R23 to R25, the gain is $1 + \frac{50\text{k}\Omega}{R23+R24+R25}$
^b Invert setpoint signal	Short: (R18 and R20) <i>or</i> (R19 and R21) omit other 2, remember that pin 3 of U9 is non-inverting and pin 2 is inverting.
Unipolar zero adjust	(short R58, omit R26, D3, C34) <i>or</i> (short R59, omit R30, D4, C35) use R27 or R29 as 0Ω as appropriate.
^a Potentiometer direction	Short: (R31 and R34) <i>or</i> (R32 and R33) omit other 2, the direction of increase depends on if it is hooked to the inverting or non-inverting pin of U9.

The several sense options are summarized in the table. The photodiode uses a logarithmic amplifier so that it may operate over many orders of magnitude. The other options are all really the same thing depending on interpretation. The current/voltage sense uses either a ‘sense’ or load resistor from a current or voltage source. R46 is included for the option of breaking the ground connection or adding additional load to the driving sensor. This option would be used for instance in a high current controller where a hall sensor is

used. Another version is a high current sense using R47, the PCB is setup for an SR20 2 Watt 4-point sense resistor (Caddock Electronics). Depending on the resistance used, this resistor can directly measure up to 15 Amps. An additional current sense that can be used is a direct output measurement. In this case, there is no control output signal, and the buf ICs directly supply up to 1/2 Amp to a load. In this low current driver mode, no external components are needed. For the higher current cases, a high power output stage is needed, and is controlled with the control output signal.

Sense options	
Photodiode	Use: R36 to R39, (R56 <i>or</i> R60), C0, C7, C8, U7 Short: R40 Omit: J3, R41, R42 to R47, R54, U8
Current/voltage sense	Use: J3, R42 to R46, U8 Short: R41 Omit: R40, R36 to R39, R47, R56, R60, C0, C7, C8, U7
High current sense	Use: R42 to R44, R47, U8 Short: R41 Omit: J3, R40, R36 to R39, R45, R46, R56, R60, C0, C7, C8, U7 connect up to 15 A (depending on R47 value) through J5 to J6
Direct output current sense	Same as high current sense, but short R54, omit R55, for use with the buffer output stage. connect load across J6 to J7.

For the BNC connectors, the board is setup to accept either the right angle receptacle (227222-1) or the vertical receptacle (227161-1). The vertical receptacle may be mounted on the top or the bottom of the board.

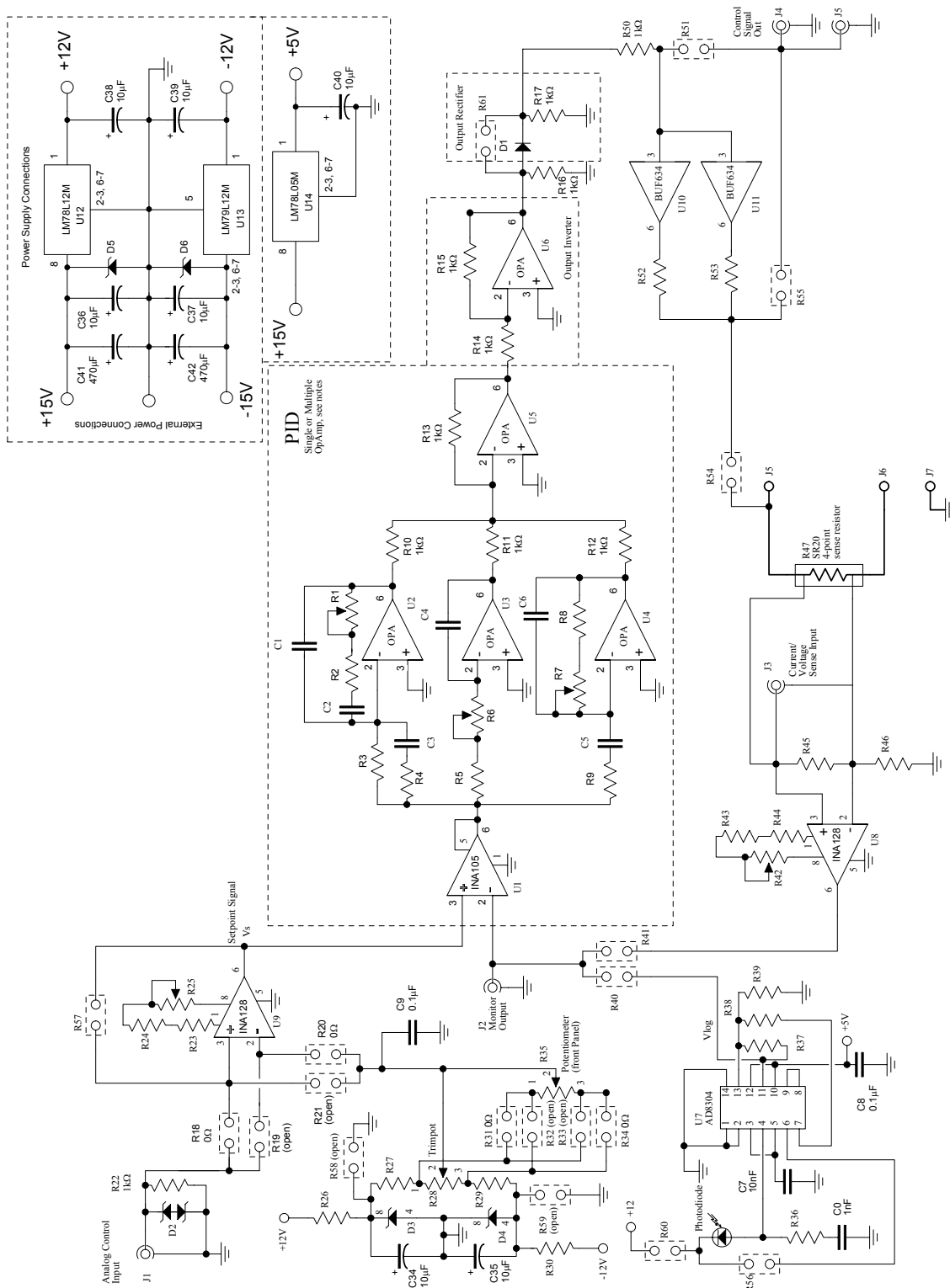


Figure C.1: Multipurpose PID controller schematic.
197

C.2 Current Controller for Laser Diodes

An older version of this design for an analog current controller based on a PID is given in [71]. That version has a few extra options for switching control not given on the multipurpose board. The multipurpose PID circuit may be hooked up to operate as in [71] for current output as a single or multiopamp PID. This would involve using the desired setpoint options as discussed in Section C.1 and using the 1/4 or 1/2 Amp current output option by including one or both of U10 and U11 for output current. This current may be directly sensed by R47 and the output terminals are at J6 and J7. In this case R45 and R46 would be omitted and U8 is directly sensing the current. At this time, we have not actually built the multipurpose PID board in this configuration, but is very similar to the well used design in [71].

C.3 Laser Intensity Stabilization

These version of the multipurpose PID uses the ‘Photodiode’ sense option. This involves a logarithmic amplifier that directly measures the current of the photodiode. The logarithmic amplifier we have used is the AD8304 from Analog Devices. The hookup used is basically that shown in Fig. 5 and explained in Table III of the AD8304 datasheet. The resistors given in the Table III correspond to our resistors as in $R37 = R_A$, $R39 = R_B$, $R38 = R_C$. The table with the accompanied equations given on the datasheet is ambiguous. The first column is written V_Y and this is actually as $V_Y' = G \times V_Y$

where $V_Y = 0.2 \text{ V/decade}$ and

$$G = 1 + \frac{R_A}{R_B || R_C}. \quad (\text{C.1})$$

The second column written I_Z should actually be written

$$I'_Z = I_Z \times 10^{(\alpha V_{\text{ref}}/V_Y)} \quad (\text{C.2})$$

where $I_Z = 100 \text{ pA}$, $V_{\text{ref}}/V_Y = 10$ (because $V_{\text{ref}} = 2 \text{ V}$ and $V_Y = 0.2 \text{ V}$), and

$$\alpha = \frac{R_A || R_B}{R_A || R_B + R_C}. \quad (\text{C.3})$$

After all of this, the output is

$$V_{\text{out}} = V'_Y \log_{10} \left(\frac{I_{\text{PD}}}{I'_Z} \right), \quad (\text{C.4})$$

where I_{PD} is the photodiode current.

For our implementation of this circuit, we typically used $V'_Y = 0.5 \text{ V/decade}$ and $I'_Z = 10 \text{ nA}$. The photodiode used was the FDS100 large area Silicon diode from Thorlabs.

In order to implement the circuit for stabilization of laser intensity, we have used the PID in conjunction with an acousto-optic modulator (AOM), see Appendix E.3.1. A functional schematic of operation is shown in Figure C.2. The computer output DAC gives the PID setpoint. The PID uses the photodiode as a sense input and then sends the control signal to an RF attenuator to adjust the RF power sent to the AOM. The attenuator used is typically from the PAS series from Minicircuits. In addition to stabilizing the laser intensity, this method also taylor's the calibration curve to the logarithmic response of the amplifier rather than the transfer characteristic of the AOM itself.

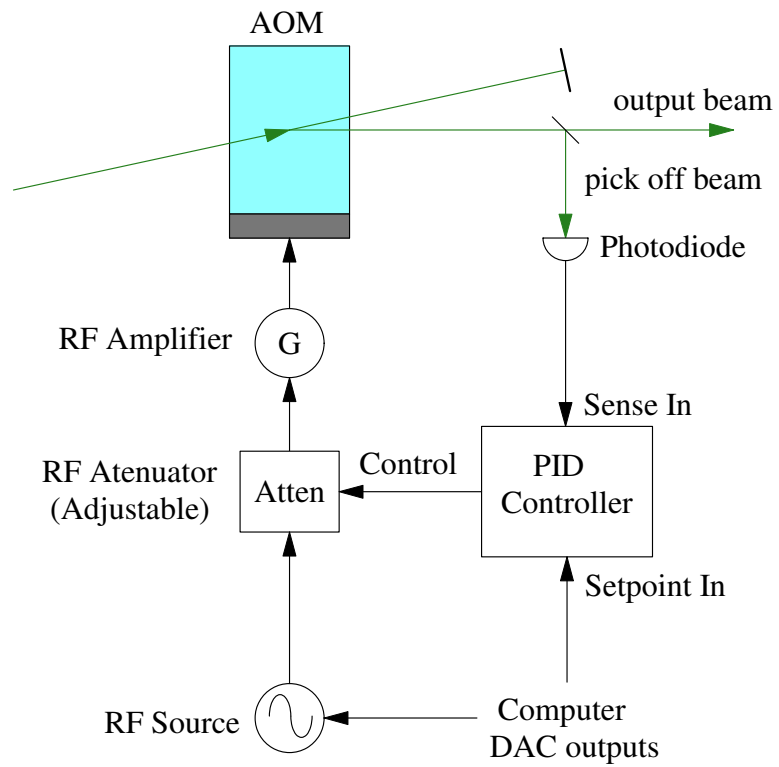


Figure C.2: Functional schematic of laser intensity stabilization.

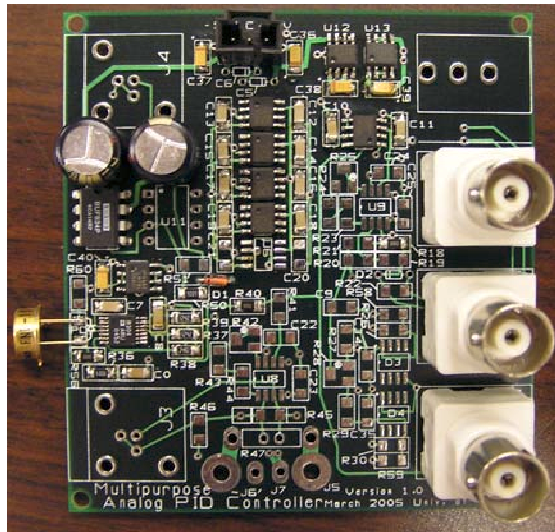


Figure C.3: Photo of multipurpose PID PCB as for laser intensity stabilization.

C.4 Uni- and Bi-directional Current Output Stages

This section gives designs that can be used in conjunction with the PID of the previous section as an output stage for driving electromagnets. One can be used to run a coil uni-directionally, the second may go both directions — a feature useful especially for small adjustment coils.

Uni-directional is easy. One method which we have used is given in Figure A.7(a). In this case, the MOSFET alone is the output stage, the coil load may be connected as shown. Most power MOSFETs have an internally connected zener diode for switch as described in that section.

Bi-directional is more tricky. For operation off a pair of power supplies, the design used for laser diode current control in Section C.2 may be used. Normally, we operate that circuit only one direction, but it can in principle be

used in both with no modification, only appropriate choice of setpoint voltage (*i.e.* negative). For such a low current device, it is not a problem to provide both positive and negative supplies despite only one being used for driving the output. Here we give a design which may be used from a single supply and can cross zero in current without zero crossing error. The output stage schematic is shown in Figure C.4 and may be used in conjunction with the PID of Section C.1.

This design is based on a pair of high power opamps which operate the coil load between their outputs floating above ground. The opamp pair switch roles as source and sink of current continuously depending on the input control voltage. We used TI's OPA549 as the power opamp. For current sense, we used the CLN-25 Hall-effect sensor from F.W. Bell. There is a single bipolar control voltage input which is added and subtracted from a center point voltage (V_{cp}). The current capacity of the stage can be increased by stacking slave opamps as in Section C.5.

The stage power supply ($V+$) must be of sufficient voltage for the resistance of the load for the current range desired, plus $2 \times 0.1 \Omega$ for the output resistors, and $2 \times$ opamp overhead voltage (around 4 V each). This power supply's common connection should be connected at only one point to the control electronics supplies, or through a small resistor.

The control voltage input from the PID will be in the range of about ± 10 V, so the gain of the OPA549's will typically be set to use the range of the power supply. The gain is given by $G = 1 + R2/R1$. The output of each

opamp is given by $V_{\text{out}\pm} = G \times (V_{\text{cp}} \pm V_{\text{control}})$. V_{control} comes from the PID and 0 V corresponds to zero current because both outputs are the same. Note: it is not important to make the gain of both opamps absolutely identical, this only means that zero current does not correspond exactly to zero volts on the control signal from the PID — this is of no concern. Generally we used a gain of at least 2. The center point voltage is set by the voltage divider and is generally set so that $G \times V_{\text{cp}}$ is around $V_s/2$.

One nice option of the OPA549 which we have used is the function of pin 9. If this pin is pulled low by an external transistor or logic chip, the opamp output is disabled. This is an easy way to have a very fast switch off of the current independent of the PID loop. The OPA549 also has an internal thermal monitor which pulls this pin low and disables the current in the case of over heating.

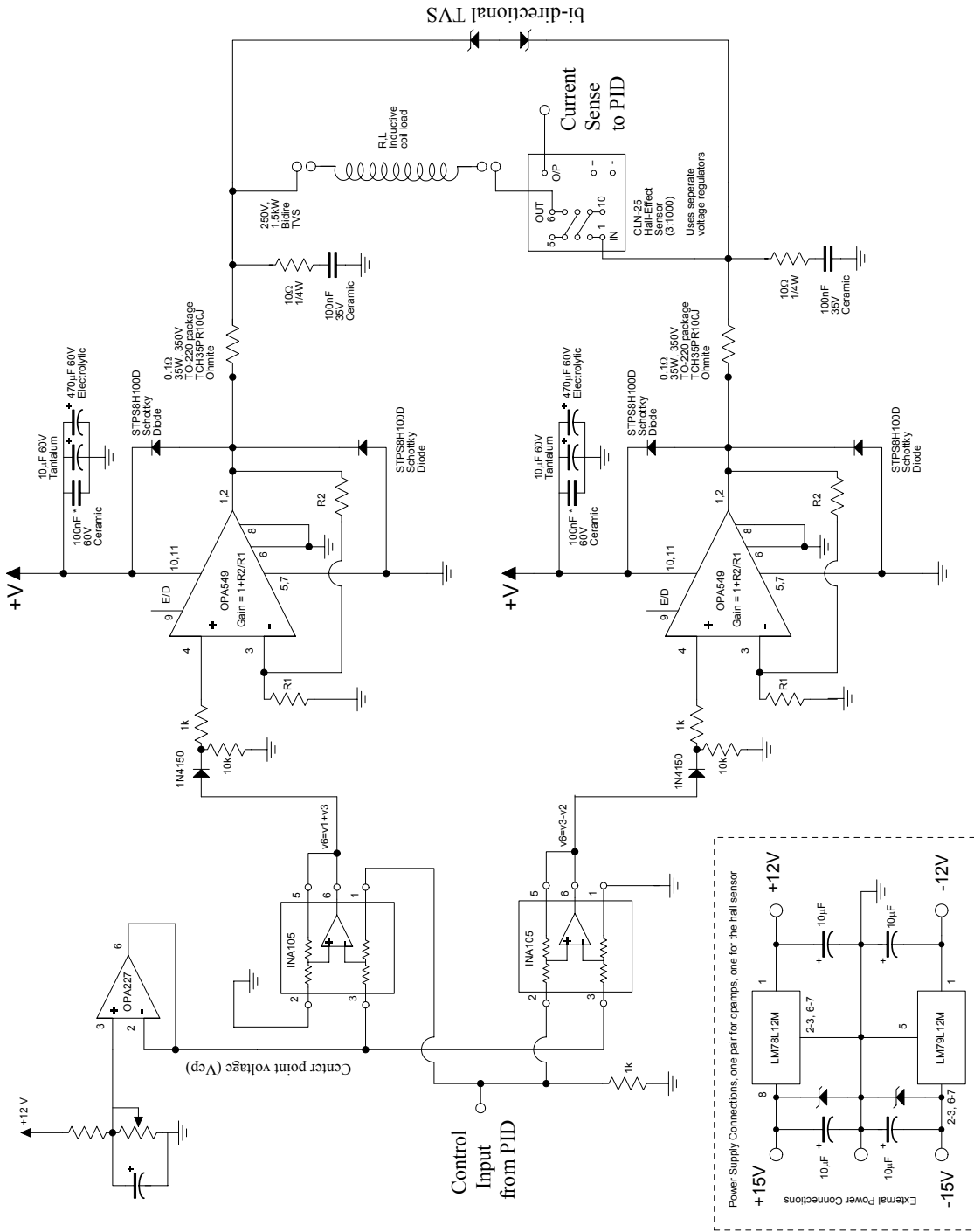


Figure C.4: Bidirectional output stage schematic.

C.5 Main Power Output Stage for QUIC Trap

This circuit is the output stage providing a very stable programmable constant current for the magnetic trap in conjunction with the PID controller. In Figure 3.27 it is labeled ‘Main Constant Current Power Supply.’ The circuit uses the most impressive OPA549 high power opamp from TI. The output stage consists of a master opamp and three slave opamps. The opamps are connected in single supply mode and have some nice features such as internal thermal shutdown against overheating. Pin 9 of each is connected to a small LED circuit on the front of the box indicating all is okay. The circuit also includes appropriate protection diodes and resistors. The ‘QUIC Trap Load’ labeled in the schematic is that which appears in Figure C.6. The components here were all mounted on a printed circuit board, the $0.1\ \Omega$ resistors heat sunk to the board itself and the opamps all attached to a water cooled copper block for cooling. This output stage is quite robust and can handle driving the load of all QUIC Trap configurations without voltage adjustment of the power supply ‘+V’ — TCR series model 605-30-1-D from Lambda EMI. However, during the experimental run, the voltage of the power supply is ramped appropriate to keep the power burnt in the opamps at a minimum. This is also done for historical reasons because the original output stage had stability problems with too great supply voltages.

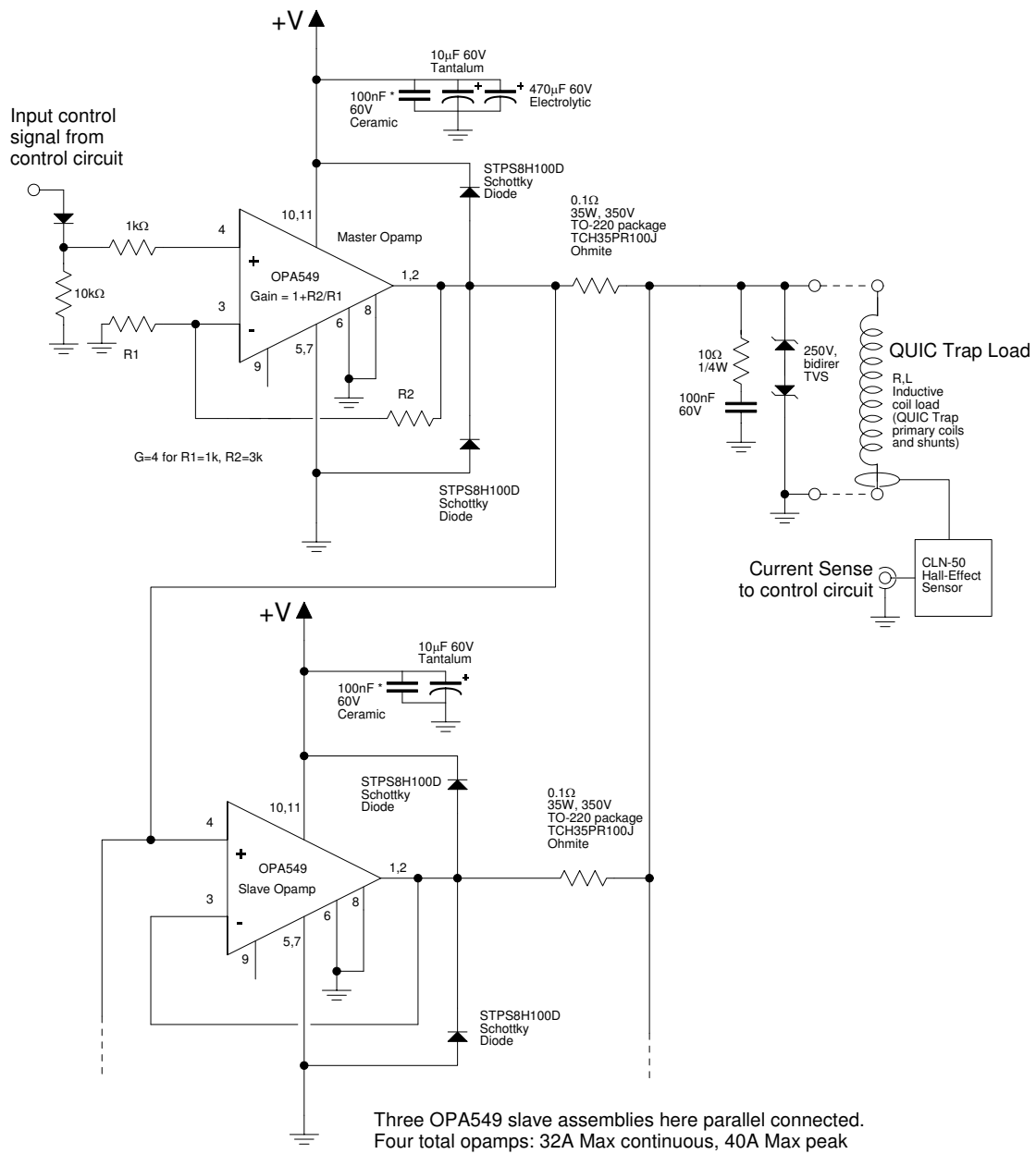


Figure C.5: Main QUIC trap current controller output stage schematic.

C.6 Shunt Power Circuit for QUIC Trap Coils

Figure 3.27 shows a simplified schematic of the operation of the QUIC trap power circuit. In actuality, the shunt current sources are MOSFETs acting as variable resistors which have value ranging from infinite to $R_{\text{ON}} = 1 \text{ m}\Omega$. Therefore, using the shunt current sources alone is not sufficient to have a situation with zero current in the coil — this is the purpose of the quadrupole and Ioffe switches in series with the coils. In that case, the coil in question is totally disconnected and there is zero current. Note that this does produce a very small jump in current as the Ioffe coil is ramped on during the compression of the QUIC trap. Because the atoms are hot at this point, they are insensitive to this. The quadrupole switch is not normally used.

There is a rule about putting current regulators in series: they can't be in series. This is because, despite being *almost* the same current, they will oscillate against each other. This is to say, the main current regulator is the only one that is always operating. Because the shunt regulators are formed with MOSFETs, it is not difficult to take them in and out of a regulation mode. If the computer is programmed to tell the shunt to regulate less than zero amps (*i.e.* negative current) the regulator shuts off and all current goes through the coil. If the computer tells it to regulate greater than what is available, the MOSFET is *wide open* — that is, it has its ON resistance and it will not regulate. In that case and only that case, it is okay to open the coil's switch MOSFET to shut the coil off completely. Without the switch, the coil then gets a current $I_{\text{main}}R_{\text{ON}}/(R_{\text{coil}} + R_{\text{ON}})$, which may or may not

be acceptable in some situation. In the between states, the shunt is free to regulate and the coil gets the ‘reject’ current.

Because of the topology, the power supplies needed for the control circuits of the shunts are required to be floating with the common attached were the label is ‘Local GND.’ The all of the analog singles for the magnetic trap are optocoupled, see Section C.7. The digital lines are also optocoupled. This allows the control electronics to float appropriately and also give protection against voltages spikes that can electrocute the computer or output hardware.

The forward diodes (HFA50PA60C) are needed during sudden switch off to prevent the coils from discharging through the shunts. This would cause a slow exponential slow turn off and also the quadrupole and Ioffe coils would turn off with different rates — kicking the atoms.

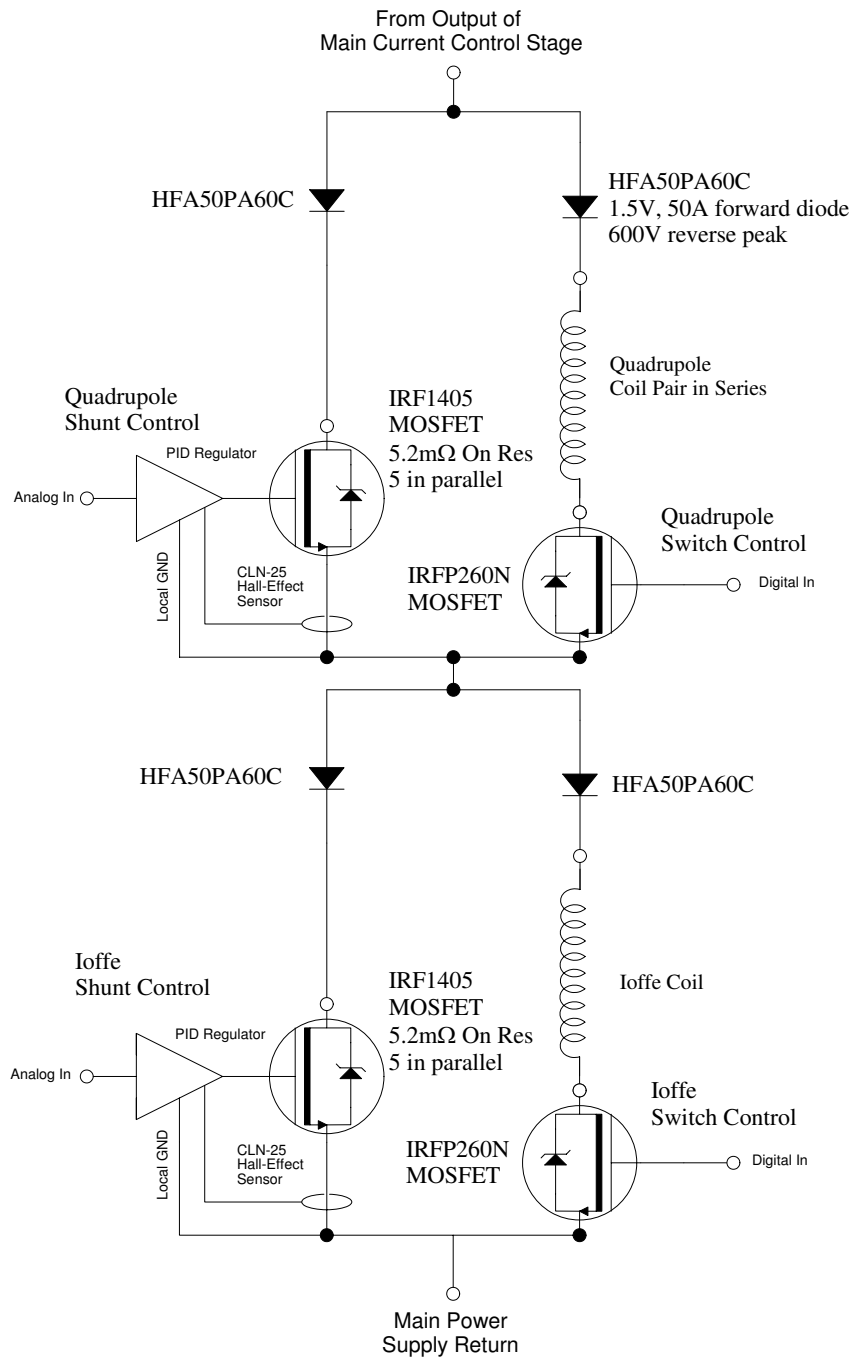


Figure C.6: Shunt power circuit for QUIC trap primary coils.

C.7 Analog Optocouplers

Optocouplers are critical for the operation of the magnetic trap. They also serve as a ground loop removal method for critical precision applications. In this section, we give a simple design for a precision analog optocoupler. A further discussion and PCB layout files are available at Ref. [72]. The circuit here is intended for precision low frequency (under 10 kHz) applications and uses a HCNR201 as the primary optocoupling device. It is based on that shown in Figure 17 of HCNR201 datasheet but includes a few extra options. The circuit given in Fig 17 has a voltage range from 1 mV to over 10 V and has high accuracy and stability. For many applications this is sufficient. However, there is a drawback in that the circuit can not actually pass a 0 V signal, the ≈ 1 mV actually is a limit since the photodiode always must be slightly reverse biased. Even a slowly rising signal below ≈ 1 mV produces a non-adiabatic spike in the output (which the author found out the hard way on a critical application). The various versions of bipolar drivers given on the data sheet suffer from cross-over transition problems when using two optocouplers. Here we use a simple solution so the circuit can be made bipolar and can have 0 V signals without cross-over problems. This is to shift the input-output range down by adding to the input voltage before the optocoupler and then subtracting it back off at the output. This allows one to shift the range by anything between 0 V and 5 V. To have 0 V to 10 V one need only add and subtract a few millivolts, or for -5 V to 5 V add and subtract 5 V. Naturally this does not increase the voltage range of the device which is still 10 V. As

drawn on the schematic, the given voltage dividers give a voltage adjustment range between 0 V and 1.5 V, the voltage dividers may be adjusted for desired range of operation. For the full 0 V to 5 V range, one must only replace R5 and R8 by 0 Ω shorts.

The board layout includes several options which may be disabled when not desired. The table here gives the options and components to be omitted when options are not used. R22 and R23 are optional gain resistors which will generally not be used.

Option to remove	Add Jumper	Omit parts
Input Adder	W1	D1, C19, R5-R7, R11, U1, R23
Output Subtractor	W2	D2, C18, R8-R10, R12, U4, R22
Output Line Driver	W3	R13, U5, U6, R20, C13-C17, R21

The optional output line driver can supply currents of up to 1/4 A. This can be used when the output is supplied to common 50 Ω loads. It includes an output integrator involving R21 and C15, which may be disabled by omitting C15 and replacing R21 by a 0 Ω short. The output integrator can improve output stability when driving some loads, especially reactive loads.

The device provides a linear response with a transfer slope near unity which is partially limited by the matching of R1 and R2+R3. It is advisable to use high quality resistors. If trimming is not desired, one may omit R3 and short the pads with a 0 Ω resistor and use a precision pair for R1 and R2.

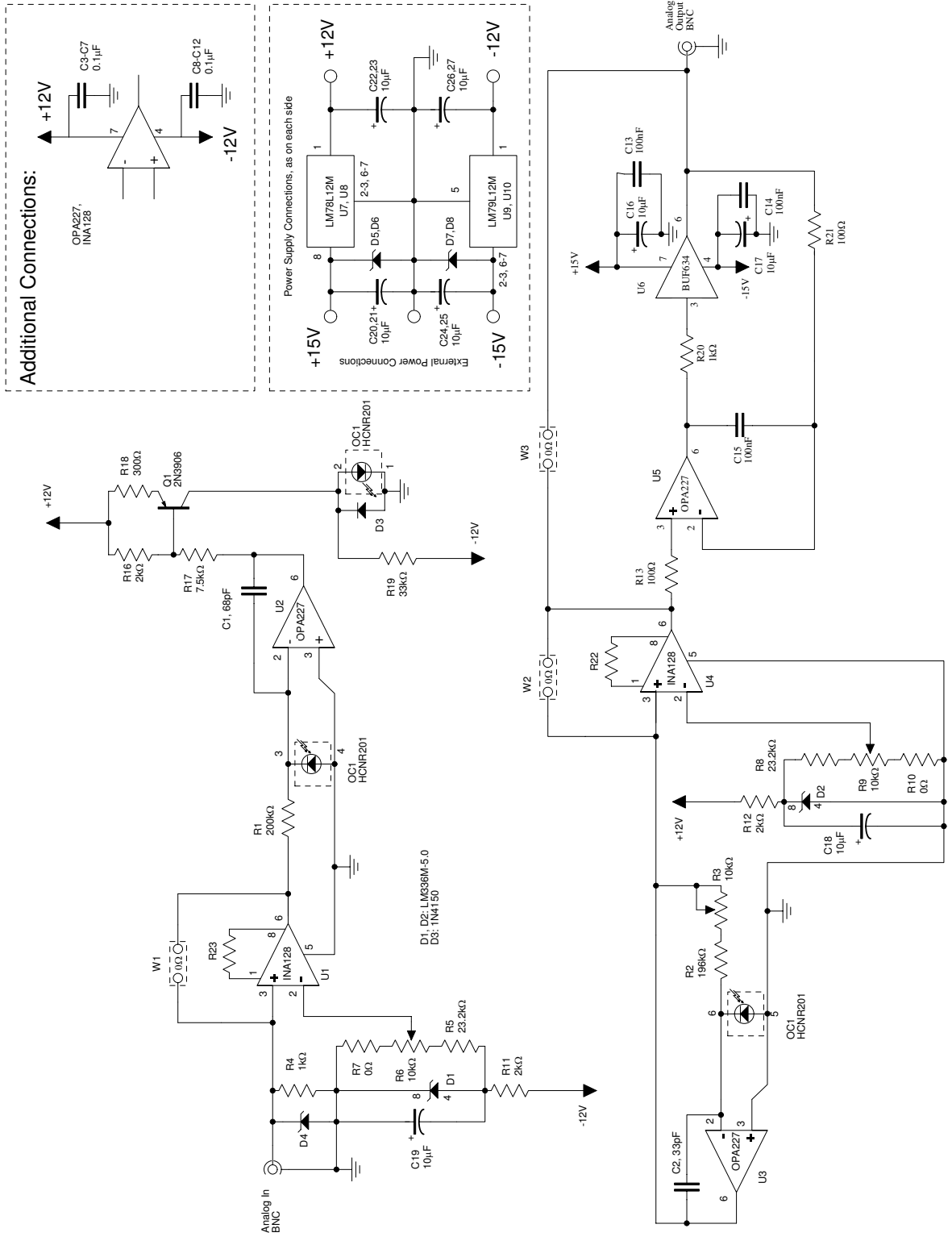


Figure C.7: Analog optocoupler schematic.

Appendix D

Computer Control System Hardware

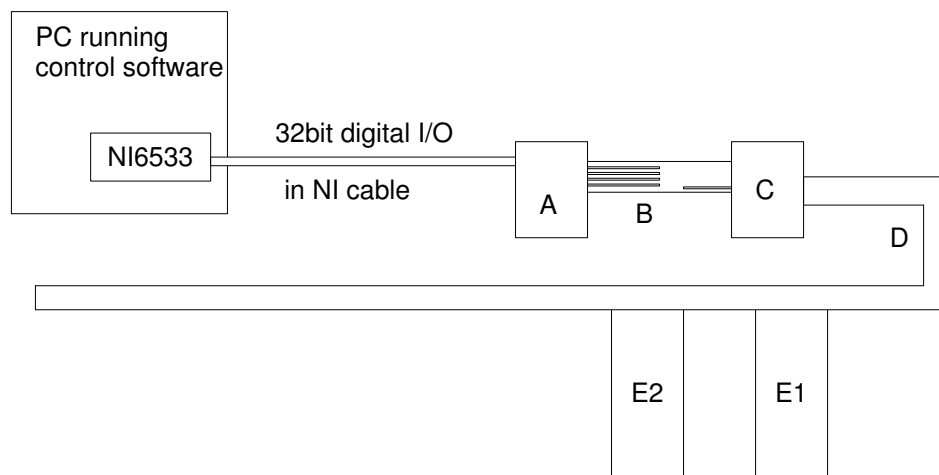
In this appendix we present the hardware of our home-built computer control system. The system concept is based on a parallel 16-bit bidirectional data bus, parallel 8-bit address bus, and strobe signal. This represents a particularly simple to understand and flexible system that is suited for a wide range of experimental control. A complete description of this system along with hardware schematics and PCB layouts are available on our website, see Ref. [28].

D.1 Digital Bus System

D.1.1 Overview

Nothing here is specific to atom physics, many experimental systems could benefit from a control system such as this one. Although these concepts are well known in the hardware community and everything here represents old technology, but much has been unknown to the experimental atom physics community. Our implementation may be considered a brute-force method where most devices used can largely be considered unintegrated where they are very flexible and appropriate for use as laboratory electronics. The sim-

plidity of the parallel bus allows easy interfacing with many devices including Digital-to-Analog Converter (DAC), Analog-to-Digital Converter (ADC), Direct Digital Synthesis (DDS), microprocessors, etc. Another important aspect of this method is simplicity of construction in that the hardware is available from many electronics distributors and can be fabricated in a few weeks by undergraduates or graduate students.



A: NI cable to flat ribbon cable converter board

B: 4x 8 bit to 1x25 bit + 1x7 bit converter flat ribbon cable

NI = National Instruments

Remark: the NI6533 cards and parts A,B can be exchanged eg. with the USB port and a USB to parallel converter

C: bus transceivers and strobe pulse generator board

D: 25 bit flat ribbon bus cable

Ex: digital or analog output PCB

Figure D.1: General layout of the control system.

Figure D.1 gives an overview of the system we are using. This setup

involves a National Instruments board, however, see below for other implementation ideas. The elements of Figure D.1 are as follows:

- Part A: The National instruments card requires a special cable using a peculiar hardware connector. The order of the signal lines are awkward on this cable. Adapter board A sorts the signals out and distributes them to four 8 bit flat ribbon connectors.
- Part B: Cable B has to be constructed combining those four 8 bit flat ribbon cables in one 25 bit and one 7 bit flat ribbon cable. The bit order of this cable is the obvious one, port A,B,C, and bit 0 of port D go to the 50 pin header (see below) and bits 1 to 7 of port D go to the 7pin header. Signal and ground lines alternate in the flat ribbon cables. The headers must be crimped in the correct orientation on the cable so that bit zero of port A goes to bit 0 of the 25 bit bus and so forth. We used a 50 line flat ribbon cable and an additional 14 line cable next to it.
- Part C is the strobe bit generator and transceiver board. It buffers the NI6533 card signals in addition to producing a time shortened strobe bit signal. The schematic is given in Figure D.4.
- Part D is the bus system 50 line flat ribbon cable. The pin configuration compatible with our output devices is given below. It is suggested that an additional buffer board be used if the ribbon cable is to travel a long distance.

- Part E1: 16-bit devices.

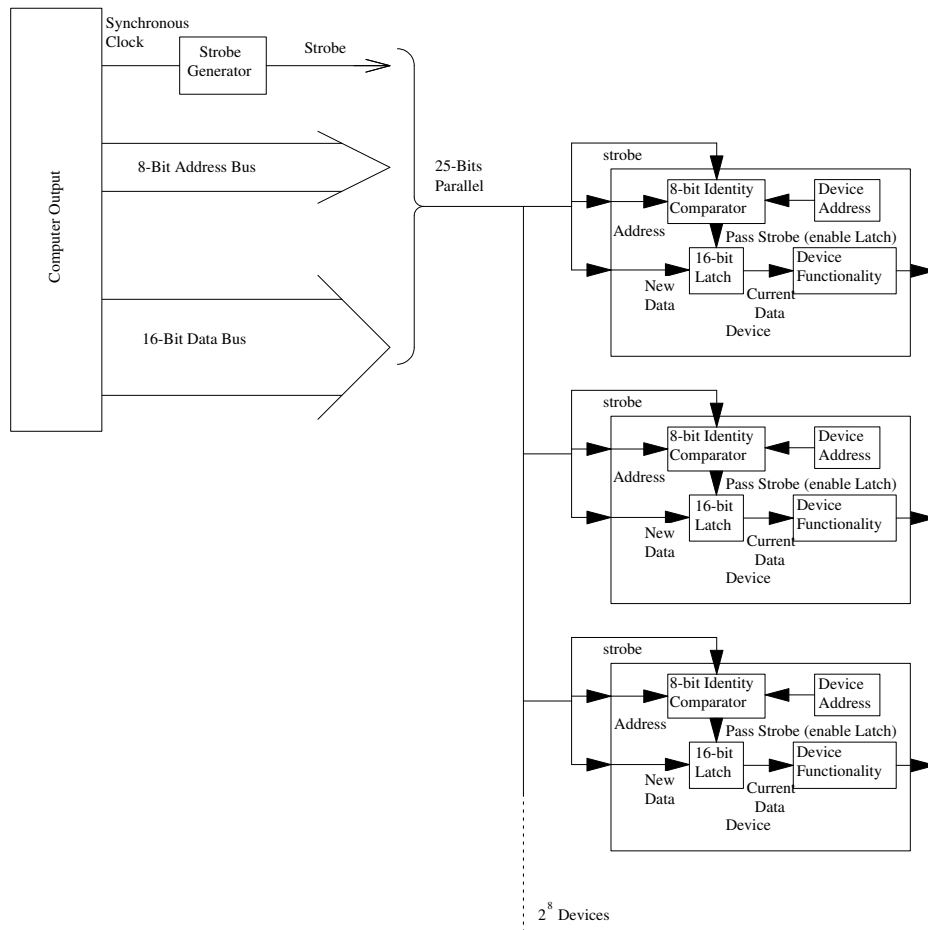


Figure D.2: Output Concept. Each 16-bit device has its own 8-bit address which typically may be set locally with DIP switches. All devices receive all 25 bits on each clock cycle, but only the device with matching address accepts the strobe bit which commands it to take the new data.

D.1.2 Concept

The concept of the system is illustrated in Figure D.2. The system consists of a 16-bit data bus, an 8-bit address bus, and a clock. The clock is converted into a strobe signal. The strobe commands the device to update its data, see next section. All 25 bits are sent to all devices but only one accepts the data. Each device has a local 8-bit address which is set on the Printed Circuit Board (PCB) of that device with DIP switches. Only when the input 8-bit address bus matches does the device accept the strobe signal. With this system, one may add up to 2^8 devices onto the bus, one of which is accessed each clock cycle.

The data bus, in fact, may be bidirectional which allows for input data as well. Our buffer/strobe generator board includes transceiver buffers which can operate bidirectionally. This requires an additional bit in the bus which talks to this board and chooses the data bus direction. In this case, it is the responsibility of the computer to address the appropriate input device. As of this writing, we have not implemented the use of this input option, but it is in principle a simple addition.

D.1.3 Why a Strobe?

The strobe serves two purposes: increase data rate and signal error protection. Firstly, the data loading implementation in a similar system is typically accomplished in three clock cycles: data input, strobe on, strobe off. This can be improved by using a time shortened pulse for the strobe rather

than full clock cycles. The strobe pulse occurs in the center of each clock period and has no dependence on clock state, only state change.

D.1.4 Flat Ribbon Connection Diagram

We adopted this pin standard for our devices connected to this bus system, all layouts given on the web site [28] use this standard.

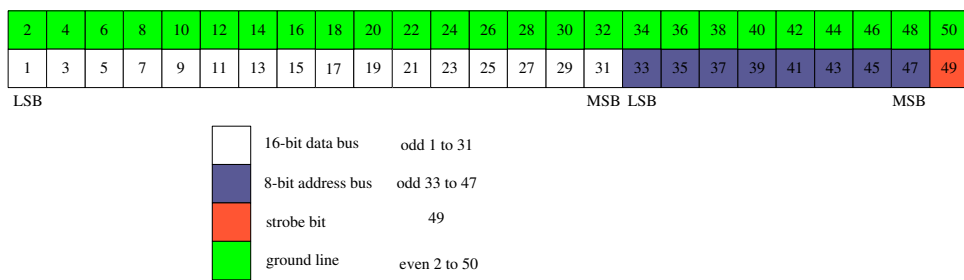
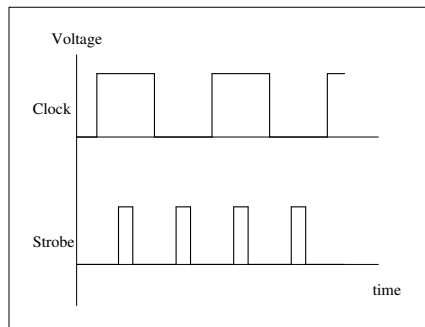
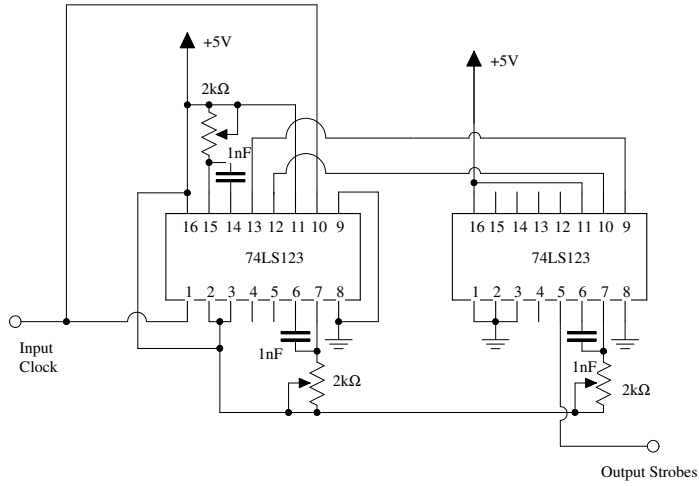


Figure D.3: Pin configuration for 50-pin connector.



Triple Data Rate Strobe

Figure D.4: Strobe Generator. Note, that the strobe bit can be high or low active (switching output pins 12 to 5). In this design, we have chosen it to be high because that is the logic used on our digital output board designs. Please note in the case of the analog output board, that the active strobe may be chosen to be high or low. Which is to say, for using this strobe generator design, the analog output boards must always have the DIP switch set to properly accept a high strobe.

D.1.5 Computer Output

How the computer actually generates the needed bus bits is flexible. The method we currently use involves a N16533 from National Instruments. This device gives an synchronous 32-bit parallel bus and clock signal which we have typically run between 500 kHz and 750 kHz. Such a fancy device is not totally needed (we used it because we had it). The computer outputs can be produced synchronously using other methods, a few of which we will suggest here in words. One method that could be used is the computer's built-in parallel printer port. This port has an 8-bit parallel I/O and various handshaking bits. In this case, the clock would be put external to the computer along with an 8-bit output FIFO, 24 or 32-bits worth of latches (74LS573) and a few logic chips. The basic idea is to put the asynchronous computer output of the parallel port into the FIFO which is synchronously triggered by the local clock and multiplexed to 24 or 32 bits and latched. The FIFO is First In First Out and consists of a triggered buffer, there are bunches of single chip FIFOs available. There are also available parallel output board available which run from USB 1.1, USB 2.0, or Firewire. The latter two being very fast. These may have the advantage over the NI cards of being less expensive and more portable.

D.2 Digital Output Boards

Here, we present the design of a 16 channel buffered digital output (schematic in Figure D.6) for use with the bus system described previously.

Full information along with the PCB layout is available on the web, see Ref. [28].

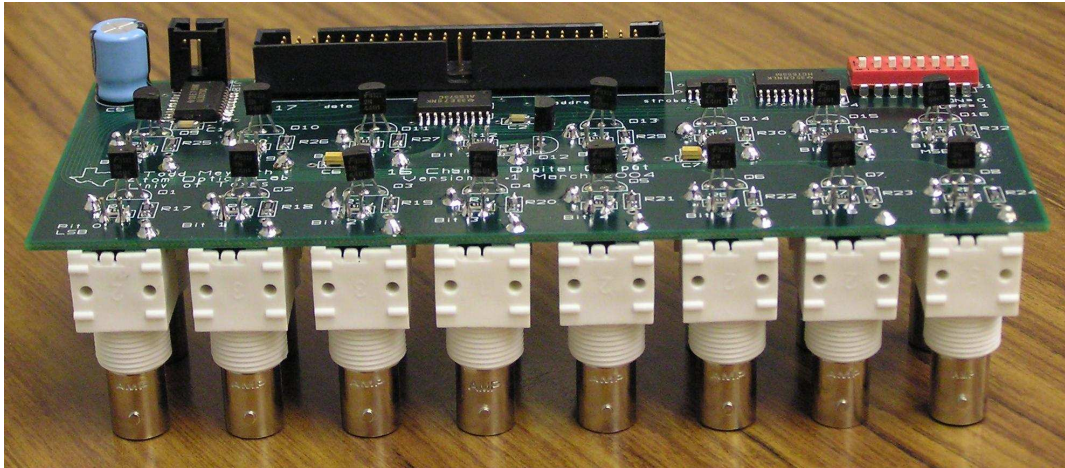


Figure D.5: Photo of PCB for Digital Outputs.

D.2.1 Features

The basic features are as follows:

- Each channel is a single bit of output of a 16-bit device
- Addressable on a simple bus system.
- Each channel has line drive capacity to drive $50\ \Omega$ loads
- Convenient setup for laboratory electronics with BNC outputs

The circuit is relatively simple to understand from the schematic and is competitive with professional output boards such as those produced by

National Instruments. The cost per board is roughly \$65 (\$40 for the board, \$5 for the ICs, transistors, and passives, \$20 for the BNC receptacles).

D.2.2 The Printed Circuit Board

The PCB is a four layer board with signal lines on the top and the bottom. The second to the top layer is the location of the ground plane the third from the top is the power plane (+5 V). All ICs are located on the top as well power connector and ribbon cable connector. The vertical BNC receptacles are located on the bottom, making the board simple to front panel mount. The PCB was designed using the free software from PCB123, this company produced our circuit boards. For the design presented here, the PCB cost was about \$400 for 10 boards including silk layer charges. The software and information is available at the web site *www.pcb123.com*. The design of the board is shown in the printout pages near the end of this document and the design file is available at the author's website.

D.2.3 Circuit Theory

This circuit is simple to understand. The input consists of a 50 pin input header for a 50 conductor ribbon cable. The signals are spaced with ground lines between them giving 25 digital signals. The first 16 are the data bit lines, the next 8 are the address bus lines, and the final line is the strobe bit. The logic circuit works as follows. The strobe signal enters the comparator and is sent out if the local address matches. In this case, the strobe passes

the comparator to command the latches to accept and hold the new 16 bits of data. Note that, for the DIP switches, the ON position indicates a LOW and the OFF position indicates a HIGH as far as the board address is concerned. The function of the latch is to have memory. The each latch holds old data in a buffer until it is commanded by the comparator's strobe to accept new data. Here, the new data is held until the next command to this board. All 16 digital outputs may be updated each clock cycle. The transistor line driver circuit is also a standard $50\ \Omega$ cable driver¹

¹see Figure 9.42 pg. 612 *The Art of Electronics 2nd Ed.* Horowitz and Hill. Cambridge Univ. Press 1989.

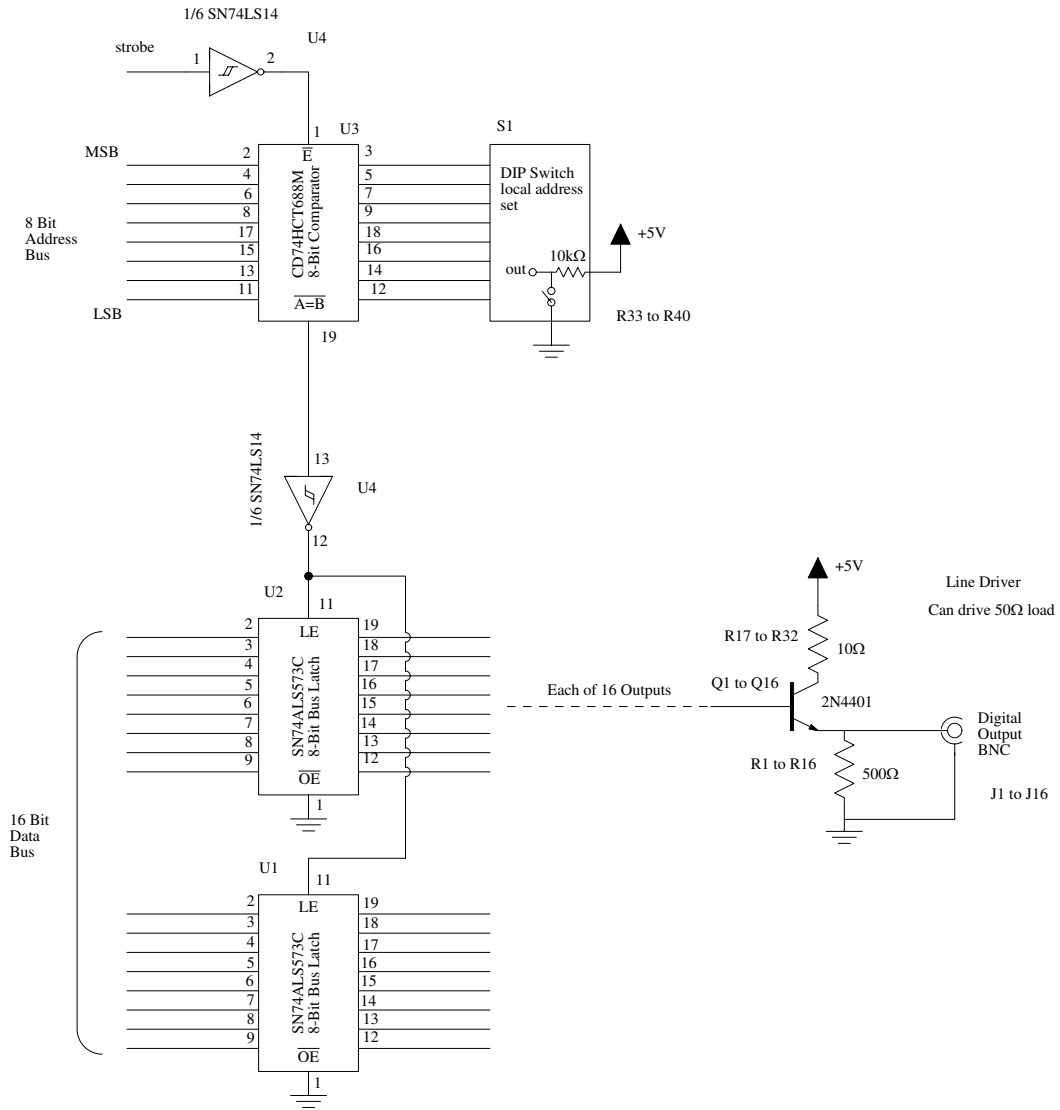


Figure D.6: Digital Outputs Schematic. This design is used for digital outputs from the bus system.

D.3 Analog Output Boards

Here, we present the design of an octal 16-bit Digital-to-Analog Converter (DAC) based on the DAC7744 from Texas Instruments, the schematic is shown in Figures D.8 and D.9. The device here is general purpose and may be easily controlled by a variety of systems involving a simple parallel bus. Each board gives eight buffered outputs. Our experiment uses 64 analog outputs at present — this capacity is tremendously useful for laboratory experiments. Full information along with the PCB layout is available on the web, see Ref. [28].

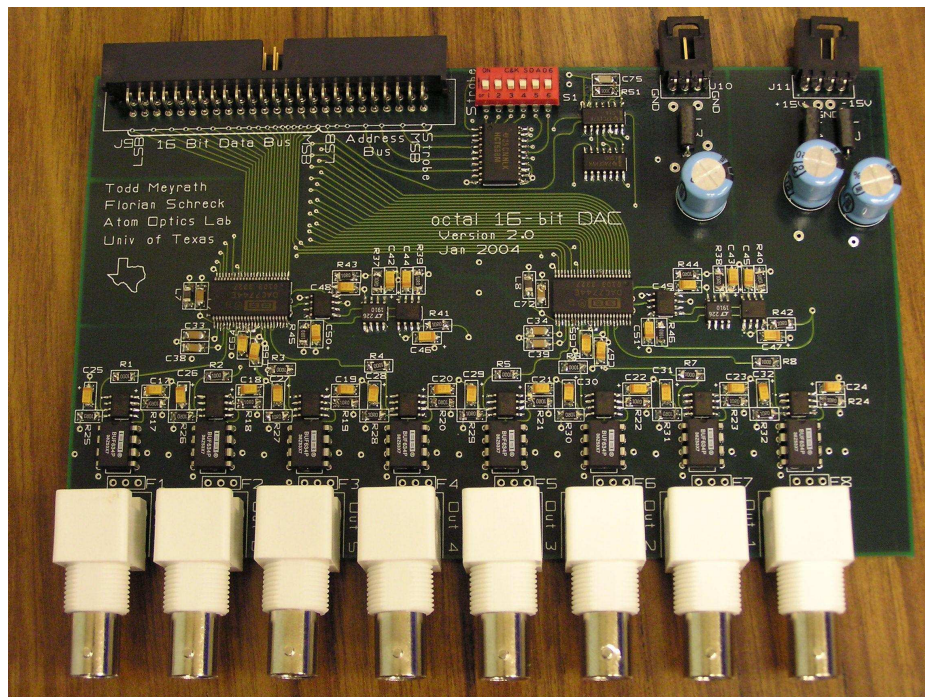


Figure D.7: A completed board, lacking only heat sinks glued onto the BUF chips.

D.3.1 Features

Each Channel features the following:

- 16-Bit accuracy
- $\pm 10\text{V}$ scale, reference drift 3ppm/C, easy to change to $\pm 5\text{V}$ by using different values of the LT1019 reference series.
- Buffered BNC outputs for $50\ \Omega$ loads, 250 mA max per channel

D.3.2 Advantages and Disadvantages

The circuit is relatively simple to understand from the schematic and is competitive with professional output boards such as those produced by National Instruments. A principle disadvantage of this design is cross talk. As opposed to a design with 8 totally independent DACs and voltage references, this design uses the DAC7744 quad DAC sharing voltage references among the four outputs. This may produce (non-DC) cross talk of order the least significant bit between the four channels when sweeping. The circuit has several advantages: firstly, it is inexpensive in comparison to National Instruments boards (order \$1500). This circuit costs about \$200 (\$50 per PCB when buying 10, \$45 per DAC IC (2), plus output buffers, opamps, capacitors, logic circuits) and the fun of building it yourself! A second advantage is the simple control bus as described in the previous section which allows us to stack our experiment with nearly limitless outputs — a capacity never to be underestimated for a project of this complexity. The circuit is in convenient form

for laboratory electronics with BNC outputs which are buffered to drive the common $50\ \Omega$ loads. The board may be easily panel mounted in an enclosure using the BNC receptacles. Such output stages are not available straight from the various (National Instruments) PCI boards and therefore must be externally added (at great expense) – which requires a similar amount of labor to construct as these designs. The generality of the bus system to run these boards is a major advantage in terms of extendibility, whereas PCI (or PXI) type analog boards have the major constraint of limited PCI slots.

The limit on the speed here is the settling time of the DAC which is specified to be 0.003% in $10\ \mu\text{s}$, giving a not-as-settled output for our clock rate. In principle, if this is tolerable, the update time can be sub- μs . There is also a limitation introduced by the lack of impedance matching on the board's digital inputs, however this should not be a problem until far beyond reasonable update times for these DACs. Should the bus system be run at a much higher frequency in any case, an impedance matched buffer board may become necessary near the digital inputs to the DAC board.

D.3.3 Outputs

Output BNCs are labeled J1 to J8 left to right on the front panel. Their addresses are given in the following table, where X's are settable for board select. Address bits are referred to as bits 0 to 7 and bit 8 is strobe.

Board Version 2		
Address	Output Conn.	Label
XXXXX 111	J1	Out 7
XXXXX 110	J2	Out 6
XXXXX 101	J3	Out 5
XXXXX 100	J4	Out 4
XXXXX 011	J5	Out 3
XXXXX 010	J6	Out 2
XXXXX 001	J7	Out 1
XXXXX 000	J8	Out 0
The value of the label is the amount to add to the base address XXXXX000.		

D.3.4 The Printed Circuit Board

The PCB is a four layer board with signal lines on the top and the bottom. The second to the top layer is the location of the two ground planes (one analog and one digital) and the third from the top is the three power planes (+5 V and ± 15 V). All ICs are located on the top as well as most passives. There are also various small items on the bottom. The PCB was designed using the free software from PCB123, this company produced our circuit boards. For the design presented here, the PCB cost was \$512 for 10 boards including silk layer charges. The software and information is available at the web site *www.pcb123.com*. The design file is available at the web site.

D.3.5 Circuit Theory

The DAC concept is explained on the DAC7744 data sheet available from Texas Instruments and there is no need to discuss it here. Here we discuss the basic idea of the digital and analog circuits on the board.

Digital Circuit:

The input to the digital side consists of a 50 pin input header for a 50 conductor ribbon cable. The signals are spaced with ground lines between them giving 25 digital signals. The first 16 are the data bit lines, the next 8 are the address bus lines (as discussed above), and the final line is the strobe bit. The logic circuit works as follows. The strobe signal enters the comparator and is sent out if the local address matches. The logic gates after the comparator insure that only one of the DACs receives the chip select (CS) signal to load the new data bits into its memory latch. Address bit 2 chooses the DAC IC and bits 0 and 1 choose the channel on that DAC. After the new data is loaded, the “load DAC” signal moves the data from memory onto the analog output and holds. The load DAC signal is also the strobe bit signal but with a delay line. Note that, for the DIP switches, the ON position indicates a LOW and the OFF position indicates a HIGH as far as the board address is concerned.

Analog Circuit:

The analog circuit consists of the voltage references and the output buffers. The voltage reference used is the LT1019 from Linear Tech. in the SOIC pkg. We used the 10 V version but it also comes in a 5 V version which may be used with no circuit modification. The other (2.5 V and 4.5 V) may not be used in this circuit without board modification because the DAC requires ± 15 V and these lower voltage references can not operate with such supplies. The negative reference is produced with the INA105 in unity inverting mode

and has similar stability as the reference itself. The reference inputs use the options given in the DAC7744 data sheet for buffered reference inputs involving the opamp and filter circuit.

The output buffers consist of a precision opamp OPA227 and a buffer line driver BUF634. The buffer boosts the current output of the opamp. The output buffer is able to drive as much as 1/4 Amp, such as required if a $50\ \Omega$ load is used.

The input filter involving a $10\ \Omega$ resistor and $10\ \mu\text{F}$ capacitor on most of the analog ICs is to provide power supply isolation for each chip. This is especially important due to the high current nature of the buffer ICs running on the same power supply.

Ground plane comments:

The ground planes (analog and digital) are entirely separate. The power supply grounds do need to be connected at some location however — but not at two. There is a location for an optional ground plane connection on the back of the board. We connected the power supply grounds near the power supplies and operate them for multiple boards. One should be careful in not forming ground loops. If it is decided to connect the ground planes, one may use a ferrite bead rather than a short. If the power supplies share a ground far from the board – if not this forms a ground loop antenna for RF, but the ferrite has an impedance for such frequencies and should prevent this. We used a ferrite similar to that of the digital IC power supply bypass to connect

the planes.

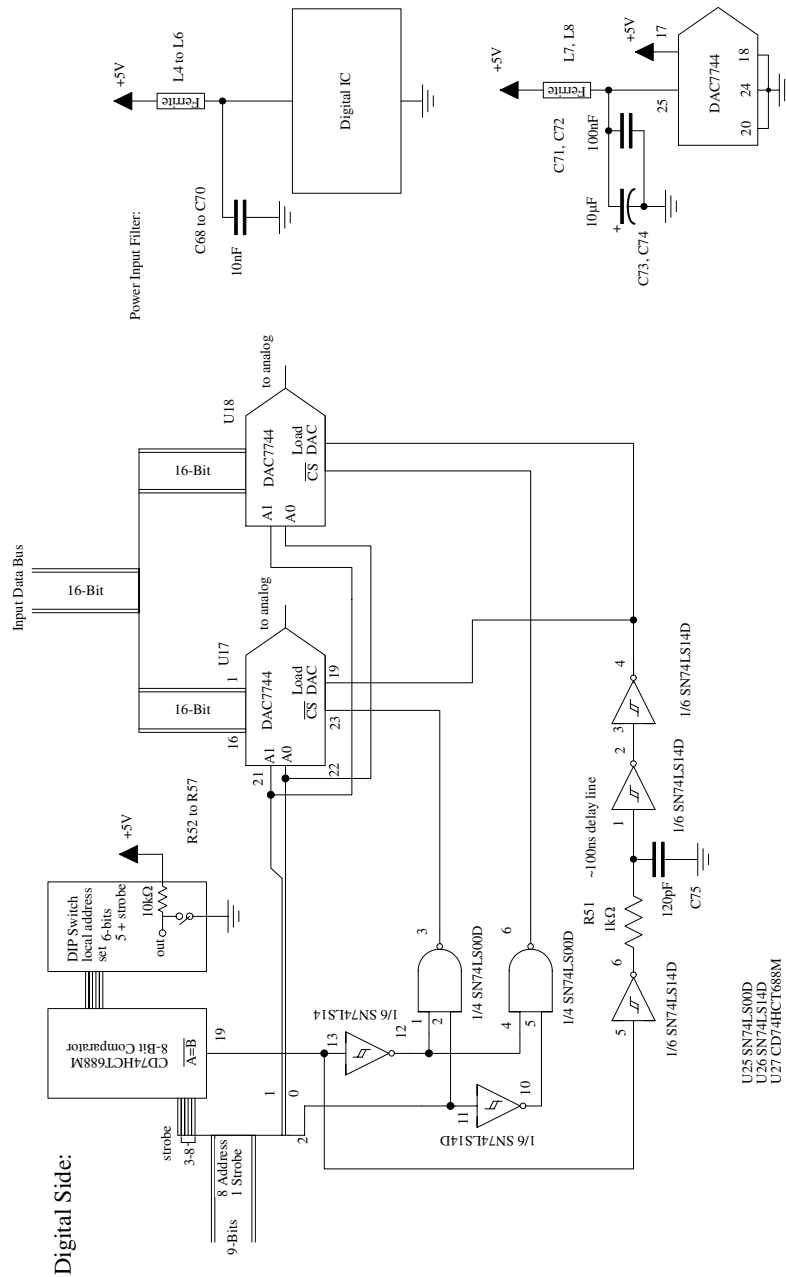


Figure D.8: DAC schematic, digital side. This section of the circuit interfaces with the digital bus to accept signals from the computer. Analog side shown in Figure D.9.

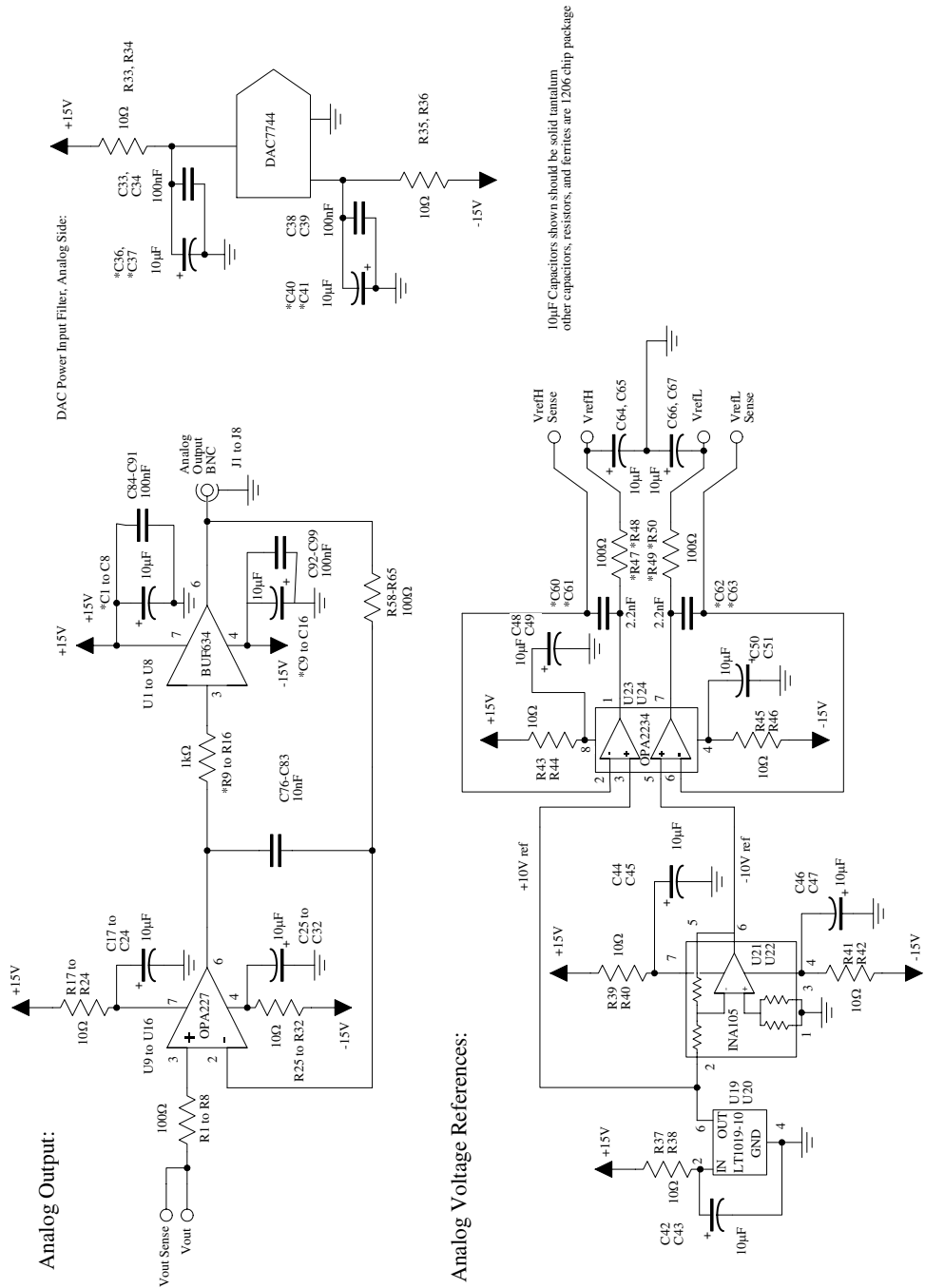


Figure D.9: DAC schematic, digital side. This section gives the output line drivers for the analog side and shows the analog voltage references. The digital side is shown in Figure D.8.

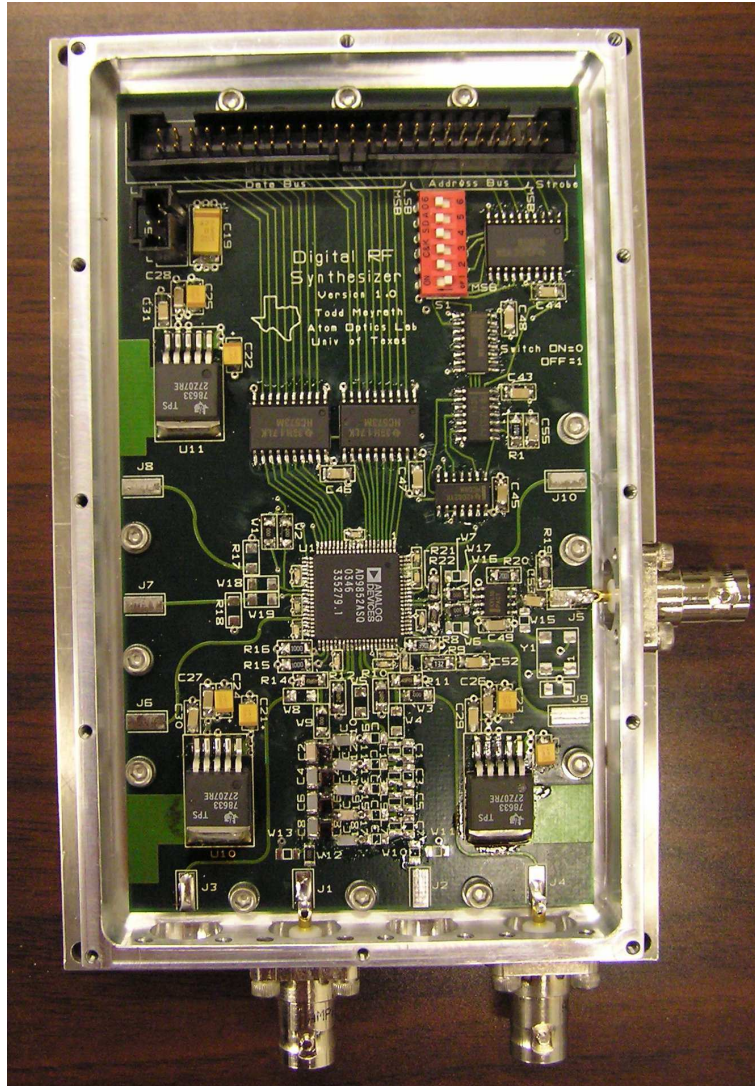


Figure D.10: Digital Radio Frequency Synthesizer. This board uses the filter option for the RF output and the unfiltered for the control DAC output.

D.4 Digital Radio Frequency Synthesizer

Here, we give a design for a Direct Digital Synthesis (DDS) device to produce Radio Frequency (RF) signals between DC and 135 MHz. The design centers around an AD9852 from Analog Devices (but will also accommodate an AD9854). This design is partially based on that of the evaluation board available from Analog Devices but contains circuits relevant to our laboratory electronics implementation and control system and a redesigned output filter. The digital interface is designed to be compatible with our digital output bus system. The most recent version is available on our website [28]. The digital interface given in this design is relatively simple and can be interfaced with a microprocessor or with the system described in Section D.

D.4.1 Digital Side

The digital inputs consist of a 24-bit bus and a strobe bit. The first 16-bits we identify as the data bus and the next 8 as the address bus.

This address bus is intended to address many boards, each with a local address set by DIP switches. In the case of this DDS device, the 16-bit ‘data bus’ is broken up into various parts as discussed below. The address bus uses the first 2 bits (first 4 addresses) to determine the strobe function on the board. The higher 6-bits of the address bus are the board select. If they do not match the address set by the DIP switches then the strobe is rejected and the board does not accept the data. Only when this address matches does the strobe bit cause the 16-bit data bus to be latched.

8-bit address bus			
A1	A0	Option number	Strobe bit function
0	0	Option 0	Latch 16-bit data bus, Master Reset
0	1	Option 1	Latch 16-bit data bus, Load data into DDS buffer
1	0	Option 2	Latch 16-bit data bus, Update output register
1	1	Option 3	Latch 16-bit data bus only

A7 to A2 must match DIP switch settings.
DIP switches: ON=0 OFF=1.

Generally, Option 0, for the master reset is called after power-up of the device.

D.4.2 Programming the DDS

Programming the DDS generally requires several loads of data. The 16-bit data bus is broken up by function as in the table here:

16-bit data bus	
D0 (LSB) to D5	Programming register address in DDS
D6	FSK/BPSK/Hold functions
D7	Shaped Keying function
D8 to D15 (MSB)	8-bit data for referenced programming register

Programming generally consists of multiple loads of data D0 to D5 and D8 to D15 in parallel using address Option 1 to load the DDS registers in the desired locations with the desired values. Then Option 2 is used for an update of the output register in which the DDS uses the previous loaded values to determine the new output characteristics. In the case of Option 2, the D values are unimportant. This is just sending the strobe to the update output. D6 and D7 are used for the named functions above with the address Option 3 or are instead triggered by the external BNC option, see below.

With D0 to D5 as a 6-bit register address location in the DDS, there are 64 memory locations in the DDS (all of which are not used), each 8-bit wide, which may be updated with the Option 1 load method. The address meanings are given in Table IV on page 26 of the AD9852 data sheet. Information on the modes of operation of the device is also given on the data sheet, see pages 15 to 26 for a description. We do not reproduce this information here. Just as a summary, this very impressive device can operate in the following modes: Single-tone, Frequency Shift Keying (FSK), Ramped FSK, Frequency Chirp, and Binary Phase Shift Keying (BPSK).

D.4.3 Clock Options

The internal PLL clock multiplier of the DDS may be set to any integer between 4 and 20 or not used. This design is intended to run at the maximum frequency of the DDS of 300 MHz. The clock for the DDS can be setup in one of 3 ways. One is to use a crystal (Y1) on the PCB, the clock multiplier must be used and set to $\times 6$ in the case that the 50 MHz crystal suggested on the parts list is used, also, C53 and R19 should be omitted and W15 included, see below. The second option is to use a single ended external clock which enters on the BNC J5, in this case W15 is not used. In this case, the input clock is converted to a differential ECL type by U8. The third option is to use a differential ECL type clock input with BNCs J9 and J10.

D.4.4 Analog Side

Aside from the output options (see below), the analog side consists principally of a pair of filters. The AD9852 has two high speed outputs. Output 1 is the RF (cosine) output and Output 2 is an arbitrary ‘control’ DAC. The AD9854 which is pin-for-pin compatible has a quadrature RF for Output 2. The filter in this design is a 9th Order 135 MHz Low Pass Elliptic Filter. Which gives a very fast drop off after 135 MHz, below 60 dB stopband begins just above 150 MHz which is the Nyquist frequency. The conceptual schematic is shown in Figure D.11 and the frequency transfer function in Figure D.12.

D.4.5 Output Options

The output BNCs are J1 to J4 and J6. The ‘normal’ output setup is labeled (1a) and (1b) in the jumper table below. In this case the two RF (cosine and control) outputs are pass the filters and exit through J1 and J2. Another possibility is to obtain a filtered differential pair for the cosine output on J1 and J2, this is labelled 2 on the jumper table. This also has a special case which can use the DDS’s internal comparator to produce an agile digital clock output (J6). And naturally, there is an option for an unfiltered output, whereas the user may add a different filter after the output of the device for desired results.

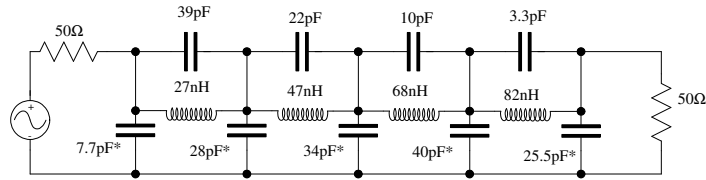


Figure D.11: 9th Order 135 MHz Low Pass Elliptic Filter. This filter gives a very fast drop off after 135 MHz, below 60 dB stopband begins just above 150 MHz. Resonances occur for the LC modes at 155.1 MHz, 156.5 MHz, 193.0 MHz, and 306.0 MHz. The starred capacitors to the ground include estimated stray capacitance due to board layout of 2.1 pF, 1 pF, 1 pF, 1 pF, and 3.5 pF left to right, respectively. These values were estimated from pad area at the nodes. Errors in these capacitances principally affect ripple in both the pass band and stop band. Note that the capacitor values given on the circuit diagram at the end are those of the 1206 chip capacitors which are to be attached to the PCB and are all of standard available values. The chip capacitors and inductors also have some small error, generally order 5% or less which can have an effect on the filter transfer characteristics. The inductors used (see parts list) all have a tiny stray capacitance (order 0.3 pF) which adds to that of its parallel capacitor. The theoretical transfer function is plotted in Figure D.12.

D.4.6 FSK, BPSK, Hold, Shaped Keying Options

The AD9852 device has a number of extra options for various modulation methods. These are described in detail on the datasheet. This design has the options of having these triggered on the programming bus (slower) or externally (faster). The necessary jumpers are discussed in the table below.

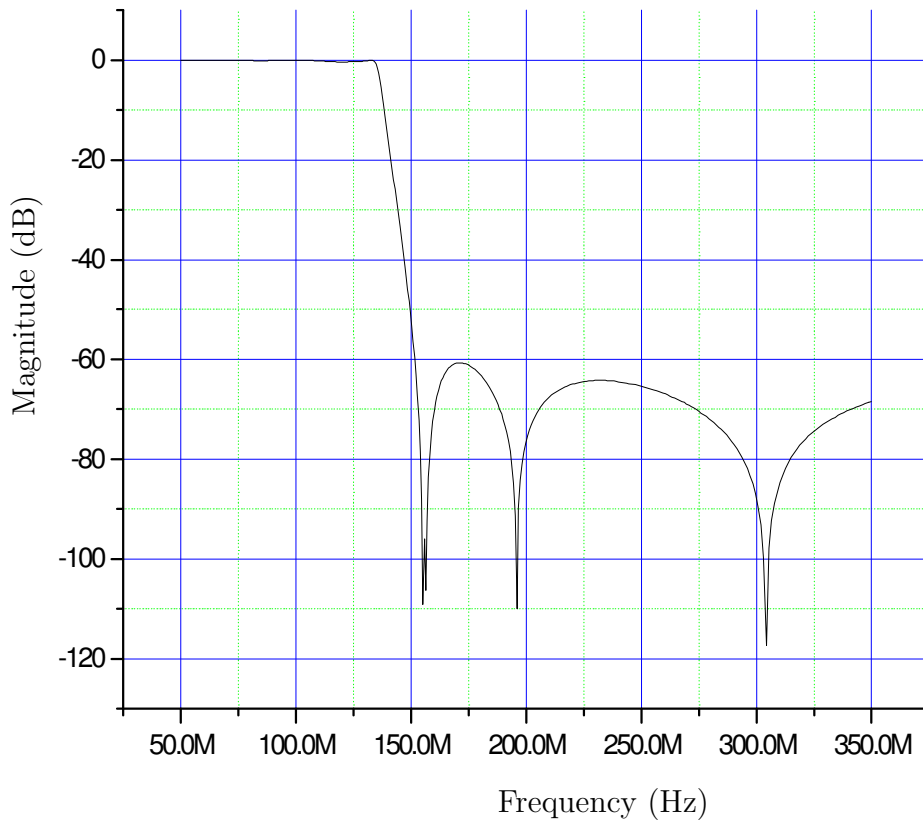


Figure D.12: Filter Transfer Function. Theoretical — SPICE plot.

D.4.7 Jumper Options

There are a number of options that may be enabled or disabled by soldering on jumpers labeled *W* on the schematic and the board. These jumpers are actually $0\ \Omega$ resistors in a 1206 surface mount package.

Option	Jumpers to connect	Jumpers to omit	Other components
Clocks: W6, W7, W15, W16, W17			
(1) Crystal - Y1	W15, W16, W17	W6, W7	omit C53 and R19
(2) Single ended input - J5	W16, W17	W15, W6, W7	
(3) Differential input - J9, J10	W6, W7	W16, W17	
Outputs: W3-W5, W8-W13			
(1a) Filtered RF 1 - J2 single ended	W9, W12	W8, W5, W13	R12 should be 25 Ω
(1b) Filtered RF 2 - J1 single ended	W4, W10	W3, W5, W11	
(2) Filtered RF 1 - J1, J2 differential	W5, W9, W10, W12	W3, W4, W8, W11, W13	R12 should be 50 Ω
(3a) Unfiltered RF 1 - J4	W8	W9, W12, W13	R12 should be 25 Ω
(3b) Unfiltered RF 2 - J3	W3	W4, W5, W10, W11	
(4) Comparator Output - J6	W5, W9, W11, W13	W3, W4, W8, W10, W12	R12 should be 50 Ω
FSK/BPSK/HOLD Input: W2, W18			
(1) From control bus - D6	W2	W18	
(2) External - J8	W18	W2	
Shaped Keying Input: W1, W19			
(1) From control bus - D7	W1	W19	
(2) External - J7	W19	W1	

D.4.8 Comments and Improvement Possibilities

Comment on digital side speed: Although the DDS device digital side may be updated at rate of order 100 MHz, the HC type devices used on the digital side limit the speed to about a quarter of this. However, before this limit, one may find a limit with the ribbon connector and layout. Typically, we operate much slower (order 500 kHz). For some options, such as the FSK, BPSK, Hold, and Shaped Keying functions, there is an available BNC to directly drive these functions with an external source at full speed. For very high speed operation, a slightly modified design involving a high speed FIFO

memory located right next to the DDS might be appropriate for a next generation device. TI and Cypress Semi. have many such appropriate memory ICs. In the case of operating at higher frequencies, the delay line for the strobe signal would have to be appropriately modified or removed all together. The various gates between pin 12 of U2 and the strobe inputs of U1 likely produce sufficient delay for the data to settle before strobing.

This design is relatively rudimentary and could likely be specialized for other tasks, such as involving a VCO and PLL type system to produce higher frequencies.

Comment: all options on this design have not been tested.

D.4.9 Soldering Method

We used solder paste (Kester water based solder paste, KE1512-ND from Digikey electronics). The solder paste is applied to the pins and the the backplane of the DDS IC. We also used the solder paste on the voltage regulators. For the solder reflow, we used a standard toaster oven and brought the temperature to about 220°C. Note: the DDS is a moisture sensitive device, so we first baked it out at about 120°C for several hours. See [73] for amateur solder paste ideas. We first filled the holes on the backplane pads for both the DDS and the voltage regulators with solder and did the baking on a steel plate so the solder did not drip out of the holes.

Appendix E

Optics Concepts

E.1 Beam Propagation

Summary in this section follows after that of many standard optics texts (see for example [22, 74]). It is given here for its relevance to the optical traps described in Chapter 5.

E.1.1 The Propagation Equation

An electromagnetic wave may be written as

$$U(\mathbf{r}, z, t) = U(\mathbf{r}, z)e^{i\omega t}, \quad (\text{E.1})$$

where $\omega/2\pi$ is the frequency of the wave and $U(\mathbf{r}, z)$ is the complex amplitude, the coordinates are $(\mathbf{r}, z) = (x, y, z)$. Propagation of this wave may be derived from the wave equation, giving the Helmholtz equation:

$$(\nabla^2 + k^2)U(\mathbf{r}, z) = 0. \quad (\text{E.2})$$

The complex amplitude may be written

$$U(\mathbf{r}, z) = A(\mathbf{r}, z)e^{-ikz}, \quad (\text{E.3})$$

where $k = \omega/c$ is the wave vector along the propagation direction z and $A(\mathbf{r})$ is the complex envelope. Under paraxial assumption where

$$\frac{\partial A}{\partial z} \ll kA, \quad \frac{\partial^2 A}{\partial z^2} \ll k^2 A, \quad (\text{E.4})$$

where the envelope can be considered to be slowly varying the Helmholtz equation becomes

$$\frac{\partial^2 A}{\partial x^2} + \frac{\partial^2 A}{\partial y^2} - i2k \frac{\partial A}{\partial z} = 0. \quad (\text{E.5})$$

The paraxial Helmholtz equation describes the propagation of beams. The solutions for the complex envelope describe the shape of the beams. Some of the relevant solutions are given below in terms of intensity:

$$I(\mathbf{r}, z) = |U(\mathbf{r}, z)|^2. \quad (\text{E.6})$$

E.1.2 Gaussian Beams

The zeroth order solution is the gaussian beam. The intensity is

$$I(r, z) = \frac{2P}{\pi w^2(z)} e^{-2r^2/w^2(z)}, \quad (\text{E.7})$$

where P is the total beam power and $w(z)$ is the waist radius at some position along the propagation axis. The *beam waist radius* is $w_0 = w(0)$ and the peak intensity is $I_0(z) = 2P/\pi w^2(z)$. Beam waist radius dependance on propagation distance z is given by

$$w(z) = w_0 \sqrt{1 + \left(\frac{\lambda z}{\pi w_0^2} \right)^2} \cong \frac{\lambda z}{\pi w_0}, \quad (\text{E.8})$$

The second equation is in the limit $z \gg z_0$. The depth of focus (twice Rayleigh range) is

$$2z_0 = \frac{2\pi w_0^2}{\lambda}. \quad (\text{E.9})$$

E.1.3 Hermite-Gaussian Beams

The complex amplitude of the Hermite-Gaussian beam is given by

$$A_{l,m}(x, y, z) = A_{l,m} \left(\frac{w_0}{w(z)} \right) G_l \left[\frac{\sqrt{2}x}{w(z)} \right] G_m \left[\frac{\sqrt{2}y}{w(y)} \right] e^{ikz + ik\frac{r^2}{2R(z)} - i(l+m+1)\zeta(z)} \quad (\text{E.10})$$

where

$$G_l(u) = H_l(u) e^{-\frac{u^2}{2}}, \quad (\text{E.11})$$

is the Hermite-Gaussian function of order l and $H_l(u)$ is the Hermite polynomial of order l . It is possible to find Hermite polynomials using the recursive relation

$$H_{l+1}(u) = 2uH_l(u) - 2lH_{l-1}(u) \quad (\text{E.12})$$

and

$$H_0(u) = 1 \quad (\text{E.13})$$

$$H_1(u) = 2u. \quad (\text{E.14})$$

By taking the square of the complex amplitude, the intensity distribution is determined to be

$$I_{l,m}(x, y, z) = |A_{l,m}|^2 \left(\frac{w_0}{w(z)} \right)^2 G_l^2 \left[\frac{\sqrt{2}x}{w(z)} \right] G_m^2 \left[\frac{\sqrt{2}y}{w(y)} \right]. \quad (\text{E.15})$$

This is a generalization of the Gaussian beam, which from this equation is the lowest order member of the Hermite-Gaussian family.

By letting $l = 0$ and $m = 1$, the intensity pattern is given by

$$I_{0,1}(x, y, z) = \frac{P}{\pi w_x(z) w_y(z)} \frac{8x^2}{w_x^2(z)} e^{-\frac{2x^2}{w_x^2(z)}} e^{-\frac{2y^2}{w_y^2(z)}}, \quad (\text{E.16})$$

in terms of the beam power P . This mode is known as a Hermite-Gaussian TEM₀₁ mode.

E.2 Fourier Optics

The concepts of Fourier optics are given in a number of texts such as in references [74, 75]. Here, we only summarize some of the relevant concepts and equations referred to in the text with regard to our TEM₀₁ mode beams, but Fourier optics has general interest and applications.

We can consider free-space propagation in the far field. This is to view the result of propagation in the Fraunhofer approximation as a Fourier transform of the initial beam. It is similarly true that a lens may image as a Fourier transform. This is especially a relevant view of beam propagation when referring to the production of the TEM₀₁ mode beams.

An optical element with transmittance $f(x, y)$ may be written as a decomposition into harmonic functions with *spatial frequencies* ν_x and ν_y as in

$$f(x, y) = \int_{-\infty}^{\infty} \int_{-\infty}^{\infty} F(\nu_x, \nu_y) e^{-i2\pi(\nu_x x + \nu_y y)} d\nu_x d\nu_y, \quad (\text{E.17})$$

where $F(\nu_x, \nu_y)$ represents the complex amplitudes (Fourier transform) of the components of $f(x, y)$ obtained from the reverse Fourier transform

$$F(x, y) = \int_{-\infty}^{\infty} \int_{-\infty}^{\infty} f(\nu_x, \nu_y) e^{-i2\pi(\nu_x x + \nu_y y)} d\nu_x d\nu_y. \quad (\text{E.18})$$

The transmitted wave is then given by

$$U(x, y, z) = \int_{-\infty}^{\infty} \int_{-\infty}^{\infty} F(\nu_x, \nu_y) e^{-i2\pi(\nu_x x + \nu_y y)} e^{-ik_z z} d\nu_x d\nu_y, \quad (\text{E.19})$$

The spatial frequencies correspond to harmonic components in the plane of the object and have corresponding propagation angles $\sin \theta_x = \lambda \nu_x$ and $\sin \theta_y = \lambda \nu_y$, where λ is the wavelength of the light. Which reveals that high spatial frequencies correspond to larger angles. In the paraxial approximation, where the angles are small, they may be approximated by $\theta_x = \lambda \nu_x$ and $\theta_y = \lambda \nu_y$.

At some long propagation distance d , so that $b^2/\lambda d \ll 1$ where b is the radius of extent of $U(x, y)$ in the plane, it can be shown that the only contribution to the output plane is made by the waves making angles $\theta_x = x/d$ and $\theta_y = y/d$ which has corresponding amplitude $F(\nu_x, \nu_y)$ at spatial frequencies $\nu_x = x/\lambda d$ and $\nu_y = y/\lambda d$. In this case, the radial profile at distance d is given by

$$U(x, y, d) = \frac{i}{\lambda d} e^{-i2\pi d/\lambda} F\left(\frac{x}{\lambda d}, \frac{y}{\lambda d}\right), \quad (\text{E.20})$$

and the intensity profile given by

$$I(x, y, d) = \frac{1}{\lambda^2 d^2} \left| F\left(\frac{x}{\lambda d}, \frac{y}{\lambda d}\right) \right|^2. \quad (\text{E.21})$$

This result is the Fraunhofer approximation.

It can also be shown that a lens produces a Fourier transform. This result is valid in the Fresnel zone and doesn't require as strict of a condition as that for the Fraunhofer approximation. A lens in a 2f system gives an output field on its imaging plane of

$$\tilde{U}(x, y) = \frac{i}{\lambda f} e^{-i2\pi f/\lambda} F\left(\frac{x}{\lambda f}, \frac{y}{\lambda f}\right), \quad (\text{E.22})$$

which is similar in form to the far field result.

E.3 Optical Modulators

E.3.1 Acousto-Optic Modulators

Our experiment uses many acousto-optic modulators (AOMs) for a variety of purposes as discussed in the preceding chapters. The two basic characteristics of the AOM's output beam is the laser frequency shift at the driving frequency and the deflection angle. The first property is used for beams of the 780 nm system to carefully tune the laser wavelength. The second is use in the far off resonance 532 nm optical traps to produce a variety of designer traps. In this section we give some of the basics of the operation of AOMs and summarize some of the results in Ref. [76] putting them into a context relevant to our experiment.

Figure E.1 gives a functional diagram of an AOM. The diffraction condition may be written as

$$2k \sin \theta = m \frac{2\pi}{\Lambda}, \quad (\text{E.23})$$

where $m = 0, \pm 1, \dots$ is the diffraction order, θ is the incident and diffracted

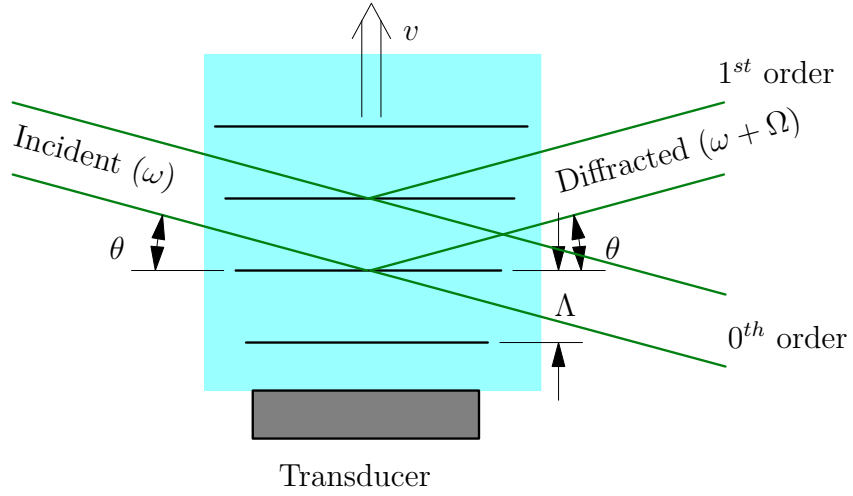


Figure E.1: Functional diagram of an acousto-optic modulator. The blue square represents an acousto-optic crystal with an attached transducer. The first order output beam is a diffraction order of the acoustic wave shown traveling with velocity v and wavelength Λ .

angle as shown, $k = 2\pi/\lambda$ is the wavevector of the light, and Λ is the wavelength of the acoustic wave. The frequency of the driving RF of the device is $f = \Omega/2\pi$ and the frequency of the laser beam is $\omega/2\pi$. The frequency shift due to the doppler effect of the outgoing first order is given by $\Delta\omega = 2\omega v_{\parallel}/c$ where $v_{\parallel} = v \sin \theta$. This shows the shift to be $\Delta\omega = 2\pi v/\Lambda = \Omega$, 2π the RF drive frequency. The angle given by Equation E.23 is typically small and may be approximated as

$$\theta \cong \frac{\lambda}{2\Lambda} = \frac{\lambda f}{2v} \quad (\text{E.24})$$

for the $m = 1$ first order. The diffraction efficiency into the first order may be

written

$$\begin{aligned}\eta = \frac{I_1}{I_0} &= \sin^2 \left(\frac{\pi L}{\lambda \sqrt{2} \cos \theta} \sqrt{M I_{\text{ac}}} \right), \\ &\cong \sin^2 \left(2.22 \sqrt{\frac{L}{H} \frac{1}{\lambda^2} M P_{\text{ac}}} \right),\end{aligned}\tag{E.25}$$

where L and H are the interaction length and height, I_{ac} and P_{ac} are the acoustic intensity and power, and M is the figure of merit of the crystal [76]. In the second equation, the approximation $\cos \theta \cong 1$ is made.

For a typical optical trap AOM on our experiment uses $\Omega = 2\pi \times 110$ MHz, with a TeO_2 crystal $v = 4.2 \times 10^3$ m/s and $M = 4 \times 10^{-15}$ m²/W, for optical trap light at 532 nm, $\theta \cong 7.0 \times 10^{-3}$ rad for the first order.

E.3.2 Electro-Optic Modulators

We use a few electro-optic modulators for intensity control of the vertical TEM_{01} optical trapping beam.

The basic operation of an EOM is to provide a high voltage (± 500 V in our case) across a birefringent crystal producing a voltage controlled wave plate. This, in conjunction with input and output polarizing beam splitter cubes gives and intensity transmission of

$$T = \frac{I}{I_0} = \sin^2 \left(\frac{\pi}{2} \frac{V}{V_{\lambda/2}} \right),\tag{E.26}$$

where $V_{\lambda/2}$ is the *half-wave voltage* which characterized the EOM and V is the applied voltage.

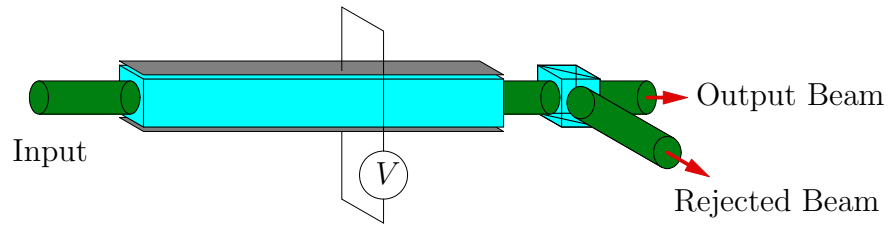


Figure E.2: Pictorial diagram of an electro-optic modulator.

We use two EOMs in series for the mentioned beam, each which provide about 1:500 extinction. They are controlled directly from the computer analog outputs through a pair of high-voltage amplifiers.

Appendix F

Rubidium Properties

Here, we summarize some of the properties of our favorite atom: rubidium. Most of this information is from Reference [77] which is a much more complete look at the atom's properties.

Because of the high vapor pressure of rubidium at room temperature, we are able to operate our upper MOT as a vapor cell. A evacuated small glass break ampoule of about 1/4 gram of Rb metal is in a copper pinch-off tube in the upper chamber. After completion of the pump down sequences and bake outs the ampoule was broken and then mildly heated for a few weeks until Rb was present in the upper chamber. From that time on, the operation of the upper MOT relies on the presence of the Rb vapor at pressures of around 3.0×10^{-7} torr in the upper chamber.

As nature gives us, only about 28% of the Rb metal in the chamber is ^{87}Rb . Most of the remainder is ^{85}Rb which is not involved in our experimental operation.

We will write the *saturation intensity* as $I_s = \pi \hbar c \Gamma / 3 \lambda^3$, as in Section 2.1.

Atomic Number	Z	37
Mass	m	87 amu $1.443\,160\,60(11) \times 10^{-25}$ kg
Melting Point	T_M	39.31°C
Vapor Pressure at 25°C	P_v	3.0×10^{-7} torr
Nuclear Spin	I	$3/2$

Table F.1: ^{87}Rb physical properties [77].

Frequency	ω_0	$2\pi \cdot 384.230\,484\,468\,5(62)$ THz
Wavelength	λ	780.241 209 686(13) nm
Lifetime	τ	26.24(4) ns
Decay Rate/ Natural Line Width (FWHM)	Γ	$2\pi \cdot 6.065(9)$ MHz
Recoil velocity	v_r	5.8845 mm/s
Recoil energy	ω_r	$2\pi \cdot 3.7710$ kHz
Recoil Temperature	T_r	361.96 nK
Saturation Intensity	I_s	1.669 mW/cm ²
s-wave scattering length	a	5.29 nm $\cong 100a_0$

Table F.2: ^{87}Rb D_2 ($5^2\text{S}_{1/2} \longrightarrow 5^2\text{P}_{3/2}$) transition optical properties. [77].

Frequency	ω_0	$2\pi \cdot 377.107\,463\,5(4)$ THz
Wavelength	λ	794.978 850 9(8) nm
Lifetime	τ	27.70(4) ns
Decay Rate/ Natural Line Width (FWHM)	Γ	$2\pi \cdot 5.746(8)$ MHz
Recoil velocity	v_r	5.7754 mm/s
Recoil energy	ω_r	$2\pi \cdot 3.6325$ kHz
Recoil Temperature	T_r	348.66 nK
Saturation Intensity	I_s	1.495 mW/cm ²

Table F.3: ^{87}Rb D_1 ($5^2\text{S}_{1/2} \longrightarrow 5^2\text{P}_{1/2}$) transition optical properties. [77].

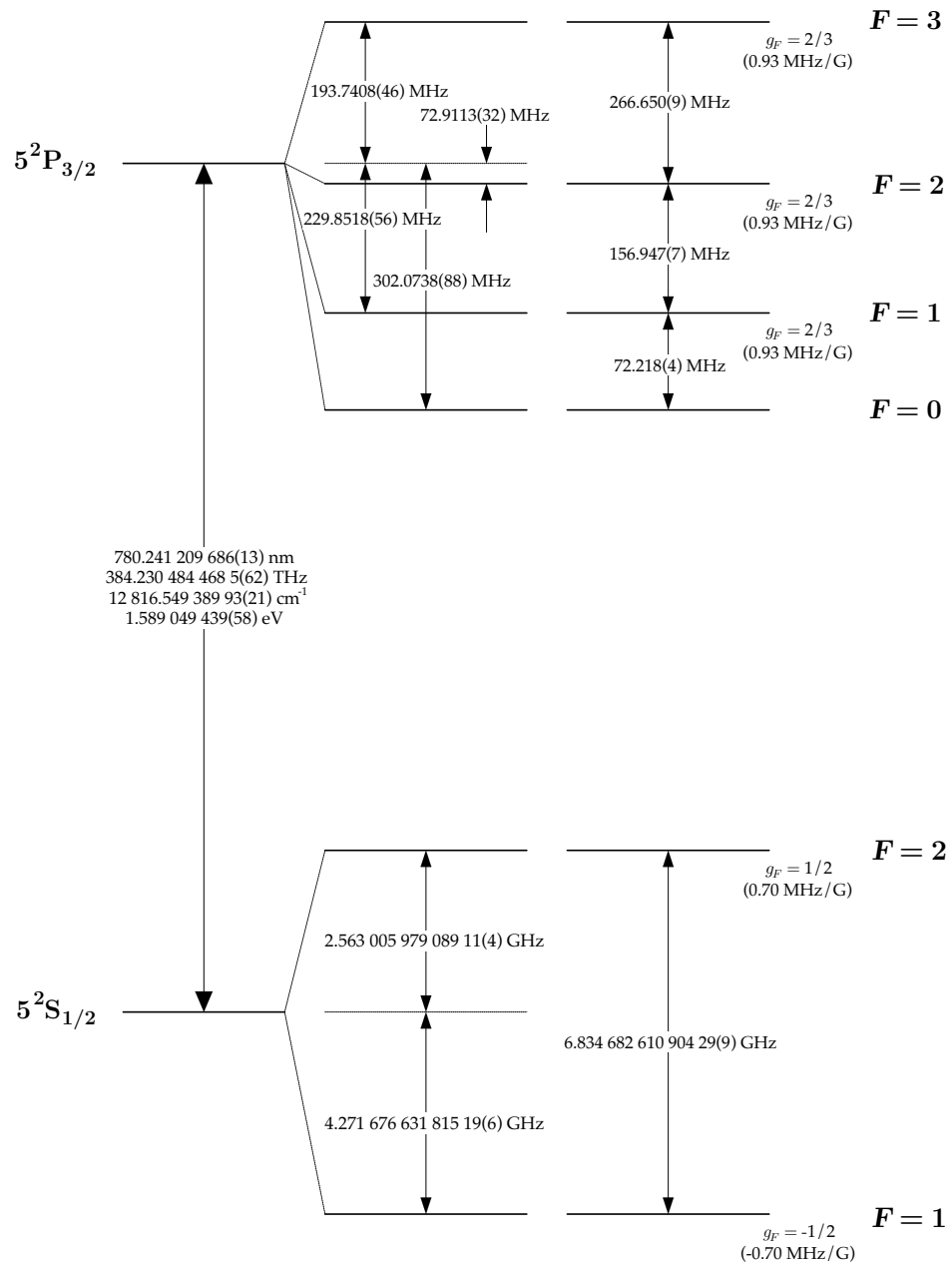


Figure F.1: Rubidium 87 D_2 line hyperfine structure. Figure courtesy of Daniel Steck [77].

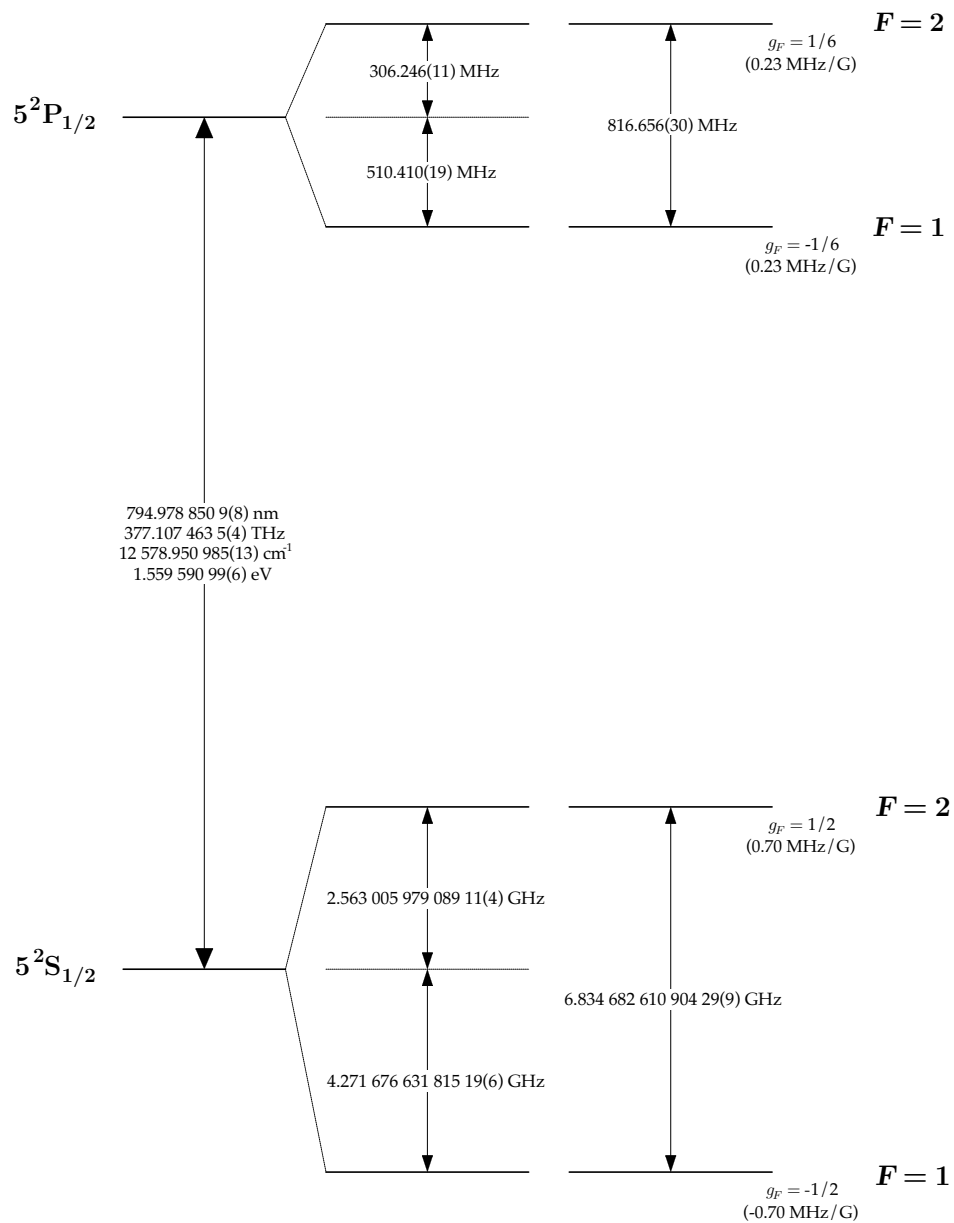


Figure F.2: Rubidium 87 D_1 line hyperfine structure. Figure courtesy of Daniel Steck [77].

Bibliography

- [1] M. H. Anderson, J. R. Ensher, M. R. Matthews, C. E. Wieman, and E. A. Cornell. Observation of Bose-Einstein condensation in a dilute atomic vapor. *Science*, 269:198, 1995.
- [2] K. B. Davis, M.-O. Mewes, M. R. Andrews, N. J. van Druten, D. S. Durfee, D. M. Kurn, and W. Ketterle. Bose-Einstein condensation in a gas of Sodium atoms. *Phys. Rev. Lett.*, 75:3969, 1995.
- [3] P. S. Jessen and I. H. Deutsch. Optical lattices. *Adv. At. Mol. Opt. Phys.*, 37:95–138, 1996.
- [4] M. Greiner, O. Mandel, T. Esslinger, T. W. Haensch, and I. Bloch. Quantum phase transition from a superfluid to a Mott insulator in a gas of ultracold atoms. *Nature*, 415:39, 2002.
- [5] B. Paredes, A. Widera, V. Murg, O. Mandel, S. Fölling, I. Cirac, G.V. Shlyapnikov, T.W. Hänsch, and I. Bloch. Tonks-girardeau gas of ultracold atoms in an optical lattice. *Nature*, 429:277, 2004.
- [6] T. Kinoshita, T. Wenger, and D.S. Weiss. Observation of a one-dimensional tonks-girardeau gas. *Science*, 305:1125, 2004.

- [7] B. Laburthe Tolra, K. M. O'Hara, J. H. Huckans, W. D. Phillips, S. L. Rolston, and J. V. Porto. Observation of reduced three-body recombination in a correlated 1d degenerate bose gas. *Phys. Rev. Lett.*, 92:190401, 2004.
- [8] R. B. Diener, B. Wu, M. G. Raizen, and Q. Niu. Quantum tweezer for atoms. *Phys. Rev. Lett.*, 89, 2002.
- [9] R. Grimm, M. Weidemuller, and Y. Ovchinnikov. Optical dipole traps for neutral atoms. *Adv. At. Mol. Opt. Phys.*, 42:95, 2000.
- [10] Meystre. *Atom Optics*. Springer, 2001.
- [11] Allen and Eberly. *Optical Resonance and Two-Level Atoms*. Dover, 1987.
- [12] Haken and Wolf. *The Physics of Atoms and Quanta*. Springer, 5th edition, 1996.
- [13] B. Gutierrez-Medina. *Quantum Transport and Atomic Motion Control Using Light*. PhD thesis, The University of Texas at Austin, 2004.
- [14] W. Wohlleben, F. Chevy, K. Madison, and J. Dalibard. An atom faucet. *Eur. Phys. J. D*, 15:237, 2001.
- [15] A. Chambers, R. K. Fitch, and B. S. Halliday. *Basic Vacuum Technology*. Institute of Physics Publishing, 1998.
- [16] Kirk Madison. private communication.

- [17] D. A. Steck. *Quantum Chaos, Transport, and Decoherence in Atom Optics*. PhD thesis, The University of Texas at Austin, 2001.
- [18] W. H. Oskay. *Atom Optics Experiments in Quantum Chaos*. PhD thesis, The University of Texas at Austin, 2001.
- [19] B. G. Klappauf. *Experimental Studies of Quantum Chaos with Trapped Cesium*. PhD thesis, The University of Texas at Austin, 1998.
- [20] T.P. Meyrath. Inexpensive mechanical shutter and driver for optics experiments.
george.ph.utexas.edu/~meyrath/informal, May 2003.
- [21] W. Demtröder. *Laser Spectroscopy*. Springer, 1998.
- [22] Seigman. *Lasers*. University Science Books, 1986.
- [23] K. B. MacAdam, A. Steinbach, and C. Wieman. A narrow-band tunable diode laser system with grating feedback, and a saturated absorption spectrometer for cs and rb. *Am. J. Phys.*, 60:1098, 1992.
- [24] C. E. Wieman and L. Hollberg. Using diode lasers for atomic physics. *Rev. Sci. Instrum.*, 62:1, 1991.
- [25] T. Esslinger, I. Bloch, and T. W. Hansch. Bose-Einstein condensation in a quadrupole-Ioffe-configuration trap. *Phys. Rev. A*, 58:R2664, 1998.
- [26] D. Pritchard. Cooling neutral atoms in a magnetic trap for precision spectroscopy. *Phys. Rev. Lett.*, 51:1336, 1983.

- [27] W. D. McCormick. Private communication.
- [28] T.P. Meyrath and F. Schreck. A laboratory control system for cold atom experiments: Hardware and software.
`george.ph.utexas.edu/~control`, March 2004.
- [29] F. Schreck. *Mixtures of Ultracold Gases: Fermi Sea and Bose-Einstein Condensate of Lithium Isotopes*. PhD thesis, École Normale Supérieure, 2002.
- [30] J. Dalibard and C. Cohen-Tannoudji. Laser cooling below the doppler limit by polarization gradients - simple theoretical models. *J. Opt. Soc. Am. B*, 6:2023, 1989.
- [31] P. J. Ungar, D. S. Weiss, S. Chu, and E. Riis. Optical molasses and multilevel atoms - theory. *J. Opt. Soc. Am. B*, 6:2058, 1989.
- [32] O. J. Luiten, M. W. Reynolds, and J. T. M. Walraven. Kinetic theory of the evaporative cooling of a trapped gas. *Phys. Rev. A*, 53:381, 1996.
- [33] H. J. Metcalf and P. van der Straten. *Laser Cooling and Trapping*. Springer, 1999.
- [34] A.H. Carter. *Classical and Statistical Thermodynamics*. Prentice Hall, 2001.
- [35] S. Kuhr, W. Alt, D. Schrader, M. Muller, V. Gomer, and D. Meschede. Deterministic delivery of a single atom. *Science*, 293:278, 2001.

- [36] W. Alt. An objective lens for efficient fluorescence detection of single atoms. *Optik*, 113:142, 2002.
- [37] L. Pitaevskii and S. Stringari. *Bose-Einstein Condensation*. Oxford University Press, 2003.
- [38] C. J. Pethick and H. Smith. *Bose-Einstein Condensation in Dilute Gases*. Cambridge University Press, 2002.
- [39] L.D. Landau and E.M. Lifshitz. *Statistical Physics*. Butterworth-Heinemann, 3rd edition, 2000.
- [40] L.D. Landau and E.M. Lifshitz. *Quantum Mechanics*. Butterworth-Heinemann, 3rd edition, 2000.
- [41] D. Guery-Odelin. *Dynamique Collisionnelle des Gaz d'Alcalins Lourds: du Refroidissement Evaporatif a la Condensation de Bose-Einstein*. PhD thesis, École Normale Supérieure, 1998.
- [42] A. Görlitz, J. M. Vogels, A. E. Leanhardt, C. Raman, T. L. Gustavson, J. R. Abo-Shaeer, A. P. Chikkatur, S. Gupta, S. Inouye, T. Rosenband, and W. Ketterle. Realization of Bose-Einstein condensates in lower dimensions. *Phys. Rev. Lett.*, 87:130402, 2001.
- [43] T.P. Meyrath, F. Schreck, J.L. Hanssen, C-S. Chuu, and M.G. Raizen. Bose-einstein condensate in a box. *Phys. Rev. A*, 71:041604(R), 2005.

- [44] T.P. Meyrath, F. Schreck, J.L. Hanssen, C-S. Chuu, and M.G. Raizen. A high frequency optical trap for atoms using hermite-gaussian beams. *Optics Express*, 13:2843–2851, 2005.
- [45] K. Bongs, S. Burger, S. Dettmer, D. Hellweg, J. Arlt, W. Ertmer, and K. Sengstock. Waveguide for bose-einstein condensates. *Phys. Rev. A*, 63:031602, 2001.
- [46] Y. Castin and R. Dum. Bose-Einstein condensates in time dependent traps. *Phys. Rev. Lett.*, 77:5315, 1996.
- [47] A. E. Leanhardt, Y. Shin, A. P. Chikkatur, D. Kielpinski, W. Ketterle, and D. E. Pritchard. Bose-einstein condensates near a microfabricated surface. *Phys. Rev. Lett.*, 90:100404, 2003.
- [48] D. Haubrich, H. Scadwinkel, F. Strauch, B. Ueberholz, R. Wynands, and D. Meschede. Observation of individual neutral atoms in magnetic and magneto-optical traps. *Europhys. Lett.*, 34:663, 1996.
- [49] D. S. Petrov, G. V. Shlyapnikov, and J. T. M. Walraven. Regimes of quantum degeneracy in trapped 1d gases. *Phys. Rev. Lett.*, 85:3745, 2000.
- [50] N. Freidman, A. Kaplan, and N. Davidson. Dark optical traps for cold atoms. *Adv. At. Mol. Opt. Phys.*, 48:99, 2002.

- [51] N.L. Smith, W.H. Heathcote, G. Hechenblaikner, E. Nugent, and C.J. Foot. Quasi-2d confinement of a bec in a combined optical and magnetic potential. *J. Phys. B: At. Mol. Opt. Phys.*, 38:223–235, 2005.
- [52] A. M. Dudarev, R. B. Diener, B. Wu, M. G. Raizen, and Q. Niu. Entanglement generation and multiparticle interferometry with neutral atoms. *Phys. Rev. Lett.*, 91:010402, 2003.
- [53] M. A. Nielsen and I. L. Chuang. *Quantum Computation and Quantum Information*. Cambridge University Press, 2000.
- [54] Z. Hu and H. J. Kimble. Observation of a single atom in a magneto-optical trap. *Opt. Lett.*, 19:1888, 1994.
- [55] F. Ruschewitz, D. Bettermann, J. L. Peng, and W. Ertmer. Statistical investigations on single trapped neutral atoms. *Europhys. Lett.*, 34:651, 1996.
- [56] D. Haubrich, H. Scadwinkel, F. Strauch, B. Ueberholz, R. Wynands, and D. Meschede. Observation of individual neutral atoms in magnetic and magneto-optical traps. *Europhys. Lett.*, 34:663, 1996.
- [57] S. Kuhr, W. Alt, D. Schrader, M. Muller, V. Gomer, and D. Meschede. Deterministic delivery of a single atom. *Science*, 293:278, 2001.
- [58] N. Schlosser, G. Reymond, I. Prosenko, and P. Grangier. Sub-Poissonian loading of single atoms in a microscopic dipole trap. *Nature*, 411:1024, 2001.

- [59] D. Jaksch, C. Bruder, J. I. Cirac, C. W. Gardiner, and P. Zoller. Cold bosonic atoms in optical lattices. *Phys. Rev. Lett.*, 81:3108, 1998.
- [60] R. B. Diener. *Quantum Dynamics of Trapped Ultracold Atoms*. PhD thesis, The University of Texas at Austin, 2003.
- [61] A. Dudarev. *Dynamics of Ultracold Atoms in Optical Potentials*. PhD thesis, The University of Texas at Austin, 2005.
- [62] C. Zener. Non-adiabatic crossing of energy levels. *Proc. R. Soc. London, Ser. A*, 137:696, 1932.
- [63] Bergeman, Erez, and Metcalf. Magnetostatic trapping fields for neutral atoms. *Phys. Rev. A*, 35:1535–1546, 1987.
- [64] Spiegel and Liu. *Mathematical Handbook of formulas and tables*. McGraw Hill, 2nd edition, 1999.
- [65] Moore, Davis, and Coplan. *Building Scientific Apparatus*. Perseus Books, 2nd edition, 1991.
- [66] Ramo, Whinnery, and Van Duzer. *Fields and Waves in Communication Electronics*. Wiley, 3rd edition, 1994.
- [67] J. Carr. *Secrets of RF Circuit Design*. McGraw Hill, 2001.
- [68] T.P. Meyrath. Quic trap schematics. george.ph.utexas.edu/~meyrath/informal, May 2003.

- [69] T.P. Meyrath. Multipurpose analog pid.
george.ph.utexas.edu/~meyrath/informal, March 2005.
- [70] Hrishikesh Kelkar. private communication.
- [71] T.P. Meyrath. An analog current controller design for laser diodes.
george.ph.utexas.edu/~meyrath/informal, November 2003.
- [72] T.P. Meyrath. Precision analog optocoupler.
george.ph.utexas.edu/~meyrath/informal, July 2002.
- [73] Kenneth Maxon. Have you seen my new soldering iron?
www.seattlerobotics.org/encoder/200006/oven_art.htm.
- [74] Saleh and Teich. *Fundamentals of Photonics*. Wiley, 1991.
- [75] Goodman. *Introduction to Fourier Optics*. McGraw Hill, 2nd edition, 1996.
- [76] Yariv and Yeh. *Optical Waves in Crystals*. Wiley, 1984.
- [77] Daniel Steck. Rubidium D₂ line data. 2002.

Vita

Todd Philip Meyrath was born on August 1, 1975 in Rochester, New York as the son of Frank and Donna Meyrath. He attended Clarke Central High School in Athens, Georgia. In 1998, he was awarded Bachelor of Science in Physics and Bachelor of Science in Applied Mathematics degrees with Highest Honor from The Georgia Institute of Technology. Todd received Master of Science in Applied Physics from The University of Texas at Austin in 2000 and Master of Science in Electrical Engineering from The California Institute of Technology in 2001.

Permanent address: 255 Selkirk Ln.
Duluth, Georgia 30097

This dissertation was typeset with \LaTeX^\dagger by the author.

[†] \LaTeX is a document preparation system developed by Leslie Lamport as a special version of Donald Knuth's \TeX Program.